University of Southampton Research Repository
ePrints Soton

Copyright © and Moral Rights for this thesis are retained by the author and/or other copyright owners. A copy can be downloaded for personal non-commercial research or study, without prior permission or charge. This thesis cannot be reproduced or quoted extensively from without first obtaining permission in writing from the copyright holder/s. The content must not be changed in any way or sold commercially in any format or medium without the formal permission of the copyright holders.

When referring to this work, full bibliographic details including the author, title, awarding institution and date of the thesis must be given e.g.

AUTHOR (year of submission) "Full thesis title", University of Southampton, name of the University School or Department, PhD Thesis, pagination

http://eprints.soton.ac.uk

UNIVERSITY OF SOUTHAMPTON

Faculty of Social and Human Sciences

School of Mathematics

Frequency domain approach to self-force calculations

by

Niels Jamie Warburton

A thesis submitted in partial fulfillment for the
degree of Doctor of Philosophy

8th June 2012

UNIVERSITY OF SOUTHAMPTON

ABSTRACT

FACULTY OF SOCIAL AND HUMAN SCIENCES
SCHOOL OF MATHEMATICS

Doctor of Philosophy

by Niels Jamie Warburton

In this thesis, the problem of computing the back-reaction, or self-force, caused by a point particle interacting with its own field is studied. In particular, motivated by the prospect of detecting gravitational waves from extreme mass ratio inspiral systems, we consider the motion of the particle in black hole spacetimes. As a toy model for the most astrophysically relevant scenario of orbits about a rotating black hole we first study the scalar-field self-force (SSF) experienced by a scalar charge moving on a fixed geodesic in Kerr spacetime for a variety of orbits. Our approach is to work in the frequency domain, fully decomposing the scalar field into spheroidal harmonic and frequency modes and numerically solving for the retarded field mode-by-mode. Regularization of the retarded field is performed using the standard mode-sum technique which requires spherical harmonic modes as input, which we obtain by projecting the spheroidal harmonic modes on to a basis of spherical harmonics.

We find for circular, equatorial orbits that the black hole spin can have a pronounced effect on the conservative piece of the SSF, causing it to (with respect to the Schwarzschild scalar-field self-force) change sign for certain spins and orbital radii. For eccentric orbits in the equatorial plane, we make use of the recently introduced method of extended homogeneous solutions to overcome the Gibbs phenomenon associated with a naïve approach. As an application of our work we compute the shift to the innermost stable circular orbit due to the conservative piece of the scalar-field self-force for a variety of black hole spins. We also present some preliminary results for the SSF along circular, inclined geodesics.

As well as studying the toy model SSF, we also consider the gravitational self-force (GSF) problem in the context of orbits around a Schwarzschild black hole. Our approach is again to work in the frequency domain, and we perform a complete decomposition of the metric perturbation in tensor spherical harmonics and frequency modes. The ten metric perturbation fields decouple with respect to the multipole indices but remain coupled within each spherical harmonic mode. We solve the resulting coupled sets numerically with a code set up to run on a computer cluster. Regularization is again performed using the mode-sum technique.

Our resulting code is extremely efficient for low eccentricity orbits, and using it we compute the GSF for a great many points in the orbital parameter space. With these results we fit an analytic model to our numerical data and then use a relativistic osculating elements scheme to evolve the orbital inspiral. This allows us, for the first time, to assess the contribution to a complete inspiral from the conservative piece of the gravitational self-force.

Finally, as an aside, we investigate the recently discovered phenomenon of isofrequency orbits, whereby it is possible to have pairs of physically distinct bound geodesics about a Kerr black hole that share the same three orbital frequencies.

Contents

List of Figures

List of Tables

List of Acronyms

CO	Compact Object
EHS	Extended Homogeneous Solution
EMRI	Extreme Mass Ratio Inspiral
EOB	Effective One Body
FD	Frequency Domain
GSF	Gravitational Self Force
ISCO	Innermost Stable Circular Orbit
ISCEO	Innermost Stable Circular Equatorial Orbit
IMRI	Intermediate Mass Ratio Inspiral
LIGO	Laser Interferometer Gravitational-wave Observatory
LISA	Laser Interferometer Space Antenna
NR	Numerical Relativity
PN	Post-Newtonian
RA	Radiative Approximation
SSF	Scalar-field Self Force
SF	Self Force
TD	Time Domain

List of Publications

1. N. Warburton, L. Barack. Scalar self-force in Kerr spacetime: circular, equatorial orbits *Phys. Rev. D.*, 81, 084039 (2010).
2. N. Warburton, L. Barack. Scalar self-force in Kerr spacetime: eccentric, equatorial orbits *Phys. Rev. D.*, 83, 124038 (2011).
3. N. Warburton, S. Akcay, L. Barack, J. Gair, N. Sago. Evolution of inspiral orbits around a Schwarzschild black hole *Phys. Rev. D*, 85, 061501(R) (2012).

DECLARATION OF AUTHORSHIP

I, **Niels Jamie Warburton**, declare that the thesis entitled **Frequency domain approach to self-force calculations** and the work presented in the thesis are both my own, and have been generated by me as the result of my own research. I confirm that:

- this work was done wholly or mainly while in candidature for a research degree at this University;
- if any part of this thesis has previously been submitted for a degree or any other qualification at this University or any other institution, this has been clearly stated;
- where I have consulted the published work of others, this is always clearly attributed;
- where I have quoted from the work of others, the source is always given. With the exception of such quotations this thesis entirely my own work;
- I have acknowledged all main sources of help;
- where the thesis is based on work done by myself jointly with others, I have made clear exactly what was done by others and what I have contributed myself;
- parts of this work have been published.

Signed:

Date: *23rd April 2012*

Acknowledgements

I have the impression that too few people are employed with work they are passionate about; the kind of work that, if money were no objective, they would still undertake simply for the pleasure of it. Consequently, I feel incredibly privileged to have spent the last three and a half years doing precisely that. Nonetheless, passion alone is not enough to see the job through. In my experience the path of research is rarely smooth and I am extremely grateful for the friendship and support I have met along the way. I would like to thank some of those people now. The successes of this thesis are as much theirs as they are mine, for none of it would have been possible without them.

First and foremost I wish to thank my supervisor Leor Barack. His guidance and clear physical insight has been, and remains, a constant source of inspiration. Working along side Leor as part of the general relativity group at Southampton has been a pleasure. Leor is of course the primary person with whom I have collaborated in my research though he was not he only one. I also wish to thank my other collaborators: Sarp Akcay, Jonathan Gair and Norichika Sago.

Those working on the self-force problem gather together annually for the Capra meeting and I am grateful to all the attendees for the many insightful discussions I have had and the talks I have seen. I have learned much from them. Of the Capra crew I particular wish to thank (in chronological order of meeting) Sam Dolan, Barry Wardell, Anna Heffernan and Patrick Nolan, with all of whom I have shared adventures over the past three and a half years.

I would also like to thank my examiners, Carsten Gundlach and Eric Poisson, for taking the time to read this thesis. Their comments and feedback were warmly received and have resulted in a much more polished final document.

A special mention must go to both César López-Monsalvo and Sarp Akcay: César for our many fantastic discussions of physics, some of which have found their way into this thesis; Sarp for his friendship and the journeys we have had together.

I am also grateful to my army of proof readers who got the job done in record time. In alphabetical order, they are: Stephanie Erickson, Michael Hogg, Lucy Keer, Christian Krüger, Tim Lemon, César Merlín-González, John Muddle and Stuart Wells. Between them they added over five hundred commas to this work!

Last but not least I would like to thank my family for their unwavering support. In particular I am grateful to my brother Sam and his wife Maddie for their hospitality over the years.

To my mother and father for their constant support in everything I do and for always fostering my curiosity about the world.

Chapter 1

Introduction

Gravitational wave astronomy promises to be an exciting and rewarding field over the coming decades. Practically unaffected by any intervening matter between the source and the Earth, gravitational waves should allow us to peer deep into some of the most violent events in the universe as well as allowing us to probe the strong field predictions of Einstein's general relativity. Expected sources of gravitational waves include many interesting astrophysical phenomena such as black hole mergers, neutron star dynamics and supernovae.

With the ongoing upgrade of the most sensitive gravitational wave detector, the Laser Interferometer Gravitational Wave Observatory (LIGO) [1], the gravitational wave community is confident of the first gravitational wave detection occurring within the decade. Given the sensitivity that LIGO and other detectors [2, 3] are now approaching, as well as reasonable estimates on the event rates of various gravitational wave sources, failure to detect gravitational waves would be a major problem for the theory of general relativity.

Once initial detection is made, attention will move to extracting interesting science from the incoming waves. The strain from gravitational waves reaching the Earth is expected to be extremely small, being on the order of 1 part in 10^{22}. To give an idea of how minuscule this change is, in a 4km long interferometric detector (such as LIGO) the change in the arm length induced by the passing of a gravitational wave is over a thousand times smaller than the diameter of a single proton. Consequently the incoming signal is extremely difficult to separate from the detector noise, and thus to detect gravitational waves from many of the sources of interest, good theoretical models have to be produced, so that matched filtering techniques can be applied: the idea here being that the more information you have about what you seek, the easier it is to find. Looking for a needle in a haystack is a challenging task, but if we know some properties of the needle we seek (such as that it is composed of a ferrous metal), then it is much easier to extract (use a magnet!) [4].

LIGO's sensitivity is greatest in the 1Hz to a few kHz range. Detection of signals below the 1Hz cut-off is extremely challenging because of the seismic noise present in and around the detector. For detection of gravitational waves with frequencies below 1Hz, we look to space-based missions such as the planned European Space Agency (ESA) mission, eLISA [5], pencilled in for launch around 2025. eLISA is expected to be sensitive to gravitational waves in the 1mHz to 0.1Hz range. This will allow it to explore a complementary set of sources to those that LIGO will observe. Included in this list of observable sources are Extreme Mass Ratio Inspirals (EMRIs).

EMRIs are binary systems where one of the bodies is significantly more massive than the other. Typical eLISA-band systems consist of a massive black hole with mass, M, of the order of

$10^6 M_\odot$ orbited by a smaller compact object (CO) of mass, μ, in the range of $1-10M_\odot$. To leading order in the mass ratio, the compact body's dynamics can be considered to be that of a point particle. This is a convenient description as it allows for a universal formulation of the particle's motion independent of its internal dynamics, allowing one to draw general conclusions about the body's motion regardless of whether it is, say, a black hole or a neutron star. Unfortunately this universality comes at a price as within a point particle model the back reaction of the particle's own field upon its motion cannot be naïvely computed as the gradient of the field at the particle's location, because precisely at that location a point-particle's field diverges. Thus, in order to perform practical calculations this divergence has to be carefully removed via an appropriate regularization scheme.

The appropriate regularization procedure was first identified by Mino, Sasaki and Tanaka [6] and Quinn and Wald [7] in 1997. Their regularization formula (the 'MiSaTaQuWa' equation) was not particular useful for practical calculations, and so shortly after, their results were recast into a more practical form by Barack and Ori [8], and we make use of their 'mode-sum scheme' in this work. Since 1997 great strides have been made (see Sec. 1.3 below) towards the 'holy grail' of self-force research: computation of theoretical gravitational waveforms, including all first-order-in-the-mass-ratio effects, from an extreme mass ratio binary in the case where the central object is a rotating Kerr-type black hole. In this thesis we present further work towards this goal in the form of the first calculation of the SF for a particle in a realistic orbit in Kerr spacetime (for a toy scalar-field model) and a new calculation of the gravitational self-force (GSF) about a non-rotating Schwarzschild black hole. In both cases we worked in the frequency domain (FD) when making our calculations and we justify this approach below (Sec. 1.4). Lastly we remark that all previous GSF calculations have been for the case of a particle moving on a geodesic of the background spacetime; there have been no calculations where the GSF has been allowed to back react upon the particle and modify its motion. In this thesis, for the first time, we compute an orbital inspiral including all first-order-in-the-mass-ratio effects for a particle in orbit about a Schwarzschild black hole. In computing the inspiral we use an osculating orbit technique, and thus, whilst this is a step forward, we must add that important questions remain regarding the approximation we use to evolve the inspiral using our FD data.

1.1 Astrophysical Motivation

We now consider the astrophysical case for the work we present in this thesis. This broadly breaks into two questions: (i) What evidence do we have to believe that EMRIs exist in the actual universe and how likely are they to occur? (ii) What could we hope to learn from the gravitational wave emissions from EMRI systems?

Answering the first question relies on demonstrating the existence of two things: compact objects and massive black holes. We remark that the best target EMRI systems will be those where the smaller component is a compact object, not just a low mass object. This is because large, low mass objects, such as main sequence stars, will be tidally disrupted and completely torn apart before they complete the inspiral (i.e., before they reach the last stable orbit) [9]. For this reason the most interesting systems are those where the smaller body in the EMRI is a compact object such a neutron star, white dwarf star or stellar mass black hole. There is a wealth of observational evidence for neutron stars and white dwarfs, as well as indirect evidence for the existence of stellar mass black holes [10].

The case for the existence of massive black holes is also good. Within our own Milky Way Galaxy there is now strong evidence supporting the existence of a massive black hole in the galactic core. This evidence comes in the form of radio emissions (presumably from the black hole's accretion disk [11]), but also crucially from the mapping of the orbits of the neighbouring stars—see Fig. 1.1—which has shown the mass of the central object to be $4.1 \pm 0.6 \times 10^6 M_\odot$ [12]. Importantly this large mass is known to be contained in a small volume as the so called 'S0-2' star has been observed to come with 120AU of the central object without colliding with it or being tidally ripped apart [12, 13]. Theory then tells us that the best candidate for the central object is a massive black hole.

It is important now to ask how often compact objects come close enough to massive black holes to be ensnared by their gravitational pull and begin inspiralling due to the emission of gravitational waves. There are currently three known possible mechanisms for the production of EMRI systems [9]: (i) mass segregation by two-body scattering in the stellar population near the galactic center whereby the more massive objects sink towards the massive black hole [14, 15], (ii) tidal disruption of binary systems passing near to a massive black hole [16] and (iii) star formation and rapid collapse into a black hole in the accretion disks surrounding massive black holes [17]. For a single massive black hole the event rates for these mechanisms is of the order of a few EMRIs per Gyr [14, 18]. Fortunately eLISA should be sensitive to EMRI signals from systems with a redshift up to 0.7 [9] (assuming a signal-to-noise ratio of 20 and a two year observation time). This volume of space encloses a large number of galaxies, most of which are believed to contain massive black holes [19], and thus over the mission lifetime eLISA is expected to observe 10s to 1000s[1] of EMRIs [22]. The large uncertainty in this result stems from the uncertainty in the event rate at which compact objects fall onto massive black holes. The number of galaxies that eLISA would be expected to hear signals from is well constrained.

We now turn our attention to the second motivation question: what could we hope to learn from the gravitational wave emissions from EMRI systems? Firstly, the CO in an EMRI system will undergo many thousands of orbits whilst the frequency of the gravitational wave emission is within the eLISA band. During this time the CO will effectively map out the space time surrounding the massive central object, allowing for precision tests of general relativity in the strong field regime [23] (and maybe tests of other competing theories of gravity [24]). In particular, it should be possible to confirm or refute the Kerr hypothesis [25]—that the spacetime around astrophysical black holes is described by the general relativistic Kerr metric. The gravitational waves from EMRI systems should also allow for accurate estimation of the orbital parameters as well as the spin and mass of the central black hole and the inspiralling CO [26]. These parameters are difficult to constrain with electromagnetic (EM) observations alone.

1.2 Approaches to the two body problem in GR

Our goal in this thesis will be to solve the two body problem in a general relativistic setting. Specifically we will be interested in the case where there is an extremely large ratio between the masses of the two bodies. Before considering how to model such setups via black hole perturbation theory, we shall outline two other approaches employed to find solutions to the general two body problem: post-Newtonian (PN) approximations and numerical relativity (NR).

---

[1] eLISA will also be sensitive to a large number of unresolvable EMRI signals, the confusion noise from which will only slightly reduce EMRI detection rates [20]. At low frequencies a much greater source of confusion noise will come from unresolvable white dwarf binaries [21].

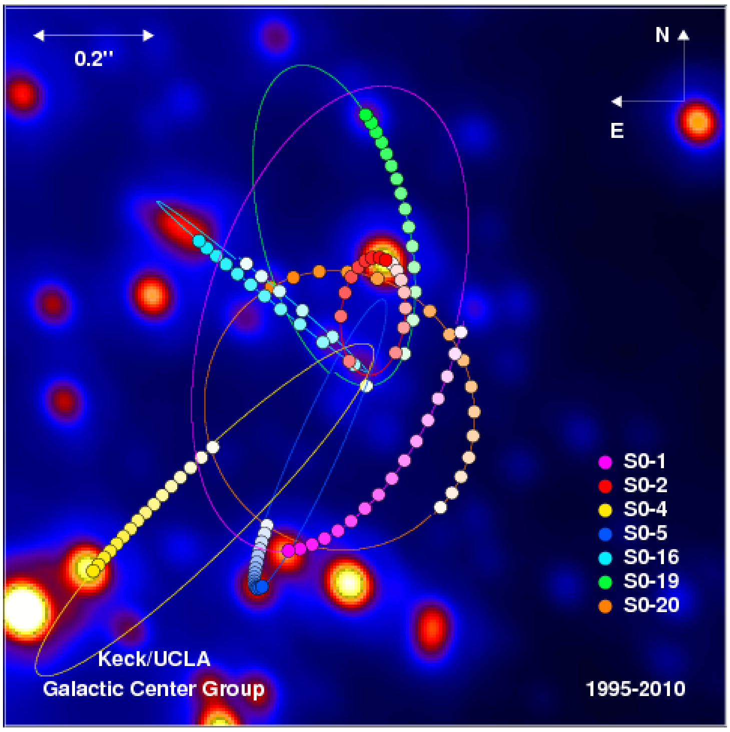

FIGURE 1.1: Motion of stars in the central arcsecond of the Milky Way Galaxy. Using these results Ghez *et al.* [12] were able to measure the mass of the central object to be $4.1 \pm 0.6 \times 10^6 M_\odot$. They also observed that the 'S0-2' star comes, during its 15 year orbit, to within 120AU of the central object without crashing into it or being tidally disrupted or torn apart. The implication then is that this large mass is contained within a small volume of space. Theory then tells us that this object is most likely a massive black hole. This image was created by Prof. Andrea Ghez and her research team at UCLA and is from data sets obtained with the W. M. Keck Telescopes.

Each of the three approaches is best suited to a particular region of the mass-ratio to average orbital separation parameter space—see Fig. 1.2. After discussing black hole perturbation theory, we also briefly outline how results from these three distinct approaches have been compared and combined.

1.2.1 Post-Newtonian theory and Numerical Relativity

The first, and oldest, approach to the general relativistic two body problem, arguably beginning with Einstein's calculation of the anomalous perihelion shift of Mercury [27], is the post-Newtonian approximation (see Blanchet for a review [28]). In this approach, the field equations are expanded perturbatively in powers of the binary's orbital velocity as a fraction of the speed of light [29]. For this reason, the domain of validity of PN results covers weak field, low velocity systems. The post-Newtonian approximation has proven itself in its domain of validity by successfully predicting relativistic corrections away from Newtonian solar system dynamics [29] as well as the celebrated prediction of the rate of inspiral of the Hurse-Taylor binary pulsar, PSR 1913+16 [30, 31, 32], and other similar systems [33]. Despite its age, post-Newtonian research continues to be an extremely active field, making important contributions to the modern day search for gravitational radiation [34, 35].

The second method, numerical relativity, can perhaps be considered the youngest approach

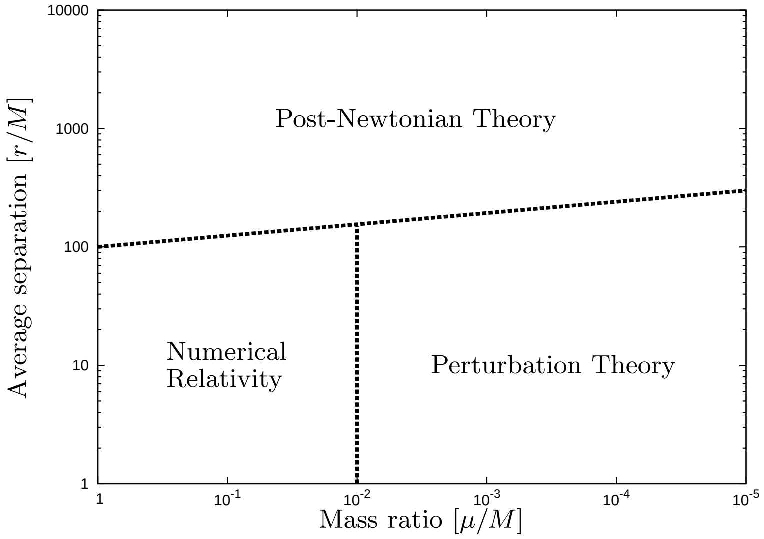

FIGURE 1.2: In this figure we show where the three main approaches to the two body problem problem in GR are valid. Post-Newtonian theory is valid when the two bodies are widely separated and moving slowly. Full numerical relativity is best suited to the strong field regime, though due to the added computational burden it is difficult to simulate systems where the bodies are too widely separate (the time until merger increases with initial separation) and/or the mass ratio is high (the required resolution increases as the mass ratio increases). Lastly, black hole perturbation theory is valid when one of the two bodies is much less massive than the other. The boundaries shown between the three calculation techniques are for illustrative purposes only, and, of course are not strictly defined (see Sec. 1.2.3)

to solving the two body problem in GR. Numerical relativity aims to model the complete spacetime dynamics of the two body system by numerically solving the full Einstein field equations. Although work has been going on in this field for the past thirty to forty years, examining situations such as head on black hole collisions [36], it was only recently that a suitable computational framework was developed to allow for stable orbital evolutions of the spacetime of a binary black hole system. Starting with Pretorius [37, 38] in 2004 and then Campanelli *et al.* [39] and Baker *et al.* [40] in 2005, the field has rapidly exploded produced many interesting new insights into the physics of black hole mergers (kicks [41], anti-kicks [42, 43] and spin-bobbing [44] to name but a few). A review of recent advances in the NR field is given by Pfeiffer [45]. The extreme resolution requirements of modelling the mass ratios encountered in EMRI systems (typically $1:10^6$) puts such systems well out of reach of current NR technology where to date the largest mass ratio explored is $1:100$ [46]. Similarly, due to computational restraints, the initial separation of the black holes in NR simulations cannot be too large if the merger is to be reached within a sensible amount of computing time.

Recently there has been a synergy between the previous two methods in the Effective One Body (EOB) approach of Buonanno and Damour [47]. This method aims to provide a scheme for solving the general relativistic two body problem along similar lines to how the Newtonian problem is solved: by reducing the problem to that of solving for the motion of single body in some effective geometry. The way this is done is by resumming the post-Newtonian results in such a way as to capture the essence of the non-perturbative corrections and matching the resultant waveforms to the known analytical results for the ring down of the black hole that occurs after merger. Numerical relativity enters into this approach by allowing fine-tuning of the resumming. Using these techniques complete waveforms have been produced that include the inspiral, merger and ring down of a binary black hole system [48]. Damour and Nagar provide a comprehensive review of the EOB approach [49]. EOB results are also important as numerical relativity simulations are computationally expensive; it can take weeks or months to evolve a single black hole binary system through a few orbits prior to merger. Consequently approximate waveforms, such as those provided by the EOB approach, need to be generated in order to fill the parameter space required to make effective gravitational wave searches.

1.2.2 Black hole perturbation theory

When one of the two bodies is substantially smaller than the other (and hence its gravitational field, considered as a perturbation over the field of the larger body, is also small) black hole perturbation theory can be used. The seminal work in this field for perturbations of a Schwarzschild black hole was carried out by Regge and Wheeler [50], where they showed that in a suitable gauge (later called the Regge-Wheeler gauge), the metric perturbation obeys a standard wave equation. Their approach was later extended to the case of electrically charged (Reissner-Nordström) black holes by Zerilli [51] and Moncrief [52, 53]. For Kerr spacetime, the reduction of the perturbation problem to that of solving a single wave equation was first demonstrated by Teukolsky [54, 55].

These approaches have proven to be very powerful for analyzing perturbations of black holes. In the context of modelling EMRI, the ideal calculation is to compute the back-reaction of a point particle's metric perturbation upon the particle's own motion. The resulting force the particle feels due to this interaction is commonly known as the gravitational self-force (GSF). As mentioned above, computing the GSF is difficult, as the perturbation from a point particle is divergent at the particle's location, and in order to compute the full effects of the interaction between the particle and its perturbation, a suitable regularization scheme must be used. In the gauges used in the aforementioned perturbation techniques, the singularity in the metric perturbation at the particle takes a complicated form, and it is not known in general how to proceed with regularization to recover the full GSF [56].

We remark at this point that the full effects of the GSF can be broadly split into conservative and dissipative pieces. Dissipative effects are responsible for driving the orbital inspiral and, in the context of an inspiral into a Kerr black hole, give rise to the secular drift in the principal orbital parameters of the orbital energy, $\mathcal{E}$, angular-momentum, $\mathcal{L}$, and Carter constant, $\mathcal{Q}$. On the other hand, conservative effects do not secularly influence the principal orbital parameters[2], but they do effect the phasing of the orbit. A complete description of the orbital motion must include both effects.

If one is only interested in the dissipative effects of the GSF on the orbital inspiral, then the above perturbation techniques can be employed by appealing to conservation laws. In the case of generic orbits about a Schwarzschild black hole and circular or eccentric equatorial orbits about a Kerr black hole, these conservation laws allow the average change in $\mathcal{E}$ and $\mathcal{L}$ to be related to the asymptotic fluxes at the spacetime boundaries, avoiding any local calculation of the SF and the need for regularization that comes with it. For the most astrophysically relevant case of generic (both eccentric and inclined) orbits about a Kerr black hole, it is necessary to track the evolution of the Carter constant, for which there is no corresponding conservation law. Though the instantaneous change in the Carter constant cannot be directly related to the asymptotic fluxes, methods have been introduced to track its average change across many orbits when the evolution is sufficiently adiabatic [57, 58, 59, 60].

---

[2] Both the dissipative and conservative effects influence the momentary values of the primary orbital parameters, but the conservative effects average out over many orbits.

In order to compute the full GSF for generic orbits, including conservative effects, we are, at the time of writing, forced to work in the Lorenz gauge in order to make use of the appropriate regularization scheme (discussed in Chapter 5). The trade off for access to the conservative effects of the GSF is that the metric perturbation decomposed in the Lorenz gauge is not as algebraically simple as say, the metric perturbation in the Regge-Wheeler or radiation gauges. The decomposition of the metric perturbation in the Lorenz gauge was first carried out by Barack and Lousto [61]. Since then, calculations of the full GSF have been made for circular orbits in Schwarzschild spacetime by Barack and Sago [62] (Lorenz gauge), Detweiler [63] (Regge-Wheeler gauge), Berndtson [64] (Lorenz gauge), Shah *et al.* [65] (radiation gauge) and Akcay [66] (Lorenz gauge). For eccentric orbits about a Schwarzschild black hole, the first GSF calculation was performed by Barack and Sago [67] (Lorenz gauge) and we present the second Lorenz gauge calculation in this thesis.

1.2.3 Comparisons between the approaches

The above approaches to the two body problem are each best suited to a particular region of the separation to mass-ratio parameter space (see Fig. 1.2), but these three regions are not disjoint. Where they overlap it has been possible to make comparisons between the results of each approach. Comparisons between NR and PN have been made by matching the initial configuration of an NR simulation (involving two non-spinning black holes) to PN results some 30 orbits prior to merger, and then evolving the NR simulation and observing how the resulting evolution compares with PN predictions, with a good comparison found over the next 15 orbits [68].

It has also been possible to compare results between GSF and PN computations. These two techniques work with different regularization procedures and in different gauges but once suitable gauge invariant quantities were identified [63, 69] a very successful comparison was made for the case of a particle in a circular orbit about a Schwarzschild black hole [70]. Favata has also used the shifted (due to the perturbation from the CO) location of the innermost stable circular orbit (ISCO) as a point of comparison between GSF and PN results [71].

Comparison between NR and GSF results has also recently been undertaken by Le Tiec *et al.* [72, 73] (Refs. [72, 73] also makes comparisons between NR, PN and EOB). Interestingly it was found that GSF results can be made to compare remarkably well with NR simulations in the case where the black holes are of comparable masses (ratios from 1:1 - 1:8), when the usual mass ratio, μ/M, is replaced by the symmetric mass ratio, $(\mu M)/(\mu + M)^2$. This opens up the exciting possibility that GSF results might be applicable to not just EMRI systems, but possibly also to Intermediate Mass Ratio Inspirals (IMRIs) (whose mass ratios are around 1:100).

1.3 SF calculation: State of the art

There have been a large number of SF calculations over the years, with a particular flurry of new results recently, owing to the renewed interest in the problem in light of the desire to produce gravitational waveform templates for EMRI systems. The theoretical framework of SF calculations has been placed on firm footing by many authors [6, 7, 44, 74] (see Poisson for a review of the motion of a point particle in curved spacetime [75]), and practical procedures for carrying out the regularization (all based upon the aforementioned theoretical work) have also been produced (see Barack [76] for a review). In brief, the main approaches to practical SF calculations are

- *Matched expansions.* This approach makes use of the MiSaTaQuWa regularization equations directly by computing the relevant Green's function via an analytic Hadamard expansion that is valid within the normal neighbourhood of the particle (the normal neighbourhood is the locus of spacetime points connected to the particle by a unique geodesic). This expansion is then matched to a numerical calculation of the distant past contribution to the Green's function [77]. So far this technique has been applied to the calculation of the self force on a scalar charge in Nariai spacetime [78] (a simple toy spacetime given by the Cartesian product of 2-dimensional de Sitter spacetime and the 2-sphere, and which shares many of the characteristics of Schwarzschild spacetime).

- *Radiation-gauge regularization.* This approach aims to recast the MiSaTaQuWa regularization procedure in terms of the radiation gauge. The numerical work is then made much easier as the powerful Teukolsky formalism mentioned above can be employed, though much of the technical challenge in this approach becomes hidden in the difficult process of metric reconstruction [79, 80].

- *Mode-sum method.* This is an approach where the retarded and singular components (as identified by MiSaTaQuWa) of the metric perturbation are considered within a multipole expansion. Importantly, from a numerical point of view, the individual modes of the expansion of the retarded field are continuous at the particle. The multipole expansion of the singular field can be treated analytically, and the regular field (which is responsible for the SF) is computed by subtracting the singular field from the retarded field mode-by-mode.

- *Puncture methods.* This is an approach aimed at 2+1D and 3+1D time-domain evolutions where the metric perturbation is divergent at the particle. The main idea behind this approach is to construct an appropriate approximation to the singular field and, in a 'puncture' region surrounding the particle, solve for the retarded field minus the approximation to the singular field, the result of which will be smooth enough to extract the correct SF. In 2+1D time-domain (TD) calculations, this approach is implemented in the m-mode scheme of Barack and Golbourn [81], and in 3+1 dimensions the effective source approach of Vega and Detweiler [82] and others [83] is taken.

Many of these techniques are complicated to implement, and so, before tackling the GSF problem, they have often been tested on toy scalar-field problems—see Table 1.1. Electromagnetic self-force calculations have also been carried out, though as they are more complicated than the equivalent scalar-field problems and not particularly physically relevant, fewer EM self-force calculations have been made over the years—see Table 1.2. The all important GSF calculations (in view of EMRI modelling) are presented in Table 1.3. All three of these tables are updated versions of the one found in Barack's review [76].

When work on this thesis began, all self-force calculations had only been performed for a particle in orbit about a Schwarzschild black hole (with the exception of one calculation by Burko and Liu [96] for a static scalar particle in Kerr-Newman spacetime). There is a growing body of evidence that both stellar mass and massive black holes are rotating [105, 106], and consequently, when modelling black hole binary systems, it will be important to assess how the black hole's spin influences the orbital dynamics. In this thesis we present the first self-force calculation for a

Spacetime	Particle motion	Author(s)	Strategy
Nariai	Static particle	Casals *et al.* [78]	matched expansions
Schwarzschild	Static particle	Burko [84]	mode-sum, analytic
		Wiseman [85]	direct, analytic
	Radial infall	Barack & Burko [86]	mode-sum, (1+1D)
	Circular orbit	Diaz-Rivera *et al.* [87]	mode-sum, FD
		Cañizares and Sopuerta [88]	mode-sum, pseudo-spectral
		Thornburg [89]	mode-sum, (1+1D), AMR
		Vega & Detweiler [82]	puncture, (1+1D)
		Vega *et al.* [90]	puncture, (3+1D)
		Dolan & Barack [91]	m-mode (2+1D)
	Eccentric orbit	Haas [92]	mode-sum
		Cañizares & Sopuerta [93]	mode-sum, pseudo-spectral
		Thornburg [94]	m-mode (2+1D)
		Diener *et al.* [95]	puncture, (3+1D)
Kerr-Newman	Static particle	Burko & Liu [96]	mode-sum, analytic
Kerr	Circular, equatorial orbits	Warburton & Barack [97]	mode-sum, FD
		Dolan *et al.* [98]	m-mode, (2+1D)
	Eccentric, equatorial orbits	Warburton & Barack [99]	mode-sum, FD
	Circular, inclined orbits	Warburton (this thesis)	mode-sum, FD

Table 1.1: State of the art: scalar-field self-force calculations. In this table we present a list of the scalar-field self-force calculations that have been performed to date. The left most column shows the spacetime in which the calculation was carried out and the second column shows the (geodesic) motion of the particle considered. The third columns gives the authors of the various works and the fourth column gives their overall calculation strategy (refer to the main text for a brief description of each approach). Note 'AMR' stands for 'with adaptive mesh refinement'.

Spacetime	Particle motion	Author(s)	Strategy
Schwarzschild	Static particle	Smith & Will [100]	analytic
		Burko [84]	mode sum, analytic
		Keidl *et al.* [101]	radiation-gauge, analytic
	Eccentric orbit	Haas [102]	mode-sum, (1+1D)

Table 1.2: State of the art: electromagnetic self-force calculations. The column format is the same as in Table 1.1.

scalar particle in orbit about a Kerr black hole (Chapters 6 and 7 and published as Refs. [97] and [99]). Our results have since been corroborated by other researchers using alternative calculation techniques [94, 98, 107].

We also consider the simpler, and less astrophysically relevant, case of the GSF for orbits in Schwarzschild spacetime. Though Schwarzschild GSF results may not be the most useful for actual signal searches within data from gravitational wave detectors, they are, due to the spherical symmetry of the spacetime, easier to obtain and as such provide an excellent test bed

Spacetime	Particle motion	Author(s)	Strategy
Schwarzschild	Radial infall	Barack & Lousto [103]	mode-sum, (1+1D), Regge-Wheeler gauge
	Static particle	Keidl *et al.* [101]	radiation-gauge, analytic
	Circular orbit	Barack and Sago [62]	mode-sum, (1+1D), Lorenz gauge
		Detweiler [63]	mode-sum, FD, Regge-Wheeler gauge
		Berndston [64]	mode-sum, FD, Lorenz gauge
		Shah *et al.* [65]	radiation-gauge, FD
		Akcay [66]	mode-sum, FD, Lorenz gauge
	Eccentric orbit	Barack and Sago [67]	mode-sum, (1+1D), Lorenz gauge
		this thesis & Akcay *et al.* [104]	mode-sum, FD, Lorenz gauge

Table 1.3: State of the art: gravitational self-force calculations. The column format is the same as in Table 1.1.

for approaching the problem in Kerr spacetime. Furthermore, as already mentioned, GSF results in Schwarzschild spacetime provide points of reference that can be used to make contact and comparison with other approaches to the general relativistic two body problem [71, 72, 108].

For all the cases presented in Tables 1.1, 1.2 and 1.3, the SF was calculated for a particle moving along a geodesic of the background spacetime. Only very recently has there been work on using SF data to compute an actual inspiraling orbit. For a particle carrying a scalar charge moving in Schwarzschild spacetime Diener, *et al.* [95] have computed a self-consistent time-domain evolution. For the GSF problem, we present in this thesis the first inspiral computed using actual GSF data, including all first-order-in-the-mass-ratio effects (Chapter 9 and published as Ref. [109]). It is important to qualify this statement though as, in computing the inspiral, we have worked within an osculating orbit approximation. The error made by using this approximation to evolve an entire inspiral is, at the time of writing, not currently clear. In particular it is not known how the error scales with the mass ratio. We discuss this point further in Chapter 9 and in the concluding remarks of this thesis we outlined how this error might be quantified in the future.

1.4 Frequency domain approach

In this thesis we opt to tackle the SF problem via frequency-domain techniques over time-domain approaches. Our reasons for taking this approach are as follows:

- In frequency domain calculations one encounters *ordinary* differential equations (ODEs) which are substantially easier to work with numerically than the partial differential equations encountered within a TD treatment. As an example, for eccentric orbits about a Schwarzschild black hole, Barack and Sago [67] found they needed to use a rather complicated 4th-order-convergent finite-difference scheme in their TD treatment. For circular orbits Barack and Sago [62] used a 2nd-order scheme and increased the convergence rate of the finite-difference algorithm using a Richardson-type extrapolation to the limit of vanishing grid-cell size. They found this approach was not possible for eccentric orbits. The FD approach avoids these technical difficulties.

- Eccentric orbit FD calculations were, until recently, hampered by the fact that for these orbits the perturbation is a non-smooth function of time for a given radius between the minimum and maximum radius obtained during the orbit. This fact means that the high-frequency convergence of the Fourier sum at the particle suffers from the well known Gibbs phenomenon, which arises from attempting to construct a discontinuous function (in the case of the radial derivatives of the metric perturbation) as a sum of smooth functions. This difficulty was recently circumvented by the introduction of the method of extended homogeneous solutions by Barack, Ori and Sago [110]. This FD technique was successfully implemented by Barack and Sago to compute the monopole and dipole modes of the metric perturbation for a particle on an eccentric orbit [67] (they found these two modes of the metric perturbation did not evolve stably in the TD). With the method of extended homogeneous solution in hand, the FD approach has become an attractive option for SF calculations.

- Lastly, we show in this thesis, with our work on scalar fields in Kerr spacetime, that the FD calculation employing the method of extended homogeneous solution can be very efficient when computing the SSF along orbits with moderate eccentricity (see Chapter 7 and in particular Sec. 7.2.3). This is what motivates us to perform a similar GSF calculation (Chapter 8) where we again find that for low eccentricity orbits our FD code runtime out strips comparable TD codes by an order of magnitude (see Sec. 8.6.1).

1.5 Organization of this thesis

In this thesis, we present three chapters, which contain essential background material, and we clearly mark the title of these chapters with the prefix 'Essential Background'. Unless otherwise stated, everything in these chapters is not original material, instead their purpose it to bring together all the necessary results required for the later chapters. These three essential background chapters cover geodesic motion in Schwarzschild and Kerr spacetime (Chapter 2), perturbations of Schwarzschild and Kerr spacetime (Chapter 4) and the self-force formalism and calculation techniques (Chapter 5).

Original content can be found in six of the other chapters. In Chapter 3, we investigate the recently discovered phenomenon of isofrequency geodesic orbits, whereby two physically distinct orbits share the same orbital frequencies. This work is unrelated to the later chapters on the SF, and for that reason we present this material immediately after the chapter on geodesics in Schwarzschild and Kerr spacetime. We then give the other two essential background chapters mentioned above before presenting work on the SSF in Kerr spacetime. This work is split into two chapters corresponding to the calculation of the SSF for circular orbits (Chapter 6) and for eccentric, equatorial orbits (Chapter 7). The results presented in these two chapters have been published [97, 99]. We then turn our attention to calculating the GSF along generic bound geodesic orbits in Schwarzschild spacetime (Chapter 8). The high efficiency of the code we present there allows us to compute the GSF for a great many geodesic orbits and, through the use of an analytical model, which we fit with our numerical data, we tackle the important problem of orbital evolution (Chapter 9 and published in Ref. [109]). In our final chapter, we present some concluding remarks and consider how the work presented in this thesis could be extended. Lastly, any results that we feel break the flow of the main text we have presented in Appendices A-I.

Throughout this work we use the metric signature $(-+++)$ and geometrized units such that the gravitational constant and the speed of light are equal to unity.

Chapter 2

Essential background: geodesic motion in Schwarzschild and Kerr spacetimes

In this ‘Essential background’ chapter we outline some of the salient features of Schwarzschild and Kerr spacetime that we will require in this thesis, placing a particular emphasis on the equations describing bound geodesic motion. We begin with an overview of Schwarzschild spacetime and geodesic motion within it. Schwarzschild spacetime describes the geometry outside of a spherically symmetry body, and this spherical symmetry leads to substantially simpler equations of motion (than those found in Kerr spacetime) through which the most prominent features of bound geodesic motion can be understood.

After considering geodesic motion in Schwarzschild spacetime, we turn out attention to Kerr spacetime, which describes the geometry of a rotating black hole (Schwarzschild spacetime is a special case of Kerr recovered when the central black hole is not rotating). In Sec. 2.2.1, we overview the concepts of the event horizon and the ergosphere. We then turn our attention to the (much richer) space of bound geodesic orbits about a Kerr black hole. Here we find it simpler to consider various types (circular, eccentric equatorial) of bound geodesic orbits separately. For generic orbits about a Kerr black hole, we do not give an orbital parametrization but we do give the formulae required to compute the orbital frequencies for these orbits as they will be crucial for the work on isofrequency orbits presented in Chapter 3.

2.1 Schwarzschild spacetime

The vacuum spacetime outside of a spherically symmetric body of mass M is described by the Schwarzschild metric, whose covariant line element is given by

$$ds^2 = -f(r)dt^2 + \frac{dr^2}{f(r)} + r^2(d\theta^2 + \sin^2\theta d\varphi^2) \ , \tag{2.1}$$

where (t, r, θ, φ) are the standard Schwarzschild coordinates and we have defined

$$f(r) \equiv 1 - \frac{2M}{r} \ . \tag{2.2}$$

We shall denote the metric tensor of the spacetime by $\mathring{g}$ and find that its determinant is given by

$$\det(\mathring{g}) = -r^4 \sin^2\theta \, . \tag{2.3}$$

Black hole spacetimes are defined by the presence of an event horizon which in this case, in Schwarzschild coordinates, is located at $r = 2M$.

2.1.1 Geodesic motion

In this section, we consider the geodesic motion of a timelike test body in Schwarzschild spacetime. We denote the worldline of the test body by $x^\alpha = x_p^\alpha(\tau)$ and its tangent four velocity by $u^\alpha = dx_p^\alpha/d\tau$, where τ is the body's proper time. The motion of a timelike test body of mass μ in *any* spacetime is governed by the geodesic equation

$$\mu u^\beta \nabla_\beta (u^\alpha) = 0 \tag{2.4}$$

where the covariant derivative is taken with respect to the metric $\mathring{g}$. For a timelike test body moving in Schwarzschild spacetime, Eq. (2.4) can be written explicitly as

$$\frac{dt_p}{d\tau} = \frac{\mathcal{E}}{f(r_p)} \, , \qquad \frac{d\varphi_p}{d\tau} = \frac{\mathcal{L}}{r_p^2} \, , \tag{2.5}$$

$$\left(\frac{dr_p}{d\tau}\right)^2 = \mathcal{E}^2 - R(r_p, \mathcal{L}^2) \, , \qquad R(r, \mathcal{L}^2) \equiv f(r)\left(1 + \frac{\mathcal{L}^2}{r^2}\right) \, , \tag{2.6}$$

where $\mathcal{E} \equiv -u_t$ and $\mathcal{L} \equiv u_\varphi$ are the integrals of motion corresponding to the test body's specific energy and angular momentum respectively and $R(r, \mathcal{L}^2)$ is an effective radial potential (see Fig. 2.1). In this work we shall be concerned solely with bound geodesic motion and so we specialize immediately to this case. Such orbits are specified uniquely, up to orientation, by their energy and angular momentum. For this reason we shall refer to the $(\mathcal{E}, \mathcal{L})$ pair as *principal* orbital parameters. Following Newtonian celestial mechanics, it will be useful to introduce an alternative orbital parametrization given by the semi-latus rectum, p, and orbital eccentricity, e. With the maximum orbital radius, $r = r_{\text{max}}$, and the minimum orbital radius, $r = r_{\text{min}}$, specified, p and e are defined through

$$p \equiv \frac{2 r_{\text{max}} r_{\text{min}}}{M(r_{\text{max}} + r_{\text{min}})} \, , \qquad e \equiv \frac{r_{\text{max}} - r_{\text{min}}}{r_{\text{max}} + r_{\text{min}}} \, . \tag{2.7}$$

Notice that $e = 0$ for circular orbits (when $r_{\text{max}} = r_{\text{min}}$) and $e \to 1$ as $r_{\text{max}} \to \infty$. Thus we have $0 \leq e \leq 1$. The value of p will be constrained below. Equations (2.7) can be inverted to give r_{max} and r_{min} in terms of p and e:

$$r_{\text{max}} = \frac{pM}{1 - e} \, , \qquad r_{\text{min}} = \frac{pM}{1 + e} \, . \tag{2.8}$$

The pair (p, e) also constitute a pair of principal orbital parameters and the one-to-one relation between them and the energy and angular momentum is given by

$$\mathcal{E}^2 = \frac{(p - 2 - 2e)(p - 2 + 2e)}{p(p - 3 - e^2)} \, , \qquad \mathcal{L}^2 = \frac{p^2 M^2}{p - 3 - e^2} \, . \tag{2.9}$$

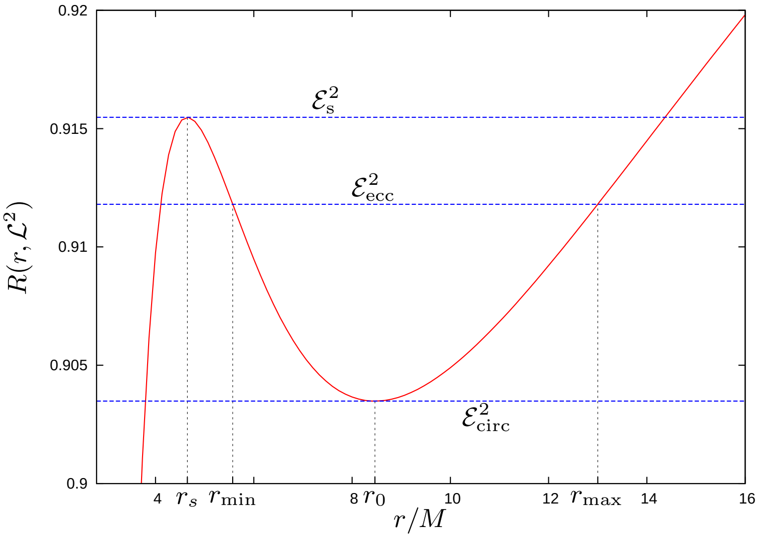

FIGURE 2.1: The effective radial potential, defined in Eq. (2.6), for test particle motion in Schwarzschild geometry shown here for value of the specific orbital angular momentum (squared) given by $\mathcal{L}^2 = 1521/116 \approx 13.1121$. We mark on three sample orbits (via their related energies) that correspond to three distinct types of orbital motion. For our example eccentric orbit [with $(p, e) = (7.8, 0.4)$], the square of the orbital energy is given by $\mathcal{E}^2 = \mathcal{E}_{\rm ecc}^2 = 1375/1508 \approx 0.911804$. The orbital motion is bound between the maximum (apastron) radius, $r_{\rm max} = 13M$, and the minimum (periastron) radius, $r_{\rm min} = 39/7M$, the values of which are given by the outer two roots of $\mathcal{E}^2 - R(r, \mathcal{L}^2) = 0$. As the orbital energy is decreased, the radial distance between the two orbital turning point decreases until they coincide at $r_{\rm max} = r_{\rm min} = r_0 \approx 8.46532$, where the square of the orbital energy is $\mathcal{E}^2 = \mathcal{E}_{\rm circ}^2 \approx 0.903485$. If the orbital energy is increased from that of our example eccentric orbit then the radial distance between the two orbital turning points increases until $\mathcal{E}^2 = \mathcal{E}_s^2 \approx 0.91548$. As $\mathcal{E}^2$ approaches $\mathcal{E}_s^2$ (from below), the radial orbital period $T_r \to \infty$. If $\mathcal{E}^2 = \mathcal{E}_s^2$ and the test body's motion begins exactly at the radius $r = r_s \approx 4.64675$ it will undergo (unstable) circular motion. If its motion begins with $r_s < r < r_0$ then it will spend a finite time moving out to the apastron radius $r_{\rm max}$ before spending an infinite amount of time returning to the periastron radius r_2. Lastly, orbits with $\mathcal{E}^2 > \mathcal{E}_s^2$ will plunge into the black hole in finite time.

Again taking the lead from Newtonian celestial mechanics, and following Darwin [111], we introduce a "relativistic anomaly" parameter χ such that the radial motion is given by

$$r_p(\chi) = \frac{pM}{1 + e\cos(\chi - \chi_0)} , \tag{2.10}$$

where χ_0 is a *positional* orbital element that specifies the orbit orientation. When $\chi = \chi_0$, the particle will be at periastron and for this reason we shall refer to χ_0 as the *periastron phase*. For the remainder of this chapter we will assume without loss of generality that $\chi_0 = 0$ so that at $\chi = 0$ the test body is at periapsis. We shall also assume, again without loss of generality, that at the initial periapsis passage $t = \varphi = 0$. The rate of change of t_p and φ_p with respect to χ is given by [112]

$$\frac{dt_p}{d\chi} = \frac{Mp^2}{(p - 2 - 2e\cos\chi)(1 + e\cos\chi)^2}\sqrt{\frac{(p-2-2e)(p-2+2e)}{p-6-2e\cos\chi}} , \tag{2.11}$$

$$\frac{d\varphi_p}{d\chi} = \sqrt{\frac{p}{p - 6 - 2e\cos\chi}} . \tag{2.12}$$

The accumulated azimuthal angle over one orbit, delimited by two successive periastron passages, is found to be

$$\Delta\varphi = \int_0^{2\pi} \frac{d\varphi}{d\chi}\, d\chi = 4\left(\frac{p}{p-6-2e}\right)^{1/2} K\left(\frac{4e}{p-6-2e}\right) , \tag{2.13}$$

where $K(k) = \int_0^{\pi/2}(1-k\sin\theta)^{-1/2}\, d\theta$ is the complete elliptic integral of the first kind. In general, $\Delta\varphi \neq 2\pi$ and and the orbit precesses (see Fig. 2.3). The coordinate time taken for one complete orbit is given by

$$T_r = \int_0^{2\pi} \frac{dt}{d\chi}\, d\chi . \tag{2.14}$$

We now define two frequencies associated with the orbital motion through

$$\Omega_r = \frac{2\pi}{T_r} , \qquad \Omega_\varphi = \frac{\Delta\phi}{T_r} . \tag{2.15}$$

Unlike $(\mathcal{E}, \mathcal{L})$ and (p, e), the pair (Ω_r, Ω_ϕ) does *not* constitute a pair of principal orbital elements; it is possible to find two physically distinct orbits that share the same orbital frequencies. This perhaps surprising result is further explored in Chapter 3. We note also that the azimuthal frequency can be considered less fundamental than the radial frequency; the φ motion of the particle is not strictly periodic as φ_p is monotonically increasing. In the language of Goldstein [113], the φ motion is a *rotation*-type periodic motion, rather than an oscillatory or *libration*-type periodicity. The frequency Ω_φ corresponds to the average rate that φ accumulates over one radial period. The azimuthal motion can thus be considered to be of the form

$$\varphi(t) = \Omega_\varphi t + \tilde{\varphi}(t) \tag{2.16}$$

where now $\tilde{\varphi}(t)$ has a libration-type periodicity with period T_r. Physically one could imagine orbiting the black hole on a circular orbit with frequency Ω_φ. In that frame of reference, the azimuthal motion of the test body will be observed to have a periodicity of T_r. Lastly, for eccentric orbits we note that as $p \to \infty$ the two frequencies become degenerate (there is no orbital precession between two point masses interacting via Newtonian gravity) and reduce to the standard Keplerian orbital frequency.

For circular orbits $(e = 0, p = r_0/M)$ the orbital frequencies reduce to

$$\Omega_r^0 = \sqrt{\frac{(r_0 - 6M)M}{r_0^4}} , \qquad \Omega_\varphi^0 = \left(\frac{M}{r^3}\right)^{1/2} , \tag{2.17}$$

where hereafter a sub/superscript ‘0’ denotes a quantity’s circular orbit value. The Ω_r frequency of circular orbits is identified with the radial frequency of an infinitesimal eccentricity perturbation. Orbits with $r_0 > 6M$ are stable to eccentricity perturbations, whilst orbits with $3M < r_0 < 6M$ are unstable; any small perturbation will cause the test body to plunge into the black hole. At $r_0 = 3M$ only massless particles can orbit the black hole and this r_0 value is said to be the radius of the *light ring*. Below the light ring there are no circular timelike or null geodesics, stable or unstable. The specific circular orbit with radius $r_0 = 6M$ is known as the innermost stable circular orbit (ISCO). The existence of the ISCO marks a major phenomenological difference between black hole and Newtonian celestial mechanics.

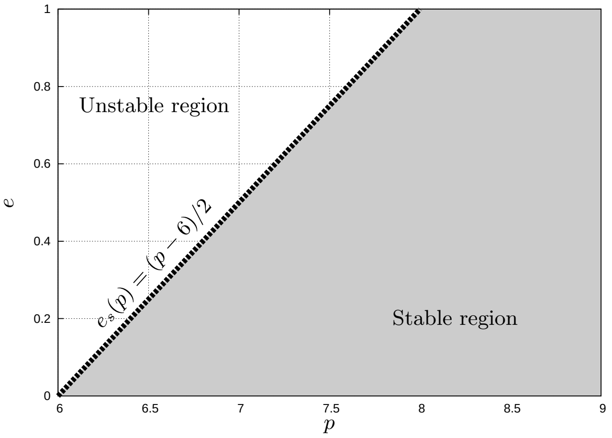

FIGURE 2.2: The (p, e) orbital parameter space. The shaded region bounded by $0 \leq e \leq 1$ and $6 + 2e \leq p < \infty$ marks the space of bound stable orbits within this parametrization. Circular orbits are when $e = 0$ and the intersection of the separatrix $e_s(p) = (p - 6)/2$ with the line $e = 0$ marks the location of the innermost stable circular orbit (ISCO).

For eccentric orbits, there exists a separatrix in the (p, e) parameter space between the space of bound stable orbits and the space of unstable orbits. The value of p at the separatrix is given by [112]

$$p_s(e) = 6 + 2e \ , \tag{2.18}$$

where, recall, $0 \leq e \leq 1$ and hereafter a sub/superscript 's' denotes a quantity's value at the separatrix. We plot the region of stable and unstable orbits in Fig. 2.2. For orbital parameters along the separatrix, both $\Delta\varphi$ and T_r are found to diverge. This is a manifestation of the well known zoom-whirl behavior of black hole orbits whereby, for orbits with parameters near the separatrix, the particle orbits ('whirls') many times just outside the periastron radius before 'zooming' back out to apastron (see Fig. 2.3).

2.2 Kerr spacetime

We now turn our attention to the more astrophysically relevant black hole spacetime of a Kerr black hole. In Boyer-Lindquist coordinates the covariant line-element in Kerr spacetime is given by [114]

$$\begin{aligned} ds^2 = &-\left(1 - \frac{2Mr}{\rho^2}\right) dt^2 + \frac{\rho^2}{\Delta} dr^2 + \rho^2 d\theta^2 + \left(r^2 + a^2 + \frac{2Mra^2}{\rho^2}\sin^2\theta\right)\sin^2\theta d\varphi^2 \\ &- \frac{4Mra\sin^2\theta}{\rho^2} dt d\varphi \ , \end{aligned} \tag{2.19}$$

where we have defined

$$\Delta \equiv r^2 - 2Mr + a^2 \ , \qquad \rho^2 \equiv r^2 + a^2\cos^2\theta \ , \tag{2.20}$$

with M being the geometric mass and a the Kerr spin parameter, related to the black hole's angular momentum, J, through $J = aM$. In this work we generally take $M \leq a$ unless otherwise

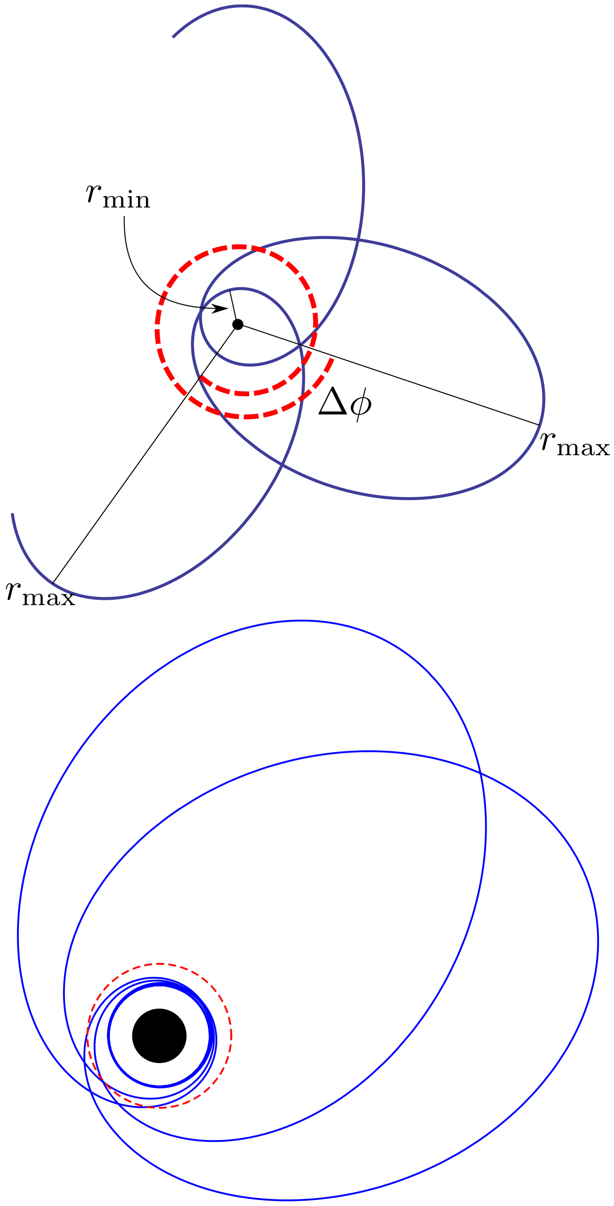

Figure 2.3: (Top panel) Example of a bound geodesic orbit about a Schwarzschild black hole. In this example, with orbital parameters $(p, e) = (15, 0.8)$, the azimuthal accumulation, $\Delta\varphi$, between successive periastron passages totals 8.16048 radians. The radial time period T_r is defined to be the Boyer-Lindquist t-time between successive periastron passages. The two orbital frequencies are then given by Eqs. (2.17). The relation between the space of orbital frequencies and the space of bound geodesics is explored in Chapter 3. (Bottom panel) Example zoom-whirl orbit with orbital parameters $(p, e) = (7.6, 0.7999)$. During one orbit the test body executes 6.10901 whirls of the black hole. Two complete orbits are shown. The red, dashed line marks the location of the ISCO at $r = 6M$.

stated. The determinant of the metric tensor is given by

$$\det(\mathring{g}) = -\rho^4 \sin^2\theta \,, \tag{2.21}$$

and the contravariant line element is

$$\begin{aligned}\left(\frac{\partial}{\partial s}\right)^2 =& \rho^{-2}\left\{\Delta\left(\frac{\partial}{\partial r}\right)^2 + \left(\frac{\partial}{\partial \theta}\right)^2 + (\sin^{-2}\theta - a^2\Delta^{-1})\left(\frac{\partial}{\partial \varphi}\right)^2 - \frac{4Mra}{\Delta}\frac{\partial}{\partial\varphi}\frac{\partial}{\partial t}\right. \\ &\left. - \left[\Delta^{-1}(r^2+a^2)^2 - a^2\sin^2\theta\right]\left(\frac{\partial}{\partial t}\right)^2\right\} \,. \end{aligned} \tag{2.22}$$

2.2.1 The event horizon and the ergosphere

The defining feature of a black hole spacetime is the presence of an event horizon, a null surface which bounds a region of space from within which null rays cannot escape to future null infinity. Due to the stationarity of Kerr spacetime the event horizon must be a spherical ($r = \text{const}$) hypersurface [115]. For this surface to be null we require that the normal vector to the surface (which in this case is proportional to $\partial_\alpha r$) be null, i.e., $g^{\alpha\beta}(\partial_\alpha r)(\partial_\beta r) \equiv g^{rr} = 0$. This occurs at the roots of the equation $\Delta = 0$ which are given, for all (t, θ, φ), by

$$r_\pm = M \pm \sqrt{M^2 - a^2} \,. \tag{2.23}$$

The outer root (r_+) marks the location of the event horizon (see [115] for a discussion of the inner horizon at r_-). For rotating black holes there is a second important hypersurface located where $g_{tt} = 0$. The properties of the interior of this region are illuminated by considering the motion of observers about the black hole [116].

Following from the stationarity and axial symmetry of the Kerr metric, there exist two Killing vector fields

$$\xi_{(t)} \equiv \frac{\partial}{\partial t} \quad \text{and} \quad \xi_{(\varphi)} \equiv \frac{\partial}{\partial \varphi} \,. \tag{2.24}$$

It will be useful in our discussion below to know the various inner products of these vector fields:

$$\xi_{(t)} \cdot \xi_{(t)} = g(\xi_{(t)}, \xi_{(t)}) = g\left(\frac{\partial}{\partial t}, \frac{\partial}{\partial t}\right) \equiv g_{tt} \,, \tag{2.25}$$

$$\xi_{(t)} \cdot \xi_{(\varphi)} = g_{t\varphi} \tag{2.26}$$

$$\xi_{(\varphi)} \cdot \xi_{(\varphi)} = g_{\varphi\varphi} \,. \tag{2.27}$$

An observer who moves along a world line of constant (r, θ, φ) is said to be *static* with respect to the distant stars. It is also useful to consider an observer who is ‘moving with the local geometry’. If an observer had a constant r and θ but rotated about the black hole with a uniform angular velocity, they would, due to axial symmetry, see an unchanging spacetime geometry in their neighbourhood. Such an observer is said to be *stationary* with respect to the local geometry. The angular velocity, as measured by someone at infinity, of such a stationary observer is given by

$$\Omega \equiv \frac{d\varphi}{dt} = \frac{d\varphi/d\tau}{dt/d\tau} = \frac{u^\varphi}{u^t} \,. \tag{2.28}$$

The 4-velocity, $\mathbf{u}$, of a stationary observer is given by

$$\mathbf{u} = \frac{d}{d\tau} = u^t \left(\frac{\partial}{\partial t} + \Omega \frac{\partial}{\partial \varphi} \right) = \frac{\xi_{(t)} + \Omega \xi_{(\varphi)}}{|\xi_{(t)} + \Omega \xi_{(\varphi)}|} \ . \tag{2.29}$$

The allowable values of Ω are found by noting that the 4-velocity of any physical observer must be timelike, i.e., $g(\mathbf{u}, \mathbf{u}) < 0$. Recalling Eqs. (2.25)-(2.27) this will be the case if

$$g_{tt} + 2\Omega g_{t\varphi} + \Omega^2 g_{\varphi\varphi} < 0 \ . \tag{2.30}$$

Thus the angular velocities of stationary observers are constrained by

$$\Omega_{\rm min} < \Omega < \Omega_{\rm max} \ , \tag{2.31}$$

where

$$\Omega_{\rm min} = \Omega_{\rm av} - \sqrt{\Omega_{\rm av}^2 - g_{tt}/g_{\varphi\varphi}} \ , \tag{2.32}$$

$$\Omega_{\rm max} = \Omega_{\rm av} + \sqrt{\Omega_{\rm av}^2 - g_{tt}/g_{\varphi\varphi}} \ , \tag{2.33}$$

$$\Omega_{\rm av} \equiv \frac{1}{2}(\Omega_{\rm min} + \Omega_{\rm max}) = -\frac{g_{\varphi t}}{g_{\varphi\varphi}} \ . \tag{2.34}$$

From Eq. (2.32) we can see that the minimum allowable angular velocity, $\Omega_{\rm min}$, is zero when $g_{tt} = 0$ or equivalently at a radius of

$$r_{\rm ergo} = r_{\rm ergo}(\theta) = M + \sqrt{M^2 - a^2 \cos^2\theta} \ . \tag{2.35}$$

This boundary lies outside the event horizon and intersects it at the poles ($\theta = 0, \pi$). This radius is known as the *static limit* and it bounds a region of space known as the *ergosphere*, wherein all observers have to co-rotate with the black hole. As a given observer presses deeper into the ergosphere towards the event horizon, $\Omega_{\rm min}$ and $\Omega_{\rm max}$ converge until at the event horizon they coincide with the value

$$\Omega_+ = \frac{a}{2Mr_+} = \frac{a}{r_+^2 + a^2} \ . \tag{2.36}$$

This is the angular velocity of a stationary observer just outside the event horizon and might be interpreted as the angular velocity of the black hole itself [115].

2.2.2 Geodesics: overview

In this section we review the properties of geodesic motion of a test particle about a Kerr black hole. Although it is possible to write down equations of motion for generic bound geodesic orbits, these are rather cumbersome. Instead we consider orbital parametrizations for the cases of bound circular and eccentric equatorial geodesics separately as doing so allows for a great deal of simplification in the resulting formulae.

2.2.2.1 Constants of motion

As discussed in Sec. 2.2.1, there exist two Killing vectors in Kerr spacetime: $\xi^\mu_{(t)} = dx^\mu/dt$ and $\xi^\mu_{(\varphi)} = dx^\mu/d\varphi$. The Kerr metric also admits a Killing tensor $\mathcal{Q}^{\mu\nu}$. To each of these there is associated a conserved quantity: the specific energy $\mathcal{E} = -\xi^{\mu}_{(t)} u_{\mu} = -u_t$, the specific azimuthal angular momentum $\mathcal{L} = \xi^{\mu}_{(\varphi)} = u_{\varphi}$, and the Carter constant $\mathcal{Q} = \mathcal{Q}^{\mu\nu} u_{\mu} u_{\nu}$. Given initial conditions these three parameters completely specify the orbit of a test particle about a Kerr black hole (up to orientation). We shall give the calculation of the energy and angular momentum for each orbit type, as we shall also do for the Carter constant though its form is simple enough to write down for generic orbits once $\mathcal{E}$ and $\mathcal{L}$ are known [116]:

$$\mathcal{Q} = u_{\theta}^2 + \cos^2\theta_p \left[a^2(1-\mathcal{E}^2) + \csc^2\theta_p \mathcal{L}^2\right] . \tag{2.37}$$

2.2.2.2 Geodesic equations

In Boyer-Lindquist coordinates the geodesic equation (2.4) for the motion of a timelike test body in Kerr spacetime can be written explicitly as [116]

$$\rho^4 \left(\frac{dr}{d\tau}\right)^2 = \left[\mathcal{E}(r^2+a^2) - a\mathcal{L}\right]^2 - \Delta\left[r^2 + (\mathcal{L} - a\mathcal{E})^2 + \mathcal{Q}\right] \equiv V_r , \tag{2.38}$$

$$\rho^4 \left(\frac{d\theta}{d\tau}\right)^2 = \mathcal{Q} - \cot^2\theta \mathcal{L}^2 - a^2\cos^2\theta(1-\mathcal{E})^2 \equiv V_{\theta} , \tag{2.39}$$

$$\rho^2 \left(\frac{d\varphi}{d\tau}\right)^2 = \csc^2\theta \mathcal{L} + a\mathcal{E}\left(\frac{r^2+a^2}{\Delta} - 1\right) - \frac{a^2\mathcal{L}}{\Delta} , \tag{2.40}$$

$$\rho^2 \left(\frac{dt}{d\tau}\right)^2 = \mathcal{E}\left[\frac{(r^2+a^2)^2}{\Delta} - a^2\sin^2\theta\right] + a\mathcal{L}\left(1 - \frac{r^2+a^2}{\Delta}\right) . \tag{2.41}$$

The roots of V_r and V_{θ} give the turning points of the orbit. In the following sections we give useful reparametrizations of the above geodesic equations for the case where the motion is that of a bound circular (equatorial or inclined) or eccentric equatorial geodesic.

2.2.3 Circular geodesics

The simplest orbits we can consider are circular orbits, whose radial velocity vanishes at all times. From Eq. (2.38) this gives us $V_r = 0 = dV_r/d\tau$. As with for orbits in Schwarzschild spacetime, we denote the Boyer-Lindquist radius of a given circular orbit by r_0.

2.2.3.1 Circular equatorial geodesics

From Eq. (2.37) we see that orbits in the equatorial plane ($\theta = \pi/2$) have $\mathcal{Q} = 0$. Solving for $V_r = dV_r/d\tau = 0$ simultaneously gives us the orbital energy and angular momentum directly as

$$\mathcal{E} = \frac{1 - 2v_0^2 + \tilde{a}v_0^3}{\sqrt{1 - 3v_0^2 + 2\tilde{a}v_0^3}} , \tag{2.42}$$

$$\mathcal{L} = r_0 v_0 \frac{1 - 2\tilde{a}v_0^3 + \tilde{a}^2 v_0^4}{\sqrt{1 - 3v_0^2 + 2\tilde{a}v_0^3}} , \tag{2.43}$$

where $v_0 = \sqrt{M/r_0}$ and $\tilde{a} = a/M$. For circular equatorial orbits we take the angular momentum to be positive and distinguish between prograde and retrograde orbits by the sign of a (with $a > 0$ for prograde motion and $a < 0$ for retrograde motion). The azimuthal angular frequency with respect to time t is given by

$$\Omega_{\varphi} = \frac{d\varphi/d\tau}{dt/d\tau} = \frac{M^{1/2}}{r^{3/2} + aM^{1/2}} , \tag{2.44}$$

where θ_p is the value of θ at the particle.

2.2.3.2 Circular inclined geodesics

For circular inclined orbits, we break with our usual convention for the black hole spin and always take $a \geq 0$, letting the sign of $\mathcal{L}$ differentiate between prograde and retrograde motion. This allows for the smooth varying of the orbital inclination from prograde orbits to retrograde orbits without flipping the sign of a. For a given black hole spin, a, we choose to parametrize circular, inclined orbits by (r_0, ι), where ι is an inclination angle defined through

$$\cos\iota = \frac{\mathcal{L}}{\sqrt{\mathcal{L}^2 + \mathcal{Q}}} \, . \tag{2.45}$$

There are other common choices of inclination angle that are made but we choose this one primarily due to its ease of computation. For a given radius r_0, the most tightly bound orbit is the prograde equatorial orbit. Likewise, the most weakly bound orbit is the retrograde equatorial orbit [117]. All other inclined circular orbits of radius r_0 will have angular momentum between these two values.

For circular, inclined orbits it is convenient to transform to a new set of coordinates so as to avoid the singularities at the orbital turning points in $(d\theta/d\tau)^{-1}$ [117] (we will encounter this term later in our numerical work). Defining $z = \cos^2\theta$, Eq. (2.39) becomes

$$\frac{d\theta}{d\tau} = \pm\frac{\sqrt{[a^2(1-\mathcal{E}^2)]z^2 - [\mathcal{Q} + \mathcal{L}^2 + a^2(1-\mathcal{E}^2)] + \mathcal{Q}}}{(r^2 + a^2 z)\sqrt{1-z}} \, , \tag{2.46}$$

$$= \pm\frac{\sqrt{\beta(z_+ - z)(z_- - z)}}{(r^2 + a^2 z)\sqrt{1-z}} \, , \tag{2.47}$$

where we have defined $\beta = a^2(1-\mathcal{E}^2)$ and $z_\pm$ are the two roots of the quadratic equation in the numerator of Eq. (2.46). The upper sign corresponds to motion from $\theta_{\rm min}$ to $\theta_{\rm max}$ and vice versa for the lower sign.

Further defining $z = z_- \cos^2\chi$, where χ is a monotonically increasing parameter along the body's worldline with $\theta = \theta_{\rm min}$ at $\chi = 0, 2\pi \ldots$ and $\theta = \theta_{\rm max}$ at $\chi = \pi, 3\pi \ldots$, we find

$$\frac{d\chi}{d\theta} = \frac{d\chi/dz}{dz/d\theta} = \pm\sqrt{\frac{1-z}{z_- - z}} \, , \tag{2.48}$$

where the ± has the same meaning as in Eq. (2.46). The zenithal angle as a function of χ is then computed via

$$\theta(\chi) = \theta_{\rm min} + \int_0^\chi \frac{d\theta}{d\chi'}\, d\chi', \qquad \theta_{\rm min} = \cos^{-1}(\sqrt{z_-}) \, . \tag{2.49}$$

Combining Eqs. (2.46) and (2.48) we get

$$\frac{d\chi}{d\tau} = \frac{\sqrt{\beta(z_+ - z)}}{r^2 + a^2 z} \, . \tag{2.50}$$

Further combining Eq. (2.50) with Eqs. (2.41) and (2.40) gives us

$$\frac{dt}{d\chi} = \frac{\gamma + a^2\mathcal{E}z}{\sqrt{\beta(z_+ - z)}} \, , \qquad \frac{d\varphi}{d\chi} = \frac{1}{\sqrt{\beta(z_+ - z)}}\left(\frac{\mathcal{L}}{1-z} + \delta\right) \, , \tag{2.51}$$

with

$$\gamma = \mathcal{E}\left[\frac{(r^2+a^2)^2}{\Delta} - a^2\right] + a\mathcal{L}\left(1 - \frac{r^2+a^2}{\Delta}\right) , \qquad \delta = a\mathcal{E}\left(\frac{r^2+a^2}{\Delta} - 1\right) - \frac{a^2\mathcal{L}}{\Delta} . \tag{2.52}$$

Lastly we find t and φ as functions of χ to be

$$t(\chi) = \int_0^\chi \frac{dt}{d\chi'} d\chi' , \qquad \varphi(\chi) = \int_0^\chi \frac{d\varphi}{d\chi'} d\chi' . \tag{2.53}$$

For a black hole of spin a and a given orbit with radius r and angular momentum $\mathcal{L}$, solving $V_r = dV_r/d\tau = 0$ gives $\mathcal{E}$ and $\mathcal{Q}$ as

$$E(r,\mathcal{L}) = \frac{a^2\mathcal{L}^2(r-M) + r\Delta^2}{a\mathcal{L}M(r^2-a^2) \pm \Delta\sqrt{r^5(r-3M) + a^4 r(r+M) + a^2 r^2(\mathcal{L}^2 - 2Mr + 2r^2)}} , \tag{2.54}$$

$$Q(r,\mathcal{L}) = \frac{\left[(a^2+r^2)E(r,\mathcal{L}) - a\mathcal{L}\right]^2}{\Delta} - \left[r^2 + a^2 E(r,\mathcal{L})^2 - 2aE(r,\mathcal{L})\mathcal{L} + \mathcal{L}^2\right] . \tag{2.55}$$

The Boyer-Lindquist time taken for the body to complete one orbit (i.e., the time taken for θ_p to return to its original value) we denote by $T_\theta = t_p(2\pi) = 2t_p(\pi)$. The azimuthal angle swept out during this time we denote by $\Delta\varphi_p = \varphi_p(2\pi) = 2\varphi_p(\pi)$. To each of these we associate a frequency via

$$\Omega_\theta = \frac{2\pi}{T_\theta} , \qquad \Omega_\varphi = \frac{\Delta\varphi_p}{T_\theta} \tag{2.56}$$

Similarly as with eccentric orbits, the θ motion is strictly periodic whilst the φ motion is not; φ monotonically increases with time (see discussion in Sec. 2.1.1).

2.2.4 Eccentric equatorial geodesics

As already noted above, for equatorial orbits the Carter constant vanishes and thus for eccentric orbits the pair $(\mathcal{E},\mathcal{L})$ suffice to uniquely specify an orbit in the equatorial plane up to initial conditions. Just as with our treatment of eccentric orbits in Schwarzschild spacetime presented in Sec. 2.1.1, it will be useful to use an alternative parametrization pair consisting of the semi-latus rectum, p, and the eccentricity, e, representing the strong field analogues of their Keplerian counterparts. We take (p,e) to be as defined via the maximum and minimum orbital radius as in Eqs. (2.7).

Returning to our usual convention for the black hole's spin ($-M \le a \le M$), the relation between (p,e) and the energy and angular momentum is then found to be [118]

$$\mathcal{E} = \left[1 - p^{-1}(1-e^2)\left\{1 - \frac{x^2}{p^2M^2}(1-e^2)\right\}\right]^{1/2} , \tag{2.57}$$

$$\mathcal{L} = x + a\mathcal{E} , \tag{2.58}$$

where the function $x = x(a,p,e)$ is defined through

$$x^2 = \frac{-N \mp \sqrt{N^2 - 4FC}}{2F} \tag{2.59}$$

with

$$
\begin{aligned}
F(p,e) &= \frac{1}{p^3}\left[p^3 - 2(3+e^2)p^2 + (3+e^2)^2 p - 4M^{-2}a^2(1-e^2)^2\right] , && (2.60)\\
N(p,e) &= \frac{2}{p}\left[-M^2p^2 + (M^2(3+e^2)-a^2)p - a^2(1+3e^2)\right] , && (2.61)\\
C(p) &= (a^2 - M^2 p)^2 . && (2.62)
\end{aligned}
$$

The azimuthal angle and time measured along the particle's worldline with respect to the radial phase parameter χ we denote by $\varphi_p(\chi)$ and $t_p(\chi)$ respectively, and they are given by [118]

$$
\begin{aligned}
\varphi_p(\chi) &= \int_0^\chi d\chi' \frac{\tilde{V}_\varphi(\chi',p,e)}{J(\chi',p,e)\tilde{V}_r^{1/2}(\chi',p,e)} , && (2.63)\\
t_p(\chi) &= \int_0^\chi d\chi' \frac{\tilde{V}_t(\chi',p,e)}{J(\chi',p,e)\tilde{V}_r^{1/2}(\chi',p,e)} , && (2.64)
\end{aligned}
$$

where we have

$$
\begin{aligned}
\tilde{V}_r(\chi,p,e) &= x^2 + a^2 + 2ax\mathcal{E} - \frac{2x^2}{p}(3 + e\cos\chi) , && (2.65)\\
\tilde{V}_\varphi(\chi,p,e) &= x + a\mathcal{E} - \frac{2x}{p}(1 + e\cos\chi) , && (2.66)\\
\tilde{V}_t(\chi,p,e) &= a^2\mathcal{E} - \frac{2ax}{p}(1+e\cos\chi) + \frac{\mathcal{E}p^2M^2}{(1+e\cos\chi)^2} , && (2.67)\\
J(\chi,p,e) &= 1 - \frac{2}{p}(1+e\cos\chi) + \frac{a^2}{p^2M^2}(1+e\cos\chi)^2 . && (2.68)
\end{aligned}
$$

As with eccentric orbits in Schwarzschild geometry, we define the orbital frequencies to be given by

$$
\Omega_r = \frac{2\pi}{T_r} , \qquad \Omega_\varphi = \frac{\Delta\varphi}{T_r} , \tag{2.69}
$$

where as before we have defined $T_r = t(2\pi) = 2t(\pi)$ and $\Delta\varphi = \varphi(2\pi) = 2\varphi(\pi)$.

2.2.4.1 Innermost stable circular equatorial orbit (ISCEO)

In this section we will derive the location of the ISCEO, ignoring all SF effects. It is possible to define ISCOs for other orbital inclinations but we do not consider them in this work. Although the result of this calculation appears in the literature [119], we present it explicitly here as in Chapter 7 we will consider the effects of the conservative component of the SF upon the location of the ISCO, the calculation of which will follow a similar thread. We begin with the radial geodesic equation for equatorial orbits in Kerr spacetime, given by Eq. (2.38) with $\theta = \pi/2$:

$$
\left(\frac{dr_p}{d\tau}\right)^2 = \frac{1}{r_p^4}\left\{[\mathcal{E}(r_p^2+a^2) - a\mathcal{L}]^2 - \Delta[r_p^2 + (\mathcal{L}-a\mathcal{E})^2]\right\} \equiv \mathcal{R}(r_p,\mathcal{E},\mathcal{L}) . \tag{2.70}
$$

Differentiating with respect to τ gives

$$
\frac{d^2r_p}{d\tau^2} = \mathcal{F}_{\rm eff}(r_p,\mathcal{E},\mathcal{L}), \qquad \mathcal{F}_{\rm eff}(r_p,\mathcal{E},\mathcal{L}) = \frac{1}{2}\frac{\partial\mathcal{R}}{\partial r_p} , \tag{2.71}
$$

with $\mathcal{F}_{\rm eff}$ being an effective radial acceleration.

For slightly eccentric geodesics ($e \ll 1$), we can expand the particle's radius as a function of τ in the form

$$r_p(\tau) = r_0 + e r_1(\tau) + O(e^2) \ , \tag{2.72}$$

where $r_1(\tau)$ is independent of e and comparison with Eq. (2.10) allows us to identify $r_0 = p$. We remind that throughout this thesis we use a subscript '0' to denote a quantity's circular-orbit value ($e = 0$). In this section, we also use a subscript '1' to denote the $O(e)$ perturbation in the quantity's value, holding r_0 fixed. Substituting Eq. (2.72) into Eq. (2.71) and reading off the $O(e)$ terms, we find

$$\frac{d^2 r_1}{d\tau^2} = \left.\frac{\partial \mathcal{F}_{\rm eff}(r_p, \mathcal{E}, \mathcal{L})}{\partial r_p}\right|_{e=0} r_1 \ , \tag{2.73}$$

where we note $\mathcal{E}_1 = \mathcal{L}_1 = 0$ by virtue of the quadratic dependence of $\mathcal{E}$ and $\mathcal{L}$ on e [see Eqs. (2.57) and (2.58), replacing p with r_0]. Hence the $O(e)$ radial motion is a simple harmonic oscillator,

$$\frac{d^2 r_1}{d\tau^2} = -\omega_r^2 r_1 \ , \tag{2.74}$$

with τ-frequency

$$\omega_r^2 = -\left.\frac{\partial \mathcal{F}_{\rm eff}(r_p, \mathcal{E}, \mathcal{L})}{\partial r_p}\right|_{e=0} = \frac{M[r_0(r_0 - 6M) + 8 a v r_0 - 3a^2]}{r_0^4 (r_0 - 3M + 2av)} \ , \tag{2.75}$$

where, as in the previous section, we have $v_0 \equiv \sqrt{M/r_0}$. Assuming a periapsis passage at $\tau = 0$, we obtain $r_1 = -r_0 \cos(\omega_r \tau)$ and hence

$$r_p(\tau) = r_0(1 - e \cos \omega_r \tau) + O(e^2) \ . \tag{2.76}$$

The location of the ISCEO is defined to be the radius $r_{\rm is}$ for which $\omega_r(r_{\rm is}) = 0$. Solving the quartic in Eq. (2.75), one finds [119]

$$r_{\rm is} \quad = \quad M\{3 + \kappa - {\rm sign}(a)[(3-\gamma)(3+\gamma+2\kappa)]^{1/2}\} \ , \tag{2.77}$$

where

$$\gamma \quad \equiv \quad 1 + (1 - \tilde{a}^2)^{1/3}\left[(1+\tilde{a})^{1/3} + (1-\tilde{a})^{1/3}\right] \ , \tag{2.78}$$

$$\kappa \quad \equiv \quad (3\tilde{a}^2 + \gamma^2)^{1/2} \ . \tag{2.79}$$

For the Schwarzschild and the extremal ($|a| = M$) prograde/retrograde cases, the unperturbed ISCEO is located at $6M$, $1M$ and $9M$, respectively.

2.2.4.2 Marginally stable geodesics

Levin and Perez-Giz [120] give an efficient formula for computing the separatrix $p_s(e)$ in the (p, e) parameter space between stable and unstable eccentric equatorial orbits about a Kerr black hole. In their work they show that each orbit at the separatrix (which in their work they refer to as a homoclinic orbit) can be paired with an unstable circular orbit of radius r_u. The relation they find between (p_s, e_s) and r_u is given by

$$e_s(r_u) = \frac{-r_u^2 + 6r_u - 8a\sqrt{r_u} + 3a^2}{r_u^2 - 2r_u + a^2}\,, \tag{2.80}$$

$$p_s(r_u) = \frac{4r_u(\sqrt{r_u} - a)^2}{r_u^2 - 2r_u + a^2}\,. \tag{2.81}$$

Though it is possible to analytically invert Eq. (2.80) to give $r_u(e)$, the resulting equation is rather cumbersome and for practical purposes it is found to be sufficient to numerically solve for r_u with a given $e_s = e$. Either way $p_s(e)$ is then given by $p_s(r_u(e))$. Glampedakis and Kennefick [118] note that for prograde orbits about an extremal black hole $(a = M)$ the location of the separatrix reduces to $p_s(e) = M(1 + e)$.

2.2.5 Generic geodesics

For generic orbits we do not give details of an orbital parametrization as one is not required in this thesis (though see Babak *et al.* [121, 122] for one such parametrization and Grossman *et al.* [123, 124] for some nice examples of the rich structure of generic orbits). We will, however, give formulae to calculate the orbital frequencies as will be required in Chapter 3. As discussed in Sec. 2.2.2.1, generic orbits have associated with them three principal orbital parameters commonly taken to be the set $(\mathcal{E}, \mathcal{L}, \mathcal{Q})$. An alternative parametrization, that we shall make use of here is the set $(p, e, \theta_{\min})$, where p and e are the semi-latus rectum and orbital eccentricity as before and $\theta_{\min}$ is the minimum θ angle attained during one orbital period. The relation between these two sets of principal orbital parameters is given in Appendix A.

A method for numerically calculating the three orbital frequencies $(\Omega_r, \Omega_\varphi, \Omega_\theta)$ was given by Schmidt [125]. More recently, Fujita and Hikida [126] gave analytic formulae (in terms of elliptic integrals) for their calculation. We give Fujita and Hikida's formulae below, in a slightly modified form. We first define

$$r_3 = \frac{1}{2}\left[A + \sqrt{A^2 - 4B}\right]\,, \qquad r_4 = \frac{B}{r_3}\,, \tag{2.82}$$

$$A = \frac{2M}{1 - \mathcal{E}^2} - (r_1 + r_2)\,, \qquad B = \frac{a^2\mathcal{Q}}{(1 - \mathcal{E}^2)r_1 r_2}\,, \tag{2.83}$$

where we defined $r_1 = r_{\max}\,, r_2 = r_{\min}$ and we note that $r_1 \geq r_2 \geq r_3 \geq r_4$. The orbital frequencies with respect to Mino time [57] (a time coordinate, λ, related to proper time by $d\lambda = \rho^{-2}d\tau$ and in which the r, θ Kerr geodesic equations decouple, a characteristic they do not possess when expressed with respect to proper time) are then defined by

$$\Upsilon_r = \frac{\pi\sqrt{(1 - \mathcal{E}^2)(r_1 - r_3)(r_2 - r_4)}}{2K(k_r)}\,, \tag{2.84}$$

$$\Upsilon_\theta = \frac{\pi\mathcal{L}\sqrt{\epsilon_0 z_+}}{2K(k_\theta)}\,, \tag{2.85}$$

$$\Upsilon_\varphi = \frac{\mathcal{L}\Pi(z_-, k_\theta)}{K(k_\theta)} + \frac{a}{r_+ - r_-}\left[\frac{2M\mathcal{E}r_+ - a\mathcal{L}}{r_3 - r_+}\left(1 - \frac{\mathcal{F}_+}{r_2 - r_+}\right) - (+ \leftrightarrow -)\right]\,, \tag{2.86}$$

where, recall, K is the complete elliptic integral of the first kind and hereafter we use the notation $(+ \leftrightarrow -)$ to denote a term formed by interchanging all of the $+/-$ subscripts in the previous terms within the bracket. The two radii $r_\pm$ are given by Eq. (2.23) and we also have $\epsilon_0 = a^2(1 - \mathcal{E}^2)/\mathcal{L}^2$, $z_- = \cos^2\theta_{\min}$, $z_+ = \mathcal{Q}/(\mathcal{L}^2\epsilon_0 z_-)$ and Π as the complete elliptic integral of the third kind given by

$$\Pi(c,k) = \int_0^{\pi/2} \frac{d\theta}{(1+c\sin^2\theta)\sqrt{(1-k\sin^2\theta)}} \ . \tag{2.87}$$

The arguments of elliptic integrals in Eqs. (2.84)-(2.86) are given by

$$k_r = \frac{r_1-r_2}{r_1-r_3}\frac{r_3-r_4}{r_2-r_4} \ , \qquad k_\theta = \frac{z_-}{z_+} \ . \tag{2.88}$$

The term $\mathcal{F}_\alpha$ with $\alpha = \{+,-,r\}$ that appears in Eq. (2.86) is given by

$$\mathcal{F}_\alpha = (r_2-r_3)\frac{\Pi(h_\alpha,k_r)}{K(k_r)} \ , \tag{2.89}$$

with

$$h_\pm = \frac{(r_1-r_2)(r_3-r_\pm)}{(r_1-r_3)(r_2-r_\pm)} \ , \qquad h_r = \frac{r_1-r_2}{r_1-r_3} \ . \tag{2.90}$$

Finally to convert from Mino time frequencies to frequencies defined with respect to Boyer-Lindquist t-time we use

$$\Omega_r = \frac{\Upsilon_r}{\Gamma} \ , \qquad \Omega_\theta = \frac{\Upsilon_\theta}{\Gamma} \ , \qquad \Omega_\varphi = \frac{\Upsilon_\varphi}{\Gamma} \ , \tag{2.91}$$

where Γ is given by[1]

$$\begin{aligned}\Gamma =& 4M^2\mathcal{E} + \frac{\mathcal{E}\mathcal{Q}(1-\mathcal{G}_\theta)}{(1-\mathcal{E}^2)z_-} + 2M\mathcal{E}(r_3+\mathcal{F}_r) \\ &+ \frac{\mathcal{E}}{2}\left[r_3(r_1+r_2+r_3) - r_1r_2 + (r_1+r_2+r_3+r_4)\mathcal{F}_r + (r_1-r_3)(r_2-r_4)\mathcal{G}_r\right] \\ &+ \frac{2M}{r_+-r_-}\left[\frac{(4M^2\mathcal{E}-a\mathcal{L})r_+ - 2Ma^2\mathcal{E}}{r_3-r_+}\left(1-\frac{\mathcal{F}_+}{r_2-r_+}\right) - (+\leftrightarrow -)\right] \ ,\end{aligned} \tag{2.92}$$

with

$$\mathcal{G}_\alpha = \frac{E(k_\alpha)}{K(k_\alpha)} \ , \tag{2.93}$$

where $E(k_\alpha) = \int_0^{\pi/2}\sqrt{1-k_\alpha\sin^2\theta}\,d\theta$ is the complete elliptic integral of the second kind, $\alpha = \{r,\theta\}$.

2.2.5.1 Marginally stable geodesics

By definition at the separatrix $\Omega_r = 0$. We are interested in the last stable orbit for generic, non-circular orbits and so r_1 is strictly greater than r_2 and hence $r_1 - r_3 \neq 0$ and similarly $r_2 - r_4 \neq 0$ (recall $r_1 \geq r_2 \geq r_3 \geq r_4$). By examining Eqs. (2.91) and (2.84), we then see $\Omega_r = 0$ can only occur if $K(k_r)$ diverges i.e., when $k_r = 1$. This in turn implies that at the separatrix we have $r_3 - r_2 = 0$. Solving this equation for fixed e and $\theta_{\min}$ gives the value of $p_s(e,\theta_{\min})$ at the separatrix. We find that this simple technique is in agreement with analytical results from Ref. [120] for equatorial orbits (see also Sec. 2.2.4.2) and in agreement with the numerical results

---

[1] There is a typo in Fujita and Hikida's paper of which the authors are aware [127]. We present the corrected equation here.

of Sundararajan [128] for generic orbits. Note that at the separatrix we have $\mathcal{F}_\alpha = \mathcal{G}_r = 0$ [For $\mathcal{G}_r$ this is clear as the $K(k_r)$ term in the denominator diverges whilst the numerator remains finite. For $\mathcal{F}_\alpha$ a little more care is required but the result is straightforward to demonstrate].

Chapter 3

Isofrequency orbits

Before pressing on with the main topic of this thesis on self-force calculations, we take an aside in this chapter to study a recently discovered feature of geodesic orbits about black holes. This chapter represents original research and all of its results are derived using the formulae presented in the proceeding 'Essential background' chapter on geodesic motion in Schwarzschild and Kerr spacetime.

We begin by reminding that generic bound geodesic orbits about a Kerr black hole can be characterised by three constants of motion: the specific orbital energy $\mathcal{E}$, angular-momentum $\mathcal{L}$ and Carter constant $\mathcal{Q}$. Any given orbit also has associated with it three frequencies related to the radial, zenithal and azimuthal motion. In this chapter we show that these two ways of characterising bound geodesics are not in one to one correspondence. Whilst the former uniquely specifies an orbit up to initial conditions the latter does not. For regions of the $\mathcal{E}, \mathcal{L}, \mathcal{Q}$ parameter space a given orbit will have a physically distinct dual orbit that shares the same three orbital frequencies.

3.1 Introduction

It was an observation of Newton's that the bound motion of a test particle in a radial potential will be closed if and only if the radial potential is proportional to either of the Newtonian $1/r$ or the harmonic oscillator potentials. Any deviation from either of these two will cause the orbit of the test body to precess. In physical gravitational two body systems precession is typically observed due to the presence of other distant bodies and/or higher multipole moments of either of the two bodies. A further possibility for the observation of orbital precession is the break down of the Newtonian potential in the strong field where general relativistic corrections can no longer be neglected. General relativity modifies the gravitation radial potential and thus test bodies orbiting in a strong gravitational field will precess even in the absence of a third body or higher multipole effects. This extra precession prediction of general relativity famously accounted for the anomalous, 42 arcseconds per century, perihelion advance of Mercury.

We remind from the proceeding chapter that the precession of a body in a radial potential can be analysed by considering two frequencies associated with the orbital motion. The first, the radial frequency, is related to the time period, T_r, it takes the test body to go from one periastron passage to the next. The second, the azimuthal frequency, is associated with the accumulated azimuthal angle, $\Delta\varphi$, over one radial time period. The two orbital frequencies are thus defined as:

$$\Omega_r \equiv \frac{2\pi}{T_r}\,, \qquad \Omega_\varphi \equiv \frac{\Delta\varphi}{T_r}\,. \tag{3.1}$$

For the case of two bodies in a Newtonian potential $\Delta\varphi = 2\pi$ and these two frequencies reduce to the Keplarian orbital frequency. For weak field gravitating systems with multiple extended bodies, such as our solar system, the magnitude of $\Delta\varphi - 2\pi$ is small being typically measured on the order of at most a few thousand arcseconds per century.

In the strong field gravity found black holes the orbits of test particles are drastically different to the extent that it is possible to find orbits that have arbitrarily large $\Delta\varphi$. Such orbits wind many times around the black hole between one periastron passage and the next.

The most astrophysically relevant description of an isolated black hole is given by the geometry of Kerr spacetime. For these axial-symmetric systems the bound motion of a test body along a geodesic orbit possesses a third orbital frequency associated with the zenithal motion. In this chapter we show that it is possible to find two physically distinct bound geodesic orbits that share the same three orbital frequencies[1]. A pair of orbits that share the same fundamental frequencies, but are physically distinct, we shall refer to as an isofrequency pair. The existence of such pairs of orbits is interesting as the rate of relativistic precession a given orbit exhibits depends on the ratios of the three orbital frequencies. In general any two orbits will have different precessional rates whereas a pair of isofrequency orbits will precess together at the same rate. Before considering the situation in Kerr spacetime we highlight our method by examining the case of bound orbits about a Schwarzschild black hole.

3.2 Orbits in Schwarzschild spacetime

Using Eqs. (2.7) and (2.9) it is straightforward to show that the Jacobian, J, of the orbital parametrization transformation $(\mathcal{E},\mathcal{L}) \leftrightarrow (p,e)$ is always non-zero implying that the transformation between these two orbital parametrizations is one-to-one. On the other hand Ref. [129] noted that the orbital parametrization transformation $(p,e) \leftrightarrow (\Omega_r,\Omega_\varphi)$ is singular along a certain curve in the (p,e) parameter space. The implication of the existence of this $J = 0$ curve is that it is possible to find two orbits, with different (p,e) or equivalently different $(\mathcal{E},\mathcal{L})$, which share the same orbital frequencies and Ref. [129] provided a numerical example of such a pair (see Fig. 3.1).

In what follows we will show that it is possible to demonstrate the existence of pairs of isofrequency orbits without resorting to a numerical calculation of the Jacobian transformation. To do so it is instructive to change to a new orbital reparametrization given by the pair (Ω_φ, e). This reparametrization is admissible as for fixed e, Ω_φ is a monotonically decreasing function of p. We will show that pairs of isofrequency orbits must exist by considering the value of Ω_r at the boundaries of the region of stable bound orbits in the (Ω_φ, e) parameter space.

For our argument we will require the value of Ω_φ at the separatrix, which we can calculate using l'Hôpital's rule:

$$\Omega^s_\varphi = \lim_{b\to 0} \frac{\int_b^{2\pi} (d\varphi/d\chi)_s \, d\chi}{\int_b^{2\pi} (dt/d\chi)_s \, d\chi} = \left(\frac{1+e}{6+2e}\right)^{3/2}\,, \tag{3.2}$$

---

[1] Barack and Sago commented in the appendix of Ref. [129] that such pairings exist around Schwarzschild black holes.

where $(dt/d\chi)_s$ and $(d\varphi/d\chi)_s$ are given by Eqs. (2.11) and (2.12) with $p = 6+2e$ respectively. A more physically intuitive way to see this result is to recall that such an orbit spends an infinite amount of time at $r = r_{\rm min}$ and thus, recalling Eq. (2.17), we have

$$\Omega^s_\varphi = r_{\rm min}^{-3/2}|_{p=6+2e} = \left(\frac{1+e}{6+2e}\right)^{3/2} , \tag{3.3}$$

which is in agreement with Eq. (3.2). Inverting this equation we find the value, e_s, of the orbital eccentricity at the separatrix for a given Ω_φ to be

$$e_s(\Omega_\varphi) = \frac{1-6\Omega_\varphi^{2/3}}{2\Omega_\varphi^{2/3}-1} . \tag{3.4}$$

We now consider the shape and orbital frequencies of the orbits at the boundaries of the permissible region for stable orbits within the (Ω_φ, e) parameter space. For clarity it may be helpful to refer to Fig. 3.2 during this discussion and the argument that follows. Orbits near the right-hand boundary are Newtonian-type orbits that have a very large p and correspondingly their $r_{\rm min}$ and $r_{\rm max}$ are also large. At the boundary itself $p = \infty$ and the radial frequency of the orbits is zero. The left-hand boundary marks the separatrix between stable and unstable orbits. Where the separatrix intersects the $e = 0$ line marks the location of the ISCO at $r = 6M$. For $0 < e < 1$, orbits with parameters along this boundary are zoom-whirl-type orbits where the zoom stage takes a finite time but the particle spends an infinite time in the whirl phase. At $e = 1$ the periastron radius is at $r_{\rm min} = 4M$ and apastron is at $r_{\rm max} = \infty$. This orbit is both marginally bound and marginally stable and it is this orbit that gets mapped to the upper boundary in the (Ω_φ, e) parameter space. As the orbital period of this orbit is infinite, the radial frequency along the upper boundary is also zero.

We are now in a position to argue for the existence of pairs of isofrequency orbits. If we consider a contour of Ω_r for a small value of Ω_r, such a contour must follow closely the $\Omega_r = 0$ contour outlined above. This means that for certain values of Ω_φ there will exist constant Ω_φ contours (straight vertical lines within the (Ω_φ, e) parametrization) that will intersect certain constant Ω_r contours twice, implying the existence of pairs of isofrequency orbits.

The argument given above is sufficient to demonstrate the existence of isofrequency orbit pairs in Schwarzschild spacetime. It can be backed up with explicit numerical calculations of the Ω_r contours in the (Ω_φ, e) parameter space. As we do not know Ω_r as a function of Ω_φ, we must first numerically invert, for a given e, the equation $\Omega_\varphi(p) = \text{const}$ to find p before we can use Eq. (3.1) to calculate Ω_r. The integrals (2.13) and (2.14) are numerically challenging to evaluate near the separatrix as they both diverge there. For these 'near separatrix' points in the parameter space we expand these integrals in $\epsilon = p - 6 - 2e$ following Ref. [112]. The resulting expansions give

$$\Delta\varphi \approx \sqrt{\frac{6+2e}{e}} \log\left(\frac{64e}{\epsilon}\right) + \mathcal{O}(\epsilon\log\epsilon) , \tag{3.5}$$

$$T_r \approx \frac{4M(3+e)^2}{\sqrt{e}(1+e)^{3/2}}\left[\log\left(\frac{64e}{\epsilon}\right) + \frac{\pi e(9+6e-7e^2)}{4(1-e^2)^{3/2}} + eI(e)\right] + \mathcal{O}(\epsilon\log\epsilon) , \tag{3.6}$$

where the integral $I(e)$ is given by

$$I(e) = \int_0^\pi (1+e\cos\chi)^{-2} D(\cos\chi)\, d\chi , \tag{3.7}$$

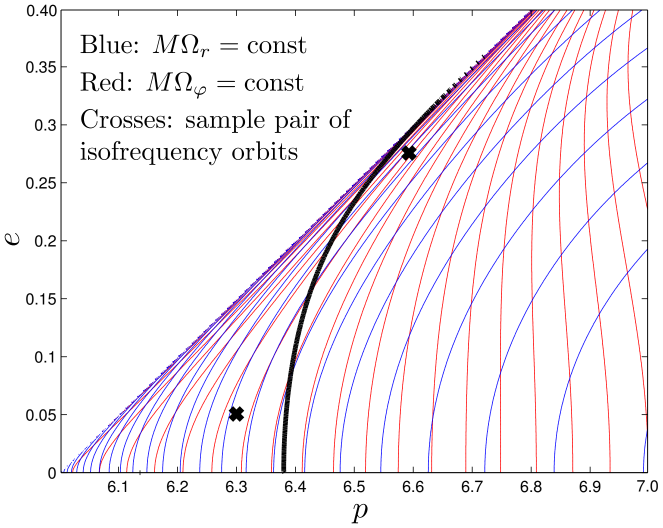

FIGURE 3.1: Contours of fixed Ω_r and Ω_φ within the (p, e) parameter space for bound geodesic orbits about a Schwarzschild black hole. The thick, black line marks the location of the $J = 0$ curve. Orbits with parameters to the left of this line have a dual isofrequency orbit on the right hand side. The two crosses shown mark one such isofrequency pairing with (p, e) values of (6.3,0.05) and (6.59274,0.27569). The contours of fixed Ω_r and Ω_φ are marked on as indicated on the figure. Note that this figure is modelled closely on one that appears in Appendix A. of Ref. [129].

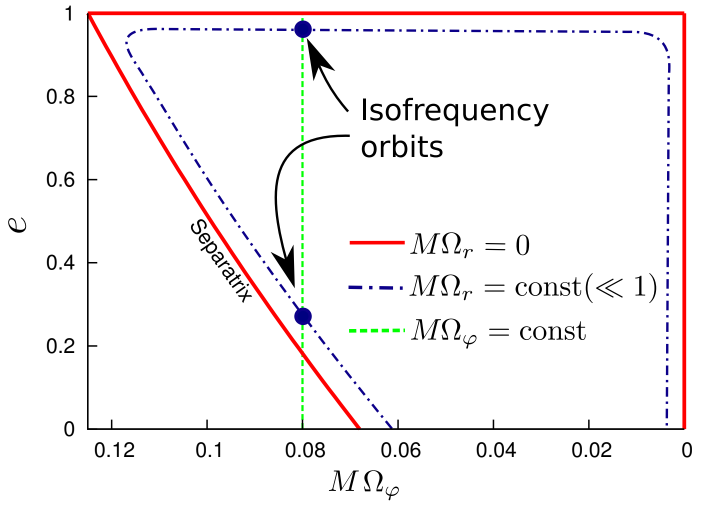

FIGURE 3.2: Diagrammatic overview of the argument given in the text for the existence of isofrequency orbits. The radial frequency Ω_r is found to be zero at the edges of the space of bound stable orbits. Thus we expect a contour of constant $M\Omega_r \ll 1$ to lie near the edge of the parameter space of bound stable orbits. Contours of Ω_φ are straight, vertical lines in the (Ω_φ, e) parametrization and thus it can be seen that some $M\Omega_\varphi = \text{const}$ contours will intersect certain $M\Omega_r = \text{const}$ contours twice, implying the existence of isofrequency orbits.

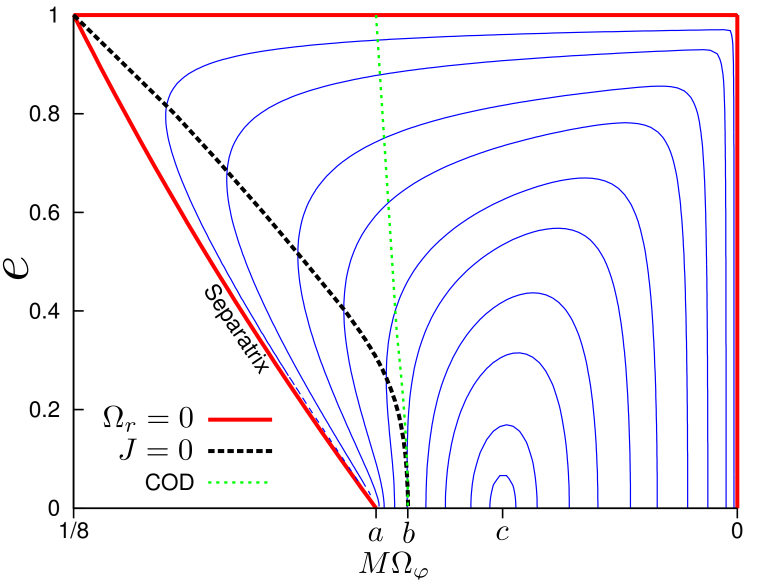

FIGURE 3.3: The (Ω_φ, e) parameter space for bound geodesic orbits about a Schwarzschild black hole. The (red) thick solid curve marks where $\Omega_r = 0$ along the boundary of the space of stable orbits. The (blue) thin lines show contours of constant Ω_r. Contours of constant Ω_φ are simply straight vertical lines in this parametrization. The (black) dashed line shows the curve along which the Jacobian transformation $(p, e) \leftrightarrow (\Omega_r, \Omega_\varphi)$ is singular. The $J = 0$ curve intersects the $e = 0$ curve at b. It can now be seen that pairs of isofrequency orbits must exist as a contour of $\Omega_\varphi = \text{const} > b = M^{1/2}/r_b^{3/2}$, where $r_b = (39 + \sqrt{145})/8M$, will intersect twice contours of Ω_r with $0 < \Omega_r < [(r_b - 6M)M)/r_b^4]^{1/2}$. The (green) dotted line shows the circular orbit dual (COD) orbits with Ω_φ between $a = 1/(6\sqrt{6})M^{-1}$ and b. The COD line also delineates the edge of the dual space. i.e. orbits to the right of this line can have no isofrequency dual, whereas orbits to the left of COD and the right of the $J = 0$ line have a dual to the left of the $J = 0$ line. We also mark on the point $c = 8^{-3/2}M^{-1}$ where Ω_r takes its greatest value along $e = 0$ (which is also the greatest value it attains anywhere within the parameter space).

with

$$D(\cos\chi) = \frac{3 + 2e - e^2\cos^2\chi}{2 + e(1 - \cos\chi)}[2(1 - \cos\chi)]^{1/2} - 3 + e - \frac{1}{4}(7e - 3)(1 + \cos\chi) .$$

Note that in the expansions given here the remaining integral, $I(e)$, is well behaved as $e \to 1$. By using the expansions near the separatrix and Eqs. (2.13) and (2.14) otherwise it is possible to numerically calculate Ω_r for all points in the (Ω_φ, e) parameter space. The results are shown in Fig. 3.3 and the observed behaviour of the Ω_r contours is as predicted by our analytical argument given above.

It is interesting to also consider the location of the $J = 0$ curve in the (Ω_φ, e) parametrization and we plot this curve on Fig. 3.3. As expected it is found to pass through the turning points of the Ω_r contours. By Taylor expanding J about $e = 0$ the intercept between the curve $J = 0$ and the line $e = 0$ is found to be at a radius of $r_0 = r_b = (39 + \sqrt{145})/8M$. This orbit is interesting as its azimuthal frequency is a lower bound on the azimuthal frequency that any orbit with an isofrequency dual can possess. We can also consider the isofrequency dual orbits of the circular orbits (recall that in general circular orbits have an associated non-zero radial frequency given by the frequency of an infinitesimal radial perturbation). We plot the curve of circular orbit dual (COD) orbits on Fig. 3.3. For a given e the COD curve gives the lower bound on the azimuthal frequency that any orbit with an isofrequency dual can possess.

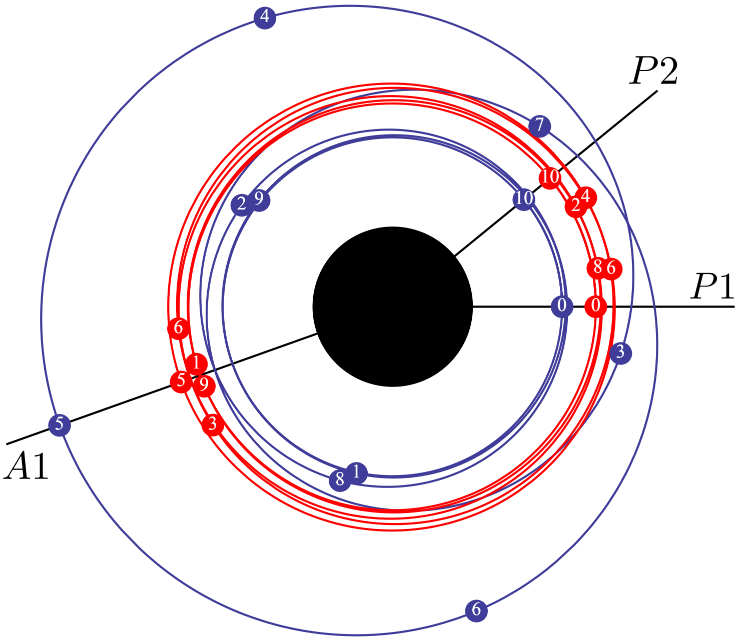

FIGURE 3.4: A sample pair of isofrequency orbits about Schwarzschild black hole. Orbit 1 (in red) has parameters $(p_1, e_1) = (6.255, 0.05)$ and orbit 2 (in blue) has parameters $(p_2, e_2) \simeq (6.718788076, 0.3522488173)$. Both share the same two orbital frequencies of $M(\Omega_r, \Omega_\varphi) \simeq (0.01257801, 0.06426083)$. The orbital period of both orbits is $T_r \simeq 499.535318M$. Both orbits start at their periastron marker '0' along the line $P1$. Each successive marker shows the location of the test body after a time period of $n \times T_r/10$ where n is the marker number. At $T_r/2$ (marker 5) both orbits are synchronised again at their apastra along the line $A1$. When each test body has completed one orbit (marker 10) they are again synchronised at the periastra along the line $P2$. Both orbits have precessed by the same amount.

As a concrete example, the two orbits with parameters $(p_1, e_1) = (6.255, 0.05)$ and $(p_2, e_2) \simeq (6.718788, 0.352249)$ share the same frequencies, namely $M(\Omega_r, \Omega_\varphi) \simeq (0.01257806, 0.06426083)$. Examining these orbits allows one to get a feel for their respective geometry (see Fig. 3.4). If both orbits start at apastron then the radius of orbit 2 is initially greater than orbit 1 and correspondingly its azimuthal phase accumulation is slower. At some later time though the radius of orbit 2 drops below that of orbit 1 and its azimuthal accumulation increases, allowing it to catch up with and overtake orbit 1. At a further later time orbit 2's radius increases beyond that of orbit 1 and orbit 1 catches up with orbit 2 as both orbits return to their apastra.

3.3 Equatorial orbits in Kerr spacetime

For orbits in the equatorial plane of a Kerr black hole the mapping $(p, e) \leftrightarrow (\Omega_r, \Omega_\varphi)$ is still not globally one-to-one. This can be demonstrated using a similar argument as we used above for orbit about a Schwarzschild black hole. The value of the azimuthal frequency at the separatrix can be constructed via l'Hôpital's rule [recall Eq. (3.2)] and using Eqs. (2.63) and (2.64), $\Omega^s_\varphi(e)$ is found to be

$$\Omega^s_\varphi(e) = \frac{\tilde{V}_\varphi(0, p_s(e), e)}{\tilde{V}_t(0, p_s(e), e)} , \tag{3.8}$$

where $\tilde{V}_\varphi(\chi, p, e)$ and $\tilde{V}_t(\chi, p, e)$ are given in Sec. 2.2.4. The value of $p_s(e)$ can be calculated using the method given by Levin and Perez-Giz [120] outlined in Sec. 2.2.4. As was noted for bound eccentric orbits about a Schwarzschild black hole this result can also be calculated by noting that a marginally stable orbit spends an infinite amount of time at $r = r_2$ and thus from Eq. (2.44) we have $\Omega^s_\varphi(e) = \Omega_\varphi(r_{\min}(e))$, where $r_{\min}(e)$ can be calculated via inverting Eq. (2.80).

Explicitly calculating $\Omega^s_\varphi(e)$ one finds that the separatrix maintains a positive slope for all spin values of both prograde orbits (whose orbital spin is aligned with the black hole's spin) and retrograde orbits (whose orbital spin is anti-aligned), with the possible exception of the extremal ($a = M$) prograde case where the separatrix becomes a vertical line i.e., $M\Omega_\varphi(e) = 0.5$ for all e. For spin values where the slope is positive our previous argument holds and isofrequency orbits can be expected (see Fig. 3.5).

Numerical computation of the Ω_r contours throughout the space of stable orbits requires, as before, expansions of $\Delta\varphi$ and T_r near the separatrix. The equivalent expansions to Eqs. (3.5) and (3.6) are derived as follows. Glampedakis and Kennefick [118] give expansions near the separatrix of T_r and $\Delta\varphi$ as

$$T_r \approx 2\left(\frac{p_s}{M}\right)^{1/2} \int_0^\pi \frac{A_t(1-\cos\chi)}{[\epsilon S + 2ex_s^2(1-\cos\chi)]^{1/2}}\, d\chi \,, \tag{3.9}$$

$$\Delta\varphi \approx 2\left(\frac{p_s}{M}\right)^{1/2} \int_0^\pi \frac{A_\varphi(1-\cos\chi)}{[\epsilon S + 2ex_s^2(1-\cos\chi)]^{1/2}}\, d\chi \,, \tag{3.10}$$

where $\epsilon = p - p_s$ and

$$A_t(y) = \frac{[a^2\mathcal{E}_s(1+e-ey)^2 - 2ax_s(1+e-ey)^3/p_s + \mathcal{E}_s p_s^2 M^2]}{(1+e-ey)^2[1-2M(1+e-ey)/p_s + a^2(1+e-ey)^2/(p_s^2M^2)]} \,, \tag{3.11}$$

$$A_\varphi(y) = \frac{[x_s + a\mathcal{E}_s - 2x_s(1+e-ey)/p_s]}{[1-2(1+e-ey)/p_s + a^2(1+e-ey)^2/(p_s^2M^2)]} \,, \tag{3.12}$$

$$S = 2p_sM^2 - (1+e)(3-e)\left(\frac{\partial x^2}{\partial p}\right)_{p=p_s} \,, \tag{3.13}$$

with argument $y = 1 - \cos\chi$ and, as usual, a subscript 's' denotes that quantity's value at the separatrix [recall x is defined in Eq. (2.59)]. Following Cutler, Kennefick and Poisson [112] we now write

$$A_t(y) = A_t(0)[1 + B_t(y)] \,, \tag{3.14}$$

$$A_\varphi(y) = A_\varphi(0)[1 + B_\varphi(y)] \,, \tag{3.15}$$

then we have

$$T_r \approx 2A_t(0)\left(\frac{p_s}{M}\right)^{1/2}\left[\int_0^\pi \frac{d\chi}{[\epsilon S + 2ex_s^2(1-\cos\chi)]^{1/2}} + \int_0^\pi d\chi \frac{B_t(1-\cos\chi)}{[\epsilon S + 2ex_s^2(1-\cos\chi)]^{1/2}}\right] \tag{3.16}$$

The first integral on the right hand side can be evaluated as

$$\int_0^\pi \frac{d\chi}{[\epsilon S + 2ex_s^2(1-\cos\chi)]^{1/2}} = \frac{1}{2}(ex_s^2)^{-1/2}\log\left[\frac{64ex_s^2}{\epsilon S}\right] + \mathcal{O}\left(\frac{\epsilon}{e}\log\left[\frac{e}{\epsilon}\right]\right) \,. \tag{3.17}$$

In the second integral in Eq. (3.16), setting ϵ to zero only introduces a discrepancy at $\mathcal{O}(\epsilon/e\log[e/\epsilon])$. Now that the divergent component of the integrals in Eqs. (3.9) and (3.10) has been isolated we can efficiently numerically evaluate T_r and $\Delta\varphi$ near the separatrix using

$$T_r \approx A_t(0)p_s^{1/2}\left\{(ex_s^2)^{-1/2}\log\left[\frac{64x_s^2}{\epsilon S}\right]+\frac{2}{\sqrt{2}ex_s}\int_0^\pi \frac{B_t(1-\cos\chi)}{(1-\cos\chi)^{1/2}}\,d\chi\right\}\,, \tag{3.18}$$

$$\Delta\varphi \approx A_\varphi(0)p_s^{1/2}\left\{(ex_s^2)^{-1/2}\log\left[\frac{64x_s^2}{\epsilon S}\right]+\frac{2}{\sqrt{2}ex_s}\int_0^\pi \frac{B_\varphi(1-\cos\chi)}{(1-\cos\chi)^{1/2}}\,d\chi\right\}\,. \tag{3.19}$$

where the error is of $\mathcal{O}(\epsilon/e\log[e/\epsilon])$. Using the above expansions and Eqs. (3.8), (2.81) and (2.80) we can compute the orbital frequencies throughout the parameter space eccentric orbits in the equatorial plane of a Kerr black hole for different values of the Kerr spin parameter (see Fig. 3.5).

3.4 Generic orbits in Kerr spacetime

Bound geodesic orbits about a Kerr black hole have a richer structure when they are no longer confined to the equatorial plane. This extra structure arises from the addition of a third orbital frequency, Ω_θ, associated with the test particle's zenithal motion (we note also that orbits in the equatorial plane also possess an Ω_θ frequency associated with an infinitesimal zenithal perturbation). In this section we will numerically demonstrate that despite the existence of this third orbital frequency it is still possible to find pairs of physically distinct orbits that share the same orbital frequencies.

As before we require an orbital parametrization that is in one-to-one correspondence with physical orbits. A common choice is $(\mathcal{E},\mathcal{L},\mathcal{Q})$ where $\mathcal{Q}$ is the Carter constant. As in the Schwarzschild case it will be useful to use an alternative parametrization which for generic orbits about a Kerr black hole consists of $(p,e,\theta_{\text{min}})$ where, recall, p and e are defined through the minimum and maximum orbital radii via Eqs. (2.7) and θ_{min} is the minimum θ angle attained during the orbital motion. Using this parametrization $(\mathcal{E},\mathcal{L},\mathcal{Q})$ can be computed using the formalism given by Schmidt [125] (see Appendix A). Numerical calculation of the orbital frequencies is also detailed by Schmidt but recently Fujita and Hikida have provided analytic formulae (in terms of elliptic integrals) for their computation [126], which we gave in Sec. 2.2.5. We find Fujita and Hikida's formula simpler to work with numerically than Schmidt's and so we prefer to make use of their equations here.

Our first approach to demonstrating the existence of generic isofrequency orbits about a Kerr black hole is to compute the Jacobian for the transformation $(p,e,\theta_{\text{min}})\leftrightarrow(\Omega_r,\Omega_\varphi,\Omega_\theta)$ throughout the parameter space and in particular consider where it might be singular. In general we observe that the Jacobian of the transformation is singular along a set of two dimensional surfaces within the three dimensional orbital parameter space (see Fig. 3.6 for an example). This structure indicates that indeed pairs of generic isofrequency orbits exist. As for bound geodesics in Schwarzschild spacetime and orbits in the equatorial plane of a Kerr black hole, this result would be more satisfying in an (Ω_φ,e)-type parametrization.

We seek to reparametrize our results in an $(\Omega_\theta,e;\Omega_\varphi)$ parametrization. In order to make this reparametrization we take the following steps. Firstly we numerically invert, for a fixed e and θ_{min}, the equation $\Omega_\varphi(p)=\text{const}$ (in the example we will present we take the constant to be $0.14M^{-1}$). This inversion is numerically delicate as one must be careful to construct a code that will not attempt to evaluate Ω_φ for values of $(p,e,\theta_{\text{min}})$ that do not correspond to stable orbits. To achieve this in our code we use a bisection method and take as the lower initial guess,

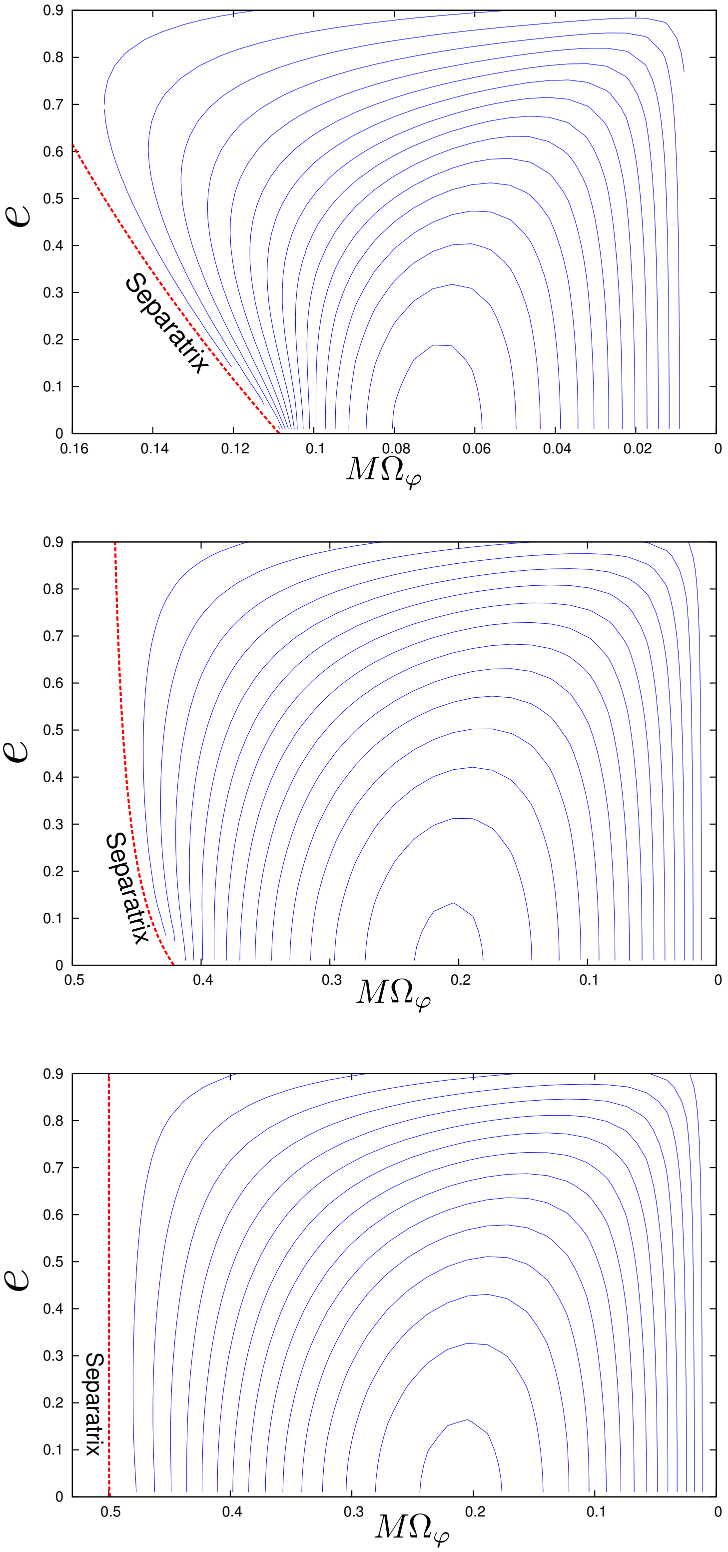

FIGURE 3.5: The (Ω_φ, e) parameter space for eccentric prograde orbits in the equatorial plane of a Kerr black hole for a variety of black hole spin values. The top plot shows the parameter space for $a = 0.5M$, the middle plot, $a = 0.998M$, and the bottom plot $a = 0.999999M$. The thin blue lines are contours of fixed Ω_r. The thick, dashed red line shows the location of the separatrix, calculated using Eq. (3.8). The parameter space of orbits about a Schwarzschild black hole is shown on Fig. 3.3. We do not show the case for retrograde orbits as we find the slope of the separatrix is only weakly dependent on the black hole spin for these orbits and the resulting plots therefore look very similar to Fig. 3.3

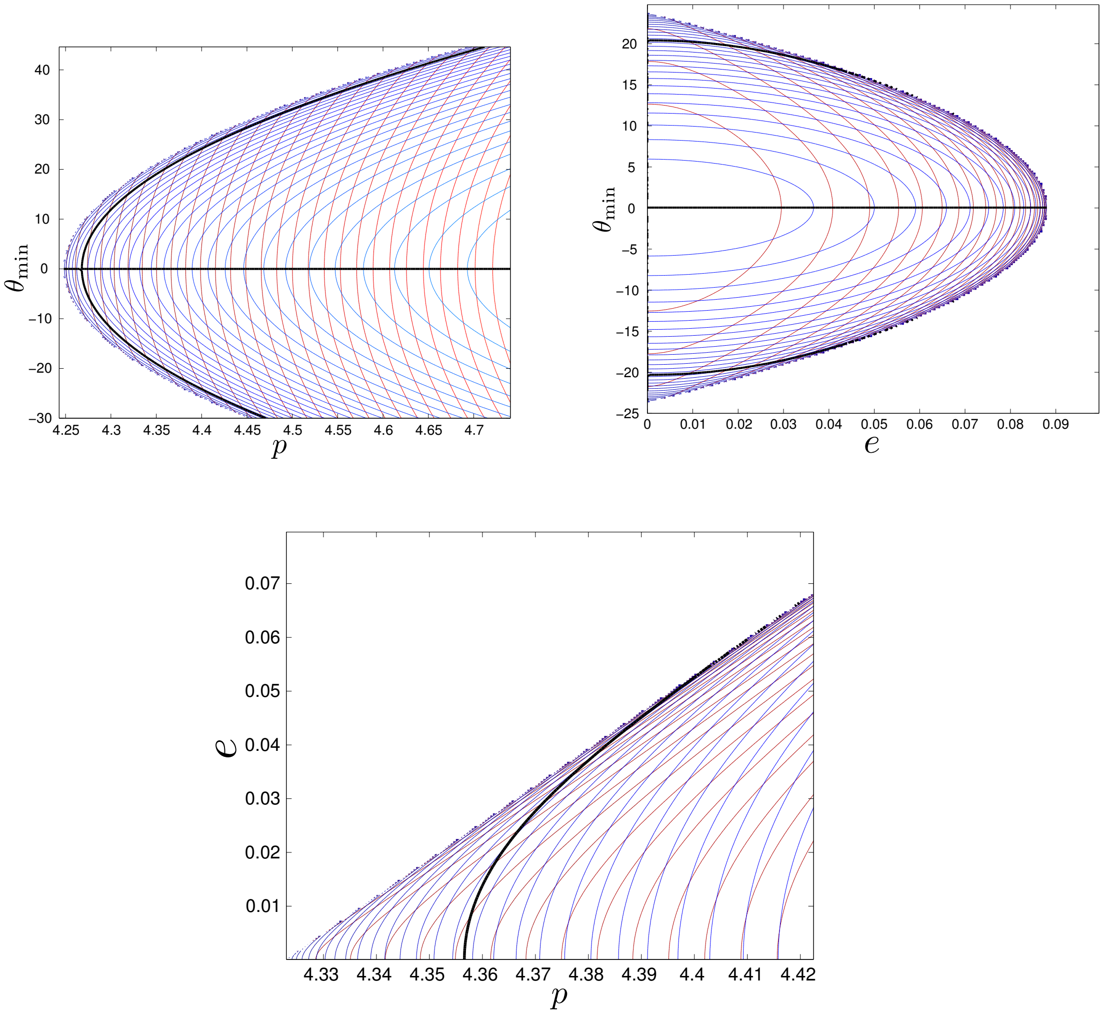

FIGURE 3.6: Slices though the $(p, e, \theta_{\rm min})$ parameter space for generic bound geodesic orbits about a Kerr black hole. All results are for a black hole with a spin of $a = 0.5M$. The thick black line marks the $J = 0$ line whose existence implies the mapping $(\mathcal{E}, \mathcal{L}, \mathcal{Q}) \leftrightarrow (\Omega_r, \Omega_\varphi, \Omega_\theta)$ is not one-to-one. The slices shown depict, reading clockwise from the top-left: fixed $e = 0.01$, fixed $p = 4.36M$ and fixed $\theta_{\rm min} = 20^\circ$

for a given e and $\theta_{\rm min}$, the value of p at the separatrix, p_s, which we construct using the method given in Sec. 2.2.5.1. Once we have the value of p which solves $\Omega_\varphi(p) = \text{const}$ (for the given e and $\theta_{\rm min}$ values) we calculate the corresponding values of Ω_θ and Ω_r. Finally we repeat the first two steps for a great many values of e and $\theta_{\rm min}$. Our technique for ensuring that we get a good coverage of the parameter space, particular near the separatrix, is as follows. For a given e we increase $\theta_{\rm min}$ by a (fixed) small increment. After each increase we check to see if the new values of $p, e, \theta_{\rm min}$ correspond to a bound orbit. If not we return to the previous value of $\theta_{\rm min}$ and increment it by a smaller amount, repeating this process until we are sufficiently close to the separatrix. The final result of the above steps is a list of values of Ω_r for given (Ω_θ, e) and fixed Ω_φ.

In Fig. 3.7 we plot the data produced by use of the above algorithm. We observe that the Ω_r contours form a similar structure as they did for orbits about a Schwarzschild black hole (cf. Fig. 3.3) and thus the existence of isofrequency pairs of generic bound geodesic orbits about a

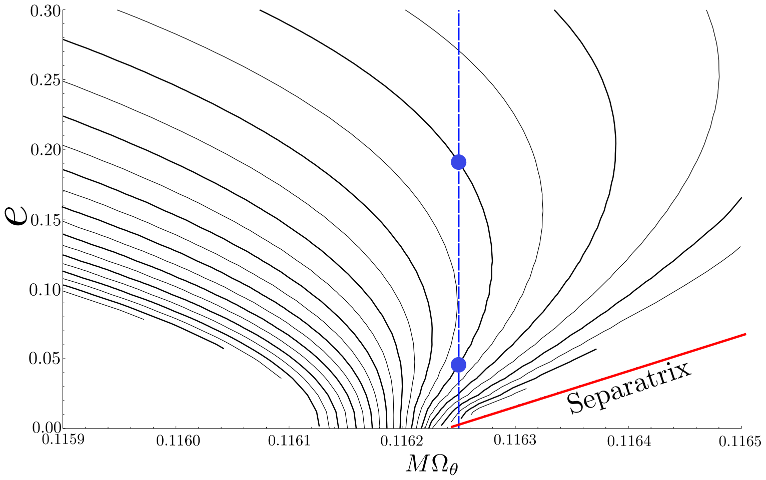

FIGURE 3.7: Contours of fixed Ω_r for generic bound geodesic orbits about a Kerr black hole with spin $a = 0.7M$. All data points in the plot represent orbits with fixed $M\Omega_\varphi = 0.14$. The solid black lines mark contours of fixed Ω_r. The dashed (blue) line shows an example contour of fixed Ω_θ and where this contour intersects one particular Ω_r contour twice we have marked two large (blue) dots. As with the Schwarzschild and Kerr equatorial cases the shape of the Ω_r contours implies that the Ω_θ contours intersect them twice in certain regions of the parameter space. As all points shown also have a fixed Ω_φ this demonstrates the existence of pairs of orbits that share the same three orbital frequencies. The separatrix is marked with the thick, red line. Lastly we note that very close to the separatrix it is difficult to numerically evaluate the orbital frequencies and for this reason we show no data in this region. The missing region of data at the bottom left is an artefact of our method for constructing this figure as outlined in the main text.

Kerr black hole is clearly demonstrated. We remark that using Fujita and Hikida's formulae in the above algorithm greatly reduces the complexity of the calculation (over, say, using Schmidt's formulae) as no expansions in ϵ near the separatrix are required; Fujita and Hikida's formulae are easy to work with throughout the parameter space of bound orbits using computational packages such as *Mathematica* which are extremely efficient at computing elliptic integrals.

As a concrete example, the two orbits about a black hole with spin $a = 0.7M$ parametrized by

$$\begin{pmatrix} p_1 \\ e_1 \\ \theta_{\text{min}\,1} \end{pmatrix} = \begin{pmatrix} 3.794125034000000 \\ 0.120010000000000 \\ 2.081308633000000 \end{pmatrix}, \quad \begin{pmatrix} p_2 \\ e_2 \\ \theta_{\text{min}\,2} \end{pmatrix} = \begin{pmatrix} 3.559672050018241 \\ 0.043235122790126 \\ 1.917751714944654 \end{pmatrix}, \tag{3.20}$$

share the same three orbital frequencies, namely

$$M \begin{pmatrix} \Omega_r \\ \Omega_\theta \\ \Omega_\varphi \end{pmatrix} = \begin{pmatrix} 0.0077004320733 \\ 0.1163563408516 \\ 0.1402005354460 \end{pmatrix}. \tag{3.21}$$

In the above two equations all the digits presented are accurate. We discuss in the concluding chapter of this work the possible physical consequences of the existence of isofrequency orbits that should be explored.

Chapter 4

Essential background: perturbations of Schwarzschild and Kerr spacetimes

In this ‘Essential background’ chapter we review the formalism of perturbations of Schwarzschild and Kerr spacetimes. In particular, we shall review scalar-field perturbations of Kerr spacetime and gravitational perturbations (in the Lorenz gauge) in Schwarzschild spacetime. In both cases the perturbation is to be sourced by a point particle and we decompose both the source and the field equations into the frequency domain.

For scalar perturbations in Kerr spacetime, if we wish to separate more than just the azimuthal dependence of the perturbation (as is done in the m-mode scheme, see Sec. 5.5), one must work in the frequency domain; it is not possible to separate the zenithal dependence without also performing a Fourier decomposition (this is also the case when working within the Teukolsky formalism). The frequency-domain approach is then the path we must take because, recall, we do wish to perform a full multipole decomposition for two reasons: (i) the individual multipole modes are continuous at the particle and (ii) the mode-sum scheme to regularize the field at the particle requires these multipole modes as input. There is some subtlety in the second point because in Kerr spacetime the full separation of the scalar-field equations is achieved in terms of *spheroidal harmonic* and frequency modes whereas, the mode-sum scheme requires *spherical harmonic* modes as input. We discuss how to overcome this mismatch in Chapter 5.

For our work on gravitational perturbations we choose to work in the Lorenz gauge for the reasons we discuss in Chapter 1 and Sec. 4.5 below. For gravitational perturbations in Schwarzschild spacetime it is not necessary, as it is for scalar-field pertubations in Kerr spacetime, to perform a frequency-domain decomposition; one can perform a multipole decomposition and work in the time-domain in 1+1 dimensions [62, 67]. We chose to go further than this though and separate out the time dependence for the reasons we gave in Sec. 1.4. Lorenz gauge gravitational perturbations are much more complicated than scalar-field perturbations and, in this chapter, we opt to give the necessary formula required for later chapters, referring to the literature where necessary for the relevant derivations.

4.1 Scalar field and multipole decomposition in Kerr spacetime

In Chapters 6 and 7 we will be interested in the scalar-field self-force (SSF) felt by a particle carrying a scalar charge on a bound geodesic orbit about a Kerr black hole. At the time of writing no fundamental scalar fields have been observed[1], so there is some arbitrariness in the choice of field equation. Several different choices have been studied, including within the context of SF calculations [130], but in this work we shall assume that the scalar field Φ associated with the particle's scalar charge q obeys the minimally coupled Klein-Gordon equation

$$\Box\Phi \equiv \Phi^{\alpha}_{;\alpha} = -4\pi T \ , \tag{4.1}$$

where ; denotes covariant differentiation with respect to the background Kerr metric and T denotes the particle's scalar charge density. In a given coordinate system the D'Alembertian operator can be expressed as

$$\Box\Phi = [-\det(\mathring{g})]^{-1/2}\frac{\partial}{\partial x^{\mu}}\left(\mathring{g}^{\mu\nu}\,[-\det(\mathring{g})]^{1/2}\,\frac{\partial\Phi}{\partial x^{\nu}}\right) \ , \tag{4.2}$$

where we remind that $\det(\mathring{g}) = -\rho^4\sin^2\theta$ is the metric determinant with $\rho^2 = r^2 + a^2\cos\theta$. In this work we choose to model the scalar charge density as a δ-function along the particle's world line

$$\begin{aligned} T &= q\int \delta^4(x^{\mu} - x^{\mu}_p(\tau))[-g(x)^{-1/2}]d\tau \ , \\ &= \frac{q}{\rho^2\sin\theta u^t}\delta(r - r_p)\delta(\theta - \theta_p)\delta(\varphi - \varphi_p) \ , \end{aligned} \tag{4.3}$$

where the second equation is obtained by changing integration variable from τ to t in the first equation. We note that the t-component of the four-velocity u^t is simply calculated as $u^t = g^{t\varphi}\mathcal{L} - g^{tt}\mathcal{E}$.

The scalar wave equation (4.1) in Kerr geometry can be completely separated [131, 132] into spheroidal harmonic and frequency modes in the form

$$\Phi = \int \sum_{\hat{l}=0}^{\infty}\sum_{m=-\hat{l}}^{\hat{l}} R_{\hat{l}m\omega}(r)S_{\hat{l}m}(\theta;\sigma^2)e^{im\varphi}e^{-i\omega t}\,d\omega \ . \tag{4.4}$$

Here $S_{\hat{l}m}(\theta;\sigma^2)$ are spheroidal Legendre functions with spheroidicity σ^2 [we reserve the term *spheroidal harmonic* for the product $S_{\hat{l}m}(\theta;\sigma^2)e^{im\varphi}$]. Notice that we label spheroidal harmonic modes by $\hat{l}m$, as we will later introduce *spherical* harmonics modes which we will label by lm. It will be useful to recall from Appendix B that the spheroidal harmonics are orthonormal with normalization given by

$$\oint S_{\hat{l}m}(\theta;\sigma^2)e^{im\varphi}S_{\hat{l}'m'}(\theta;\sigma^2)e^{-im'\varphi}d\Omega = \delta_{\hat{l}\hat{l}'}\delta_{mm'} \ , \tag{4.5}$$

with area element $d\Omega = \sin\theta d\theta d\varphi$, and with $\delta_{n_1n_2}$ being the standard Kronecker delta.

In appendix C.1 we show that the source spectra for the orbits examined in this work are

---

[1] The Higgs field of the standard model is the only widely accepted candidate for a fundamental physical scalar field.

given by

$$\omega = \begin{cases} m\Omega_\varphi & \text{circular, equatorial orbits ,} \\ m\Omega_\varphi + k\Omega_\theta & \text{circular, inclined orbits ,} \\ m\Omega_\varphi + n\Omega_r & \text{eccentric, equatorial orbits ,} \end{cases} \tag{4.6}$$

where m, n, k are integers and Ω_φ, Ω_θ and Ω_r are given by Eqs. (2.44),(2.56) and (2.69) for their respective orbits. The nature of the source spectra implies that the integral in Eq. (4.4) can be rewritten as a sum over discrete modes.

The point particle source is decomposed in a similar fashion to the field as

$$\rho^2 T = \sum_{\hat{l}=0}^{\infty} \sum_{m=-\hat{l}}^{\hat{l}} \sum_{n,k=-\infty}^{\infty} \tilde{T}_{\hat{l}m\omega}(r) S_{\hat{l}m}(\theta; \sigma^2) e^{im\varphi} e^{-i\omega t} \ , \tag{4.7}$$

where the ρ^2 factor is introduced for later convenience and the innermost sum is taken over n or k depending on the orbit type. Using the orthonormal properties (4.5) of spheroidal harmonics and taking the inverse Fourier transform of (4.7), the radial dependence of the source is found to be

$$\tilde{T}_{\hat{l}m\omega}(r) = \begin{cases} \dfrac{q}{T_\theta} \displaystyle\int_0^{T_\theta} \frac{S_{\hat{l}m}(\theta_p(t); -a^2\omega^2)}{u^t(\theta_p(t))} e^{i(\omega t - m\varphi_p(t))} \delta(r - r_0) dt \ , & \text{circular inclined ,} \\ q S_{\hat{l}m}(\pi/2; -a^2\omega^2) T_r^{-1} \displaystyle\int_0^{T_r} (u^t)^{-1} \delta[r - r_p(t)] e^{i(\omega t - m\varphi)} dt \ , & \text{eccentric equatorial .} \end{cases} \tag{4.8}$$

For circular equatorial orbits ($r_p = r_0$, $\varphi_p = \Omega_\varphi t$, $\omega = m\Omega_\varphi$, $\theta = \pi/2$) the above equation reduces to

$$\tilde{T}_{\hat{l}m\omega}(r_0) = q \frac{S_{\hat{l}m}(\pi/2; -a^2\omega^2)}{u^t(r_0)} \delta(r - r_0) \ , \qquad \text{circular equatorial .} \tag{4.9}$$

For eccentric equatorial orbits we note that $\tilde{T}_{\hat{l}m\omega_m}(r)$ only has support for $r_{\min} < r < r_{\max}$ and changing integration variable from t to r_p (assuming a periapsis passage at $t = 0$), we have

$$\tilde{T}_{\hat{l}m\omega}(r) = -\frac{2qS_{\hat{l}m}(\pi/2; -a^2\omega^2)}{T_r |u^r(r)|} \cos[\omega t_p(r) - m\varphi_p(r)] \times \Theta(r - r_{\min}) \times \Theta(r_{\max} - r) \ , \tag{4.10}$$

where Θ is the standard Heaviside step function.

Substituting the field decomposition (4.4) into the field equation (4.1) and using the source decomposition above, we find the radial and angular equations to be

$$\begin{aligned} &\Delta \frac{\partial}{\partial r}\left(\Delta \frac{\partial R_{\hat{l}m\omega}}{\partial r}\right) + \left[a^2 m^2 - 4Mrma\omega + (r^2 + a^2)^2 \omega^2 - a^2\omega^2 \Delta - \lambda_{\hat{l}m} \Delta\right] R_{\hat{l}m\omega} \\ &= -4\pi \Delta \tilde{T}_{\hat{l}m\omega}(r) \ , \end{aligned} \tag{4.11}$$

$$\frac{1}{\sin\theta} \frac{\partial}{\partial\theta}\left(\sin\theta \frac{\partial S_{\hat{l}m}}{\partial\theta}\right) + \left(\lambda_{\hat{l}m} + a^2\omega^2 \cos^2\theta - \frac{m^2}{\sin^2\theta}\right) S_{\hat{l}m} = 0 \ , \tag{4.12}$$

where we remind that $\Delta \equiv r^2 - 2Mr + a^2$. The angular equation (4.12) takes the form of the spheroidal Legendre equation with spheroidicity $\sigma^2 = -a^2\omega^2$ (see Appendix B). Its eigenfunctions are the spheroidal Legendre functions $S_{\hat{l}m}(\theta; -a^2\omega_{mn}^2)$ and its eigenvalues are denoted by

$\lambda_{\hat{l}m}$. In general there is no closed form for $S_{\hat{l}m}$ or $\lambda_{\hat{l}m}$, but they can be calculated using the spherical harmonic decomposition method described in Appendix B. When $a = 0$, the spheroidal harmonics $S_{\hat{l}m}e^{im\varphi}$ coincide with the spherical harmonics $Y_{\hat{l}m}$ and their eigenvalues reduce to $\lambda_{\hat{l}m} = \hat{l}(\hat{l}+1)$.

To simplify construction of boundary conditions and later assist our numerical scheme, it is convenient to transform to a new variable

$$\psi_{\hat{l}m\omega}(r) \equiv rR_{\hat{l}m\omega}(r) \ , \tag{4.13}$$

and introducing the tortoise radial coordinate r_* defined through

$$\frac{dr_*}{dr} = \frac{r^2}{\Delta} \ . \tag{4.14}$$

With the above definition the tortoise coordinate is given explicitly in terms of r as

$$r_* = r + M\ln(\Delta/M^2) + \frac{(2M^2 - a^2)}{2(M^2 - a^2)^{1/2}} \ln\left(\frac{r - r_+}{r - r_-}\right) \ , \tag{4.15}$$

where we have specified the constant of integration and $r_\pm$ are given by Eq. (2.23). There are other common choices for the tortoise coordinate. Our choice is motivated by the observation of Bardeen *et al.* [119] that it leads to a simpler radial potential than other common choices [132], which in particular simplifies constructing the numerical boundary conditions for the resulting radial equation (see Chapter 6).

In terms of $\psi_{\hat{l}m\omega}(r)$ and r_*, the radial equation (4.11) takes the simpler form,

$$\frac{d^2\psi_{\hat{l}m\omega}}{dr_*^2} + W_{\hat{l}m\omega}(r)\psi_{\hat{l}m\omega} = -\frac{4\pi\Delta}{r^3}\tilde{T}_{\hat{l}m\omega} \equiv Z_{\hat{l}m\omega}(r) \ , \tag{4.16}$$

where $\tilde{T}_{\hat{l}m\omega}$ is given in Eq. (4.10) and $W_{\hat{l}m\omega}$ is an effective (ω-dependent) radial potential given by

$$W_{\hat{l}m\omega}(r) = \left[\frac{(r^2 + a^2)\omega - am}{r^2}\right]^2 - \frac{\Delta}{r^4}\left[\lambda_{\hat{l}m} - 2am\omega + a^2\omega^2 + \frac{2(Mr - a^2)}{r^2}\right] \ . \tag{4.17}$$

There is no known analytic solution to the radial equation (4.16) for general $\hat{l}m\omega$ and thus it has to be solved numerically, the details of which we give in Chapter 6.

4.2 Scalar field boundary conditions

Equation (4.16) determines the radial field $\psi(r)$ anywhere outside the black hole once boundary conditions are specified on the horizon ($r_* \to -\infty$) and at spatial infinity ($r_* \to \infty$). The boundary conditions follow from physical considerations: at the event horizon radiation should be “ingoing” and at spatial infinity radiation should be “outgoing”. For reasons discussed above, we choose to describe the radial equation (4.16) using the r_* tortoise coordinate, but in constructing the asymptotic boundary conditions we choose to work with an alternative tortoise coordinate given by

$$\frac{d\tilde{r}_*}{dr} = \frac{r^2 + a^2}{\Delta} \ . \tag{4.18}$$

This definition of the tortoise coordinate is useful, in that $v \equiv t + \tilde{r}_*$ and $u \equiv t - \tilde{r}_*$ are then the standard advanced and retarded null coordinates in Kerr spacetime with t as the proper time at infinity. These coordinates have the feature that along an ingoing null geodesic v is constant, and similarly along an outgoing null geodesic u is constant [115]. In order to convert between the two tortoise coordinates we note the asymptotic relations,

$$r_* \to \begin{cases} \tilde{r}_* + \text{const} & \text{as} \quad r_* \to \infty \ , \\ [r_+/(2M)]\tilde{r}_* + \text{const} & \text{as} \quad r_* \to -\infty \ . \end{cases} \tag{4.19}$$

As the boundaries are approached, the potential $W(r)$ in the radial equation approaches a constant value and the equation becomes that of a simple harmonic oscillator with frequencies,

$$W^{1/2}(r_* \to \infty) = \omega \ , \tag{4.20}$$

$$W^{1/2}(r_* \to -\infty) = \frac{2Mr_+\omega - am}{r_+^2} \equiv \gamma \ . \tag{4.21}$$

Combining this observation with the field decomposition given by Eq. (4.4), we observe that, at infinity, the t, r-dependence of the $\hat{l}m\omega$-mode contribution to the full field Φ will have the asymptotic form $\Phi_{\hat{l}m\omega} \sim \exp[-i\omega(t \pm \tilde{r}_*)]/r$, where we have converted from r_* to $\tilde{r}_*$ using Eq. (4.19). Choosing the lower sign in the exponent makes it a function of the retarded time coordinate $u = t - \tilde{r}_*$ only, ensuring that any radiation will be purely outgoing at infinity. Thus the correct asymptotic boundary condition for the radial field is given by

$$\psi_{\hat{l}m\omega}(r_* \to \infty) \sim e^{+i\omega r_*} \ . \tag{4.22}$$

At the horizon we require the scalar field to be regular and this in turn will guarantee all radiation is either purely ingoing or purely outgoing at the horizon. The asymptotic radial solutions admit the form $\psi_{\hat{l}m\omega} \sim \exp(\pm i\gamma r_*) \sim \exp[\pm i(\omega - m\Omega_+)\tilde{r}_*]$, where again we have expressed r_* in terms of $\tilde{r}_*$ using Eq. (4.19), and Ω_+, the angular velocity of a stationary observer just outside the event horizon, is given by Eq. (2.36).

In ensuring that each $\hat{l}m\omega$-mode contribution to the full field Φ is regular at the horizon care must be taken. This is because the Boyer-Lindquist coordinate φ is *singular*[2] at the horizon [115], and hence the factor $\exp(im\varphi)$ in Eq. (4.4) is singular too. We must instead express the field in terms of a regular azimuthal coordinate and, following [133], we introduce

$$\varphi_+ \equiv \varphi - \Omega_+ t. \tag{4.23}$$

In terms of the regular coordinate φ_+, we obtain, as $r_* \to -\infty$, $\Phi_{\hat{l}m\omega} \sim \exp[im\varphi_+ - i(\omega - m\Omega_+)(t \mp \tilde{r}_*)]$, where $\mp$ correspond to $\pm$ in the radial solutions $\psi_{\hat{l}m\omega} \sim \exp(\pm i\gamma r_*)$. For this to represent purely ingoing radiation, the lower sign must be selected, so that $\Phi_{\hat{l}m\omega}$ becomes asymptotically a function of the advanced time $v = t + \tilde{r}_*$ only. We thus find that the correct boundary condition at the horizon is given by

$$\psi_{\hat{l}m\omega}(r_* \to -\infty) \sim e^{-i\gamma r_*} \ . \tag{4.24}$$

---

[2] Whilst an observer can make the trip to the event horizon in a finite proper-time, the corresponding interval of coordinate time is infinite. As $d\varphi/dt$ remain finite at the horizon (see Sec. 2.2.1) φ increases by an infinite amount.

4.3 Energy and angular momentum of the scalar waves

In this section we briefly review the relevant formalism for computing the radiative flux of the scalar wave. The stress-energy tensor of the scalar field is given by[115]

$$T_{\alpha\beta}^{\text{field}} = \frac{1}{4\pi}(\Phi_{,\alpha}\Phi_{,\beta} - \frac{1}{2}g_{\alpha\beta}\Phi^{,\mu}\Phi_{,\mu}) \ . \tag{4.25}$$

In order to consider the scalar-field energy and angular momentum flowing to infinity and down through the event horizon, we define two spherical (timelike) hypersurfaces $\Sigma^{\pm}$ by the relation

$$\Theta^{\pm} = r - \text{const}^{\pm} = 0 \ , \tag{4.26}$$

where $\text{const}^{+} \gg M$ and $r_*(\text{const}^{-}) \ll -M$. The unit normal to $\Sigma^{\pm}$ is then given by

$$n_\alpha \equiv \frac{\Theta_{,\alpha}}{|g^{\mu\nu}\Theta_{,\mu}\Theta_{,\nu}|^{1/2}} = \delta^r_\alpha \rho \Delta^{-1/2} \ , \tag{4.27}$$

where we have dropped the $\pm$ from Θ, as the unit normal is not explicitly dependent on $\text{const}^{\pm}$. Lastly we note that the determinant of the induced metric on $\Sigma^{\pm}$ is given by

$$\det(g^{(3)}) \equiv -\Delta\rho^2 \sin^2\theta \ . \tag{4.28}$$

Let $d\Sigma^{\pm}$ represent an element of $\Sigma^{\pm}$ over a small time span dt. The amount of scalar-field energy and angular-momentum flowing through $\Sigma^{\pm}$, over time dt, is then expressed by

$$dE_{\pm} = \mp \oint T^{\alpha}{}_{\beta}\xi^{\beta}_{(t)} d\Sigma^{\pm}_{\alpha} \ , \qquad dL_{\pm} = \mp \oint T^{\alpha}{}_{\beta}\xi^{\beta}_{(\varphi)}\, d\Sigma^{\pm}_{\alpha} \ , \tag{4.29}$$

(see e.g., Sec. 4.3.6 of [115]), where $d\Sigma^{\pm}_{\alpha} = [-\det(g^{(3)})]^{1/2} n_\alpha d\theta d\varphi dt$ represent outward-pointing surface elements on $d\Sigma^{\pm}$, and the integral is performed over the corresponding 2-spheres of constant r, t. Recall that, in coordinate form, the Killing vectors $\xi^{\beta}_{(t)}$ and $\xi^{\beta}_{(\varphi)}$ are given by δ^{β}_{t} and δ^{β}_{φ} respectively [see Eq. (2.24)]. The signs are chosen such that the *outflow* of energy through Σ^{+} and the *inflow* of energy through Σ^{-} is positive in the Schwarzschild case (recall, however, that dE_{-} can turn negative in the Kerr case, when superradiance is manifest). The (time-independent) flux of energy and angular momentum through $\Sigma_{\pm}$ is, hence, given by

$$\dot{E}_{\pm} \equiv \frac{dE_{\pm}}{dt} = \mp\Delta \oint T_{tr}\, d\Omega \ , \qquad \dot{L} \equiv \frac{dL_{\pm}}{dt} = \mp\Delta \oint T_{\varphi r}\, d\Omega \ . \tag{4.30}$$

Noting that Φ is a real field and using Eq. (4.25) we have $T_{tr} = (4\pi)^{-1}\Phi_{,t}\Phi^{*}_{,r}$ and $T_{\varphi r} = (4\pi)^{-1}\Phi_{,\varphi}\Phi^{*}_{,r}$ where we have taken the complex conjugate (denoted by an asterisk) of $\Phi_{,r}$ in order to facilitate the angular integrations in Eqs. (4.30). We then substitute the spheroidal-harmonic decomposition

$$\Phi = \frac{1}{r}\sum_{\hat{l}m} \psi_{\hat{l}m}(r) S_{\hat{l}m}(\theta; -a^2\omega^2) e^{im\varphi} e^{-i\omega_m t} \equiv \sum_{\hat{l}m} \Phi_{\hat{l}m} \ , \tag{4.31}$$

making the replacement $(\Phi_{\hat{l}m})_{,t} = -i\omega\Phi_{\hat{l}m}$. The asymptotic relations (4.22) and (4.24) allow us to replace $(\Phi^{*}_{\hat{l}m})_{,r} = -i\omega\Phi^{*}_{\hat{l}m}$ for $r \to \infty$, and $(\Phi^{*}_{\hat{l}m})_{,r} = 2iMr_{+}\Delta^{-1}(\omega - m\Omega_{+})\Phi^{*}_{\hat{l}m}$ for $r \to r_{+}$ [where in the last equality we used Eqs. (4.14), (4.21) and (2.36)]. With these substitutions, and explicitly writing

$$\begin{aligned} \psi_{\hat{l}m}(r \to \infty) &= \tilde{c}_0^+ \exp(i\omega r) \,, \\ \psi_{\hat{l}m}(r \to r_+) &= \tilde{c}_0^- \exp(-i\gamma r_*) \,, \end{aligned} \tag{4.32}$$

where $\tilde{c}_0^+$ and $\tilde{c}_0^-$ are constants, the integrals in Eq. (4.30) are readily evaluated using the orthonormality property of the spheroidal harmonics (B.28), giving

$$\langle \dot{E}_+ \rangle = \frac{1}{4\pi} \sum_{\hat{l}m\omega} \omega^2 |\tilde{c}_0^+|^2, \qquad \langle \dot{E}_- \rangle = \frac{M}{2\pi r_+} \sum_{\hat{l}m\omega} \omega(\omega - m\Omega_+) |\tilde{c}_0^-|^2 \,, \tag{4.33}$$

$$\langle \dot{L}_+ \rangle = \frac{1}{4\pi} \sum_{\hat{l}m\omega} m\omega |\tilde{c}_0^+|^2, \qquad \langle \dot{L}_- \rangle = \frac{M}{2\pi r_+} \sum_{\hat{l}m\omega} m(\omega - m\Omega_+) |\tilde{c}_0^-|^2 \,, \tag{4.34}$$

where the $+$ and $-$ subscripts denote the flux radiated to infinity and down the event horizon, respectively, an overdot denotes differentiation with respect to t, and $\langle \cdot \rangle$ denotes a t-average over an orbital period. For eccentric equatorial orbits the relevant orbital period is T_r. For circular, inclined orbits the relevant period is T_θ. For circular equatorial orbits, due to the stationarity of the setup, no averaging is required.

4.4 Superradiance

We now consider the case of scattered radiation in Kerr spacetime. As the black hole will absorb some of any radiation incident upon it, one would naturally expect any radiation scattered to infinity to have a smaller amplitude than the incoming radiation. For rotating black holes this turns out to not always be the case; an incoming wave can be amplified in a process known as superradiant scattering, with the additional energy being sourced from the black hole's rotational energy.

For a scalar field Φ, the condition for superradiant scattering is derived as follows. If we irradiate an isolated Kerr black hole with radiation from past null infinity, with amplitude A_{in}, and consider the amplitude of the outgoing radiation A_{out}, then, following the derivation in Sec. 4.2, asymptotically the field will take the form

$$\Phi \sim \begin{cases} e^{-i(\omega - m\Omega_+)\tilde{r}_*} & \text{as} \quad r \to r_+ \,, \\ A_{\text{out}}(\omega) e^{i\omega\tilde{r}_*} + A_{\text{in}}(\omega) e^{-i\omega\tilde{r}_*} & \text{as} \quad r \to \infty \,, \end{cases} \tag{4.35}$$

where we have, without loss of generality, normalized the incoming radiation so that the amplitude of the radiation absorbed by the black hole is equal to one. As the field equation (4.16) contains no first order derivatives, the Wronskian formed by the two linearly independent solutions is a constant. Using Eq. (4.35) and comparing the Wronskian near infinity and at the event horizon gives the relation

$$\left(1 - \frac{m\Omega_+}{\omega}\right) = A_{\text{in}}^2 - A_{\text{out}}^2 \,. \tag{4.36}$$

Thus we see that the amplitude A_{out} of the outgoing radiation will be greater than the amplitude

A_{in} of the incident radiation when

$$\omega < m\Omega_+ = \frac{ma}{2Mr_+} \ . \tag{4.37}$$

When this condition holds, an observer at infinity sees radiation leaving the event horizon, though a local observer at the horizon always sees any radiation as ingoing.

For circular equatorial orbits, the mode frequency is given by $\omega_m = m\Omega_\varphi$ and the condition (4.37) translates to $\Omega_\varphi < \Omega_+$. Using Eqs. (2.44) and (2.36), this then implies that all m-modes of the scalar field are superradiant for prograde circular equatorial geodesic orbits, with $r_0 > r_0^{\text{sr}}(a)$ with radius

$$r_0^{\text{sr}}(a) \equiv M\left(\frac{r_+^2}{aM}\right)^{2/3} \ . \tag{4.38}$$

Since the discovery of superradiance [134], there has been interest in the possibility of *floating orbits* [135]; i.e., orbits that absorb as much radiation as they emit. Hughes [117] has shown for the gravitational two body problem where one of the bodies is compact with a small, but finite, mass that the total energy 'radiated from the horizon' is, at most 10%, of the energy radiated to infinity, thus excluding the possibility of floating orbits.

4.5 Gravitational perturbations in the Lorenz gauge and multipole composition in Schwarzschild spacetime

In Chapter 8 we will be concerned with numerically solving for the metric perturbation from a point-like particle and in this section we give the decomposition of the metric perturbation into multipole modes. Let us denote the full spacetime metric by g, which we shall consider to be the sum of the metric perturbation, h, and the background Schwarzschild metric, $\mathring{g}$, such that $g = \mathring{g} + h$, where, recall, an overring denotes a quantity's value in the background (vacuum) spacetime. In a given coordinate system, the Einstein field equations will then take the form

$$G_{\mu\nu}\left[\mathring{g}_{\mu\nu} + h_{\mu\nu}\right] = 8\pi T_{\mu\nu} \ , \tag{4.39}$$

where G is the Einstein tensor, a functional of the full spacetime metric g, and T is the stress energy tensor. Let us define the trace of the metric perturbation by $\text{Tr}(h) = \mathring{g}^{\mu\nu}h_{\mu\nu}$. We shall find the that the field equations for the metric perturbation take a simpler form when expressed in terms of the trace-reversed metric perturbation, $\bar{h}_{\mu\nu}$, defined by

$$\bar{h}_{\mu\nu} \equiv h_{\mu\nu} - \frac{1}{2}\mathring{g}_{\mu\nu}\text{Tr}(h) \ , \tag{4.40}$$

so named because $\text{Tr}(\bar{h}) = -\text{Tr}(h)$. We also make the choice to work in the Lorenz gauge, defined by

$$\nabla_\mu \bar{h}^{\mu\nu} = 0 \ , \tag{4.41}$$

where the covariant derviative is taken with respect to the background metric. In Chapter 1 we briefly touched upon why the Lorenz gauge is motivated in our context and we briefly expand upon our reasons now [61]:

- The regularization formalism for the GSF, that we outline in Chapter 5, has only been prescribed in the Lorenz gauge. For generic orbits, it is not known how to construct the

GSF in other gauges, though it has been shown that the same regularization procedure can be employed in alternative gauges when there exists a regular gauge transformation between the alternative gauge and the Lorenz gauge [56]. This has allowed the GSF to be computed in the Regge-Wheeler gauge, in the particular case of particle falling radially into a Schwarzschild black hole [103]. It has also been possible to extract gauge-independent results from calculations based upon the Regge-Wheeler gauge, when the particle is moving on a circular orbit about a Schwarzschild black hole [63]. Recently, there has been progress in performing GSF calculations in the radiation gauge, again for a particle on a circular orbit about a Schwarzschild black hole [80, 65]. There has also been recent progress defining the GSF in a more general class of gauges [136].

- In the Lorenz gauge one solves directly for the metric perturbation components, avoiding the need for the complicated reconstruction procedures that come when working in either the Regge-Wheeler or radiation gauges [137, 138, 65]. In particular, from a numerical point of view, these reconstruction procedures are undesirable, as they involve taking multiple derivatives of the field variables in order reconstruct the metric perturbation (numerical differentiation often results in a loss of numerical accuracy).

- The components of metric perturbation expressed in the Lorenz gauge take a more regular form than they do when expressed in either of the commonly used variables of Teukolsky or Moncrief [56]. For the work presented in this thesis, this has an important practical upshot with regard to our numerical implementation: when a tensor spherical harmonic decomposition is made, the individual multipoles of the Lorenz gauge metric perturbation are *continuous* at the particle, with only their first derivatives discontinuous there. On the other hand, the multipole modes of the metric perturbation expressed in Teukolsky's or Moncrief's variables are discontinuous at the particle, as are, in general, the multipole modes of the metric perturbation in the Regge-Wheeler gauge.

We now seek the (Lorenz gauge) linearized Einstein equation, which is obtained by expanding the Einstein tensor, $G_{\mu\nu}$, and only retaining terms up to linear order in the metric perturbation, the result of which gives

$$\Box\bar{h}_{\mu\nu} + 2\mathring{R}^{\alpha}{}_{\mu}{}^{\beta}{}_{\nu}\bar{h}_{\alpha\beta} = -16\pi T_{\mu\nu} \ , \tag{4.42}$$

where $\Box = \nabla_\mu \nabla^\mu$ and $\mathring{R}$ is the Riemann tensor of the background spacetime. In this work we shall consider the metric perturbation to be sourced by a point particle of mass μ. The gauge equation (4.41) and field equation (4.42) are consistent so long as the particle is moving on a geodesic of the background spacetime (as then $\nabla_\mu T^{\mu\nu} = 0$). The corresponding energy-momentum tensor is given by

$$T_{\mu\nu} = \mu \int_{-\infty}^{\infty} [-\det(\mathring{g})]^{-1/2} \delta^4(x^\mu - x_p^\mu) u_\mu u_\nu \, d\tau \ , \tag{4.43}$$

where, recall, $\det(\mathring{g})$ is the determinant of the background metric tensor.

The field equation (4.42) is numerically challenging to work with directly, as the full (trace reversed) metric perturbation is singular at the particle (though recently developed puncture and effective source techniques can be used to overcome these difficulties — see Sec. 5.5). Instead, in this work we choose to decompose the metric perturbation into *tensor* spherical harmonics modes. As was mentioned above, this has the key advantage that the individual multipole modes of the metric perturbation are continuous at the location of the particle, a fact that greatly assists numerical solving the field equations. The decomposition of the Lorenz gauge field equation (4.42) into tensor harmonic modes was first carried out by Barack and Lousto [61] and we present the result of that decomposition here in preparation for the FD decomposition, which we give in the following section.

The decomposition of the metric perturbation into multipole modes is achieved by projecting $\bar{h}_{\mu\nu}$ onto a basis of 2nd-rank tensor harmonics based on, in the background Schwarzschild geometry, the scalar, vector and tensor harmonics on the 2-sphere. The spherical symmetry of the background geometry ensures that the individual multipole modes decouple and can be evolved independently though, in general, the ten tensorial components of each multipole mode will remain coupled.

There are many different notations and conventions used when defining tensor harmonics (see Thorne [190] for a review of multipole expansions of gravitational perturbations). In this thesis we use the tensor harmonics of Barack and Lousto [61] which we denote by $Y^{(i)lm}_{\mu\nu}(\theta,\varphi;r)$. They are constructed from the usual spherical harmonics and their explicit form can be found in Appendix A of Ref. [61]. Note that the definition of these tensor harmonics also includes simple multiplicative factors of r and $f(r)$ in order to balance the dimensions and simplify the resulting equations. The important property of the tensor harmonics is that they form a 10-dimensional basis for any second rank, symmetric 4-dimensional tensor field. Explicitly, the $Y^{(i)lm}_{\mu\nu}$ are orthonormal in the sense that

$$\int \eta^{\alpha\mu}\eta^{\beta\nu}[Y^{(i)lm}_{\mu\nu}]^{*}Y^{(j)l'm'}_{\alpha\beta}\,d\Omega = \delta_{ij}\delta_{ll'}\delta_{mm'}\ , \tag{4.44}$$

where $i,j=1,\ldots,10$, $\eta^{\alpha\mu}=(1,f,r^{-2},r^{-2}\sin^{-2}\theta)$, a '$*$' denote complex conjugation and the integration is taken over a 2-sphere of constant t and r. Using the orthogonality condition any covariant 2nd-rank symmetric tensor can be expanded in tensor harmonics. For instance, the energy-momentum tensor defined in Eq. (4.43) can be expanded as

$$T_{\mu\nu} = \sum_{lm}\sum_{i=1}^{10} T^{(i)}_{lm}(r,t)Y^{(i)lm}_{\mu\nu}\ , \tag{4.45}$$

where

$$T^{(i)}_{lm}(r,t) = \int d\Omega\, T_{\mu\nu}\eta^{\mu\alpha}\eta^{\nu\beta}[Y^{(i)lm}_{\alpha\beta}]^{*}\ , \tag{4.46}$$

$$\tag{4.47}$$

An explicit calculation of $T^{(i)}_{lm}$ gives

$$T^{(i)}_{lm}(r,x_p) = \frac{\mu}{u^t r_p^2}u_\alpha u_\beta \eta^{\alpha\mu}(x_p)\eta^{\beta\nu}(x_p)Y^{(i)lm*}_{\mu\nu}(\theta_p,\varphi_p;r_p)\delta(r-r_p)\ . \tag{4.48}$$

where, recall, x_p denotes the particle's trajectory. We now proceed by writing the metric perturbation in the form

$$\bar{h}_{\mu\nu}(t,r,\theta,\phi) = \frac{\mu}{r}\sum_{lm}\sum_{i=1}^{10}\bar{h}^{(i)lm}(t,r)Y^{(i)lm}_{\mu\nu}(\theta,\varphi;r)\ , \tag{4.49}$$

and substituting it into the linearized Einstein equation (4.42), whereupon one finds that the angular component decouples [61]. The remaining (t, r) dependence of the metric perturbation obeys the partial differential equation,

$$\Box_l^{sc}\bar{h}_{lm}^{(i)} + \mathcal{M}_{(j)}^{(i)l}\bar{h}_{lm}^{(j)} = 4\pi\mu^{-1}rfT^{(i)lm} \equiv \mathcal{S}_{lm}^{(i)}\delta(r-r_p) \quad (i=1,...,10)\ , \tag{4.50}$$

where $\Box_l^{sc}$ is the scalar wave operator,

$$\Box_l^{sc} = \frac{1}{4}\left[\partial_t^2 - \partial_{r_*}^2 + V_l(r)\right]\ , \tag{4.51}$$

with the potential term given by

$$V_l(r) = f\left[\frac{2M}{r^3} + \frac{l(l+1)}{r^2}\right]\ . \tag{4.52}$$

The $\mathcal{M}_{(j)}^{(i)l}$ that appear in Eq. (4.50) are first order differential operators that couple between the ten components of the metric perturbation. The explicit form of the $\mathcal{M}_{(j)}^{(i)l}$ can be found in Appendix B of Ref. [67] and we give the coefficients of the delta function, $\mathcal{S}^{(i)}$, in Appendix E.

It will be useful to note that the ten field equations (4.50) are not all coupled together, instead they form two disjoint sets of equations. This follows from the parity property of the tensor spherical harmonic basis. Basis elements with $i = 1, \dots, 7$ are *even*, remaining unchanged under the parity operation $(\theta, \varphi) \to (\pi - \theta, \varphi + \pi)$, whereas basis elements $i = 8, 9, 10$ change sign under parity and hence are *odd*. For bound equatorial orbits, even(odd) implies that $l + m =$ even(odd). The field equations now separate under these two parity sectors. Furthermore, by examining the source presented in Appendix E it can be seen that

$$\mathcal{S}^{(i=1,\dots,7)} \propto Y^{lm}(\pi/2, \varphi_p) = 0 \qquad \text{for} \quad l+m = \text{odd}\ , \tag{4.53}$$

$$\mathcal{S}^{(i=8,9,10)} \propto \partial_\theta\left[Y^{lm}(\theta,\varphi_p)\right]_{\theta=\pi/2} = 0 \qquad \text{for} \quad l+m = \text{even}\ . \tag{4.54}$$

Consequently, the even(odd) solutions are trivially zero for odd(even) parity modes, that is, $h^{(i=1,\dots,7)} = 0$ for $l + m =$ odd and $h^{(i=8,9,10)} = 0$ for $l + m =$ even.

4.6 Frequency domain decomposition

In this section we give details of the frequency domain decomposition of the field equation (4.50). This decomposition was first carried out by Akcay [66] for the case of circular orbits in about a Schwarzschild black hole. Our motivation for working in the FD was presented in Sec. 1.4.

As our particle is moving on a bound period geodesic orbit, the spectrum of the Fourier decomposition is found to be discrete (see Appendix C.1), with each mode labeled by two integers—the azimuthal number, m, and the Fourier number, n. The mode frequency is given by $\omega = m\Omega_\varphi + n\Omega_r$, where Ω_r and Ω_φ are the orbit frequencies given in Eq. (2.17). We can, therefore, write the (t, r) dependence of the trace reversed metric perturbation as a sum over discrete Fourier modes,

$$\bar{h}_{lm}^{(i)}(t,r) = \sum_n R_{lmn}^{(i)}(r)e^{-i\omega t}\ . \tag{4.55}$$

By substituting the above into Eq. (4.50), one finds that the radial dependence of the trace reversed metric perturbation completely separates and the field equations reduce to a set of 10 coupled ordinary differential equations. At this point we introduce the tortoise radial coordinate, r_*, defined through $dr_*/dr = f^{-1}$ and, hence, given by

$$r_* = r + 2M \log\left(\frac{r}{2M} - 1\right) , \tag{4.56}$$

where we have specified the constant of integration. Writing the FD field equations using the tortoise coordinate allows for further simplification and the resulting equations now take the compact form

$$\frac{d^2 R^{(i)}_{lmn}(r)}{dr_*^2} - \left[V_l(r) - \omega^2\right] R^{(i)}_{lmn}(r) - 4\tilde{\mathcal{M}}^{(i)l}_{(j)} R^{(j)}_{lmn}(r) = J^{(i)}_{lmn} , \tag{4.57}$$

where $\tilde{\mathcal{M}}^{(i)l}_{(j)}$ is the Fourier transformed version of $\mathcal{M}^{(i)l}_{(j)}$ and $J^{(i)}_{lmn}$ is the Fourier transformed sources. We give the explicit form of the former in Appendix D and the latter in Appendix E. We note also that the separation under parity of the TD field equations carries over to the FD. Thus $R^{(i=1,\ldots,7)} = 0$ for $l + m =$ odd and $R^{(i=8,9,10)} = 0$ for $l + m =$ even.

The Fourier and angular decomposition of the Lorenz gauge condition $\nabla_\mu \bar{h}^\mu{}_\nu = 0$ results in four equations that also separate under parity with the first three (as ordered below) in the even sector and fourth one in the odd sector. For each lmn-mode these equations read

$$i\omega R^{(1)} + f\left(i\omega R^{(3)} + R^{(2)}_{,r} + \frac{R^{(2)}}{r} - \frac{R^{(4)}}{r}\right) = 0 , \tag{4.58}$$

$$-i\omega R^{(2)} - f R^{(1)}_{,r} + f^2 R^{(3)}_{,r} - \frac{f}{r}\left(R^{(1)} - R^{(5)} - f R^{(3)} - 2f R^{(6)}\right) = 0 , \tag{4.59}$$

$$-i\omega R^{(4)} - \frac{f}{r}\left(r R^{(5)}_{,r} + 2R^{(5)} + l(l+1)R^{(6)} - R^{(7)}\right) = 0 , \tag{4.60}$$

$$-i\omega R^{(8)} - \frac{f}{r}\left(r R^{(9)}_{,r} + 2R^{(9)} - R^{(10)}\right) = 0 . \tag{4.61}$$

The gauge conditions can be used to reduce the number of fields that have to be solved for simultaneously. For the odd sector, which has in general three coupled fields, the gauge constraint equation (4.61) implies that at most two fields need to be solved for at once, with the third constructed algebraically. The even sector consists of seven coupled fields and three gauge constraint equations [Eqs. (4.58)–(4.60)]. We thus need only to solve for four radial fields and can and construct the remaining three fields using the gauge equations. In practice though we shall follow Ref. [67] and instead only make use of Eqs. (4.59) and (4.60). This means that in the even sector we will solve for five fields and can use the third even sector gauge equation (4.58) as a consistency check on our numerical results. This hierarchical scheme for constructing all 10 scalar fields of the metric perturbation is outlined in Table 4.1, where we have also included information regarding the construction of the static modes (discussed below).

4.6.1 Odd sector

We now consider the odd sector FD field equations for the radiating $\omega \neq 0$ modes, with the static ($\omega = 0$) modes to be considered shortly. As outlined in the hierarchical structure in Table 4.1, we solve for fields $i = 9, 10$ and construct field $i = 8$ from the gauge equation (4.61). The

$l+m=$ even			$l+m=$ odd	
$l=0$	$n=0$	$i=1,3,6$		no field
	$n\neq 0$	$i=1,3,6\to 2$		
$l=1$		$i=1,3,5,6\to 2,4$	$m=n=0$	$i=8$ only
			$n\neq 0$	$i=9\to 8$
$l\geq 2$	$m=n=0$	$i=1,3,5\to 6,7$	$m=n=0$	$i=8$ only
	$n\neq 0$	$i=1,3,5,6,7\to 2,4$	$n\neq 0$	$i=9,10\to 8$

Table 4.1: Hierarchical scheme for solving the ten FD field equations. The right arrow '→' denotes using the gauge equations (4.58)-(4.61) to calculate the radial field(s) with labels to the right of the arrow from the radial fields with labels to the left.

two homogeneous odd sector field equations are

$$\partial^2_{r_*} R^{(9)} = \left[V_l - \omega^2 + \frac{4f}{r^2}\left(1-\frac{9M}{2r}\right)\right] R^{(9)} - \frac{2f}{r^2}\left(1-\frac{3M}{r}\right) R^{(10)} \ , \tag{4.62}$$

$$\partial^2_{r_*} R^{(10)} = \left(V_l - \omega^2 - \frac{2f}{r^2}\right) R^{(10)} - \frac{2f\lambda}{r^2} R^{(9)} \ , \tag{4.63}$$

where we have defined $\lambda \equiv (l+2)(l-1)$. The solutions to Eqs. (4.62) and (4.63) have to be obtained numerically, our method for which is presented in Chapter 8.

Barack and Lousto [61] showed that the homogeneous static ($\omega = 0$) odd modes can be analytically constructed from a single function, $R^{(8)}_{l,m=0}$. The ODE governing the odd sector static modes is given by

$$\partial_r R^{(8)}_{l,m=0} + V_l(r) R^{(8)}_{l,m=0} = -4f^{-2} J^{(8)}_{m=\omega=0} \ . \tag{4.64}$$

For $l \leq 2$ the two linearly independent homogeneous solutions to Eq. (4.64) take the form

$$R^{(8)-}_{l,m=0} = \frac{x}{1+x}\sum_{n=0}^{l+1} a^l_n x^n \ , \tag{4.65}$$

$$R^{(8)+}_{l,m=0} = R^{(8)-}_{l,m=0} \log f + \frac{1}{1+x}\sum_{n=0}^{l+1} b^l_n x^n \ , \tag{4.66}$$

where

$$x \equiv \frac{r}{2M} - 1 \ , \tag{4.67}$$

and the series coefficients are given by

$$a^l_n = \frac{l(l+1)(l+n-1)!}{(l-n+1)!(n+1)!n!} \ , \qquad b^l_n = \sum_{k=0}^{l-n+1} (-1)^k \frac{a^l_{n+k}}{k+1} \ . \tag{4.68}$$

For $l = 1$, Eq. (4.66) fails to be a solution of the homogeneous part of Eq. (4.64). Instead, the general homogeneous solution takes the form

$$R^{(8)+}_{l=1,m=0} = c_1 r^2 + c_2/r \ , \tag{4.69}$$

where c_1 and c_2 are constants.

4.6.2 Even sector

We now turn our attention to the even parity sector FD field equations. As discussed above, we can use the Lorenz gauge equation to reduce the number of fields that we need to solve for simultaneously. We choose to compute the $i = 1, 3, 5, 6, 7$ fields and construct the $i = 2, 4$ fields using the gauge constraint equations. The homogeneous field equations for the $i = 1, 3, 5, 6, 7$ fields are given by

$$\partial^2_{r_*} R^{(1)} = \left(V_l - \omega^2\right) R^{(1)} + \frac{4M}{r^2} f \partial_{r_*} R^{(3)} + \frac{2f}{r^2}\left(1 - \frac{4M}{r}\right)\left(R^{(1)} - R^{(5)} - fR^{(3)}\right) - \frac{2f^2}{r^2}\left(1 - \frac{6M}{r}\right) R^{(6)} \,, \tag{4.70}$$

$$\partial^2_{r_*} R^{(3)} = \left(V_l - \omega^2\right) R^{(3)} - \frac{2f}{r^2}\left[R^{(1)} - R^{(5)} - \left(1 - \frac{4M}{r}\right)\left(R^{(3)} + R^{(6)}\right)\right] \,, \tag{4.71}$$

$$\partial^2_{r_*} R^{(5)} = \left(V_l - \omega^2\right) R^{(5)} + \frac{4f}{r^2}\left[\left(1 - \frac{9M}{2r}\right) R^{(5)} - \frac{\mathfrak{L}}{2}\left(R^{(1)} - fR^{(3)}\right) + \frac{1}{2}\left(1 - \frac{3M}{r}\right)\left(\mathfrak{L}R^{(6)} - R^{(7)}\right)\right] \,, \tag{4.72}$$

$$\partial^2_{r_*} R^{(6)} = \left(V_l - \omega^2\right) R^{(6)} - \frac{2f}{r^2}\left[R^{(1)} - R^{(5)} - \left(1 - \frac{4M}{r}\right)\left(R^{(3)} + R^{(6)}\right)\right] \,, \tag{4.73}$$

$$\partial^2_{r_*} R^{(7)} = \left(V_l - \omega^2\right) R^{(7)} - \frac{2f}{r^2}\left(R^{(7)} - \lambda R^{(5)}\right) \,, \tag{4.74}$$

where we have defined $\mathfrak{L} \equiv l(l+1)$ and, recall, $\lambda = (l+2)(l-1)$. As with the odd sector, the solution to the even sector modes have to be obtained numerically.

For the static, time symmetric modes we must have $h_{ti} = 0$ for $i = r, \theta, \varphi$. Inspection of Eqs. (F.4), (F.6) and (F.7) shows that these components of the metric perturbation depend only on $\bar{h}^{(2)}$ and $\bar{h}^{(4)}$. Consequently, we must have $h^{(2)} = R^{(2)} = 0$ and $h^{(4)} = R^{(4)} = 0$. This brings the total number of even sector fields down from 7 to 5 and eliminates the the gauge equation (4.58), reducing it to the trivial $0 = 0$. Using the remaining gauge equations (4.59) and (4.60), we can now write our field equations as the reduced coupled set,

$$\partial^2_{r_*} R^{(1)} = \left[V_l - \omega^2\right] R^{(1)} + \frac{4M}{r^2} f R^{(3)}_{,r_*} + \frac{2f}{r^2}\left(1 - \frac{4M}{r}\right)\left(R^{(1)} - R^{(5)} - fR^{(3)}\right) - \frac{f}{r^2}\left(1 - \frac{6M}{r}\right)\left(R^{(1)} + \frac{r}{f}\partial_{r_*} R^{(1)} - fR^{(3)} - r\partial_{r^*} R^{(3)} - R^{(5)}\right) \,, \tag{4.75}$$

$$\partial^2_{r_*} R^{(3)} = \left[V_l - \omega^2\right] R^{(3)} - \frac{2f}{r^2}\left\{R^{(1)} - R^{(5)} - \left(1 - \frac{4M}{r}\right)\left[R^{(3)} + \frac{1}{2f}\left(R^{(1)} + \frac{r}{f}\partial_{r_*} R^{(1)} - fR^{(3)} - r\partial_{r^*} R^{(3)} - R^{(5)}\right)\right]\right\} \,, \tag{4.76}$$

$$\partial^2_{r_*} R^{(5)} = \left[V_l - \omega^2\right] R^{(5)} - \frac{4f}{r^2}\left[\left(1 - \frac{9M}{2r}\right) R^{(5)} - \frac{\mathfrak{L}}{2}\left(R^{(1)} - fR^{(3)}\right) + \frac{1}{2}\left(1 - \frac{3M}{r}\right)\left(2R^{(5)} + \frac{r}{f}\partial_{r^*} R^{(5)}\right)\right] \,, \tag{4.77}$$

and recover the $R^{(6)}$ and $R^{(7)}$ fields from the gauge equations (4.59) and (4.60).

4.6.3 Boundary conditions for the radial fields

For radiating modes ($\omega \neq 0$) we select the retarded solution to our field equations by placing ingoing/outgoing boundary conditions at the event horizon and spatial infinity respectively. Defining

$$R^{(i)\pm} \equiv R^{(i)}(r_* \to \pm\infty) , \tag{4.78}$$

the asymptotic form of the radial fields take the form

$$R^{(i)\pm} \sim e^{\pm i\omega r} . \tag{4.79}$$

Making this choice we find that the asymptotic form of the (t, r) dependence of the fields, $\bar{h}^{(i)\pm}(t, r) \equiv R^{(i)\pm}e^{-i\omega t}$, takes the form $\bar{h}^{(i)\pm}(t, r) \sim e^{-i\omega(t \mp r_*)}$. At the event horizon this implies that $\bar{h}^{(i)-}(t, r)$ is purely a function of the retarded null coordinate,

$$v = t + r_* , \tag{4.80}$$

ensuring that any radiation is purely ingoing. Likewise, at spatial infinity $\bar{h}^{(i)+}(t, r)$ becomes a function of the advanced null coordinate $u = t - r_*$ only, ensuring that all radiation is outgoing as desired.

The boundary conditions for the static time-independent modes take the form of regularity conditions. At spatial infinity we demand that radial fields $\bar{R}^{(i)} \to 0$ as $r \to \infty$. At the event horizon we demand that the radial fields be regular. In order to verify that a given field is regular at the horizon, we must change coordinates to a horizon penetrating coordinate system, as the Schwarzschild coordinates themselves are irregular at the horizon. A common choice is the ingoing Eddington-Finkelstein coordinate (v, r, θ, φ), where v is the retarded null coordinate defined above. In this coordinate system the Schwarzschild metric covariant line element is given by

$$ds^2 = -f dv^2 + 2dvdr + r^2(d\theta^2 + \sin^2\theta d\varphi^2) . \tag{4.81}$$

It is then straightforward to convert any tensor in the Schwarzschild (t, r, θ, φ) coordinate basis to the ingoing Eddington-Finkelstein (v, r, θ, φ) coordinate basis, where regularity at the horizon can be assessed.

4.6.4 Analytic solution for the static monopole mode

The static piece of the monopole ($l = m = n = 0$) mode of the metric perturbation describes the mass perturbation due to the smaller body. For this mode the field equations simplify enough that analytic solutions can be obtained. The static Lorenz gauge monopole was first derived for a particle in a circular orbit by Detwieler and Poisson [139] and was given explicitly in Ref. [61]. For eccentric orbits the monopole solution was given by Golbourn [140] and implemented by Barack and Sago [67] (though they do no provide details of their implementation for this mode). Here we do not provide the derivation of the static monopole contribution, instead opting to simply state the known solution (we will present a derivation in a forthcoming paper [104]).

In the following we adopt the notation of Ref. [140] and present the solutions in terms of the metric perturbation components $h_{\mu\nu}$. In this notation, where $\vec{h}_k \equiv \{h_{tt}, h_{rr}, r^{-2}h_{\theta\theta}\}$, the general basis of homogeneous solutions is given by

$$\vec{h}_1 = \{-f, f^{-1}, 1\} \,, \tag{4.82}$$

$$\vec{h}_2 = \left\{-\frac{2fM}{r^3}P(r), \frac{2}{r^3 f}Q(r), \frac{2f}{r^2}P(r)\right\} \,, \tag{4.83}$$

$$\vec{h}_3 = \left\{\frac{M^4}{r^4}, \frac{M^3(3M-2r)}{r^4 f^2}, \frac{M^3}{r^3}\right\} \,, \tag{4.84}$$

$$\begin{aligned}\vec{h}_4 = \bigg\{ & \frac{M}{r^4}\left[W(r) + rP(r)\log f - 8M^3\log(r/M)\right] \,, \\ & \frac{1}{r^4 f^2}\left[K(r) - L(r)\log f - 8M^3(2r-3M)\log(r/M)\right] \,, \\ & \frac{1}{r^3}\left[3r^2 - W(r)rP(r)f\log f + 8M^3\log(r/M)\right]\bigg\} \,,\end{aligned} \tag{4.85}$$

with

$$P(r) = r^2 + 2Mr + 4M^2 \,, \tag{4.86}$$

$$Q(r) = r^3 - Mr^2 - 2M^2 r + 12M^3 \,, \tag{4.87}$$

$$W(r) = 3r^3 - Mr^2 - 4M^2 r - 28M^3/3 \,, \tag{4.88}$$

$$K(r) = Mr^3 - 5M^2 r^2 - 20M^3 r/3 + 28M^4 \,, \tag{4.89}$$

$$L(r) = r^4 - 3Mr^3 + 16M^3 r - 24M^4 \,. \tag{4.90}$$

Using the above basis of homogeneous solutions, the general form of the inhomogeneous solution is known to take the form [140, 141, 104, 142]

$$\begin{aligned}\vec{h} = & \left[a_1\vec{h}_1 + a_2\vec{h}_2\right]\Theta(r_p[t] - r) \\ & + \left[b_1\vec{h}_3 + b_2(\vec{h}_4 - 3\vec{h}_1 + 3/2\vec{h}_2) + \mathcal{E}/M(2\vec{h}_1 - \vec{h}_2)\right]\Theta(r - r_p[t]) \,,\end{aligned} \tag{4.91}$$

where Θ is the usual Heaviside step function and a_1, a_2, b_1, b_2 are constants to be determined (we discuss how this is done in practice in Sec. 8.2). Lastly we note that, using the relations in Appendix F, the $\bar{h}^{(i)}$ fields can be recovered via

$$\bar{h}^{(1)}_{l=0}(r) = 2\sqrt{\pi}\mu^{-1}r\left(h_{tt} + f^2 h_{rr}\right) \,, \tag{4.92}$$

$$\bar{h}^{(6)}_{l=0}(r) = 2\sqrt{\pi}\mu^{-1}rf\left(h_{tt} - f^2 h_{rr}\right) \,, \tag{4.93}$$

$$\bar{h}^{(3)}_{l=0}(r) = 4\sqrt{\pi}\mu^{-1}r^{-1}h_{\theta\theta} \,. \tag{4.94}$$

Chapter 5

Essential background: self-force formalism and calculation techniques

In this 'Essential background' chapter we review the problem of calculating the (self-) force felt by a charged particle moving in a curved spacetime. This self-force arises from the particle's interactions with its own field. We will first give an overview of the theoretical problem of regularization of the particle's field, a requirement when using a point particle model if one wishes to calculate the full SF (recall from Chapter 1 that it is possible to calculate the average dissipative component of the SF from conservation laws without resorting to regularization). Our approach here will be to use the electromagnetic case as an introduction, before considering the scalar and gravitational cases. This choice of ordering is made because, though we do not consider the electromagnetic self-force (EMSF) in this thesis, the EM field is physical and familiar whilst the scalar case is unphysical and exhibits unusual effects (such as a dynamically varying rest mass). We do not begin with the gravitational case either as there is some subtlety to it, and we do not want this to cloud the main concepts behind SF calculations.

Historically, the development of self-force calculations began with Dirac's seminal paper, 'Classical theory of radiating electrons' [143]. The equation Dirac derived for the motion for a single electron in flat Minkowski space interacting with its own field was the special relativistic version of the already known Abraham-Lorentz equation for the recoil of an accelerated electron due to emission of electromagnetic radiation. Dirac's work was later extended by DeWitt and Brehme [144] to the case of a point-like electron moving in a curved spacetime. They found that the resulting equations of motion contained, in addition to the flat space term identified by Dirac, an extra 'tail' term involving an integral over the entire past history of the particle (as noted by Hobbs [145], there was also an extra Ricci term which DeWitt and Brehme's original calculation missed).

The equations of motion for a particle of finite mass interacting with its own metric perturbation were arrived at sometime later by Mino, Sasaki and Tanaka [6] and Quinn and Wald [7]. Point particles are not valid solutions to Einstein's equations [146] and so Mino *et al.*, as well as providing a derivation along the lines of DeWitt and Brehme's electromagnetic calculation, also provided a more rigorous derivation via the method of matched asymptotic. In this approach, the spacetime local to the compact object is assumed to take the form of a tidally distorted Schwarzschild black hole, whereas far away from the compact object the spacetime is assumed to take the form of a perturbation of the background geometry. By matching these two expansions in a region where both are valid, Mino *et al.* obtained the same equations of motion that their first method gave. In Quinn and Wald's derivation they took an axiomatic approach to the problem and also arrived at the same equations of motion. Quinn also later derived the equivalent results for a particle carrying a scalar charge. Since the original papers these results have been rigorously derived without resorting to the troublesome notion of point particles [44, 74, 75, 147].

Despite there being more rigorous derivations, in the discussion of the formalism of the self-force we present below we will make use of the concept of point particles. We make this choice because our goal in these sections is not to provide anything approaching a rigorous derivation of the self-force but instead to give a flavour for some of the important concepts. We also note that in Secs. 5.1, 5.2 and 5.3 on the formalism of the electromagnetic, scalar-field and gravitational self-force respectively we follow the review of Poisson [75] in our presentation. In these sections we also adopt the notation of Poisson whereby, x, denotes a generic spacetime point and, x', denotes a source point.

It will turn out that the equations we arrive at in these sections are not particularly useful for practical self-force calculations and thus they were recast into more amenable forms. In this thesis we will make use of the mode-sum approach to regularize the fields and, after we introduce the method in Sec. 5.4, we spend some time discussing its implementation in Schwarzschild and Kerr spacetime. Everything prior to this point will have been review material but for the discussion of the mode-sum approach in Kerr spacetime we include some original content detailing the practical calculation of the SSF in Kerr spacetime. We then return to presenting review material and briefly give an overview of other approaches to the practical regularization problem. Finally we consider how to decompose the self-force into dissipative and conservative components.

5.1 Electromagnetic self-force

In the following section we will review the computation of the back reaction or 'self-force' felt by an accelerating electric charge. First we shall examine the situation in flat spacetime and then consider the important extension to motion in a curved spacetime. As mentioned above, in flat spacetime Dirac [143] derived the special relativistic equations of motion. For curved spacetimes the equations of motion were first obtained by DeWitt and Brehme [144].

5.1.1 Motion of an electrically charged particle in flat spacetime

We wish to consider the motion of a single point particle of mass, μ, carrying an electric charge, q_e, moving in flat, Minkowski spacetime. We shall denote the vector potential at an arbitrary spacetime point x by $A^\alpha(x)$. Making the choice to work in the Lorenz gauge, defined through $\partial_\alpha A^\alpha = 0$, our governing equation then takes the form

$$\Box A^\alpha = -4\pi j^\alpha \ , \tag{5.1}$$

where $\Box$ is the usual flat spacetime D'Alembertian operator. We shall model our source, j^α, as a delta function along the particle's world line:

$$j^\alpha = q_e \int u^\alpha \delta(x, x'(\tau))\, d\tau \ , \tag{5.2}$$

where $\delta(x, x')$ is the Dirac delta function. The two important solutions to Eq. (5.1) that we shall consider here are the retarded and advanced solutions which we denote by A^α_{ret} and A^α_{adv}, respectively. For concreteness, if we consider an example of a point particle moving on a circular orbit then the retarded solution physically corresponds with the particle emitting radiation to infinity as its orbit decays. The advanced solution represents the time-reversed scenario whereby radiation is ingoing from infinity and absorbed by the particle, causing its radius of motion to increase. Because our source is pointlike, both solutions diverge at the particle's location (i.e. as $x \to x'$). The divergence of the physically relevant potential, A^α_{ret}, at the particle's location makes it difficult to work out precisely how it affects the particle's motion.

We shall proceed by constructing a solution to the field equation (5.1) that is finite at the location of the particle and is solely responsible for the dynamics. The first step is to consider the time-symmetric 'S' solution, A^α_S, given by

$$A^\alpha_S = \frac{1}{2}(A^\alpha_{\text{ret}} + A^\alpha_{\text{adv}}) \ . \tag{5.3}$$

As A^α_S is the linear combination of the retarded and advanced solutions it is itself a solution of the field equation (5.1). As such it is just as singular at the particle's location as either the retarded or advanced solutions. For this reason the 'S' subscript could also be interpreted to mean 'Singular' as well as 'Symmetric'. Using A^α_S we then construct a regular solution, A^α_R, via

$$A^\alpha_R = A^\alpha_{\text{ret}} - A^\alpha_S = \frac{1}{2}(A^\alpha_{\text{ret}} - A^\alpha_{\text{adv}}) \ . \tag{5.4}$$

As this solution is the difference of two solutions that satisfy the inhomogeneous wave equation, A^α_R satisfies the homogeneous wave equation so that we have

$$\Box A^\alpha_R = 0 \ . \tag{5.5}$$

Thus we see that A^α_R is a sourceless, radiative-only field. Consequently the subscript 'R' could also be interpreted to mean 'Radiative' as well as 'Regular'. It will transpire that A^α_R alone gives rise to the correct equations of motion with A^α_S having no effect on the dynamics (instead it is responsible for a mass renormalization [75]). Defining a regular electromagnetic field tensor

$$F^R_{\alpha\beta} = \partial_\alpha A^R_\beta - \partial_\beta A^R_\alpha \ , \tag{5.6}$$

the correct equations of motion are then given by

$$\mu a_\alpha = F^{\text{ext}}_\alpha + q_e F^R_{\alpha\beta} u^\beta \ , \tag{5.7}$$

where F^{ext}_α is some external force acting on the particle and $a_\alpha = du_\alpha/d\tau$ is the particle's acceleration.

Dirac first postulated Eq. (5.7) and performed an explicit calculation of A^α_R by balancing the electromagnetic-field momentum that flowed out of a thin worldtube surrounding the particle's worldline with the corresponding change in the particle's momentum. The result of this calculation gives the self-force [in this case commonly known as the Abraham-Lorentz-Dirac (ALD) force] to be

$$\mu a^\alpha = F^\alpha_{\text{ext}} + F^\alpha_{(\text{ALD})} \qquad \text{where} \quad F^\alpha_{(\text{ALD})} \equiv \frac{2}{3} q_e^2 (\delta^\alpha{}_\beta + u^\alpha u_\beta)\dot{a}^\beta \; , \tag{5.8}$$

where an overdot denotes differentiation with respect to t.

One immediately striking property of this equation is that it contains a term proportional to the derivative of the acceleration. As was first pointed out by Dirac this leads to *runaway* and *pre-accelerating* solutions for the particle's motion. This troublesome term has been much discussed in the literature (see for example [7, 44, 143, 148, 149, 150, 151]) and the general consensus is that these unwanted solutions arise due to the inconsistent nature of a point particle description coupled to the electromagnetic field. If instead the point particle model is considered as an approximation to a physical situation involving an extended body, valid through to $\mathcal{O}(q_e^2)$, then a *reduction of order* technique can be used to cure the pathological difficulties with the model. Roughly speaking, the reduction of order is achieved by equating by differentiating Eq. (5.8) with respect to τ and rearranging for $\dot{a}$. This result is then substituted back into Eq. (5.8) and, by ignoring terms of greater than $\mathcal{O}(q_e^2)$, the resulting equations of motion are then given by

$$\mu a^\alpha = F^\alpha_{\text{ext}} + \frac{2}{3}\frac{q_e^2}{\mu}(\delta^\alpha{}_\beta + u^\alpha u_\beta)\frac{dF^\beta_{\text{ext}}}{d\tau} \; . \tag{5.9}$$

The solutions to this equation are free from the difficulties associated with the solutions of Eq. (5.8).

Though it was not necessary to the discussion above, we now introduce the Green's functions associated with the retarded and advanced potentials so that we may compare their properties with the equivalent Green's functions in curved spacetime below. The retarded ('+') and advanced ('−') Green's functions are defined as solutions to

$$\Box G^\alpha_{\pm\beta'}(x,x') = -4\pi\delta^\alpha_{\beta'}\delta(x,x') \; , \tag{5.10}$$

where $\delta^\alpha_{\beta'}$ is the usual Kronecker delta and hereafter tensors defined at x have unprimed indices whilst tensors defined at x' have primed indices. The retarded and advanced Green's functions satisfy the relation

$$G^\alpha_{+\beta'}(x,x') = G^{\beta'}_{-\alpha}(x',x) \; , \tag{5.11}$$

and can be used to construct the retarded and advanced potentials via

$$A^\alpha_{\text{ret}}(x) = \int G^\alpha_{+\beta'}(x,x') j^{\beta'} \, dV' \; , \tag{5.12}$$

$$A^\alpha_{\text{adv}}(x) = \int G^\alpha_{-\beta'}(x,x') j^{\beta'} \, dV' \; , \tag{5.13}$$

where in general the spacetime volume element is given by $dV' = \sqrt{-\det[\mathring{g}(x')]}d^4x'$, with $\det(\mathring{g})$ being the determinant of the background metric. For Minkowski spacetime, dV' reduces to simply d^4x' as $\det(\mathring{g}) = -1$ for all values of x' . Writing $x = (t, \mathbf{x})$ and $x' = (t', \mathbf{x}')$, the retarded and advanced Green's functions are given explicitly by [75]

$$G^\alpha_{\pm\beta'}(x,x') = \delta^\alpha_{\beta'} \frac{\delta(t - t' \mp |\mathbf{x} - \mathbf{x}'|)}{|\mathbf{x} - \mathbf{x}'|} \; . \tag{5.14}$$

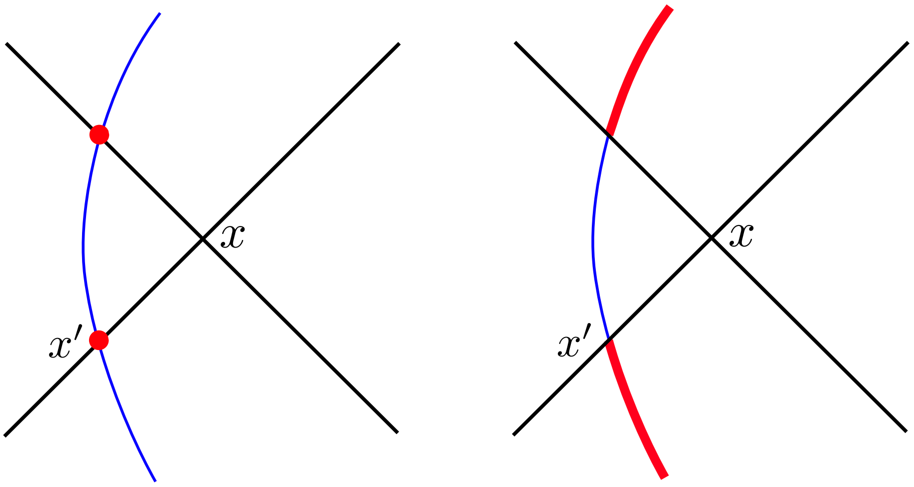

FIGURE 5.1: Light cone diagram of the support of the regular Green's function, $G^{\alpha}_{R\beta'}(x,x')$, as defined via Eq. (5.16), in flat spacetime (left panel) and curved spacetime (right panel). The (black) straight lines mark the past and future light cone of the spacetime point x. The thin (blue) curved line is the particle's worldline. The thick (red) lines or circles show the support of the Green's function. In flat spacetime the Green's function only has support where the light cones of x intersect the particle's world line. In curved spacetime the Green's function also has support within the lights cones of x. The regular Green's function defined this way is not useful for computing the self-force as, in the limit $x \to x'$, the regular potential, $A^{\alpha}_{R}(x)$, depends on the entire past *and* future history of the particle's motion.

From this we see that the retarded Green's function has support only on the past light cone of x'. Likewise, the advanced Green's function's support is only on the future light cone of x'. This implies that the retarded potential at a spacetime point, x, only has a contribution from where the past light cone of x intersects the particle's world line. This reflects the fact that in flat spacetime, disturbances in the EM field propagate at the speed of light.

For completeness we also introduce singular and regular Green's functions, defined via

$$G^{\alpha}_{S\beta'}(x,x') = \frac{1}{2}\left[G^{\alpha}_{+\beta'}(x,x') + G^{\alpha}_{-\beta'}(x,x')\right] \ , \tag{5.15}$$

$$G^{\alpha}_{R\beta'}(x,x') = \frac{1}{2}\left[G^{\alpha}_{+\beta'}(x,x') - G^{\alpha}_{-\beta'}(x,x')\right] \ , \tag{5.16}$$

and through which the singular and regarded potentials can be written as

$$A^{\alpha}_{S}(x) = \int G^{\alpha}_{S\beta'}(x,x') j^{\beta'}\, dV' \ , \tag{5.17}$$

$$A^{\alpha}_{R}(x) = \int G^{\alpha}_{R\beta'}(x,x') j^{\beta'}\, dV' \ . \tag{5.18}$$

From Eq. (5.11) it can be seen that the singular and regular Green's functions obey the relations

$$G^{\alpha}_{S\beta'}(x,x') = G^{\beta'}_{S\alpha}(x',x) \ , \tag{5.19}$$

$$G^{\alpha}_{R\beta'}(x,x') = -G^{\beta'}_{R\alpha}(x',x) \ . \tag{5.20}$$

5.1.2 Motion of an electrically charged particle in curved spacetime

We now consider the motion of a single electrically charged particle moving in a curved spacetime. Defining the vector potential as before our field equation now reads

$$\Box A^\alpha - \mathring{R}^\alpha{}_\beta A^\beta = -4\pi j^\alpha \ , \tag{5.21}$$

where now $\Box = \mathring{g}^{\alpha\beta}\nabla_\alpha\nabla_\beta$ is the covariant wave operator with covariant derivatives taken with respect to the background metric and $\mathring{R}$ is the Ricci tensor of the background metric. Again we choose to work in the Lorenz gauge, which now reads $\nabla_\alpha A^\alpha = 0$. We can define advanced and retarded potentials as before and write them as integrals over Green's functions [see Eqs. (5.12) and (5.13)]. As one might expect, Eq. (5.14) is no longer the correct form of the Green's functions. In fact it turns out that, whereas in flat spacetime the retarded Green's functions was supported only the future light cone of x', in curved spacetime the retarded Green's function has support *on and within* the future light cone of x'. This implies that the retarded potential, $A^\alpha_{\rm ret}(x)$, at a spacetime point x has contributions from the entire past history of the particle up to the point where the past light cone of x intersects the particle's world line (see Fig. 5.1). This reflects the fact that in curved spacetime disturbances in the EM field propagate at all speeds less than or equal to the speed of light [75] (Huygen's principle does not apply in curved spacetimes).

In a similar fashion, the advanced Green's function has support on and within the past light cone of x'. This will turn out to be problematic if we wish to construct the self-force in the same manner as we did in flat spacetime. As before, the singular nature of the retarded potential at the particle's location makes it difficult to understand how it influences the particle's motion. Following the route we took in flat spacetime, we can construct a singular potential A^α_S via Eq. (5.3), and then further construct a regular potential A^α_R via Eq. (5.4) which then satisfies the homogeneous version of the field equation (5.21). Unfortunately when we make these constructions we find that, in the limit $x \to x'$, A^α_R depends on the entire past *and* future of the particle. Clearly then, A^α_R constructed this way will not provide for a suitable law of physics.

Detweiler and Whiting [152] proposed and demonstrated that the correct Green's function required to construct A^α_S is given by

$$G^\alpha_{S\beta'}(x,x') = \frac{1}{2}\left[G^\alpha_{+\beta'}(x,x') + G^\alpha_{-\beta'}(x,x') - H^\alpha{}_{\beta'}(x,x')\right] \ , \tag{5.22}$$

where $H^\alpha{}_{\beta'}(x,x')$ is chosen in such a way as to remove the acausal features encountered with a naïve construction of A^α_R as described above. Specifically $H^\alpha{}_{\beta'}$ is chosen to coincide with the advanced Green's function, $G^\alpha_{-\beta'}(x,x')$, whenever x' is within the future light cone of x. As we want $G^\alpha_{S\beta'}(x,x')$ to be symmetric under interchange of x and x', $H^\alpha{}_{\beta'}$ must also coincide with the retarded Green's function, $G^\alpha_{+\beta'}(x',x)$, whenever x' is in the past light cone of x. Another important feature of $H^\alpha{}_\beta$ is that it is constructed to be a solution to the homogeneous wave equation,

$$\Box H^\alpha{}_{\beta'}(x,x') - R^\alpha{}_\lambda H^\lambda{}_{\beta'}(x,x') = 0 \ . \tag{5.23}$$

The two point function $H^\alpha{}_{\beta'}$ with the above properties has support on the entire worldline of the particle. Furthermore we see that $G^\alpha_{S\beta'}(x,x')$ is a solution to the inhomogeneous wave equation (i.e., the above wave equation with a delta-function source on the right-hand side). We thus have that the singular Green's function is just as singular as the retarded Green's function as

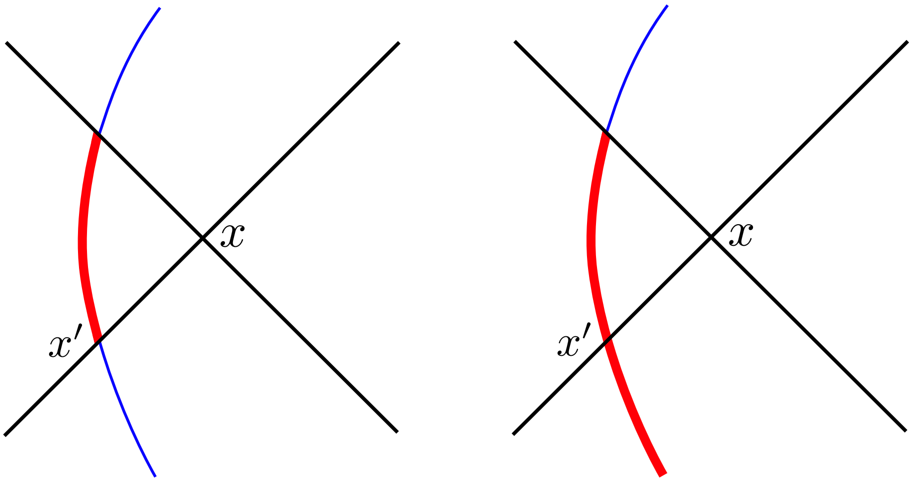

FIGURE 5.2: Support of the singular and regular Green's functions in curved spacetime. The (black) straight lines mark the past and future light cone of the spacetime point x. The thin (blue) curved line is the particle's worldline. The thick (red) lines show the support of the Green's function. The left panel shows the support of the singular Green's function, $G^{\alpha}_{S\beta'}(x,x')$, as defined via Eq. (5.22). The corresponding regular Green's function, $G^{\alpha}_{R\beta'}(x,x')$, defined via Eq. (5.24), has support along the particle's worldline wherever the worldline is outside the future light cone of x. The regular Green's function constructed this way has the important property that in the limit $x \to x'$ it only has support within the past light cone of x'.

$x \to x'$. Consequently the regular Green's function

$$G^{\alpha}_{R\beta'}(x,x') = \frac{1}{2}\left[G^{\alpha}_{+\beta'}(x,x') - G^{\alpha}_{S\beta'}(x,x')\right] \tag{5.24}$$

$$= \frac{1}{2}\left[G^{\alpha}_{+\beta'}(x,x') - G^{\alpha}_{-\beta'}(x,x') + H^{\alpha}{}_{\beta'}(x,x')\right] \tag{5.25}$$

is finite as $x \to x'$ and importantly, in this limit the it only has support within the past light cone of x' (see Fig. 5.2). The regular potential defined via Eq. (5.4) using this Green's function is thus a solution to the homogeneous wave equation implying that it is well defined throughout the entire spacetime, including at the particle's location. It can also be shown that the singular potential A^{α}_{S} exerts no force on the particle [75] and so, just as in flat spacetime, we conclude that the regular potential, A^{α}_{R}, is solely responsible for the self-force.

Once the regular potential has been correctly identified, the self-force itself is then computed much as before by defining a regular EM field tensor

$$F^{R}_{\alpha\beta} = \nabla_{\alpha}A^{R}_{\beta} + \nabla_{\beta}A^{R}_{\alpha}\ , \tag{5.26}$$

and the force law

$$\mu a_{\alpha} = F^{\rm ext}_{\alpha} + q_e F^{R}_{\alpha\beta}u^{\beta}\ , \tag{5.27}$$

where now $a_{\alpha} = Du_{\alpha}/d\tau$. An explicit calculation of the equations of motion then gives [75]

$$\mu a^{\alpha} = F^{\alpha}_{\rm ext} + F^{\alpha}_{\rm (ALD)} + F^{\alpha}_{\rm (Ricci)} + F^{\alpha}_{\rm (Tail)}\ , \tag{5.28}$$

where $F^{\alpha}_{(\mathrm{ALD})}$ is defined as for flat spacetime in Eq. (5.8) and we have

$$F^{\alpha}_{(\mathrm{Ricci})} = \frac{1}{3} q_e^2 (\delta^{\alpha}{}_{\beta} + u^{\alpha} u_{\beta}) \mathring{R}^{\beta}{}_{\lambda} u^{\lambda} \ , \tag{5.29}$$

$$F^{\alpha}_{(\mathrm{Tail})} = q_e^2 u_{\beta} \lim_{\epsilon \to 0} \int_{-\infty}^{\tau-\epsilon} \left[\nabla^{\alpha} G^{\beta}_{+\lambda'} - \nabla^{\beta} G^{\alpha}_{+\lambda'} \right] u^{\lambda'} \, d\tau' \ . \tag{5.30}$$

As in flat space, this equation, due to the presence of the $F^{\alpha}_{(\mathrm{ALD})}$ term, admits unphysical solutions which can be cured by the reduction of order method outlined above. The interesting feature of Eq. (5.28) is the non-local 'Tail' term. To see how it arises in the form given above recall that in the limit $x \to x'$ the regular and the retarded Green's function coincide within the past light cone of x' whilst at x' itself their values differ (the former diverges whilst the latter is finite). Thus in the coincidence limit we can write

$$A^{\alpha}_{R}(x'(\tau)) = q G^{\alpha}_{R\beta'}(x', x') u^{\beta} + q \lim_{\epsilon \to 0} \int_{-\infty}^{\tau-\epsilon} G^{\alpha}_{+\beta'}(x, x') u^{\beta'} \, d\tau' \tag{5.31}$$

where we have used $j^{\alpha}(x') = q u^{\alpha}$. When the force is calculated using Eq. (5.27) the first term in Eq. (5.31) gives rise to the local ALD and Ricci terms and the second term can be readily seen to give the Tail term in Eq. (5.30). The presence of the tail term implies that the force felt by the particle at a given time, τ, depends upon the entire past history of the particle. Evaluating this tail term for different setups is the main task of self-force calculations in curved spacetimes.

At this point we remind that Eq. (5.28) was first derived by DeWitt and Brehme [144] (with a correction by Hobbs [145] as the original version did not include the Ricci-tensor term). Their derivation followed a different path from the outline presented here (which takes after Detweiler and Whiting's work). In DeWitt and Brehme's work they considered the retarded potential to be split into *direct* and *tail* contributions (see Fig. 5.3). The direct contribution to the vector potential at a spacetime point x is the piece that propagates along the past light cone of x from the point where the past light cone intersected the particle's worldline. The tail contribution is the piece that propagates *within* the past light cone of x from the entire past history of the particle, up to, but excluding, the point where the light cone intersects the worldline. They then showed that it was the direct piece of the full potential that diverged as $x \to x'$ and the self-force was entirely due to the tail contribution. This decomposition of the potential into direct and tail components is useful for describing the SF but we note that neither of these parts individually is a solution of the field equation (5.21).

Lastly we note that Eq. (5.28) possesses a seemingly unusual feature in that in the absence of any acceleration the particle will experience a (self-) force in curved spacetime (for zero acceleration the $F_{(\mathrm{ALD})}$ term vanishes but in curved space the $F_{(\mathrm{Ricci})}$ and $F^{\alpha}_{(\mathrm{Tail})}$ terms remain in general). At first glance this looks like it might violate the equivalence principle, as, for example, a (point-like) electron freely falling in a gravitational field will experience a (self) force whereas an electron in stationary in flat space will not (recall that by the equivalence principle these two situation are indistinguishable for an uncharged test mass). The resolution to this seeming violation of the equivalence principle lies in realising that an electrically charged particle cannot be separated from its extended electromagnetic field and so the equivalence principle does not apply in this case. This issue is discussed in detail by DeWitt and DeWitt [153].

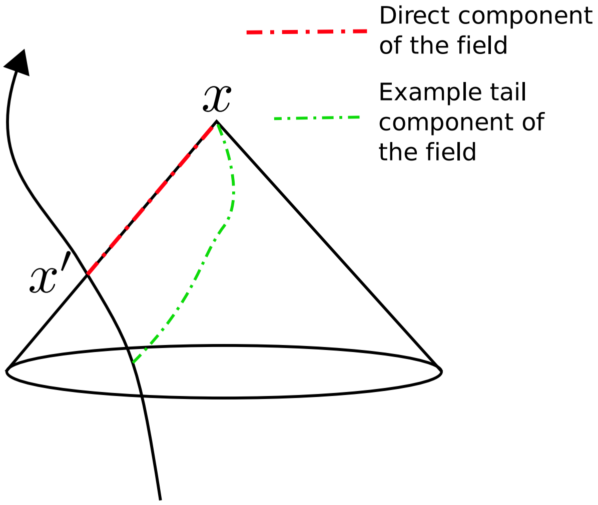

FIGURE 5.3: Failure of Huygens' principle in curved spacetime: a sharp pulse of light will not remain sharp. Similarly the force felt by a test particle at x is composed of two contributions, one from the field that has propagated along the light cone and the other from the field that has propagated within it. The first contribution is referred to as the direct piece, the second, the tail piece of the force. In a point particle model, as the field point x tends to a point x' on the particle's world line, the force diverges. DeWitt and Brehme [144] showed that this divergence was entirely due to the direct component of the force; the tail contribution remains finite in the limit and is entirely responsible (for non-accelerated motion in Ricci flat space) for the self-force felt by the particle.

5.2 Scalar-field self-force

In this section we give the equations governing the motion of a particle carrying a scalar charge q moving in a curved spacetime. Recall that we take our equation of motion to be the minimally coupled Klein-Gordon equation [see Eq. (4.1)], from which we can define retarded and advanced solutions Φ_{ret} and Φ_{adv} respectively. We can proceed then as with the EM case and define suitable singular and regular fields, Φ^S and Φ^R, respectively. It can then be shown that only Φ^R contributes to the dynamics [130]. We then choose (see below for discussion) our force law to read

$$u^\beta \nabla_\beta (\mu u^\alpha) = F^\alpha_{\text{ext}} + q \nabla^\alpha \Phi^R \ , \tag{5.32}$$

where, as before, F^α_{ext} is some external force acting on the particle

The explicit calculation of F^α_{self} was first carried out by Quinn [130] for the minimally coupled scalar field, and extended to included Ricci coupling in Ref. [75]. The resulting equations of motion for the case of minimal coupling are given by

$$u^\beta \nabla_\beta (\mu u^\alpha) = F^\alpha_{\text{ext}} + F^\alpha_{\text{self}} \quad \text{with} \quad F^\alpha_{\text{self}} = \frac{q^2}{3\mu}\frac{dF^\alpha_{\text{ext}}}{d\tau} + \frac{1}{6} R^{\alpha\beta} u_\beta + \lim_{\epsilon\to 0} \frac{q^2}{\mu} \int_{-\infty}^{\tau-\epsilon} \nabla_\alpha G_+ \, d\tau' \ , \tag{5.33}$$

where we have reduced the order of the differential equation so as to remove the unphysical $da/d\tau$ term. A surprising feature of Eq. (5.33) is that the SSF has a component tangential to the particle's four-velocity so that $u_\alpha F^\alpha_{\text{self}}$ is generally non-zero. The consequences of this can be seen by expanding the derivative in Eq. (5.32), whereupon one finds a term orthogonal to the particle's four-velocity, which is responsible for driving the orbital dynamics, and a term tangential to the four-velocity, which gives rise to a dynamically varying rest mass. With no external force, equating these components with the orthogonal and tangential components of F^{α}_{self} gives

$$\mu\frac{du^{\alpha}}{d\tau} = (\delta^{\alpha}_{\beta} + u^{\alpha}u_{\beta})F^{\alpha}_{\text{self}} \equiv F^{\beta}_{\perp(\text{self})} \,, \tag{5.34}$$

$$\frac{d\mu}{d\tau} = -u^{\alpha}F^{\text{self}}_{\alpha} \,. \tag{5.35}$$

By combining Eqs. (5.32) and (5.35) we can write the rest mass explicitly as a function of τ which gives

$$\mu(\tau) = \mu_0 - q\Phi^{R}(\tau) \,, \tag{5.36}$$

where μ_0 is a constant of integration (sometimes called the bare mass). For a stationary setup (where Φ_R is constant in time) the rest mass of the particle will remain constant along the orbit, but for more general setups the rest mass will vary along the orbit. This unusual feature of our particular scalar-field setup can be understood ‘physically’ by noting that a scalar charge can radiate monopole waves with the radiated energy coming at the expense of the particle’s rest mass [75].

We remind at this point that there are no known fundamental scalar fields, and so the choice of field equation and force law are somewhat arbitrary. It turns out to be possible to construct a scalar field theory where the rest mass is conserved, but at the cost of losing the linearity of the resulting theory [130]. For this reason we choose to work with a scalar field governed by the Klein-Gordon equation, even though the resulting theory has a time-dependent rest mass.

5.3 Gravitational self-force

The concept of a gravitational self-force is a little more subtle than in the EM and scalar cases. For EM and scalar fields it is conceptually straightforward to consider the field to be a perturbation over a fixed background geometry (at least to leading order in q/M, where q is either the scalar or electric charge. For higher orders the back reaction of the field’s stress-energy on the spacetime geometry must be taken into account). For the gravitational problem, the field in question is a perturbation of the spacetime geometry and as such the distinction between the field and the background spacetime is ambiguous. If we consider the metric g to be the sum of the background metric $\mathring{g}$ and the perturbation h then there is in principle no unique way to map a point from $g = \mathring{g} + h$ to $\mathring{g}$. One consequence of this is that a change of gauge will result in a change in the computed self-force [56]. Thus a complete description of problem requires knowledge of both the GSF and the gauge in which it was computed.

It may be objected that, as we have a point mass moving in a purely gravitational field, we should expect it to move along a geodesic in some physical spacetime and that by considering it to be moving along a geodesic in a background spacetime we have artificially given rise to the ambiguity mentioned above. The problem with constructing such a description is that, as we are using a point particle model, the spacetime has a singularity at the particle’s location making it challenging to describe the particle’s motion as geodesic in the ‘physical’ spacetime (in fact point particles are not valid solutions to the full Einstein field equations [146]). Rigorously defining a suitable limit procedure so that once can talk about point particles as sourced to the linearized Einstein field equations encountered in SF calculations has been a major achievement over the last few years [44]). Nonetheless this alternative viewpoint of the GSF was developed by Detweiler and Whiting [152]. In their work they restore some of the original spirit of the equivalence principle to the GSF problem by considering the particle to be moving along geodesics of an *effective spacetime*. It is important to note, though, that this effective spacetime is not the physical spacetime and so, just as with the 'force' point of view it should be considered a calculation tool.

The correct equations of motion (through first order in the mass ratio) were first identified by Mino, Sasaki and Tanaka [6], and Quinn and Wald [7]. Their results show the gravitational self-force to be given by

$$F^\alpha_{\text{self}} = \mu^2 k^{\alpha\beta\gamma\delta} \lim_{\epsilon\to 0} \int_{-\infty}^{\tau-\epsilon} \nabla_\delta G^{+}_{\beta\gamma\beta'\gamma'}(x,x') u^{\beta'} u^{\gamma'}\, d\tau' \ , \tag{5.37}$$

where

$$k^{\alpha\beta\gamma\delta} = \frac{1}{2}\mathring{g}^{\alpha\delta}u^\beta u^\gamma - \mathring{g}^{\alpha\beta}u^\gamma u^\delta - \frac{1}{2}u^\alpha u^\beta u^\gamma u^\delta + \frac{1}{4}u^\alpha \mathring{g}^{\beta\gamma}u^\delta + \frac{1}{4}\mathring{g}^{\alpha\delta}\mathring{g}^{\beta\gamma} \ . \tag{5.38}$$

Equation (5.37) is often referred to as the MiSaTaQuWa equation after the authors of the original papers and they represent the gravitational equivalent of Eqs. (5.28) and (5.33). The equation we have given here has had the reduction of order technique applied which, in this case, completely removes the term proportional to $da/d\tau$ (the reduced term is found to be at second order in the mass ratio and so when working only to first order, as we do in this thesis, it can be ignored [7]).

5.4 Self-force via the mode-sum method

In this work we will always consider the particle to moving on a geodesic of a vacuum spacetime (i.e. $\mathring{R}_{\alpha\beta} = 0$). From Eqs. (5.28), (5.32) and (5.37) we see that this means we only need concern ourselves with the calculation of the regular/tail contribution to the SF so that we have

$$F^\alpha_{\text{self}}(x_p) = F^\alpha_R(x_p) = \begin{cases} q\nabla^\alpha \Phi_R(x_p) \ , & \text{scalar field,} \\ q_e \mathring{g}^{\alpha\gamma}u^\beta[\nabla_\gamma A^R_\beta(x_p) - \nabla_\beta A^R_\gamma(x_p)] \ , & \text{EM field,} \\ \mu k^{\alpha\beta\gamma\delta}(x_p)\nabla_\delta \bar{h}^R_{\beta\gamma}(x_p) \ , & \text{gravitational field.} \end{cases} \tag{5.39}$$

Formally F^α_{self} is constructed via Eqs. (5.28), (5.33) and (5.37). Unfortunately, these equations are difficult to work with directly (though some progress has been made in this direction with the method of matched expansions [78]). In Sec. 1.3 we briefly reviewed the current set of practical methods for computing the self-force and in this work we will make use of the mode-sum scheme which we will detail now.

As discussed in the proceeding sections, we can write the regular contribution as the difference between the retarded field and the singular contribution in the limit $x \to x_p$. This gives us

$$F^\alpha_{\text{self}}(x_p) = F^\alpha_R(x_p) = \lim_{x\to x_p} \left[F^\alpha_{\text{ret}}(x) - F^\alpha_S(x)\right] \ , \tag{5.40}$$

where $F^\alpha_{\text{ret}/S}$ are computed via Eq. (5.39) with the replacements $x_p \to x$ and $R \to \text{ret}/S$. For the gravitational case, this involves an additional subtlety as $k^{\alpha\beta\gamma\delta}$ depends upon the particle's four-velocity [see Eq. (5.38)] and as such is only defined on the particle's worldline. We therefore have to choose a suitable extension of $k^{\alpha\beta\gamma\delta}$ from the particle's worldline. This extension can be arbitrarily chosen so long as we have $k^{\alpha\beta\gamma\delta}(x) \to k^{\alpha\beta\gamma\delta}(x_p)$ as $x \to x_p$ and we choose the same extension for both $F^\alpha_{\rm ret}(x)$ and $F^\alpha_S(x)$. The particular extension we choose in this work will be discussed below.

Equation (5.40) is still not in a practical form, as both $F^\alpha_{\rm ret}(x)$ and $F^\alpha_S(x)$ diverge as $x \to x_p$. At this point we turn to the mode sum prescription, whereby the full retarded field, regular field and the singular field are decomposed into *scalar* spherical harmonic modes. This decomposition has the advantage that the individual lm-modes of the retarded and singular fields are finite at the particle's location. We can thus write the force due to the regular field as

$$F^\alpha_R(x_p) = \lim_{x\to x_p} \sum_l \left[F^{\alpha l}_{\rm ret}(x) - F^{\alpha l}_S(x)\right] \,, \tag{5.41}$$

where $F^{\alpha l}_{{\rm ret}/S}$ denotes the contribution to $F^\alpha_{{\rm ret}/S}$ from its spherical harmonic l-mode (summed over m). Generally the retarded force per l-mode has to be computed numerically and this computation is the subject of Chapters 6, 7 and 8 of this thesis. The singular piece on the other hand is accessible to an analytical treatment. The structure of the singular component of the field was first analysed by Mino *et al.* [6] and the practical mode sum method for computing the SF was developed shortly after by Barack and Ori [8, 154]. The formula they obtained for regularizing the field is given by

$$F^{\rm self}_\alpha = q\sum_{l=0}^\infty \left(F^{l({\rm full})}_{\alpha\pm} - A_{\alpha\pm}L - B_\alpha - C_\alpha L^{-1}\right) - D_\alpha \equiv \sum_{l=0}^\infty F^{l({\rm reg})}_\alpha \,, \tag{5.42}$$

where $L = l + 1/2$ and

$$D_\alpha \equiv \sum_{l=0}^\infty \left[\lim_{x\to x_p} F^{Sl}_\alpha - A_\alpha L - B_\alpha - C_\alpha L^{-1}\right] . \tag{5.43}$$

Each $F^{({\rm full})l}_\alpha$ is finite at the particle's location, although in general the sided limits $r \to r_p^\pm$ yield two different values, denoted $F^{({\rm full})l}_{\alpha\pm}$ respectively. The coefficients $A_\alpha, B_\alpha, C_\alpha, D_\alpha$ are l-independent *regularization parameters*, the values of which are known for generic bound orbits about a Schwarzschild [8] or Kerr black hole [154].

As the series in Eq. (5.42) is truncated at $\mathcal{O}(L^{-1})$ we expect, for high l, the contributions to $F^{\rm self}_\alpha$ to drop off as l^{-2}. It is possible to add higher order regularization terms to the series that increase the convergence rate with l. These terms are known to take the form [155]

$$\frac{D_{\alpha,2}}{(2l-1)(2l+3)} + \frac{D_{\alpha,4}}{(2l-3)(2l-1)(2l+3)(2l+5)} + \cdots = \sum_{n=1}^\infty D_{\alpha,2n}\left[\prod_{k=0}^n (2L-2k)(2L+2k)\right]^{-1} \tag{5.44}$$

where the $D_{\alpha,2n}$ are extra regularization parameters that serve to increase the differentiability of the field at the particle's location (they do not affect the value of the SF as, for instance, $\sum_{l=0}^\infty[(2l-1)(2l+3)]^{-1} = 0$). With the addition of each extra parameter the convergence rate of the mode-sum increases by a factor of l^{-2} (note that the coefficients of the odd powers of L are known to be zero [155]). Thus knowledge of the higher order regularization parameters is of great use in practical calculations. In principle if all the higher order regularization parameters are know then the convergence of the mode sum becomes exponential with l. In particular this implies that if the field component requires no regularization (i.e., all regularization parameters are known to be zero), then we expect to observe exponential convergence. Lastly we note that there is no relation between the $D_{\alpha,2n}$ and D_α defined in Eq. (5.43).

For comparisons between GSF and PN calculations (which we do not undertake in this thesis but are a future application of our work) it turns out to be useful to replace the particle's proper time, τ (defined with respect to the background metric) by the proper time $\tilde{\tau}$ defined with respect to the perturbed metric $\mathring{g}_{\alpha\beta} + h^R_{\alpha\beta}$ [156, 157]. The two proper times are related, through $\mathcal{O}(\mu)$, via

$$\frac{d\tau}{d\tilde{\tau}} = 1 + H^R \,, \tag{5.45}$$

where

$$H^{\text{full}} = \frac{1}{2} h^{\text{full}}_{\alpha\beta} u^\alpha u^\beta \,, \tag{5.46}$$

with the R-field perturbation $h^R_{\alpha\beta}$ evaluated at the particle. Barack and Sago [157] showed that H^R can be computed from the full (retarded) metric perturbation using the regularization formula

$$H^R = \sum_{l=0}^{\infty} \left[H^{\text{full}}_l - B_H + C_H L^{-1} \right] \,, \tag{5.47}$$

where B_H and C_H are regularization parameters.

5.4.1 Mode-sum in Schwarzschild spacetime

The $A_\alpha, B_\alpha, C_\alpha, D_\alpha$ regularization parameters for the scalar, EM and gravitational self-force were first derived by Barack and Ori [8]. For the scalar self-force they found the values of these first four parameters to be

$$A_{\pm r} = \mp \frac{q^2}{r_p^2} \frac{\mathcal{E}}{fV}, \qquad A_{\pm t} = \pm \frac{q^2}{r_p^2} \frac{\dot{r}}{V}, \qquad A_\varphi = 0 \,, \tag{5.48}$$

$$B_r = \frac{q^2}{r_p^2} \frac{(\dot{r}^2 - 2\mathcal{E}^2) K(w) + (\dot{r}^2 + \mathcal{E}^2) E(w)}{\pi f V^{3/2}} \,, \tag{5.49}$$

$$B_t = {\frac{q^2}{r_p}}^{2} \frac{\mathcal{E}\dot{r}[K(w) - 2E(w)]}{\pi V^{3/2}} \,, \tag{5.50}$$

$$B_\varphi = \frac{q^2}{r_p} \frac{\dot{r}[K(w) - E(w)]}{\pi(\mathcal{L}/r_p) V^{1/2}} \,, \tag{5.51}$$

$$C_\alpha = D_\alpha = 0 \,, \tag{5.52}$$

with K, E being the complete elliptic integrals of the first and second kind respectively and

$$w \equiv \frac{\mathcal{L}^2}{\mathcal{L}^2 + r_p^2}, \qquad V \equiv 1 + \frac{\mathcal{L}^2}{r_p^2} \,. \tag{5.53}$$

For the EM and gravitational self-force Barack and Ori [158] found the regularization parameters were related to the scalar ones above via

$$A^{(\text{grav})}_\alpha = -A^{(\text{EM})}_\alpha = A^{(\text{sca})}_\alpha \,, \tag{5.54}$$

$$B^{(\text{grav})}_\alpha = -B^{(\text{EM})}_\alpha = (\delta^\beta_\alpha + u_\alpha u^\beta) B^{(\text{sca})}_\beta \,, \tag{5.55}$$

$$C^{(\text{grav,EM})}_\alpha = D^{(\text{grav,EM})}_\alpha = 0 \,, \tag{5.56}$$

where the (grav), (EM), (sca) superscripts are used to denote the regularization parameters for the gravitational, EM and scalar self-force respectively.

For the metric perturbation the regularization parameters are given by [129]

$$B_H = \frac{2\mu}{\pi\sqrt{r_p^2+\mathcal{L}^2}} K\left(\frac{\mathcal{L}^2}{r_p^2+\mathcal{L}^2}\right) , \qquad C_H = 0 \, . \tag{5.57}$$

For the SSF for a particle in a circular orbit, Detweiler *et al.* [155] derived the next order regularization parameter, D_2. Very recently Heffernan *et al.* [159] were able to derive the D_2, D_4 and D_6 for generic orbits about a Schwarzschild black hole for the scalar, EM and gravitational SF. They also derived higher order regularization parameters for the metric perturbation.

As we saw in Sec. 4.5 the angular component of the gravitational perturbation decouples when expanded in *tensor* spherical harmonics whereas the mode-sum formula requires *scalar* spherical harmonic modes as input. Therefore before we can use Eq. (5.42) we must project the tensor harmonics onto a basis of scalar harmonics. In doing so it is important to make a good choice of extension of $k^{\alpha\beta\gamma\delta}$ off the world line as some choices will lead to infinite coupling between the tensor and scalar spherical harmonic modes [160]. The choice we make here is that of Ref. [67] whereby, if the SF is to evaluated at a point x_p on the particle's worldline, we take the four-velocity u^α that appears Eq. (5.38) to be $u^\alpha(x_p)$ for all x. With this choice of extension the expansion of the full force $F^{l(\text{full})}_{\alpha\pm}$ in scalar spherical harmonics occurs in such a way that each tensor spherical harmonic $l'm$-mode only couples to the seven scalar harmonic lm-modes with $l-3 \leq l' \leq l+3$, with no coupling between the m-modes. Performing the expansion is a straightforward but rather tedious calculation. The resulting formula for the full component of the force per l-mode is given by

$$\begin{aligned} F^{\alpha l}_{\text{full}} = \sum_{m=-l}^{l} \frac{\mu^2}{r_p^2} \Big\{ & \mathcal{F}^{\alpha l-3,m}_{(-3)} + \mathcal{F}^{\alpha l-2,m}_{(-2)} + \mathcal{F}^{\alpha l-1,m}_{(-1)} + \mathcal{F}^{\alpha l,m}_{(0)} \\ & + \mathcal{F}^{\alpha l+1,m}_{(+1)} + \mathcal{F}^{\alpha l+2,m}_{(+2)} + \mathcal{F}^{\alpha l+3,m}_{(+3)} \Big\} Y^{lm}(\theta_p,\varphi_p) \, , \end{aligned} \tag{5.58}$$

where the $\mathcal{F}$'s are given explicitly in Appendix of C of Ref. [67] (we do not repeat them here as they are rather lengthy equations). The metric perturbation likewise needs to be projected onto a basis of scalar harmonics before regularization. The required formula is given by

$$H^{\text{full}}_l = \frac{1}{2} \sum_{m=-l}^{l} \left\{ \mathcal{G}^{l+2,m}_{(+2)} + \mathcal{G}^{l+1,m}_{(+1)} + \mathcal{G}^{lm}_{(0)} + \mathcal{G}^{l-1,m}_{(-1)} + \mathcal{G}^{l-2,m}_{(-2)} \right\} Y^{lm} \, , \tag{5.59}$$

where the $\mathcal{G}$'s are given in Appendix F (although Barack and Sago were the first to calculate H^R [129], they did not explicitly give the required coupling formula between the scalar and tensor spherical harmonic modes).

5.4.2 Mode-sum in Kerr spacetime

The regularization parameters in Kerr spacetime for the scalar, EM and gravitational SF were first derived by Barack and Ori [154]. Their explicit form is rather unwieldy so we do not repeat them here (but we do give their form for circular equatorial orbits in Appendix G). More recently Heffernan *et al.* [159, 161] have also derived the next order regularization parameter, D_2, for the case of a scalar particle in a circular equatorial orbit about a Kerr black hole.

We now discuss some subtleties of implementing the mode-sum formula in Kerr spacetime (note the remainder of this section is original material). As we saw in Sec. 4.1, in Kerr spacetime the scalar field naturally decomposes into *spheroidal harmonic* modes. The mode-sum scheme on the other hand requires[1] *spherical harmonic* modes as input even in Kerr spacetime. Hence in order to regularize using the standard mode-sum approach we first need to project the spheroidal harmonic modes onto a basis of spherical harmonics. We do this by expanding each spheroidal harmonic in a series of spherical harmonics

$$S_{\hat{l}m}(\theta;\sigma^2)e^{im\phi} = \sum_{l=0}^{\infty} b^{\hat{l}}_{lm}(\sigma^2)Y_{lm}(\theta,\varphi) \ , \tag{5.60}$$

where the σ-dependent coefficients $b^{\hat{l}}_{lm}$ are determined from a recursion relation found by substituting the series expansion into the angular differential equation (4.12) (see Appendix B and also Ref. [117]). The spheroidal harmonics reduce to the standard spherical harmonics when $\sigma^2 = 0$. Therefore when $\sigma^2 = 0$ the coefficients $b^{\hat{l}}_{lm}$ reduce to the Kronecker delta $\delta^{\hat{l}}_{l}$. Using the $b^{\hat{l}}_{lm}$'s we can write the spherical harmonic multipole contribution to the full SSF as

$$F^{(\mathrm{full})l}_{\alpha}(x) = q\nabla_{\alpha} \sum_{m=-l}^{l} \phi_{lm}(t,r)Y_{lm}(\theta,\varphi)/r \ , \tag{5.61}$$

where $\alpha = \{t, r, \varphi\}$ (we discuss the situation for $\alpha = \theta$ below) and ϕ_{lm} is given by

$$\phi_{lm}(t,r) = \sum_{n=0}^{\infty}\sum_{\hat{l}=0}^{\infty} b^{\hat{l}}_{lm}\psi_{\hat{l}m\omega}(r)e^{-i\omega t} \ . \tag{5.62}$$

We now make some comments regarding the practical use of Eqs. (5.61) and (5.62). Formally when constructing ϕ_{lm} one has to sum over all spheroidal $\hat{l}$ modes. In practice this is not necessary, as the coupling between the spheroidal and spherical harmonic modes is relatively weak for the spheroidicities encountered in our calculation. We have numerically demonstrated that the contribution from a given spheroidal $\hat{l}m$ mode to the spherical harmonic lm modes of the field is strongly peaked around $l = \hat{l}$ and that its contribution to other spherical harmonic modes decreases exponentially as one moves away from this value (see Fig. 5.4). As would be expected, the coupling strengthens as the magnitude of the spheroidicity, σ^2, increases.

Equation (5.61) cannot be used in its given form to compute the F_θ component of the SSF. Recall that the regularization formula (5.42) requires the full SF per l-mode, summed over m, as input. When taking the θ derivative of the spherical harmonics Y_{lm} one finds that the resulting formula couples between l-modes. Before regularization this coupling must be correctly taken into account by expanding the $Y_{lm,\theta}$ in a basis of spherical harmonics as we now demonstrate.

The most naïve route to computing F_θ is to expand $Y_{lm,\theta}$ as as series of Y_{lm}'s much as we did with the spheroidal harmonics [see Eq. (5.60)]. In this approach we would write

$$Y_{\bar{l}m,\theta}(\theta,\varphi) = \sum_{l=0}^{\infty} a^{\bar{l}}_{lm}Y_{lm}(\theta,\varphi) \ , \tag{5.63}$$

---

[1] At least within its current formulation the standard mode-sum scheme requires spherical harmonic modes as input. It may be possible to re-formulate it and regularize directly the spheroidal harmonic modes but this has not yet been attempted. The Discussion section of Ref. [110] gives an overview of the difficulties involved with this approach.

and then using the orthogonality relation (B.4) compute the series coefficients $a^{\bar{l}}_{lm}$ via

$$a^{\bar{l}}_{lm} = \int Y_{\bar{l}m,\theta} Y^*_{lm}\, d\Omega \ , \tag{5.64}$$

Unfortunately when we do this we find that the bandwidth of the coupling is extremely wide so that, for instance, the $(l, m) = (44, 10)$ mode couples strongly to modes with $l > 100$ (see Fig. 5.5). This makes any numerical computation impractical. Instead our technique for computing F_θ is to multiply the scalar field by a suitable function $f(\theta)$ that has the properties: (i) when we take the derivative with respect to θ and then the limit $\theta \to \theta_p$ we recover the correct result, and (ii) allows us to expand the combination $f(\theta)Y_{lm,\theta}$ in a finite series of spherical harmonics. After some experimentation, one such function that presents itself is

$$f(\theta) = \frac{3\sin^2\theta_p \sin\theta - \sin^3\theta}{2\sin^3\theta_p} = 1 + \mathcal{O}(\theta-\theta_p)^2 \ . \tag{5.65}$$

This function clearly satisfies condition (i), as we have $(fY_{lm})_{,\theta} = fY_{lm,\theta} + f_{,\theta}Y_{lm} \to Y_{lm,\theta}$ as $\theta \to \theta_p$. Furthermore, using the identities (B.9) and (B.12) we can expand $fY_{lm,\theta}$ as series that couples only to the $l \pm 1$ and $l \pm 3$ modes. Performing the expansions we find our final result takes the form

$$F^{(\text{full})l}_\theta(x \to x_p) = q \sum_{m=-l}^{l} \phi_{lm}(t_p, r_p)\mathcal{F}_{lm}(\theta_p)Y_{lm}(\theta_p, \varphi_p)/r \ , \tag{5.66}$$

where $\mathcal{F}_{lm}$ is given by

$$\mathcal{F}_{lm}(\theta_p) = \frac{3}{2\sin\theta_p}\left(\delta^{l-1,m}_{(+1)} + \delta^{l+1,m}_{(-1)}\right) - \frac{1}{2\sin^3\theta_p}\left(\zeta^{l-3,m}_{(+3)} + \zeta^{l-1,m}_{(+1)} + \zeta^{l+1,m}_{(-1)} + \zeta^{l+3,m}_{(-3)}\right) \ , \tag{5.67}$$

with the δ's and ζ's given in Appendix B. Note that whilst Eq. (5.61) gives the force felt a test body of charge q anywhere throughout space except at the particle (where it diverges and hence requires regularization at this point), Eq. (5.66) is only useful for regularizing the θ component of the force at the particle (i.e., it does not give the correct θ component of the force away from the particle).

We also note that for the EM and gravitational SF calculations we can use the fact that the four-velocity are orthogonal ($u^\alpha F_\alpha = 0$), from which, once F_t, F_φ and F_r are known, one can compute F_θ. However recall from Sec. 5.2 that for the scalar field problem the quantity $u^\alpha F_\alpha$ is generally non-zero and thus for the SSF we must compute F_θ directly via the method given above.

5.5 Alternative practical regularization techniques

As discussed in Sec. 1.3, alternative practical regularization techniques have recently emerged in the form of matched expansions, radiation gauge regularization and puncture methods. The former technique aims to use the MiSaTaQuWa equations directly to compute the SF and we will not say more about it here. The development of the latter two techniques has been driven by a desire to calculate the GSF in Kerr spacetime, where the mode-sum approach is less appropriate due to a lack of separability of the Lorenz gauge gravitational field equations in Kerr spacetime (see Chapter 10 for a brief discussion). The puncture technique in particular relates to computing

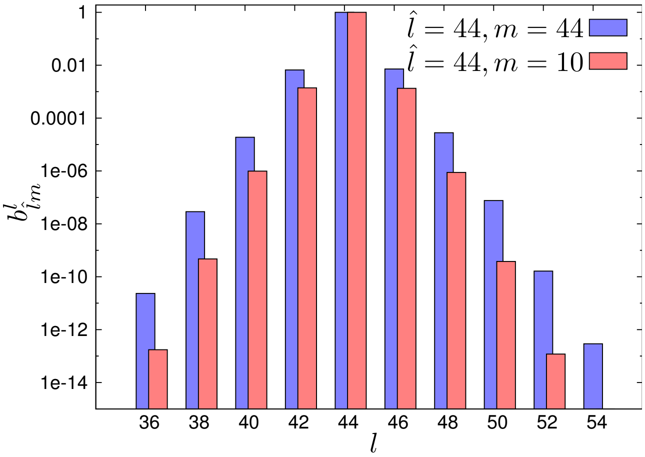

FIGURE 5.4: Coupling of spheroidal and spherical modes for $\theta = \pi/2$. Shown are the contributions from a given $\hat{l}$-mode to $b^{\hat{l}}_{lm}$ for various spherical harmonic l-modes. (Note that for $\theta = \pi/2$ we have that the $b^{\hat{l}}_{lm} = 0$ identically for odd values of $l - \hat{l}$.) The width of the l distribution depends mainly on the magnitude of the spheroidicity parameter, $|\sigma^2|$, which in the two cases illustrated here of $(\hat{l}, m) = (44, 34)$ and $(\hat{l}, m) = (44, 10)$, we have set the spheroidicity to be $\sigma^2 = -11.821$ and -1.022, respectively (the particular choice of spheroidicities used here is motivated by greatest values we encounter later for the circular equatorial orbit—see Chapter 6).

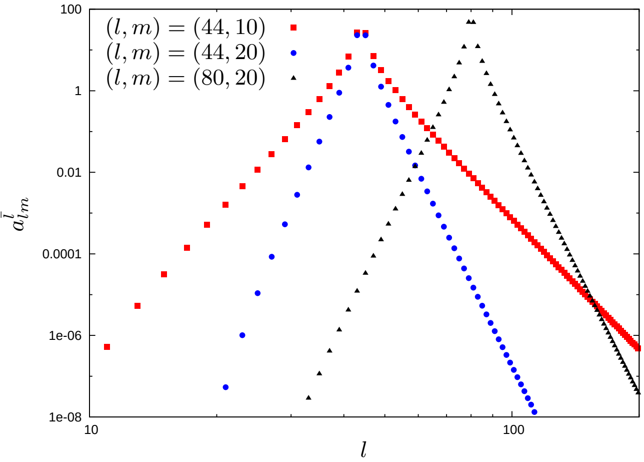

FIGURE 5.5: Projection of $Y_{lm,\theta}$ on to a basis of spherical harmonics [see Eq. (5.63)]. The convergence of the series is seen to exhibit power-law behaviour (note the log-log scale). This wide bandwidth of the coupling makes practical calculations of F_θ via this method infeasible and instead we make use of the alternative method outlined in the text.

the Lorenz gauge GSF using 2+1D or 3+1D evolutions and we outline the basic idea behind this approach now.

We begin by supposing that we can construct a ‘puncture’ field, Φ_P, that approximates the singular field, Φ_S, near the particle in such a way that we have

$$\lim_{x \to x_p} (\Phi_S - \Phi_P) = 0 , \tag{5.68}$$

$$\lim_{x \to x_p} \nabla^\alpha (\Phi_S - \Phi_P) = 0 . \tag{5.69}$$

We then write the regular field Φ_R, which we recall is the difference between the retarded field,

$\Phi_{\rm ret}$, and the singular field, in the form

$$\Phi_R(x) = \Phi_{\rm ret}(x) - \Phi_S(x) + \Phi_P(x) - \Phi_P(x) \ , \tag{5.70}$$

$$= \Phi_{\rm res}(x) - [\Phi_S(x) - \Phi_P(x)] \ , \tag{5.71}$$

where we have defined the *residual* field, $\Phi_{\rm res}$, by

$$\Phi_{\rm res}(x) \equiv \Phi_{\rm ret} - \Phi_P(x) \ . \tag{5.72}$$

Now recalling that the SSF is entirely due to the regular field we have

$$F^\alpha_{\rm self}(x_p) = q\nabla^\alpha \Phi_R(x_p) = q \lim_{x\to x_p} \nabla^\alpha \left\{\Phi_{\rm res}(x) - [\Phi_S(x) - \Phi_P(x)]\right\} \ , \tag{5.73}$$

$$= q\nabla^\alpha \Phi_{\rm res}(x_p) \ , \tag{5.74}$$

where in moving from the first to the second line we have used Eq. (5.69). By combining Eqs. (5.72) and (4.1) we can write the governing equation for $\Phi_{\rm res}$ as

$$\Box \Phi_{\rm res} = -4\pi T - \Box \Phi_P \equiv Z_{\rm res} \ , \tag{5.75}$$

where $Z_{\rm res}$ is an extended source free of any delta functions.

The effective source approach has been used in a few practical calculations of the SF. In Barack and Golbourn's approach [81] they, in anticipation of working in the axially symmetric Kerr spacetime, first decomposed the residual source and field and the retarded field into azimuthal m-modes

$$\Phi_{\rm res/ret} = \sum_{m=-\infty}^{m} \phi^m_{\rm res/ret}(t,r,\theta)e^{im\varphi}, \qquad Z_{\rm res} = \sum_{m=-\infty}^{m} Z^m_{\rm res}(t,r,\theta)e^{im\varphi} \ . \tag{5.76}$$

In making this decomposition one finds that each m-mode the retarded field, $\phi^m_{\rm ret}$, is logarithmically divergent at the particle making it challenging to numerically solve for it directly. They overcame this problem by implementing the puncture scheme outlined above in a 2+1D code [162] for a scalar particle on a circular orbit in Schwarzschild spacetime. Their technique was to solve Eq. (5.75) inside a world tube surrounding the particle and $\Box\Phi_{\rm ret} = 0$ outside the world tube, using Eq. (5.72) to continue the evolution across the worldtube boundary. They discovered that the convergence of field was power-law in m, and that the rate of convergence depended upon the regularity of the residual source. The closer the puncture field approximates the singular field, the faster the convergence rate with m. In their original work they did not have a sufficiently regular residual field to calculate the self-force. Later Dolan and Barack [91] were able to compute the SSF via the m-mode technique and then Dolan *et al.* [98] extended the calculation to circular, equatorial orbits in Kerr spacetime. The results they obtained were found to be in agreement with the work presented in this thesis (and published as Ref. [97]). Very recently the m-mode approach has been extended to calculate the GSF for circular orbits in Schwarzschild spacetime [142].

A similar approach was taken by Vega and Detweiler [82] who performed a 1+1D calculation for a scalar particle in a circular orbit about a Schwarzschild black hole. In their calculation they make use of a smooth 'window' function, W, constructed in such a way as to allow for a smooth transition from solving for the residual field in the vicinity of the particle to solving for the retarded field far away from the particle. This is achieved by introducing a regular field defined by

$$\Phi^R = \Phi^{\rm ret} - W\Phi^P \ , \tag{5.77}$$

and then solving for

$$\Box\Phi^R = -\Box(W\Phi_P) - 4\pi T \equiv S_{\rm eff} \ , \tag{5.78}$$

where $S_{\rm eff}$ is an effective extended source that can be computed analytically. Since Vega and Detweiler's 1+1D calculation this approach has been applied to full 3+1D SSF simulations [95] in Schwarzschild spacetime in anticipation of tackling the Kerr GSF problem. A comprehensive review of the effective source approach can be found in Refs. [83, 163]. Working in 3+1D has the advantage that it can leverage much of the evolution code that has been developed by those working in the NR field [90].

5.6 Conservative and dissipative components of the SF

When analysing the different physical effects of the SF it is insightful to consider its conservative and dissipative effects separately [76, 164]. Splitting the SF into its conservative and dissipative components is also practically beneficial, as the two pieces admit l-mode sums with different convergence properties, which are better dealt with separately. Before showing how we practically go about splitting the SF into conservative and dissipative pieces in this work, we first give the standard definition in terms of the advanced and retarded fields [76]. We first remind that we denote the retarded and advanced solutions to the scalar field equation (4.1) by $\Phi_{\rm ret}$ and $\Phi_{\rm adv}$ respectively. The advanced SF is then defined by

$$F^{\rm adv}_\alpha = \sum_{l=0}^{\infty}[F^{\rm full}_{\alpha l\pm}(\Phi_{\rm adv}) - A_{\alpha\pm}(l+1/2) - B_\alpha] \ . \tag{5.79}$$

Since the singular behavior near the particle is the same for the retarded and advanced fields, the regularization parameters A_α and B_α in Eq. (5.79) are as given in Sec. 5.4. The conservative and dissipative components of the SF are defined to be the parts of the SF which are symmetric and anti-symmetric under interchanges of the retarded and advanced fields respectively:

$$F^{\rm cons}_\alpha \equiv \frac{1}{2}(F^{\rm ret}_\alpha + F^{\rm adv}_\alpha), \qquad F^{\rm diss}_\alpha \equiv \frac{1}{2}(F^{\rm ret}_\alpha - F^{\rm adv}_\alpha) \ . \tag{5.80}$$

The full SSF is then the sum of the two:

$$F^{\rm self}_\alpha(\equiv F^{\rm ret}_\alpha) = F^{\rm cons}_\alpha + F^{\rm diss}_\alpha \ . \tag{5.81}$$

Substituting into formulae (5.80) from equations (5.42) and (5.79), we obtain the mode-sum regularization formulae for the conservative and dissipative components

$$F^{\rm cons}_\alpha = \sum_{l=0}^{\infty}\left[F^{\rm full(cons)}_{\alpha l\pm} - A^{\pm}_\alpha(l+1/2) - B_\alpha\right] \ , \tag{5.82}$$

$$F^{\rm diss}_\alpha = \sum_{l=0}^{\infty}F^{\rm full(diss)}_{\alpha l\pm} \ , \tag{5.83}$$

where

$$F^{\text{full(cons)}}_{\alpha l} \equiv \frac{1}{2}[F^{\text{full}}_{\alpha l\pm}(\Phi_{\text{ret}}) + F^{\text{full}}_{\alpha l\pm}(\Phi_{\text{adv}})], \qquad F^{\text{full(diss)}}_{\alpha l\pm} \equiv \frac{1}{2}[F^{\text{full}}_{\alpha l\pm}(\Phi_{\text{ret}}) - F^{\text{full}}_{\alpha l\pm}(\Phi_{\text{adv}})] \ . \tag{5.84}$$

In the frequency domain, constructing the advanced field is straightforward. One simply reverses the boundary conditions so that radiation is ingoing at infinity and outgoing at the horizon. Often in TD calculations boundary conditions are not imposed at the edges of the numerical domain, so extracting the advanced field is not as straightforward as in the FD, though techniques do exist [92]. In both domains though using the above method to compute the conservative and dissipative components effectively doubles the computation cost. Fortunately, by considering the symmetries of the orbit it turns out to be possible to decompose the field into conservative and dissipative pieces with only knowledge of the retarded field [76].

The relevant symmetries for bound orbits about a Kerr black hole were first noted in this setting by Mino [57]. These symmetries imply that for circular (possibly inclined) and equatorial (possibly eccentric) orbits about a Kerr black hole the following relation holds [76]:

$$F^{\text{adv}}_{\alpha}(\tau) = \epsilon_{(\alpha)} F^{\text{ret}}_{\alpha}(-\tau) \ , \tag{5.85}$$

where $\epsilon_{(\alpha)} = (-1, 1, 1, -1)$ in Boyer-Lindquist coordinates and we have assumed, without loss of generality, that periastron passage occurs at $\tau = 0$. This relation can be used to re-express equations (5.80) as

$$F^{\text{cons}}_{\alpha}(\tau) = \frac{1}{2}[F^{\text{ret}}_{\alpha}(\tau) + \epsilon_{(\alpha)} F^{\text{ret}}_{\alpha}(-\tau)], \qquad F^{\text{diss}}_{\alpha}(\tau) = \frac{1}{2}[F^{\text{ret}}_{\alpha}(\tau) - \epsilon_{(\alpha)} F^{\text{ret}}_{\alpha}(-\tau)] \ . \tag{5.86}$$

The above formulae allow for the calculation of the conservative and dissipative components of the SF for circular and also equatorial orbits about a Kerr black hole with only knowledge of the retarded SF. For inclined eccentric orbits, the symmetry relation (5.85) does not hold. For these orbits explicit calculation of the advanced field, and use of the standard method outlined above may be required to extract the conservative and dissipative components of the SF.

Chapter 6

Scalar-field self-force in Kerr spacetime: circular orbits

In this chapter we detail the calculation of the SSF for circular (equatorial or inclined) geodesic orbits about a Kerr black hole. For each orbit we calculate the dissipative and conservative components of the SSF. In the case of circular, equatorial orbits we find that the spin of the black hole can have a pronounced effect on the conservative component of the SSF, causing its sign to differ from that of Schwarzschild orbits for a large portion of the (a, r_0) parameter space. For circular, equatorial orbits we also produce a PN-like fit for the conservative component of the SSF for large radii and show that the addition of a single spin-orbit coupling term to the previous analytically calculated Schwarzschild PN formula [165] results in a good fit of our Kerr data (see Sec. 6.2.4). The work here presented on circular, equatorial orbits has been published [97], and since publication the results have been replicated by other researchers [98, 107]. For inclined circular orbits we include some preliminary results in Sec. 6.3 (these results have not yet been published).

For all the orbits considered we have performed two tests upon the validity of the results: the high l asymptotics of the contribution to the SSF, and the energy and angular momentum flux balances described in Secs. 6.2.1 and 6.2.2 respectively. We further test the results of our code by setting the black hole spin to zero and comparing our results with SSF results for orbits about a Schwarzschild black hole previously published in the literature [87, 88].

6.1 Numerical implementation

In the following subsections we detail the numerical calculation of the SSF for circular orbits. We provide details of the construction of the numerical boundary conditions in Sec. 6.1.1 and the construction of the inhomogeneous fields in Sec. 6.1.2. We then provide a prescriptive algorithm for computing the SSF in Sec. 6.1.3 and also discuss how to estimate the contribution from the uncomputed high l-modes (Sec. 6.1.4).

6.1.1 Numerical boundary conditions

The main numerical task is to solve the inhomogeneous radial equation (4.16) with the correct physical boundary conditions described by Eqs. (4.22) and (4.24). Formally these boundaries are placed at spatial infinity and the event horizon. Practically we must place boundary conditions on the edge of our truncated numerical domain which extends from $r_* = r_{*\text{in}} \ll -M$ out to $r_* = r_{*\text{out}} \gg M$ (how the location of these boundaries are chosen in practice will be discussed in the Algorithm section below). In constructing boundary conditions at the edges of our numerical domain we assume that the radial field $\psi_{\hat{l}m}$ admits an asymptotic expansion in $1/r$ at $r \to \infty$ and an asymptotic expansion in $r - r_+$ at $r \to r_+$. Recalling the leading-order behavior of the physical solutions, expressed in Eqs. (4.22) and (4.24), we thus write

$$\psi_{\hat{l}m}(r_{\text{out}}) = e^{+i\omega r_{*\text{out}}} \sum_{k=0}^{\bar{k}_{\text{out}}} c_k^\infty r_{\text{out}}^{-k} , \tag{6.1}$$

$$\psi_{\hat{l}m}(r_{\text{in}}) = e^{-i\gamma r_{*\text{in}}} \sum_{k=0}^{\bar{k}_{\text{in}}} c_k^{eh} (r_{\text{in}} - r_+)^k , \tag{6.2}$$

where $r_{\text{in}} = r(r_{*\text{in}})$, $r_{\text{out}} = r(r_{*\text{out}})$ and the truncation parameters $\bar{k}_{\text{in,out}}$ are chosen such that the boundary conditions reach a prescribed accuracy (see discussion below). The expansion coefficients are determined by substituting each of the above series into the radial equation. This gives recursion relations for the coefficients $c_{k>0}^{\infty,eh}$ respectively in terms of $c_0^{\infty,eh}$. These relations are rather unwieldy so we relegate their explicit forms to Appendix H. Though we have not made it explicit in Eq. (6.1), we remark that the outer boundary series is formally an expansion in $(\omega r_{\text{out}})^{-1}$ and thus when constructing the outer boundary condition it is important to that the outer boundary is placed so that $\omega r_{\text{out}} \gg 1$ in order to ensure convergence of the series.

Note, although we have constructed the boundary conditions here in the context of circular orbits they do in fact apply to all orbit types; the boundary conditions only depend on the particular orbit being considered through the mode frequency ω.

6.1.2 Junction conditions for circular orbits

The homogeneous solutions to the radial equation (4.16), obtained with the above boundary conditions (6.1) and (6.2), are proportional to the constants c_0^∞ and c_0^{eh} respectively. These constants are determined by imposing suitable matching conditions at the location of the particle. For circular orbits the inhomogeneous solutions can be written in the form

$$\psi_{\hat{l}m}(r) = \psi_{\hat{l}m}^-(r)\Theta(r_0 - r) + \psi_{\hat{l}m}^+(r)\Theta(r - r_0) , \tag{6.3}$$

where $\Theta(x)$ is the Heaviside step function. Substituting this into the radial equation (4.16) and comparing the coefficients of the delta function and its derivative we find

$$\left.(\psi_{\hat{l}m}^+ - \psi_{\hat{l}m}^-)\right|_{r_0} = 0 , \tag{6.4}$$

$$\left.(\psi_{\hat{l}m}^{+\,\prime} - \psi_{\hat{l}m}^{-\,\prime})\right|_{r_0} = -\frac{4\pi q}{r_0 T_\theta} \int_0^{T_\theta} \frac{S_{\hat{l}m}(\theta_p(t); -a^2\omega^2)}{u^t(\theta_p(t))} \cos(\omega t - m\varphi(t))\, dt \equiv \alpha_{\hat{l}m} , \tag{6.5}$$

where a prime denotes differentiation with respect to r_*. The first equation tells us that the $\hat{l}m$ contribution to the field is continuous at the particle, whilst the second describes the nature of the discontinuity in the radial derivative of each $\hat{l}m$ mode as a consequence of the delta-function source. For circular, equatorial orbits Eq. (6.5) becomes

$$\left(\psi^{+\,\prime}_{\hat{l}m}-\psi^{-\,\prime}_{\hat{l}m}\right)\Big|_{r_0}=-\frac{4\pi q}{u^t r_0}S_{\hat{l}m}(\pi/2,-a^2\omega^2)\equiv\alpha_{\hat{l}m}\ ,\qquad\text{circular equatorial}\ ,\tag{6.6}$$

In order to determine the correct values of c_0^{∞} and c_0^{eh}, for which the conditions (6.4) and (6.5) are satisfied, we first numerically solve the radial equation (i) starting from the boundary $r_{*\text{out}}$ with $c_0^{\infty}=1$ and integrating inward, and (ii) starting from the boundary $r_{*\text{in}}$ with $c_0^{eh}=1$ and integrating outward. We denote the two corresponding homogeneous solutions by $\tilde{\psi}^{+}_{\hat{l}m}(r)$ and $\tilde{\psi}^{-}_{\hat{l}m}(r)$ respectively, so

$$\psi^{+}_{\hat{l}m}=c_0^{\infty}\tilde{\psi}^{+}_{\hat{l}m}\quad\text{and}\quad\psi^{-}_{\hat{l}m}=c_0^{eh}\tilde{\psi}^{-}_{\hat{l}m}.\tag{6.7}$$

where $\alpha_{\hat{l}m}$ is defined in Eq. (6.5). Substituting these relations in Eqs. (6.4) and (6.5) gives two algebraic equations for c_0^{∞} and c_0^{eh}, whose solutions read

$$c_0^{eh}=\alpha_{\hat{l}m}\left[\frac{\tilde{\psi}^{+}_{\hat{l}m}(r_0)}{\tilde{\psi}^{-}_{\hat{l}m}(r_0)\tilde{\psi}^{+\,\prime}_{\hat{l}m}(r_0)-\tilde{\psi}^{+}_{\hat{l}m}(r_0)\tilde{\psi}^{-\,\prime}_{\hat{l}m}(r_0)}\right]\ ,\tag{6.8}$$

$$c_0^{\infty}=c_0^{eh}\frac{\tilde{\psi}^{-}_{\hat{l}m}(r_0)}{\tilde{\psi}^{+}_{\hat{l}m}(r_0)}\ .\tag{6.9}$$

where $\alpha_{\hat{l}m}$ is as defined in Eq. (6.5). Once the coefficients $c_0^{\infty,eh}$ have been determined, the physical solution is constructed using Eqs. (6.3) and (6.7).

In the case of circular equatorial orbits, axially-symmetric (static) modes (i.e., ones with $m=0$) have vanishing spheroidicity and $\lambda_{\hat{l},m=0}=\hat{l}(\hat{l}+1)$. For these modes the radial equation (4.16) admits a simple analytic solution given by

$$\psi_{\hat{l},m=0}=\begin{cases}\tilde{\alpha}_{\hat{l}}rQ_{\hat{l}}(x_0)P_{\hat{l}}(x)\ , & r\le r_0\ ,\\ \tilde{\alpha}_{\hat{l}}rP_{\hat{l}}(x_0)Q_{\hat{l}}(x)\ , & r\ge r_0\ ,\end{cases}\tag{6.10}$$

where

$$x\equiv\beta(r-M)\quad\text{and}\qquad\beta\equiv\sqrt{\frac{M^2+a^2}{M^4-a^4}}\ ,\tag{6.11}$$

with $x_0\equiv x(r_0)$, and $P_{\hat{l}}$ and $Q_{\hat{l}}$ being the Legendre polynomials of the first and second kind respectively. The coefficient $\alpha_{\hat{l}}$ is derived from the jump condition in the derivative of the field at the location of the particle and is given explicitly by

$$\tilde{\alpha}_{\hat{l}}=\frac{-4\pi q(u^t\beta\Delta_0)^{-1}S_{\hat{l}0}(\pi/2;0)}{Q'_{\hat{l}}(x_0)P_{\hat{l}}(x_0)-P'_{\hat{l}}(x_0)Q_{\hat{l}}(x_0)}\ ,\tag{6.12}$$

$$=\frac{-4\pi q(u^t\beta\Delta_0)^{-1}S_{\hat{l}0}(\pi/2;0)(x_0^2-1)}{(l+1)[P_{\hat{l}}(x_0)Q_{\hat{l}+1}(x_0)-P_{\hat{l}+1}(x_0)Q_{\hat{l}}(x_0)]}\ ,\tag{6.13}$$

where a prime denotes differentiation with respect to x.

6.1.3 Algorithm

In this section we provide a summary of the numerical procedure we implement for constructing the SSF for circular, equatorial orbits. We outline the major steps in the calculation and give some details about the numerical method and the choice of numerical parameters.

- Fix a black hole spin a and orbit radius r_0, and then calculate: the orbital parameters $\mathcal{E}, \mathcal{L}$ and Ω_φ [Eqs. (2.42), (2.43) and (2.44))], the spherical harmonic decomposition coefficients $b^l_{\hat{l}m}$ and the spheroidal harmonic eigenvalues $\lambda_{\hat{l}m}$ (see Appendix B) for all $\hat{l}$ and m in the range $0 \leq \hat{l} \leq \hat{l}_{\max}$, $0 \leq m \leq \hat{l}$. In this work we typically take $\hat{l}_{\max} = 55$, which is sufficient for calculating all spherical harmonic contributions $F^{(\text{full})\text{l}}_{\alpha\pm}$ up to $l \sim 50$ in most cases; see below. (The estimation of the contribution to the mode-sum from the remaining large-l tail will be discussed in the next subsection.)

- For each $\hat{l}$ mode obtain the axially-symmetric (static) mode of the radial variable, $\psi_{\hat{l},m=0}$, via Eq. (6.10).

- For the radiating ($m \neq 0$) modes, obtain the boundary conditions for the radial variable using Eqs. (6.1) and (6.2), setting $c_k^{\infty,eh} = 1$. Through experimentation we found it practical to set the inner boundary at $r_{*\text{in}} = -60M$. The location of the outer boundary depends upon mode frequency as, in order for Eq. (6.1) to converge, we require that $\omega r_{\text{out}} \gg 1$. Though experimentation we find that setting $r_{*\text{out}} = 10/\omega$ ensures rapid convergence of the series for all modes. We chose $\bar{k}_{\text{in,out}}$ such that the magnitude of the $\bar{k}_{\text{in,out}} + 1$ term drops below a certain threshold, which we set to 10^{-14}.

- For the radiating ($m \neq 0$) modes, integrate the homogeneous part of the radial equation (4.16) numerically to obtain $\tilde{\psi}^{\pm}_{\hat{l}m}(r)$. For this we used the standard Runge–Kutta Prince–Dormand (8,9) method from the GNU Scientific Library (GSL) [166]. The GSL Runge-Kutta routine allows us to set a global fractional accuracy target of 10^{-12}, and, as a test of our integrator we used it to solve for a few $m = 0$ modes and compared them with the known analytic solution (6.10). We made further use of the GSL library to calculate many of the special functions (Legendre polynomials, elliptic integrals, Clebsch-Gordan coefficients, etc) that our code requires.

- Given the numerical solutions $\tilde{\psi}^{\pm}_{\hat{l}m}$, determine the matching coefficients $c_0^{\infty,eh}$ via Eqs. (6.8) and (6.9), and construct the inhomogeneous solutions $\psi_{\hat{l}m}$ using Eqs. (6.7) and (6.3). Record the values of $\psi_{\hat{l}m}$ and its (one-sided) r and t derivatives at the radius of the particle.

- Given $\psi_{\hat{l}m}(r_0)$ and $\nabla_{\alpha\pm}\psi_{\hat{l}m}(r_0)$ for all spheroidal $\hat{l}m$ modes up to $\hat{l}_{\max}$, use Eq. (5.61) to construct the spherical-harmonic l modes of the full force at the location of the particle, $F^{(\text{full})\text{l}}_{\alpha\pm}$. This procedure allows us to obtain all l-modes which do not have significant contributions (through coupling) from the uncalculated modes $\hat{l} > \hat{l}_{\max}$. The highest such l mode, denoted $l_{\max}$, is determined by calculating the contributions from the $\hat{l}_{\max} + 1$ spheroidal mode to the various l-modes $F^{(\text{full})\text{l}}_{\alpha\pm}$, and identifying the highest value of l for which this contribution falls below a given threshold, set here to 10^{-12} (fractionally). With $\hat{l}_{\max} = 55$ we find $l_{\max} \geq 44$ for all a, r_0 within the parameter range considered in this work (lower values of $l_{\max}$ for larger $|a|$ and smaller r_0, with typical values around $l_{\max} \sim 50$) — See Fig. 6.1.

- In the final step, calculate the regularized modes $F^{l(\text{reg})}_{\alpha}$ defined in Eq. (5.42) using the regularization parameters given in Appendix G. Then sum over l modes to obtain the SSF. Formally, the mode-sum formula (5.42) requires summation over all l modes from $l = 0$ to

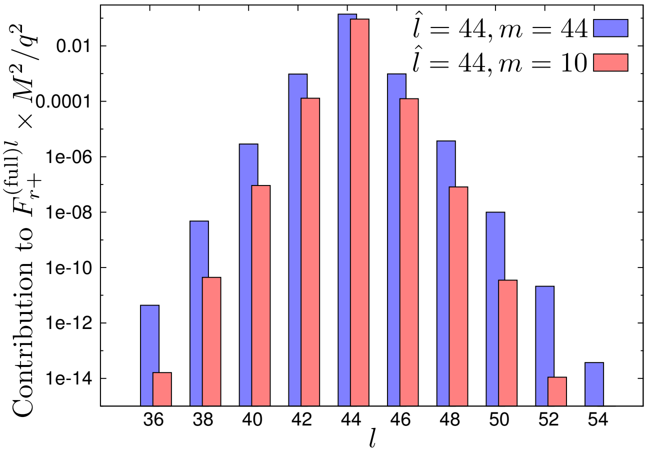

FIGURE 6.1: Coupling of spheroidal and spherical modes of the SSF, illustrated here for $a = 0.9M$ and $r_0 = 4M$. We show the contributions from a given $\hat{l}$-mode $F_{r+}^{(\text{full})l}$. This figure demonstrates that for practical SF calculations one only needs to calculate a handful more spheroidal $\hat{l}$ modes than the desired maximum spherical l mode, especially as for smaller a and/or larger r_0 the coupling is weaker than in this example.

$l = \infty$. In practice, of course, this is neither possible nor necessary. As the t component does not require regularization the mode sum converges exponentially fast, and we typically find that the contribution from the modes with $l \gtrsim 15$ can be neglected. For the radial component, as the mode sum converges only as $\sim 1/l$ in this case, artificially truncating the series at $l \sim 50$ may potentially result in an error of as much as a few tens of percent in the final SSF. It is therefore important to estimate the contribution from the $l > l_{\max}$ tail of the mode sum. The method we used for this estimation follows that of Barack and Sago [62], and for completeness we review it in the next subsection.

For circular, inclined orbits the algorithm to compute the SSF is very similar to the one given, but with the additional step of summing over k modes in order to construct each m mode.

6.1.4 Estimation of the high-l tail contribution

As discussed in Sec. 5.4, for components of the SF that require regularization the regularized l-modes (5.42) exhibit power law drop off with l, with the exponent of the the power law depending on the number of regularization parameters employed. When only making use of the Barack-Ori regularization parameters (i.e., $A_\alpha, B_\alpha, C_\alpha, D_\alpha$) the convergence of the mode sum is expected to go as l^{-1}. With the addition of each extra regularization parameter the convergence rates improves by a further factor of l^{-2}. This slow power law convergence with l necessitates estimating the uncomputed contribution to the total SF. Our technique for doing this follows Ref. [155] whereby, after regularization with all the known regularization parameters, we numerically fit for the higher order regularization parameters and then use these to estimate the contribution from the uncomputed modes. We detail this technique now.

We begin by reminding that not all components of the SSF (depending on the orbit type) require regularization. The convergence of those components that do not require regularization is expected to be exponential and thus it is possible to compute them accurately from the first ten or so l modes. For the components of the SSF that do require regularization we write the total component of the SSF as a sum of two pieces, a numerically computed piece, and a large-l

tail:

$$F_\alpha^{\rm self} = F_\alpha^{l\leq l_{\rm max}} + F_\alpha^{l>l_{\rm max}}\ , \tag{6.14}$$

where

$$F_\alpha^{l\leq l_{\rm max}} \equiv \sum_{l=0}^{l_{\rm max}} F_\alpha^{l({\rm reg})} \qquad \text{and} \qquad F_\alpha^{l>l_{\rm max}} \equiv \sum_{l=l_{\rm max}+1}^{\infty} F_\alpha^{l({\rm reg})}\ . \tag{6.15}$$

with

$$F_\alpha^{l({\rm reg})} = F_\alpha^{l({\rm full})} - A_\alpha L - B_\alpha - \sum_{n=0}^{\hat{n}} D_{\alpha,2n}\left[\prod_{k=0}^{n}(2L-2k)(2L+2k)\right]^{-1}\ , \tag{6.16}$$

where, recall, $L = l + 1/2$ and we have defined $D_{\alpha,0} \equiv 0$. In this notation $\hat{n}$ denotes the index of the maximum higher order regularization parameter used to regularize the SSF (so if only the Barack-Ori regularization parameters are used we have $\hat{n} = 0$). The large-l contribution $F^\alpha_{l>l_{\rm max}}$ can be computed by extrapolating the last $\bar{n}$ numerically calculated l-modes. In order to achieve this we first fit these modes to a formula based on the known large-l behaviour of the mode sum whereby, for large l, the contribution to the regularized force takes the form[1]

$$F_\alpha^{l({\rm reg})} \simeq \sum_{n=\hat{n}+1}^{N} \frac{D_{\alpha,2n}}{L^{2n}}\ . \tag{6.17}$$

In our code we then use a standard least-squares algorithm from the GSL [166] to fit for the $D_{\alpha,2n}$ coefficients using our numerical data for l-modes with $l_{\rm max} - \bar{n} \leq l \leq l_{\rm max}$. How we chose the $\bar{n}$ and N parameters in practice is discussed below. Given the (numerically fitted) regularization parameters $D_{\alpha,2n}$, we then estimate the high-l contribution using the formula

$$F_\alpha^{l>l_{\rm max}} \simeq \sum_{n=\hat{n}+1}^{N} D_{\alpha,2n} \sum_{l=l_{\rm max}+1}^{\infty} L^{-2n} = \sum_{n=\hat{n}+1}^{N} \frac{D_{\alpha,2n}}{(2n-1)!}\Psi_{2n-1}(l_{\rm max}+3/2)\ , \tag{6.18}$$

where $\Psi_n(x)$ is the polygamma function of order n defined as

$$\Psi_n(x) = \frac{d^{n+1}[\log\Gamma(x)]}{dx^{n+1}}\ , \tag{6.19}$$

with $\Gamma(x)$ being the standard gamma function.

Practical use of this estimation method requires some experimentation. For a given $\hat{n}$ (which depends on the number of known regularization parameters) and $N \in \{3,4,5\}$ we considered a weighted average of the values obtained for $F_\alpha^{\rm self}$ as we vary $\bar{n}$ from 20 to 35, where the weighting for each term is given by the square of the inverse of the fractional difference in the value of $F_\alpha^{\rm self}$ as we increase $\bar{n}$ by one (this procedure aims to bias the average in favour of $\bar{n}$ values for which $F_\alpha^{\rm self}$ depends only weakly on the number of fitting modes). We obtain three different average values corresponding to $N = 3, 4, 5$, and use the variance of these values to estimate our numerical accuracy (we record as significant figures only those that remain fixed as we vary N). This error dominates the overall error budget of the SSF, and we hence use it to estimate the over all accuracy of our SSF results.

---

[1] We could have also taken the fitting formula to have the form for the higher order regularization parameters, i.e., the form of Eq. (5.44). This would have the advantage that the sum from $l_{\rm max}+1$ to infinity of Eq. (5.44) has a simple form. We have not chosen this route though as in estimating the high-l tail we have followed Ref. [62].

It should be noted that the relative contribution from the large l tail is particularly important in SSF calculations (as compared with the GSF case) as the contribution from the first few l modes turns out to be relatively large and opposite in sign with respect to that of the higher modes. In the Schwarzschild case, the contributions from the $l = 0, 1$ modes are both negative and conspire to nearly cancel out the combined contributions from $l = 3$–6. In the Kerr case this cancellation sometimes involves an even greater number of modes (particularly near a, r_0 values for which the radial SSF vanishes—see below). This behavior is not observed in the Lorenz gauge gravitational case [62].

6.2 Code validation and results: circular, equatorial orbits

We now present some sample results from our code for the case of circular, equatorial orbits about a Kerr black hole. When this work was undertaken only the Barack-Ori regularization parameters were known and unless otherwise stated it should be assumed that the results presented make use of just these regularization parameters.

6.2.1 High-l behavior

For circular, equatorial orbits only the radial component of the self force requires regularization and, as discussed in Sec. 5.4, we expect that regularized modes $F_r^{l(\mathrm{reg})}$ in the mode-sum formula (5.42) should drop off as $\sim 1/l^2$ for large l. This behavior relies sensitively on the delicate cancellation of as many as three leading terms in the $1/l$ expansion of the full modes $F_{r\pm}^{(\mathrm{full})l}$ and thus provides an excellent test of validity for our numerical results. In our numerical data we have indeed confirmed a clear $\sim 1/l^2$ behavior—an example is presented in Fig. 6.2. Similarly for the time component, which requires no regularization, we know from Sec. 5.4 that the regularized contributions $F_t^{l(\mathrm{reg})}$ drops off exponentially with l, and again we observe this behavior in our numerical results—see again Fig. 6.2 for an illustration. The above two tests provide us with confidence that the high-$\hat{l}$ spheroidal contributions are calculated correctly, and that the spherical-harmonic decomposition procedure is implemented properly. These tests also confirm, for the first time, the validity of the regularization parameters in the Kerr case (for circular equatorial orbits).

With the addition of higher order regularization parameters the convergence of $F_r^{l(\mathrm{reg})}$ improves. In Fig. 6.3 we show, for a sample orbit in Schwarzschild spacetime, the effect of employing the extra regularization parameters recently derived by Heffernan *et al.* [159].

6.2.2 Energy and angular momentum flux in the scalar waves

The validity test presented above examines only the high-l output of our code. In this section we present a complimentary and more quantitative test which probes primarily the lower-l portion of the mode sum. From global energy conservation we know that the work done by the dissipative piece (here the t and φ components) of the SSF must be balanced by the flux of energy and angular momentum carried away in scalar-field radiation. We can use our code to compute the fluxes radiated to infinity and down through the black hole's event horizon, and then check that the result is consistent with the value of the local dissipative SSF. Following from Eq. (4.33) it can be seen that for circular equatorial orbits, where $\omega = m\Omega_\varphi$, the total radiated energy $\dot{E}_{\mathrm{total}}$

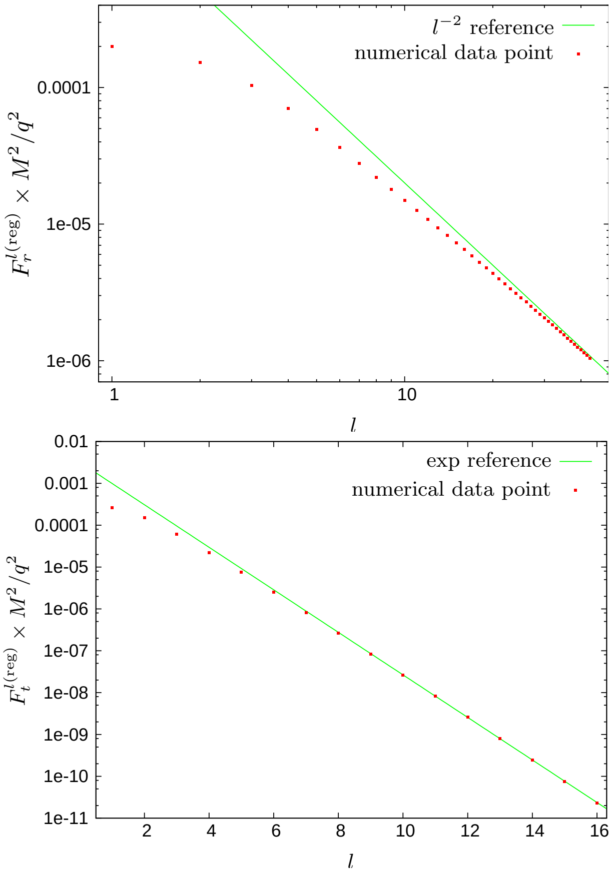

FIGURE 6.2: (Upper panel) The regularized modes $F_r^{l(\mathrm{reg})}$ as a function of l for $r_0 = 5M$ and $a = 0.5M$. The solid reference line is $\propto 1/l^2$. The regularized modes demonstrate an asymptotic $\propto 1/l^2$ behavior at large l, as expected from theory (note the log-log scale). (Lower panel) The regularized modes $F_t^{l(\mathrm{reg})}$ as a function of l for $r_0 = 5M$ and $a = 0.8M$. The solid reference line is exponentially decreasing with l. The regularized modes of the t component show a clear exponential decay at large l, as predicted by mode sum theory (note the semi-log scale). Similar behavior is observed for other values of r_0 and a.

and angular momentum $\dot{L}_{\mathrm{total}}$ are related by

$$\dot{E} = \Omega_\varphi \dot{L} \; . \tag{6.20}$$

Consequently, we need only consider either the radiated energy or angular momentum. In this work we examine the fluxes of energy that must be balanced by the t component of the SSF. For circular, equatorial orbits the t component of the SSF does not require regularization [recall Eqs. (5.48) and (5.50) with $\dot{r} = 0$] and hence the mode-sum converges exponentially fast. For this reason, the energy-balance test presented in this section is mostly sensitive to the low-l portion of the mode-sum.

In Table 6.1 we display numerical values for the total energy flux, $\dot{E}_{\mathrm{total}} \equiv \dot{E}_{+} + \dot{E}_{-}$, as computed using our code based on Eqs. (6.20). For a similar orbital setup, Gralla *et al.* [167] previously calculated the total flux of scalar-field *angular momentum*, $\dot{L}_{\mathrm{total}}$. Using Eq. (4.33) we can compare our results for the energy flux with the results presented in Ref. [167] for angular momentum flux. The data in Table 6.1 shows good agreement between our fluxes and those of Gralla *et al.*, with relative differences comparable in magnitude to the estimated relative numerical error in their data.

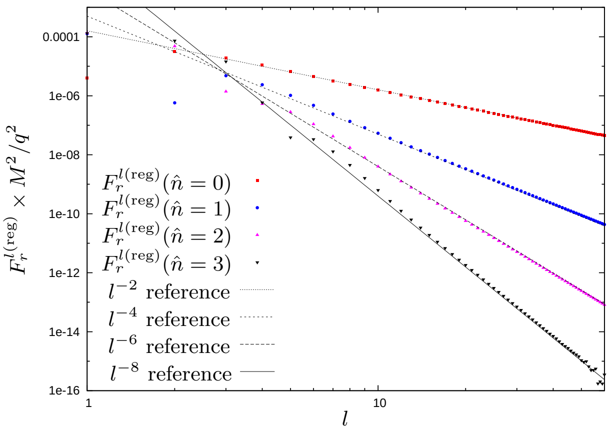

FIGURE 6.3: The effect of additional regularization parameters on the regularized $F_r^{l(\mathrm{reg})}$ modes for an example orbit in Schwarzschild spacetime ($a = 0$) with orbital radius $r_0 = 10M$. With the addition of each of the post Barack-Ori regularization parameters derived by Heffernan *et al.* [159] the convergence rate of the mode-sum can be clearly seen to increase by l^{-2} as predicted by mode-sum theory (see Sec. 5.4). In this graph we have used $F_r^{l(\mathrm{reg})}$ as defined in Eq. (6.16). In this notation $\hat{n} = 0$ implies that the force was regularized using only the Barack-Ori regularization parameters. When using the next three regularization parameters ($\hat{n} = 3$) 60 l modes are sufficient to compute the entire radial component of the SF to machine accuracy, removing the need to calculate the high l tail contribution as outlined in Sec. 6.1.4.

Table 6.1 also displays numerical results for the horizon flux, $\dot{E}_-$, expressed as a fraction of $\dot{E}_{\mathrm{total}}$. Recall from Sec. 4.4 that superradiance ($\dot{E}_- < 0$) is manifest whenever $\Omega_+ > \Omega_\varphi$. Horizon absorption does not normally exceed $\sim 10\%$ even for strong-field orbits (a similar observation was made by Hughes [117] in the gravitational case), but prograde orbits around a rapidly rotating hole can display extreme superradiance behavior [nearly 25% negative absorption in the example of $(a, r_0) = (0.998M, 2M)$]. The graph in Fig. 6.4 displays further horizon absorption data.

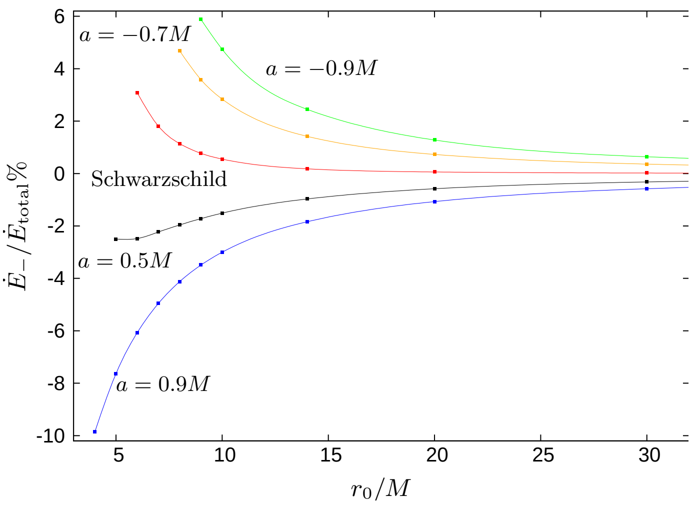

FIGURE 6.4: The horizon flux of scalar-field energy, $\dot{E}_-$, as a percentage of the total flux for different orbital radii r_0 and spin parameters a. The curves are interpolations based on the numerical data points shown. Superradiance behavior ($\dot{E}_- < 0$) is manifest whenever the horizon's angular velocity Ω_+ is greater than that of the particle.

a/M	r_0/M	$q^{-2}\dot{E}_{\rm total}$	$\dot{E}_-/\dot{E}_{\rm total}$	$1-\dot{E}_{\rm total}/\dot{E}^{\rm GFW}_{\rm total}$	$1-\dot{E}_{\rm total}/\dot{\mathcal{E}}$
0.998	2	$4.3975979e-3$	-0.2486	$7.06e-7$	$-4.7e-10$
	4	$6.65618888e-4$	-0.1168	$2.12e-7$	$-1.6e-10$
	6	$1.69712483e-4$	-0.0692	$1.12e-6$	$-9.2e-11$
	8	$6.04494314e-5$	-0.0464	$-2.12e-6$	$-4.6e-11$
	10	$2.64845608e-5$	-0.0337	$6.65e-8$	$-3.7e-11$
	20	$1.87388789e-6$	-0.0120		$-2.8e-12$
	40	$1.23796212e-7$	-0.0041		$7.7-11$
0.5	6	$2.02918608e-4$	-0.0248	$-5.19e-7$	$-8.9e-11$
	8	$6.76202950e-5$	-0.0196	$-1.76e-6$	$-6.8e-11$
	10	$2.86637838e-5$	-0.0151	$7.33e-7$	$-3.3e-11$
	20	$1.92605066e-6$	-0.0058		$-1.0e-12$
	40	$1.24998716e-7$	-0.0021		$-3.5e-11$
0.0	6	$2.55199967e-4$	0.0308		$-9.2e-11$
	8	$7.72547978e-5$	0.0114	$1.98e-6$	$-6.2e-11$
	10	$3.13766525e-5$	0.0054	$1.28e-7$	$-4.1e-11$
	20	$1.98366995e-6$	0.0006		$-4.6e-12$
	40	$1.26226716e-7$	0.0001		$4.2e-11$
-0.5	8	$9.02315446e-5$	0.0468	$-5.01e-7$	$-4.9e-11$
	10	$3.47579647e-5$	0.0284	$5.20e-6$	$-4.6e-11$
	20	$2.04718763e-6$	0.0073		$3.4e-12$
	40	$1.27600490e-7$	0.0022		$5.2e-11$
-0.998	9	$6.22560292e-5$	0.0644	$-7.86e-7$	$-5.0e-11$
	10	$3.88839360e-5$	0.0519	$-1.56-6$	$-4.2e-11$
	20	$2.11643277e-6$	0.0142		$2.2e-11$
	40	$1.28992555e-7$	0.0044		$-6.1e-11$

TABLE 6.1: Scalar-field energy flux for various values of the spin parameter a and orbital radius r_0. The 3rd column displays the total flux of energy radiated to infinity and down the black hole, as extracted from our numerical solutions. The 4th column presents the fraction of the total power absorbed by the black hole, with negative values indicating superradiance. The 5th column compares our fluxes to those obtained by Gralla, Friedman and Wiseman (GFW) [167], showing a good agreement. (GFW provide results for the radiated angular momentum, which we convert here to radiated energy using the relation $\dot{E}_{\rm total} = \Omega_\varphi \dot{L}_{\rm total}$; their results are given with 6 significant figures.) In the last column we test our SSF results (for the dissipative component) against the balance relation (6.22) as discussed in Sec. 6.2.3; $\dot{\mathcal{E}}(<0)$ is the rate at which the particle's scalar energy is dissipated, as computed from the local SSF using Eq. (6.21). In this Table (and all subsequent Tables in this chapter) we use an exponential notation whereby (e.g.) 'e−3' stands for $\times 10^{-3}$. All decimal places presented are significant.

6.2.3 Dissipative component of the SSF

In the case of circular, equatorial orbits information about the dissipative effect of the SSF in contained entirely in the two components F_t and F_φ. Recall from Sec. 5.2 that for our stationary setup we have the relation $u^\alpha F_\alpha = 0$ (i.e., $d\mu/d\tau = 0$). Thus, using Eq. (5.32), we have

$$\mu\dot{\mathcal{E}} = -(u^t)^{-1}F_t, \qquad \mu\dot{\mathcal{L}} = (u^t)^{-1}F_\varphi, \tag{6.21}$$

where an overdot denotes d/dt. The relation $u^\alpha F_\alpha = 0$ further implies that in practice we need only calculate one of the two components F_t or F_φ—here we choose to calculate the former. Sample numerical data for F_t is presented in Table 6.2.

In our stationary setting, the rate at which the particle is loosing scalar energy, given by $-\mu\dot{\mathcal{E}}$, must equal the rate at which energy flows to infinity and down the black hole [i.e., no averaging is required in Eqs. (4.33)]. The total energy flowing to infinity and down though the

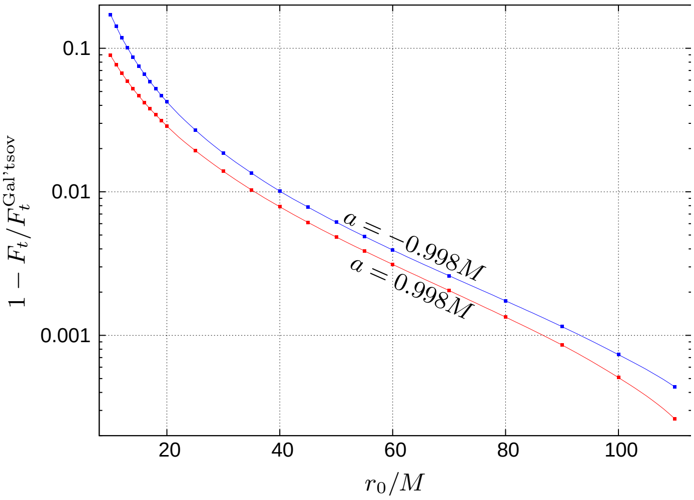

FIGURE 6.5: Time component of the SSF: comparison with Gal'tsov's slow-motion formula. Plotted is the relative difference between our "full" SSF F_t and Gal'tsov's weak-field/slow motion analytic approximation (6.23) as a function of orbital radius r_0. Solid lines are interpolations of the data points shown. We show results for $a = \pm 0.998M$; similar agreement between F_t and $F_t^{\rm Gal'tsov}$ at large r_0 is manifest for other values of a too.

event horizon we denote by $\dot{E}_{\rm total}$. Using Eq. (6.21) we can express the energy balance directly in terms of the SSF:

$$F_t = -\mu u^t \dot{\mathcal{E}} = \mu u^t \dot{E}_{\rm total} \, . \tag{6.22}$$

As discussed above, this allows us to test our computation of F_t (whose contributions are primarily from the low-l portion of the mode-sum) by verifying that our numerical results satisfy Eq. (6.22). As the data presented in the right-most column of Table 7.1 demonstrates, we do indeed find a very good agreement.

It is also interesting to compare our results with the weak-field/slow-motion analytic formula derived by Gal'tsov [168],

$$F_t^{\rm Gal'tsov} = \frac{1}{3} q^2 \Omega_\varphi \left(r_0^2 \Omega_\varphi^3 + \frac{2M^3 r_+}{r_0^4} (\Omega_\varphi - \Omega_+) \right) \, , \tag{6.23}$$

which is valid for $r_0 \gg M$. Here the first term corresponds to the radiation heading out to the infinity and the second to the radiation absorbed by the black hole. In Fig. 6.5 we plot the relative difference between our computed F^t and $F_t^{\rm Gal'tsov}$, as a function of r_0 for two near extremal values of a. As Gal'tsov's analytical formula leaves out many post-Newtonian corrections that occur between the flux at infinity and the flux at the horizon we only expect our numerical data to approach the value given by Eq. (6.23) for large orbital radii, a result we indeed observe.

Lastly, we note that our value of F_t for $(a, r_0) = (0, 6M)$ (see Table 6.2) coincides through all 9 significant figures with the value computed by Haas and Poisson in Ref. [169].

6.2.4 Conservative component of the SSF

For circular equatorial orbits the conservative effect of the SSF is entirely accounted for by its radial component, F_r. The computation of this component is more involved, as, in this case the mode-sum requires regularization, and (relatedly, see Sec. 5.4) the mode-sum series exhibits slow convergence. While results for the dissipative SSF in Kerr already exist in the literature [167], our results for F_r represent the first calculation of the conservative component of the SSF for a particle in orbit about a Kerr black hole (these results have since been replicated by Dolan, Wardell and Barack [98]).

Table 6.3 presents F_r data obtained for a range of a and r_0 values. Our results for Schwarzschild ($a = 0$) agree with those of Diaz-Rivera *et al.* [87] through all significant figures. The most striking feature of our results is that—unlike in the Schwarzschild case where the radial SSF is always repulsive (outward pointing)—here we find that for certain prograde orbits F_r becomes *attractive* (inward pointing). This behavior is better illustrated in Fig. 6.6, where we present a contour plot of F_r across the parameter space of a, r_0. A few fixed-r_0 and fixed-a cross-sections of the contour plot are presented in Fig. 6.7.

In our results we observe the following: (i) For retrograde orbits ($a < 0$) the radial SSF is always repulsive, as in the Schwarzschild case. (ii) For prograde orbits ($a > 0$) there exists an a-dependent radius, r_c, at which the radial SSF vanishes; it is repulsive for $r_0 < r_c$ and attractive for $r_0 > r_c$. (iii) The critical radius r_c *decreases* monotonically with increasing a. (iv) The critical orbit coincides with the ISCO for $a \simeq 0.461M$; hence, all stable circular geodesics experience an attractive radial SSF when $a \gtrsim 0.461M$. It is interesting to note that Burko [170] observed a similar change of sign in the radial SSF when studying accelerated (non-geodesic) circular orbits in Schwarzschild geometry.

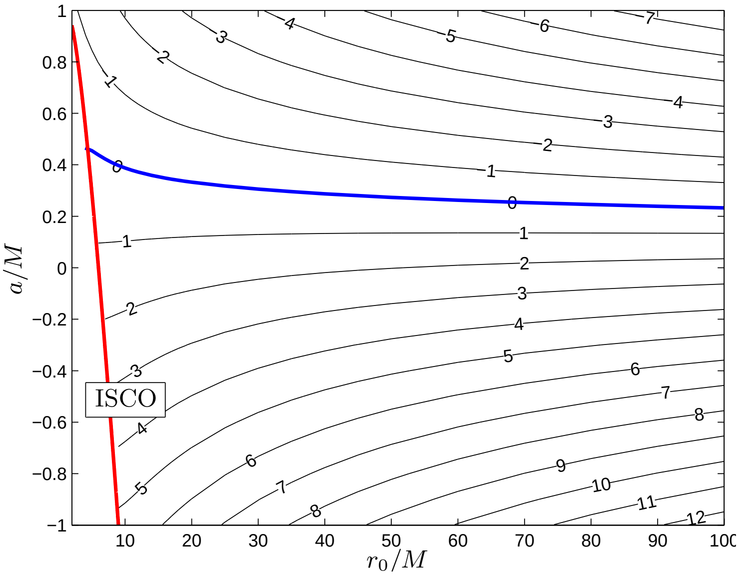

FIGURE 6.6: The radial component of the SSF, multiplied by r_0^5 for convenience, across the a, r_0 parameter space. Contour lines are lines of fixed $r_0^5 F_r$, with labels giving the value of $(M/q)^2(r_0/M)^5 F_r$. The near-vertical thick line indicates the location of the ISCO, while the near-horizontal thick line marks the curve $r_0 = r_c(a)$ along which the radial SSF vanishes. The two lines intersect at $a \simeq 0.461M$; for $a \gtrsim 0.461M$ all stable circular geodesics experience an attractive radial SSF.

It is instructive to analyze our results in weak-field as, in the Schwarzschild spacetime, a weak-field expression for the radial SSF was worked out to high PN order by Hikida *et al.* in

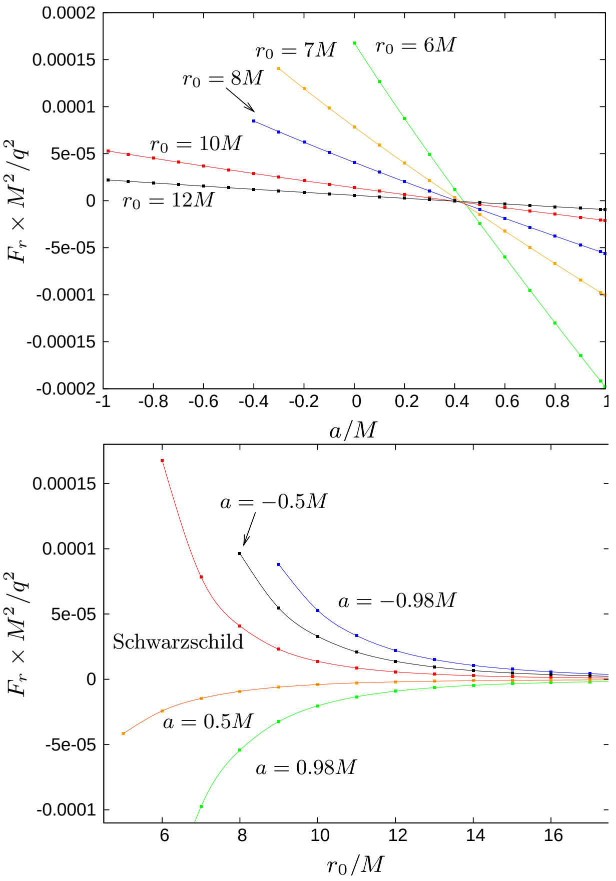

FIGURE 6.7: *Upper panel:* Radial component of the SSF as a function of a for various fixed values of the orbital radius r_0. *Lower panel:* Radial component of the SSF as a function of r_0 for various fixed values of the spin parameter a. In both panels dots represent numerical data points, and solid lines are interpolations.

Ref. [165]. Only the leading 3PN and 4PN terms are given explicitly in that work. They read[2]

$$F_r^{(a=0)}(r_0 \gg M) = \frac{q^2}{r_0^2}\left[\left(\frac{M}{r_0}\right)^3\left[p_3 + p_3^{\log}\ln(r_0/M)\right] + \left(\frac{M}{r_0}\right)^4\left[p_4 + p_4^{\log}\ln(r_0/M)\right]\right] , \quad (6.24)$$

where the p_n coefficients are given by

$$\begin{aligned} p_3 &= -\frac{4}{3}(\gamma + \ln 2) + \frac{7}{64}\pi^2 - \frac{2}{9} = -0.836551\dots , \\ p_3^{\log} &= \frac{2}{3} , \\ p_4 &= -\frac{14}{3}\gamma - \frac{66}{5}\ln 2 + \frac{29}{1024}\pi^2 + \frac{604}{45} = 1.85852\dots , \\ p_4^{\log} &= \frac{7}{3} , \end{aligned} \quad (6.25)$$

with $\gamma = 0.577215\dots$ being the Euler number. Using Eq. (6.24) as an ansatz for $a = 0$, we performed a two-dimensional fit of a large-r_0 subset of our numerical data to a model of the

---

[2] Note our definition of the scalar field differs from that of Hikida *et al.* [165] by a factor 4π, leading to a similar relative factor in the SSF.

form $F_r = F_r^{(a=0)} + a\mathcal{L}\times$ (power series in M/r_0). We find, at leading order,

$$F_r(r \gg M) = F_r^{(a=0)} + p_3^{\rm so}\frac{q^2 a\mathcal{L}}{r_0^2}\left(\frac{M}{r_0}\right)^3 , \tag{6.26}$$

with

$$p_3^{\rm so} \simeq -1.00091. \tag{6.27}$$

Our numerical accuracy was not sufficient to distinguish between different PN models at higher PN orders, so we do not present any results beyond the leading 3PN spin term. This leading term has the interpretation of a spin-orbit coupling. We are not aware of any explicit analytic calculation of this term in the PN literature (it might be possible to extract the 3PN spin-orbit term from the formal results of Ref. [171], which, however, we have not attempted here). Our numerical fit suggests that the coefficient $p_3^{\rm so}$ of the leading 3PN spin-orbit term is simply -1.

In Fig. 6.8 we plot some of our F_r numerical data points against the analytic PN model (6.26). A good agreement is manifest down to radii as small as $r_0 = 10M$ where the difference between our fitted PN formula (6.26) and our numerical results is in all cases no more than 8%. At $r_0 = 20M$ this difference is never greater than 3%.

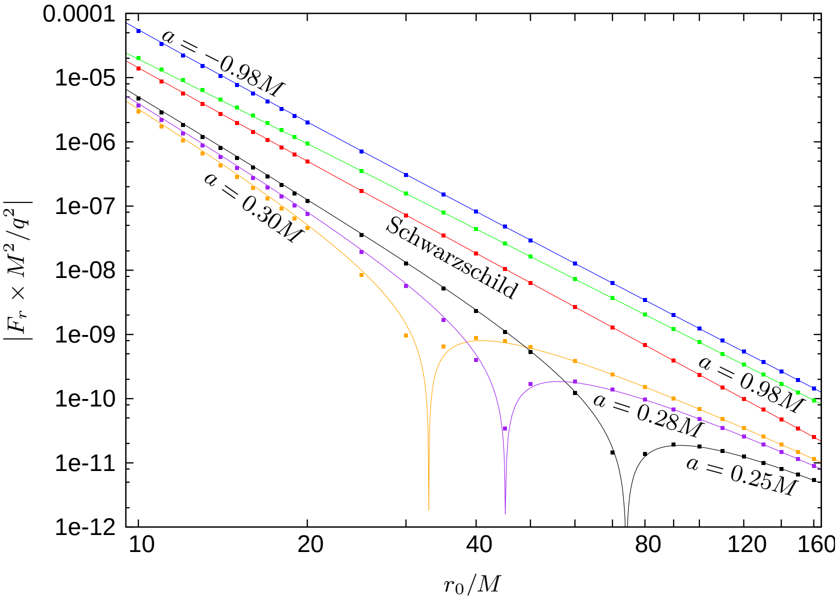

FIGURE 6.8: Comparison of numerical data for F_r (dots) with the PN fit model (6.26) (solid lines). For prograde orbits with $a \lesssim 0.461M$ the radial SSF changes sign at $r_0 = r_c(a)$; cf. figures 6.6 and 6.7.

We note that $\mathcal{L} \sim r_0^{1/2}$ for large r_0 [recall Eq. (2.43)], and hence the leading spin term in Eq. (6.26) dominates the overall behavior of F_r at sufficiently large r_0, falling off as $\sim r_0^{-4.5}$. At intermediate values of r_0, this term, which is negative for $a > 0$, competes with the leading "Schwarzschild" term, which falls of as $\sim r_0^{-5}\ln r_0$ and is positive. This competition between these two terms gives rise to the change-of-sign observed for F_r in our numerical data.

6.3 Code validation and results: circular, inclined orbits

In this section we present some preliminary results for the calculation of the SSF for circular, inclined orbits about a Kerr black hole. The calculation of the SSF for these orbits is much the same as for circular, equatorial orbits with the main extra challenges being (i) the more complicated orbital parametrization (see Sec. 2.2.3.2) and (ii) the computation of the θ integral in the junction condition [see Eq. (6.5)]. Owing to the bi-periodic nature of the mode frequency (recall for circular, inclined orbits $\omega = m\Omega_\varphi + k\Omega_\theta$) the computational burden is also much greater than for circular, equatorial orbits (as we must sum over both m and k to construct each l-mode). We find that the time taken to compute the SSF for circular, inclined orbits is typically around a few hours on a standard (3GHz, dual cored) desktop machine, with an estimated accuracy of four-five significant figures in the resulting SSF (based upon the fit error discussed in Sec. 6.1.4).

At the time of writing we have not implemented a flux balance test similar to that presented in Sec. 6.2.2 for circular, equatorial orbits, so we do not yet have a good test of the low modes of our calculation. On the other hand we have verified that the high l contributions to the SSF behave as expected (i.e. the exhibit the l^{-2} drop as of as expected from theory). In particular, the observed correct regularization of the θ-component of the SSF provides a test of our technique for using mode-sum regularization for this component presented in Sec. (5.4.2) (recall that a naïve calculation of the θ-component of the SSF leads to very strong coupling between the spheroidal harmonic $\hat{l}$-modes and the spherical harmonic l-modes). We present an example of the observed convergence of both the conservative and dissipative components of F_θ in Fig. 6.9.

In Fig. 6.10 we present sample results the SSF for an orbit setup with parameters $(a, r_0, \iota) = (0.998M, 3M, 27.5573°)$. Probably the most interesting feature of this preliminary result is the observed difference in the phasing of the various components of the SSF along the orbit. How the relative phasing between the four components is affected by the black hole spin and the orbital inclination remains to be investigated.

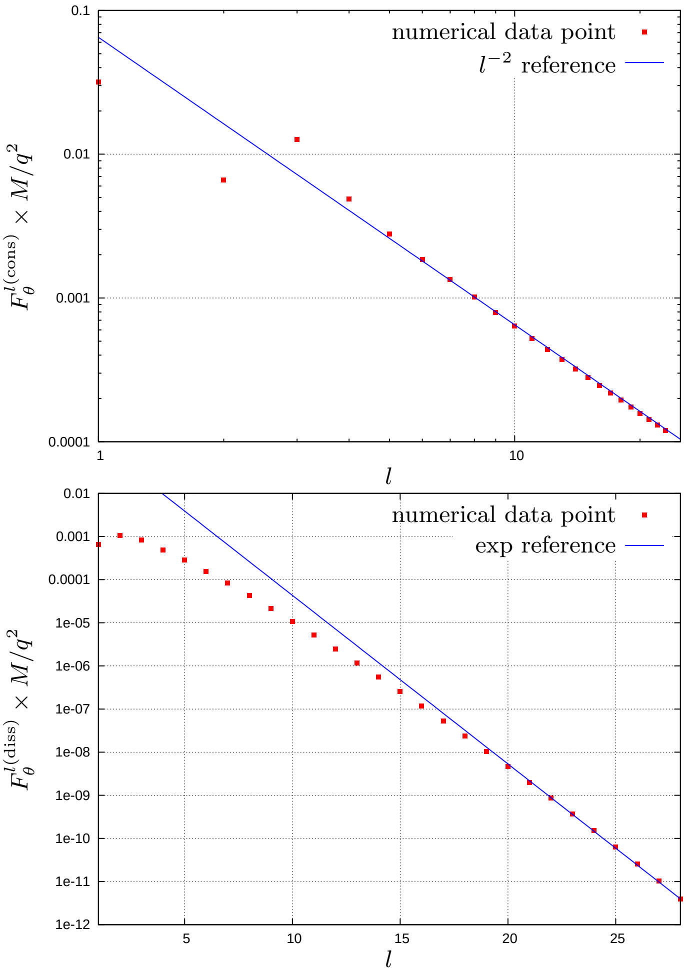

FIGURE 6.9: Convergence of $F_\theta^{l(\mathrm{cons/diss})}$ components of the SSF for a circular, inclined orbit about a black hole with $a = 0.998M$ and with orbital parameters $(r_0, \iota) = (3M, 27.5573^\circ)$ shown at $\chi = 0.816814$. The top panel depicts the contributions per l-mode to the conservative component of the F_θ alongside a l^{-2} reference line. As theory predicts, for high l-modes the drop off follows closely to the reference line. The bottom panel shows the contributions per l-mode to the dissipative component of the F_θ alongside an exponential reference line and similarly, as expected from theory, the high l mode drop off follows closely to this line. Similar convergence behavior is observed for the conservative and dissipative pieces of the other three components (F_r, F_t, F_φ) of the SSF.

	$(M^2/q^2)F_t$						
r_0/M	$a=-0.9M$	$a=-0.7M$	$a=-0.5M$	$a=0$	$a=0.5M$	$a=0.7M$	$a=0.9M$
4	-	-	-	-	-	$1.35921815e-3$	$1.14204820e-3$
5	-	-	-	-	$6.07684087e-4$	$5.35768561e-4$	$4.79634985e-4$
6	-	-	-	$3.60907254e-4$	$2.78394798e-4$	$2.55161013e-4$	$2.35733853e-4$
7	-	-	-	$1.76732019e-4$	$1.46366447e-4$	$1.37103703e-4$	$1.29046747e-4$
8	-	-	$1.15781360e-4$	$9.77204485e-5$	$8.44876316e-5$	$8.02407393e-5$	$7.64519160e-5$
10	$4.60475173e-5$	$4.38590519e-5$	$4.18429073e-5$	$3.75022727e-5$	$3.40410532e-5$	$3.28611197e-5$	$3.17760168e-5$
14	$1.03173965e-5$	$1.00539090e-5$	$9.80387438e-6$	$9.23672660e-6$	$8.74728207e-6$	$8.57077224e-6$	$8.40373578e-6$
20	$2.28457108e-6$	$2.25311511e-6$	$2.22274047e-6$	$2.15159216e-6$	$2.08709237e-6$	$2.06300902e-6$	$2.03980574e-6$
30	$4.30761267e-7$	$4.27729235e-7$	$4.24767592e-7$	$4.17678576e-7$	$4.11035602e-7$	$4.08496912e-7$	$4.06021007e-7$
50	$5.43419839e-8$	$5.41729302e-8$	$5.40064364e-8$	$5.36016621e-8$	$5.32132722e-8$	$5.30623647e-8$	$5.29138807e-8$
70	$1.40256823e-8$	$1.39999178e-8$	$1.39744575e-8$	$1.39121644e-8$	$1.38518165e-8$	$1.38282103e-8$	$1.38048982e-8$
100	$3.35072295e-9$	$3.34717963e-9$	$3.34366914e-9$	$3.33503895e-9$	$3.32661812e-9$	$3.32330755e-9$	$3.32002917e-9$

TABLE 6.2: Sample numerical results for the t component of the SSF. Entries left empty correspond to orbits below the inner-most stable circular orbit (ISCO). All figures presented are significant.

				$(M^2/q^2)F_r$			
r_0/M	$a=-0.9M$	$a=-0.7M$	$a=-0.5M$	$a=0$	$a=0.5M$	$a=0.7M$	$a=0.9M$
4	-	-	-	-	-	$-5.24194e{-4}$	$-9.5941e{-4}$
5	-	-	-	-	$-4.160235e{-5}$	$-2.044174e{-4}$	$-3.63448e{-4}$
6	-	-	-	$1.677283e{-4}$	$-2.421685e{-5}$	$-9.528095e{-5}$	$-1.645525e{-4}$
7	-	-	-	$7.850679e{-5}$	$-1.467677e{-5}$	$-4.980678e{-5}$	$-8.410331e{-5}$
8	-	-	$9.642777e{-5}$	$4.082502e{-5}$	$-9.21907e{-6}$	$-2.829488e{-5}$	$-4.696081e{-5}$
10	$4.939995e{-5}$	$4.100712e{-5}$	$3.28942e{-5}$	$1.378448e{-5}$	$-4.03517e{-6}$	$-1.091819e{-5}$	$-1.768232e{-5}$
14	$9.968208e{-6}$	$8.303689e{-6}$	$6.67043e{-6}$	$2.720083e{-6}$	$-1.07573e{-6}$	$-2.561183e{-6}$	$-4.02935e{-6}$
20	$1.878548e{-6}$	$1.565128e{-6}$	$1.2550019e{-6}$	$4.93790e{-7}$	$-2.50260e{-7}$	$-5.43942e{-7}$	$-8.35474e{-7}$
30	$2.873310e{-7}$	$2.389538e{-7}$	$1.90843e{-7}$	$7.1719e{-8}$	$-4.595209e{-8}$	$-9.26682e{-8}$	$-1.391883e{-7}$
50	$2.74358e{-8}$	$2.272902e{-8}$	$1.803392e{-8}$	$6.3467e{-9}$	$-5.27419e{-9}$	$-9.90589e{-9}$	$-1.452810e{-8}$
70	$5.87543e{-9}$	$4.8525e{-9}$	$3.8312e{-9}$	$1.2845e{-9}$	$-1.25352e{-9}$	$-2.26649e{-9}$	$-3.27820e{-9}$
100	$1.1508e{-9}$	$9.4715e{-10}$	$7.4364e{-10}$	$2.356e{-10}$	$-2.7134e{-10}$	$-4.7388e{-10}$	$-6.7625e{-10}$

TABLE 6.3: Sample numerical results for the (conservative) r component of the SSF. Entries left empty correspond to orbits below the ISCO. All figures presented are significant. The numerical accuracy is lower compared to that of F_t as a result of (i) the regularizion procedure involved in obtaining F_r, and (ii) the slow decay of the large-l tail in the case of F_r (compared with the exponential decay of the tail for F_t).

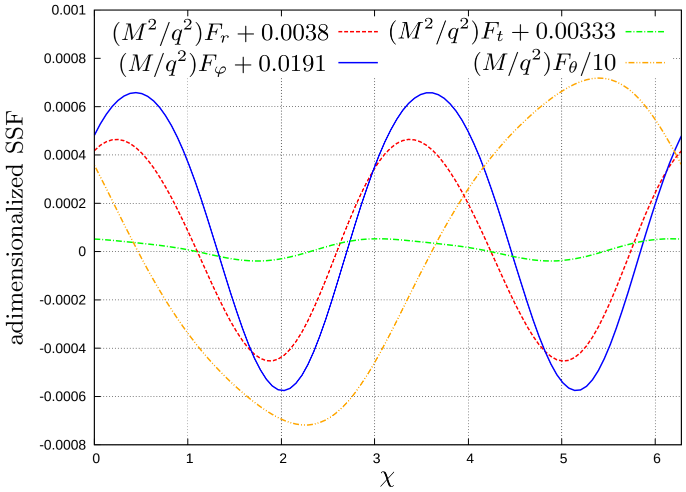

FIGURE 6.10: SSF for a circular, inclined orbit about a black hole with $a = 0.998M$ and with orbital parameters $(r_0, \iota) = (3M, 27.5573°)$ (this corresponds to an orbit with $\mathcal{L} = 1.9M$). For clarity we have shifted the F_r, F_t and F_φ components so that they are roughly centered around zero (in shifting the components we have adimensionalized them and then added the relevant constant). We have also rescaled F_θ so that it fits on the same scale as the other components. The F_r, F_t and F_φ component exhibit periodic behaviour, reaching their maximum/minimum value twice during one orbit. The χ value when the maximum/minimum is obtained differs for each of the three components. The F_θ component behaves differently, reaching a maximum/minimum only once over an orbital period. The observed form of the oscillatory behavior of the four components of the SSF is expected from symmetry considerations: from the reflective symmetry of Kerr spacetime about the equatorial plane we have the relations $(F_r, F_t, F_\theta, F_\varphi) \to (F_r, F_t, -F_\theta, F_\varphi)$ as $\chi \to \chi + \pi$.

Chapter 7

Scalar-field self-force in Kerr spacetime: eccentric, equatorial orbits

In this chapter we discuss the calculation of the SSF for a particle on an eccentric equatorial orbit about a Kerr black hole. Construction of the inhomogeneous fields in the FD for eccentric equatorial orbits is less straightforward than for circular orbits, as now the spherical harmonic components of the scalar field are not smooth functions of time (for fixed r between $r_{\min}$ and $r_{\max}$). Consequently, when constructing the (t, r)-dependence of the scalar field as a sum over (smooth) Fourier modes, one encounters the well known Gibbs phenomenon. We discuss this issue further in Sec. 7.1.1 and in Sec. 7.1.2 we discuss how to sidestep the difficulties associated with the Gibbs phenomenon, by making use of the recently introduced method of *extended homogeneous solutions* (EHS). We find that using this technique allows for the FD calculation of the SSF for a variety of orbital eccentricities, though the computational burden, particularly for orbits about a Kerr black hole, limits the eccentricity we can explore to $e \lesssim 0.7$. As our eccentric orbit SSF calculation represents the first SF calculation to be made entirely using the method of EHS, we take time to consider the efficiency of the technique in Sec. 7.2.3. As an application of our code, we also present in this chapter a calculation of the shift in the ISCEO location and frequency due to the conservative SSF (Sec. 7.3). We also examine the change in rest mass of the scalar particle over one orbital period (Sec. 7.4). Our work on eccentric, equatorial orbits has been published [99] and very recently our results have been corroborated by Thornburg [94].

As with circular orbits we employ two validation tests to check our numerical results, as well as comparing the $a = 0$ output of our code with previously published results in the literature [92, 93].

7.1 Numerical implementation

In this section we detail the numerical computation of the SSF, for a particle on an eccentric equatorial orbit about a Kerr black hole. We remark that the boundary conditions presented in Sec. 6.1.1 for circular equatorial orbits also apply to eccentric, equatorial orbits (the boundary conditions depend on the orbit type only through the mode frequency). The main challenge with the treatment of eccentric orbits in the FD is overcoming the difficulties associated with the Gibbs phenomenon, which we review now.

7.1.1 Junction conditions for eccentric orbits: the high frequency problem

For eccentric orbits, correctly calculating the inhomogeneous fields is much more involved than for circular orbits. In particular, if the standard *variation of parameters* approach is taken to the problem serious difficulties are encountered. For completeness we outline this approach now and, as we shall see, the problems associated with this technique stem from attempting to construct a non-smooth function from a sum of smooth harmonic modes.

Let $\psi^-_{\hat{l}m\omega}(r)$ and $\psi^+_{\hat{l}m\omega}(r)$ be two homogeneous solutions to the radial equation (4.16) satisfying the boundary conditions at spatial infinity and the event horizon respectively (Sec. 4.2). These two homogeneous solutions form a basis that can be used to construct the inhomogeneous solution using the variation of parameters technique for generating inhomogeneous solutions to second-order ODEs. Explicitly, the inhomogeneous radial field is given by

$$\begin{aligned}\psi_{\hat{l}m\omega}(r) &= \psi^+_{\hat{l}m\omega}(r)\int_{r_{\min}}^{r}\frac{\psi^-_{\hat{l}m\omega}(r')Z_{\hat{l}m\omega}(r')r'^2}{\Delta(r')W}dr' + \psi^-_{\hat{l}m\omega}(r)\int_{r}^{r_{\max}}\frac{\psi^+_{\hat{l}m\omega}(r')Z_{\hat{l}m\omega}(r')r'^2}{\Delta(r')W}dr' \\ &\equiv \psi^{\text{inh}}_{\hat{l}m\omega}(r) \qquad (7.1)\end{aligned}$$

where $Z_{\hat{l}m\omega}$ is the source term defined in Eq. (4.16) and

$$W \equiv \psi^-_{\hat{l}m\omega}(d\psi^+_{\hat{l}m\omega}/dr_*) - \psi^+_{\hat{l}m\omega}(d\psi^-_{\hat{l}m\omega}/dr_*) = \text{const} \qquad (7.2)$$

is the Wronskian. In the regions $r \le r_{\min}$ and $r \ge r_{\max}$ this formula reduces to the homogeneous solutions

$$\psi_{lm\omega}(r) = \begin{cases} C^-_{\hat{l}m\omega}\psi^-_{\hat{l}m\omega} \equiv \tilde{\psi}^-_{\hat{l}m\omega}(r), & r \le r_{\min} \\ C^+_{\hat{l}m\omega}\psi^+_{\hat{l}m\omega} \equiv \tilde{\psi}^+_{\hat{l}m\omega}(r), & r \ge r_{\max} \end{cases} \qquad (7.3)$$

where the scaling coefficients $C^-_{\hat{l}m\omega}$ and $C^+_{\hat{l}m\omega}$ are given by

$$C^\pm_{\hat{l}m\omega} = W^{-1}\int_{r_{\min}}^{r_{\max}}\frac{\psi^\mp_{\hat{l}m\omega}(r)Z_{\hat{l}m\omega}(r)r^2}{\Delta(r)}dr\ . \qquad (7.4)$$

The source term, $Z_{\hat{l}m\omega}(r)$, has singularities at the orbital turning points ($r = r_{\max}, r_{\min}$) which make the above integral difficult to evaluate numerically. This problem can be sidestepped by changing integration variables from r to t. In terms of an integral over t (with periastron taken to be at $t = 0$) the scaling coefficients $C^\pm_{\hat{l}m\omega}$ are given by

$$C^\pm_{\hat{l}m\omega} = -\frac{8q\pi S_{\hat{l}m}(\pi/2; -a^2\omega^2)}{T_r W}\int_0^{T_r/2}\frac{\psi^\mp_{\hat{l}m\omega}(r_p(t))\cos(\omega t - m\varphi_p(t))}{r_p(t)u^t(r_p(t))}dt\ , \qquad (7.5)$$

where now the integrand is free from singularities.

The final step is to construct the spherical harmonic ϕ_{lm} modes of the field and its derivatives.

Recalling Eq. (5.62), the field is constructed via

$$\phi_{lm}(t,r) = \sum_n \psi_{lmn}(r)e^{-i\omega_{mn}t} , \tag{7.6}$$

with $\omega_{mn} = m\Omega_\varphi + n\Omega_r$ [see Eq. (4.6)] and

$$\psi_{lmn}(r) = \sum_{\hat{l}=0}^{\infty} b^{\hat{l}}_{lm}\psi^{\text{inh}}_{\hat{l}m\omega_{mn}}(r) , \tag{7.7}$$

where the $b^{\hat{l}}_{lm}$'s are the spheroidal-spherical harmonic coupling coefficients from Eq. (5.60).

For a given r_0 between r_{min} and r_{max} the field $\phi_{lm}(t,r_0)$ is not a smooth function of time; as the particle crosses r_0 it is continuous but not differentiable (recall from Sec. 5.4 that in general the limits $r \to r_p^\pm$ give different values). Standard Fourier theory then tells us that the sum over n in Eq. (7.6) converge slowly near the particle. Even more troubling, the (discontinuous) derivatives of the field $\phi_{lm,\alpha}$ will suffer from the Gibbs phenomenon near the particle and as a consequence the sum over n may fail to converge to the correct value at the particle.

It should be noted that these poor convergence properties do not occur in the case of circular orbits, even if they are inclined, as for these orbits the field at any fixed radius is a smooth function of time.

7.1.2 Method of extended homogeneous solutions

Any FD SF calculation made via the variation of parameters approach outlined above will, for eccentric orbits, encounter the Gibbs phenomenon . At first sight this seems to make SF calculations in the frequency domain rather unattractive. Recently though, Barack, Ori and Sago [110] proposed a technique for overcoming these difficulties. They named their scheme the *method of extended homogeneous solutions* (EHS). In their work they outline the details of the method and provide a numerical example using the method of EHS to calculate the monopole contribution to the scalar field for a particle in an eccentric orbit about a Schwarzschild black hole. Here we will give an overview of the method and provide the necessary formula to extend their calculation to eccentric equatorial orbits about a Kerr black hole.

The general idea behind the method of extended homogeneous solution is that, instead of using a single radial field to construct the (t,r) dependence of the field, we form an 'inner solution' that is valid for $r < r_p(t)$. Likewise, an 'outer solution' is formed that is valid for $r > r_p(t)$. We now describe how to construct these two solutions. The first step in the method (as its name suggests) is to extend the homogeneous solutions to the entire domain so that

$$\tilde{\psi}^\pm_{\hat{l}m\omega}(r) \equiv C^\pm_{\hat{l}m\omega}\psi^\pm_{\hat{l}m\omega}(r), \qquad r > 2M , \tag{7.8}$$

where the scaling coefficients $C^+_{\hat{l}m\omega}$ and $C^-_{\hat{l}m\omega}$ are as given in Eq. (7.4) and hereafter an overtilde denotes an extended homogeneous quantity. We then define the two spherical-harmonic time-domain extended homogeneous solutions $\tilde{\phi}^+_{lm}$ and $\tilde{\phi}^-_{lm}$ by

$$\tilde{\phi}^\pm_{lm}(t,r) \equiv \sum_n \tilde{\psi}^\pm_{lmn}(r)e^{-i\omega_{mn}t} , \tag{7.9}$$

where we have

$$\tilde{\psi}^{\pm}_{\hat{l}mn}(r) = \sum_{\hat{l}=0}^{\infty} b^{\hat{l}}_{lm} \tilde{\psi}^{\pm}_{\hat{l}m\omega_{mn}}(r) \; . \tag{7.10}$$

Ref. [110] demonstrates that the sum in equation (7.9) converges exponentially in $|n|$ and that the convergence is uniform in t and r throughout $r > 2M$. Since the homogeneous radial functions $\tilde{\psi}^{\pm}_{lm\omega}(r)$ are analytic, the uniform exponential decay of the individual terms in the sum in Eq. (7.9) implies that the extended homogeneous solutions $\tilde{\phi}^{\pm}_{lm}(t,r)$ are analytic functions of r and t throughout $r > 2M$. Ref. [110] then argues that the actual time-domain function $\phi_{lm}(t,r)$ coincides with the extended homogeneous solutions on each side of the curve $r = r_p(t)$

$$\phi_{lm}(t,r) = \begin{cases} \tilde{\phi}^{+}_{lm}(t,r), & r \geq r_p(t) \; , \\ \tilde{\phi}^{-}_{lm}(t,r), & r \leq r_p(t) \; . \end{cases} \tag{7.11}$$

They justify the first equality as follows: (i) Both the actual time-domain function $\phi_{lm}(t,r)$ and time-domain extended homogeneous solutions $\tilde{\phi}^{\pm}_{lm}(t,r)$ are analytic for $r > r_{\max}$. (ii) For $r > r_{\max}$ the two functions coincide [compare Eqs. (7.3) and (7.8)]. (iii) The two functions are analytic throughout the domain $r > r_p(t)$, and coincide for $r > r_{\max}$ and therefore they must coincide throughout $r > r_p(t)$. (iv) Finally, by continuity of both functions, they coincide at $r = r_p(t)$ as well. Similar reasoning will justify the second equality in Eq. (7.11) .

The advantages of the method of extended homogeneous solutions over the standard variation of parameters approach are as follows. Firstly, and most importantly, the troublesome Gibbs phenomenon encountered when constructing the (discontinuous) derivative of the field is no longer present. With the above method the radial derivative of the field converges exponentially everywhere, including at the location of the particle. This leads to our second remark that for practical numerical calculations, the exponential convergence of the Fourier sum is extremely desirable.

7.1.3 Algorithm

For clarity we now outline the explicit steps in our numerical calculation in the context of eccentric equatorial orbits. The algorithm for circular orbits presented in Sec. (6.1.3) followed a similar pattern, with the main difference being that the homogeneous solutions are rescaled using equations (6.8) and (6.9), instead of using the method of EHS.

- *Orbital parameters.* For a given black hole spin a, orbital eccentricity e and semi-latus rectum p calculate the various properties of the orbit ($\mathcal{E}, \mathcal{L}, \Omega_r, \Omega_\varphi, T_r$ etc) using the relevant formulae given in Chapter 4.

- *Boundary conditions.* For a given $\hat{l}mn$ mode calculate the boundary conditions using equations (6.1) and (6.2). For both boundaries we choose $k_{\max}$ such that the relative magnitude of the $k_{\max} + 1$ term drops below a given threshold which we take to be 10^{-12}. In order to solve the radial equation (4.11), we need to numerically invert equation (4.15) to get $r(r_*)$. Machine accuracy places a limit on the smallest r_* that the inverter can distinguish from the event horizon and we take this value to be the event horizon side boundary of our numerical domain $r_{*\text{in}}$. For $a = 0$ we find this value to be at $r_{*\text{in}} = -65M$ and for $|a| = 0.998M$ we find $r_{*\text{in}} = -262M$. The outer boundary condition is calculated using Eq. (6.1). This series will only converge if $\omega r_{\text{out}} \gg 1$ and so, as with circular orbits, we set the outer boundary to be at $r_{*\text{out}} = 10/\omega$ which ensures rapid convergence of the boundary series.

- *Homogeneous solutions.* Using the boundary conditions as determined above we numerically solve the radial equation (4.11) for $\psi^{\pm}_{\hat{l}m\omega}$ using the Runge-Kutta Prince-Dormand (8,9) method from the Gnu Scientific Library (GSL) [166]. As we are using the method of homogeneous solutions we solve for the outer field $\psi^{+}_{\hat{l}m\omega}$ between $r_{*\text{out}}$ and $r_{*\text{min}}$ and the inner field $\psi^{-}_{\hat{l}m\omega}$ from $r_{*\text{in}}$ to $r_{*\text{max}}$. We store the value of the fields $\psi^{\pm}_{\hat{l}m\omega}$ and their r_* radial derivatives at 300 points between $r*_{\text{min}}$ and $r_{*\text{max}}$ equally spaced in χ.

- *Inhomogeneous solutions.* Compute the scaling coefficients $C^{\pm}_{\hat{l}m\omega}$ using Eq. (7.5). Because of the form of Eqs. (2.63) and (2.64) we compute this integral in χ rather than in t. The integration is performed numerically using the standard 'QAG' adaptive integrator from the GSL [166]. The integrator automatically requests the values of the integrand between r_{min} and r_{max} (or equivalently between $\chi = 0$ and $\chi = \pi$) that it requires to perform the integral to within a set accuracy (which we take to be a relative accuracy of 10^{-12}). The values of $\psi^{\pm}_{\hat{l}m\omega}$ requested are generated by locating the nearest of the 300 data points points stored between $r_{*\text{min}}$ and $r_{*\text{max}}$ and using it as input to the Runge-Kutta algorithm in order to calculate the value of the field at the requested point.

- *Determine n_{max}.* Although the sum in equation (7.10) is technically over all n modes, in practice, to reach a prescribed relative accuracy (which we take to be 5×10^{-11}), it is only necessary to sum over $|n| < n_{\text{max}}$. In our code we calculate the $n = 0$ mode, followed by the $n = -1, 1, -2, 2\ldots$ modes and stop calculating once the relative contribution to both the field and its r derivative from the last n mode drops below a given threshold. Typically we find that the contribution from the negative n modes drops below the convergence threshold before the equivalent positive n mode does, especially for higher $\hat{l}$ and e (similar results are found by Hopper and Evans [172]).

- *Spheroidal to spherical harmonic decomposition.* Once we have computed all the required $\hat{l}mn$ modes up to some maximum $\hat{l} = \hat{l}_{\text{max}}$, we construct the spherical harmonic lmn-modes using Eq. (7.9). The actual time-domain function is then constructed using equation (7.11) and the spherical harmonic multipole mode contribution to the full force is given by Eq. (5.61). When $a \neq 0$ the coupling between the spheroidal and spherical harmonics implies that some of the spherical harmonic modes, with $l < \hat{l}_{\text{max}}$, will have contributions from the uncomputed spheroidal modes with $\hat{l} > \hat{l}_{\text{max}}$. We denote the highest spherical mode below which, to a relative accuracy of 10^{-12}, the uncomputed spheroidal modes have no contribution, by l_{max}. To determine this value in practice we track which l-modes the spheroidal $\hat{l}mn$ modes (with $\hat{l} = \hat{l}_{\text{max}}$) couple to (within the specified accuracy) and set l_{max} to be the lowest l-mode minus one contributed to by any of those $\hat{l}mn$ modes.

- *Estimate large l-tail contribution.* As discussed below, for eccentric orbits it is convenient to split the SSF into its conservative and dissipative components using Eqs. (5.86). Regularization of the two components is then done using Eqs. (5.82) and (5.83) respectively. The dissipative component requires no regularization and the contribution from the high l-modes converges exponentially, whereas the conservative piece converges like l^{-2}. For a typical $\hat{l}_{\text{max}} = 25$ the dissipative component is computed to a high degree of accuracy but

> the slow convergence of the conservative piece necessitates extrapolating the regularized modes. Our method for extrapolation and estimation of the associated errors is the same as presented in Sec. 6.1.4. We find that the contribution to the SSF from the first few l modes has the opposite sign from that of the higher modes and, as a result, the contribution from the extrapolated 'tail' modes can be up to 120 percent of the total calculated conservative SSF values. This extrapolation of the high-l modes constitutes the largest source of numerical error in our final results.
>
> Once the conservative and dissipative pieces of the SSF are known, the full SSF is calculated by simply adding the two together [see Eq. (5.81)]. Constructing the full SSF this way is more numerically efficient than using the normal mode-sum formula given by Eq. (5.42). For example, the high l-mode contributions to the t-component of the SSF transition from an l^{-2} to an exponential fall off near the orbital turning points (see Figs. 7.1 and 7.2) which makes extrapolation to extract the full SSF more difficult in these regions.

In the case of eccentric equatorial orbits, the bandwidth of the spheroidal-spherical harmonic coupling is larger than for circular equatorial orbits as the mode spectrum is now bi-periodic ($\omega = m\Omega_\varphi + n\Omega_r$), and the value of ω, and consequently σ^2, can be much larger than in the circular equatorial orbit case. Nonetheless we find that the coupling is still weak enough to allow for SSF computations in reasonably short times (see Sec. 7.2.3 for details of the efficiency of the method). As an example, for an orbit with parameters $(a, p, e) = (0.9M, 10, 0.5)$ (which represents the orbit with a mode with the highest spheroidicity considered in this work) if one computes 25 spheroidal harmonic modes, then the coupling bandwidth is ± 10 modes. For generic inclined orbits, this situation will worsen further and place limits upon which regions of the (a, p, e) parameter space can be explored using this method. We discuss the impact of strong coupling for generic bound orbits further in the concluding chapter of this thesis.

7.2 Code validation and results: eccentric, equatorial orbits

In this section we present results for the SSF experienced by a particle on an eccentric, equatorial orbit about a Kerr black hole. As with our calculation of the SSF for circular, equatorial orbits our confidence in our results is based primarily on two validation tests. In our numerical results we observe both the high l contributions to the conservative components and the dissipative components of the SSF drop off as expected from theory (i.e., as l^{-2} for the conservative components and exponentially for the dissipative components — see Figs. 7.1 and 7.2). The energy and angular momentum balance validation test is more involved for eccentric orbits and so we detail it now.

7.2.1 Energy and angular momentum balance

As for circular, equatorial orbits in Sec. 6.2.2, we now check that in our numerical eccentric equatorial orbit calculations, the energy and angular momentum radiated by the particle is correctly accounted for by the radiation carried to infinity and down through the event horizon. The average energy and angular momentum carried by the scalar waves to infinity and down through the event horizon over one orbital period, T_r, is calculated via Eqs. (4.33) and (4.34)

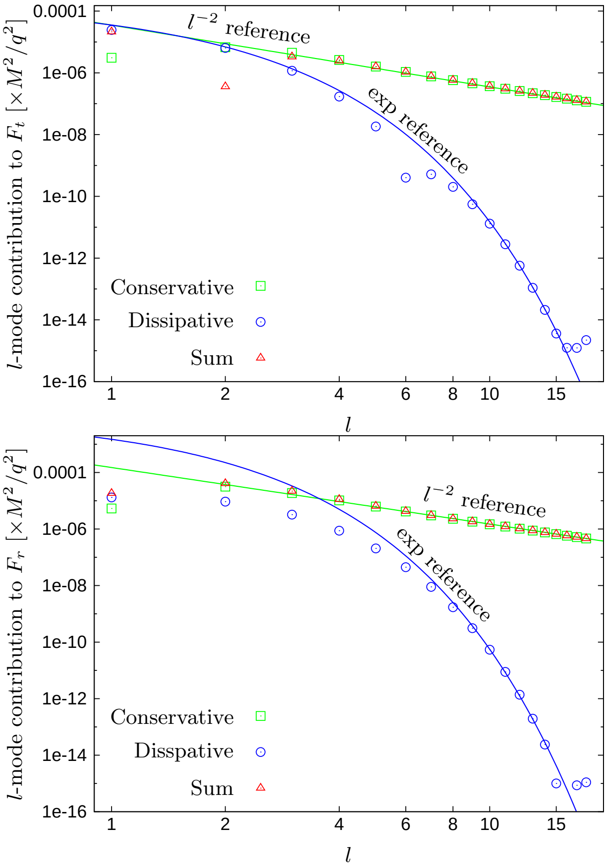

FIGURE 7.1: Decomposition of the F_t (top panel) and F_r (bottom panel) components of the SSF into conservative and dissipative pieces for orbital parameters $(a,p,e) = (0.5M, 10, 0.2)$ and $\chi = \pi/2$. The straight solid line is a reference line with slope l^{-2}. As discussed in Sec. 5.4 we expect the l-mode contributions to the full SSF and the conservative component of the SSF to fall off as l^{-2} for large l. The curved solid line is an exponential reference line. We expect the l-mode contributions to the dissipative component of the SSF to decay exponentially. Far away from the orbital turning point all the components of the SSF (including the F_φ component not shown here) are dominated by their conservative contributions. Near the orbital turning points this behavior changes for the F_t and F_φ components of the SSF where then the magnitude of their dissipative pieces is comparable to their conservative contribution (see figure 7.2). For modes with $l \geq 15$ the exponential fall-off of the dissipative piece is not evident as for those modes the magnitude of the dissipative piece is below our numerical accuracy.

respectively. For eccentric, equatorial orbits the amplitude coefficients $\tilde{c}_0^\pm$ are given by

$$\tilde{c}_0^\pm = C^\pm_{\hat{l}mn} c_0^\pm, \tag{7.12}$$

where, recall, $C^\pm_{\hat{l}mn}$ are given in Eq. (7.4), and $c_0^\pm$ are the leading order coefficients in boundary condition expansions given in Eqs. (6.1) and (6.2).

Using Eqs. (5.34) and (5.35), and noting that the conservative contribution over one orbital period to $\langle\dot{\mathcal{E}}\rangle$ and $\langle\dot{\mathcal{L}}\rangle$ vanish [see Eq. (5.86)], we obtain the relations

$$\mu\langle\dot{\mathcal{E}}\rangle = -\frac{1}{T_r}\left(\int_0^{T_r} \frac{F_t^{\text{diss}}(t)}{u^t(t)}dt + \mathcal{E}\Delta\mu\right), \tag{7.13}$$

$$\mu\langle\dot{\mathcal{L}}\rangle = \frac{1}{T_r}\left(\int_0^{T_r} \frac{F_\varphi^{\text{diss}}(t)}{u^t(t)}dt - \mathcal{L}\Delta\mu\right), \tag{7.14}$$

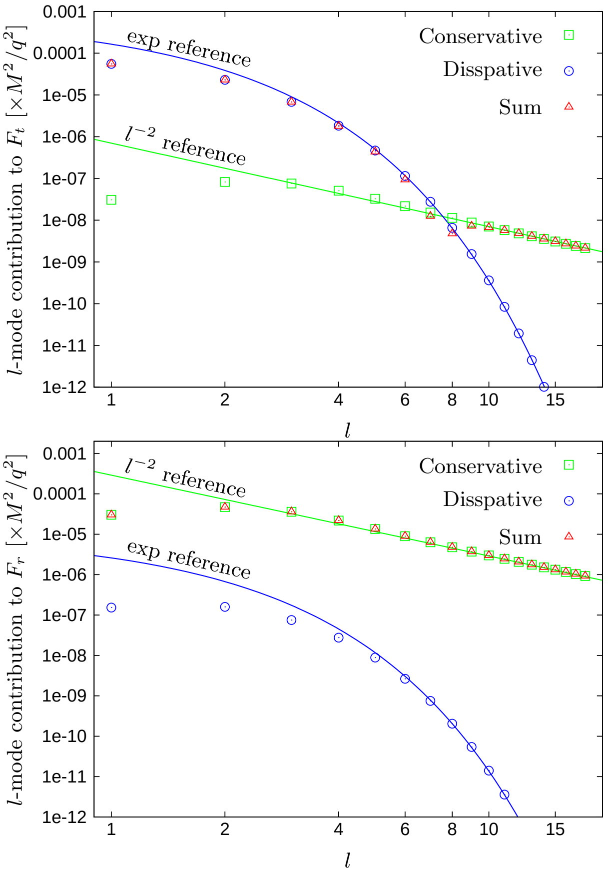

FIGURE 7.2: (Top panel) Decomposition of the F_t component of the SSF into conservative and dissipative pieces for orbital parameters $(a, p, e) = (0.5M, 10, 0.2)$ and $\chi = 0.010472$. Near to the orbital turning points (for instance at the χ value shown here) the contributions to the full SSF transition from an exponential decay to a l^{-2} fall off. This transition around $l \approx 8$ makes extrapolating the full SSF difficult in these regions of the orbit. This problem is completely avoided if we separate the SSF into conservative and dissipative pieces, extrapolate the value of the conservative piece and add the two together to recover the full SSF. Similar behaviour is observed for the F_φ component (not shown). (Bottom panel) Decomposition of the F_r component of the SSF into conservative and dissipative pieces for the same orbital parameters as in the left panel. No transition is observed as the conservative piece dominates the total r component of the SSF, even near the turning orbital turning point.

where we have used $u_t = -\mathcal{E}$ and $u_\varphi = \mathcal{L}$, and where $\Delta\mu$ is the net change in the particle's rest mass over a period T_r. The latter is found from Eq. (5.36) to be identically zero,

$$\Delta\mu = 0, \tag{7.15}$$

since in our case, where the particle moves along a bound geodesic, $\Phi^R(\tau)$ comes back to itself after a period, T_r. The orbital energy and angular momentum dissipated by the SSF over a period, T_r, should be balanced by the total energy and angular momentum radiated to infinity and down through the event horizon over that same period, i.e.,

$$-\mu\langle\dot{\mathcal{E}}\rangle = \langle\dot{E}\rangle_{\text{total}} \equiv \langle\dot{E}_+\rangle + \langle\dot{E}_-\rangle, \tag{7.16}$$

$$-\mu\langle\dot{\mathcal{L}}\rangle = \langle\dot{L}\rangle_{\text{total}} \equiv \langle\dot{L}_+\rangle + \langle\dot{L}_-\rangle. \tag{7.17}$$

We used our code to calculate both sides of Eqs. (7.16) and (7.17) for a variety of orbits and black holes spins and we display a sample of our results in Table 7.1. For all the cases we considered we found a good agreement between the local dissipative SSF and the radiated fluxes. This comparison tests primarily the low-l mode contributions to the SSF, because the amplitude of these contributions falls off exponentially with $\hat{l}$.

a/M	p	e	$\langle\dot{\mathcal{E}}\rangle \times \mu(M/q)^2$	$1-\mu\lvert\langle\dot{\mathcal{E}}\rangle/\langle\dot{E}\rangle_{\rm total}\rvert$	$\langle\dot{\mathcal{L}}\rangle \times \mu M/q^2$	$1-\mu\lvert\langle\dot{\mathcal{L}}\rangle/\langle\dot{L}\rangle_{\rm total}\rvert$
0.9	10	0.2	2.6862422×10^{-5}	-7.4×10^{-8}	$-8.3593539 \times 10^{-4}$	-7.4×10^{-8}
0.9	10	0.5	2.4856622×10^{-5}	9.5×10^{-8}	$-6.2962019 \times 10^{-4}$	7.2×10^{-8}
0	10	0.2	$3.213314062 \times 10^{-5}$	1.2×10^{-10}	$-9.62608845 \times 10^{-4}$	1.0×10^{-10}
0	10	0.5	3.329332×10^{-5}	1.6×10^{-7}	-7.844684×10^{-4}	3.3×10^{-7}
-0.5	10	0.2	$3.65656098 \times 10^{-5}$	2.8×10^{-10}	$-1.06932319 \times 10^{-3}$	2.0×10^{-10}
-0.5	10	0.5	4.33567×10^{-5}	3.1×10^{-6}	-9.70033×10^{-4}	2.4×10^{-6}
0.2	6.15	0.4	3.42797×10^{-4}	2.5×10^{-6}	-3.92668×10^{-3}	2.2×10^{-6}

TABLE 7.1: Orbital energy and angular momentum dissipated by the SSF and comparison with the radiated fluxes, for a variety of orbits with $p = 10$. The last row shows data for a "zoom-whirl"-type orbit (cf. Fig. 7.5). The average dissipation rates $\langle\dot{\mathcal{E}}\rangle$ and $\langle\dot{\mathcal{L}}\rangle$ (4th and 6th columns) are calculated from the local SSF using Eqs. (7.13) and (7.14). The radiated energy and angular momentum $\langle\dot{E}\rangle_{\rm total}$ and $\langle\dot{L}\rangle_{\rm total}$ are extracted independently from the asymptotic fluxes using Eqs. (4.33) and (4.34). The relative differences displayed in the 5th and the last columns verify that the balance relations (7.16) and (7.17) are satisfied. We believe the dominant source of residual discrepancy comes from the numerical integration in Eqs. (7.13) and (7.14).

7.2.2 Sample results

Using the algorithm outlined in Sec. 7.1.3, we calculated the SSF for a variety of black hole spins and orbital parameters. We find our code is able to compute the SSF for orbits with $e \lesssim 0.7$ (see below for a discussion). In Fig. 7.4 we present results for the SSF along the sample orbits shown in Fig. 7.3 and in Fig. 7.5 we show an example of the SSF for a zoom-whirl-type orbit. Tables 7.2 and 7.3 display a sample of numerical results for the dissipative and conservative component of the SSF respectively. Note that the errors are greater than those for the conservative component calculated for circular equatorial orbits, as for eccentric orbits it is numerically challenging to calculate as many l modes (for circular orbits we typically calculated up to $l_{\rm max} = 50$ whereas for eccentric orbits $l_{\rm max} \leq 15$—see computational performance section below).

In the Schwarzschild case ($a = 0$) it is possible to compare our results with those from the recent work of Cañizeras *et al.* [93], who used a pseudospectral algorithm formulated in the time domain. We find a good agreement with their results—see Table 7.4. We have also tested the output of our code (in the $a = 0$ case) against more detailed (unpublished) data from a time-domain code by Haas [92].

7.2.3 Computational performance

For a given black hole spin, the computational burden generally increases rapidly with e. The higher the eccentricity, the broader the Fourier spectrum becomes and the more n modes need to be calculated for each $\hat{l}, m$. Moreover, larger e and/or $|a|$ also leads to a stronger spheroidal–spherical coupling, because the spheroidicity parameter σ^2 that determines the strength of this coupling is proportional to $a^2\omega^2$, which is larger for higher n harmonics and higher a. Using the current version of our code we were able to explore spin parameters in the range $-0.99M \lesssim a \lesssim 0.99M$ and eccentricities in the range $0 \lesssim e \lesssim 0.7$. Beyond these ranges the computational burden becomes prohibitive.

a/M	p	e	χ	$(M^2/q^2)F_t^{\rm diss}$	$(M/q^2)F_\varphi^{\rm diss}$	$(M^2/q^2)F_r^{\rm diss}$
0.9	10	0.2	0	4.9986822×10^{-5}	$-1.7303353 \times 10^{-3}$	0
0.9	10	0.2	$\pi/2$	3.6334552×10^{-5}	$-1.0515349 \times 10^{-3}$	1.391751×10^{-5}
0.9	10	0.5	0	7.5738990×10^{-5}	$-3.2035416 \times 10^{-3}$	0
0.9	10	0.5	$\pi/2$	6.0154547×10^{-5}	$-1.1478358 \times 10^{-3}$	3.116102×10^{-5}
0	10	0.2	0	7.0051203×10^{-5}	$-2.0550050 \times 10^{-3}$	0
0	10	0.2	$\pi/2$	4.1885325×10^{-5}	$-1.2029711 \times 10^{-3}$	8.8783391×10^{-6}
0	10	0.5	0	1.5516962×10^{-5}	$-4.1743275 \times 10^{-3}$	0
0	10	0.5	$\pi/2$	6.5775426×10^{-5}	$-1.2989343 \times 10^{-3}$	1.7666437×10^{-5}
-0.5	10	0.2	0	8.8065099×10^{-5}	$-2.3164172 \times 10^{-3}$	0
-0.5	10	0.2	$\pi/2$	4.4975282×10^{-5}	$-1.3172287 \times 10^{-3}$	9.3313239×10^{-6}
-0.5	10	0.5	0	2.5761765×10^{-4}	$-4.9889604 \times 10^{-3}$	0
-0.5	10	0.5	$\pi/2$	6.2299563×10^{-5}	$-1.4030678 \times 10^{-3}$	2.1787580×10^{-5}
0.2	6.15	0.4	0	$1.48866752 \times 10^{-3}$	$-1.4008151 \times 10^{-2}$	0
0.2	6.15	0.4	$\pi/2$	$3.27980552 \times 10^{-4}$	$-4.6436085 \times 10^{-3}$	-1.563318×10^{-5}

TABLE 7.2: Numerical results for the dissipative piece of the SSF for a sample of orbits. The full SSF is obtained by adding the data in this table to that in Table 7.3. The SSF is sampled at χ values corresponding to the points marked along the orbits in Figs. 7.4 and 7.5. The computation of the dissipative SF requires no large-l extrapolation and as such the accuracy of the final result is greater than for the conservative SSF; in this case we believe all figures shown are significant. The SSF data for this table was obtained with typical values of $l_{\rm max}$ between 15 and 20.

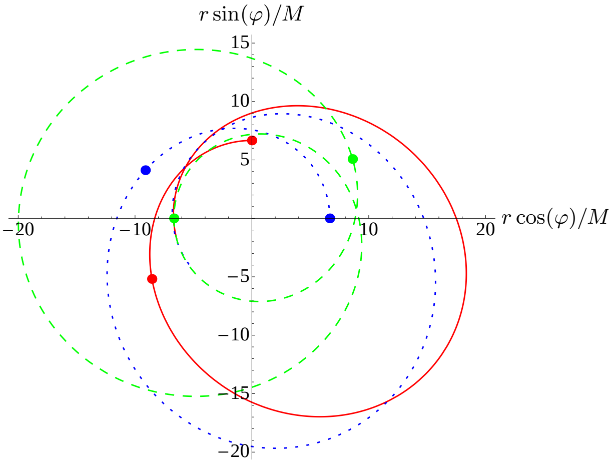

FIGURE 7.3: Sample orbits with $(p, e) = (10, 0.5)$ in the equatorial plane, for three different black hole spins: $a = 0$ (dotted, blue curve), $a = 0.9M$ (solid, red curve) and $a = -0.5M$ (dashed, green curved). For each orbit we show one complete revolution, from one periastron to the next, with markers indicating the points taken for the sample data in Tables 7.2 and 7.3

In Fig. 7.6 we plot the CPU time required to compute the SSF on a standard desktop machine (dual-core, 3GHz). We used a fiducial $l_{\rm max} = 15$, giving SSF fractional accuracies of order $\sim 10^{-4}$. We show results for $a = 0.9M$ and, for comparison, $a = 0$; results for $a = -0.9M$ are found to be similar to those for $a = 0.9M$. Note that for $a = 0$ the observed performance probes the efficiency of the EHS method, while the Kerr results also reflect the increased computational burden due to spheroidal-to-spherical harmonic mode coupling.

In the Schwarzschild case ($a = 0$), we find that for $e \lesssim 0.4$ the computation time grows only $\sim$ linearly with e, somewhat more rapidly at higher eccentricities, and very fast for $e \gtrsim 0.6$.

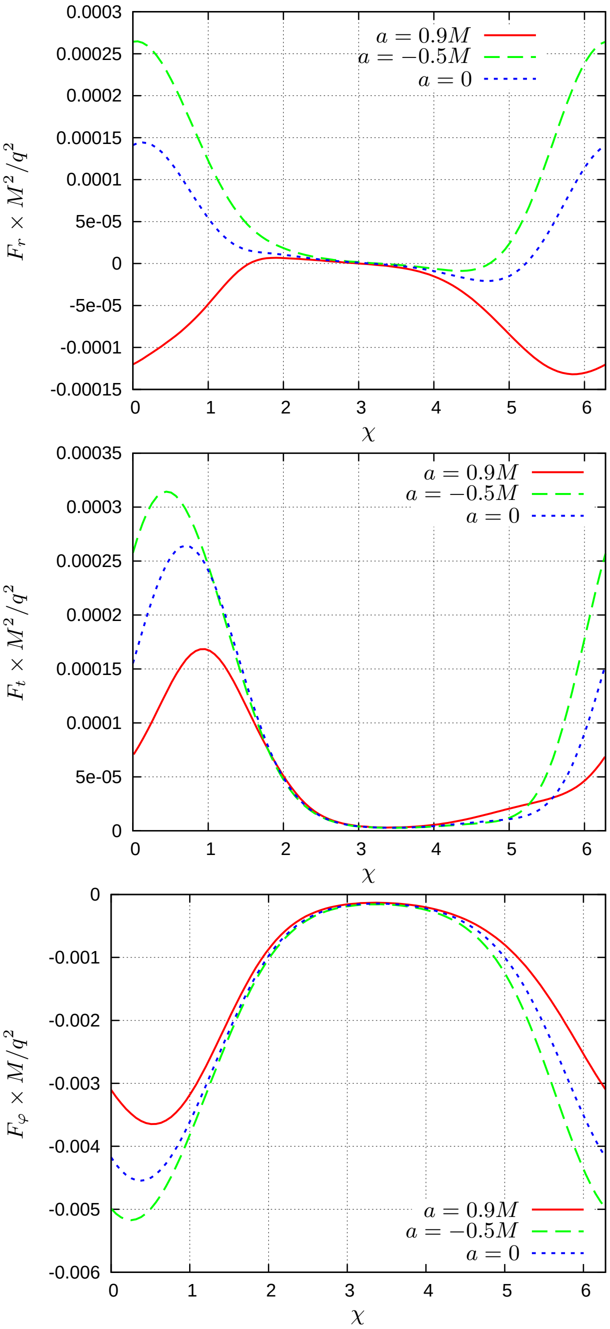

FIGURE 7.4: Sample SSF results for three different black hole spins: $a = 0$ (dotted, blue curve), $a = 0.9M$ (solid, red curve) and $a = -0.5M$ (dashed, green curved). The three panels show (reading from top to bottom) the F_r, F_φ and F_t components of the SSF, for the three orbits shown Fig 7.3. Periastron passage occurs at $\chi = 0$.

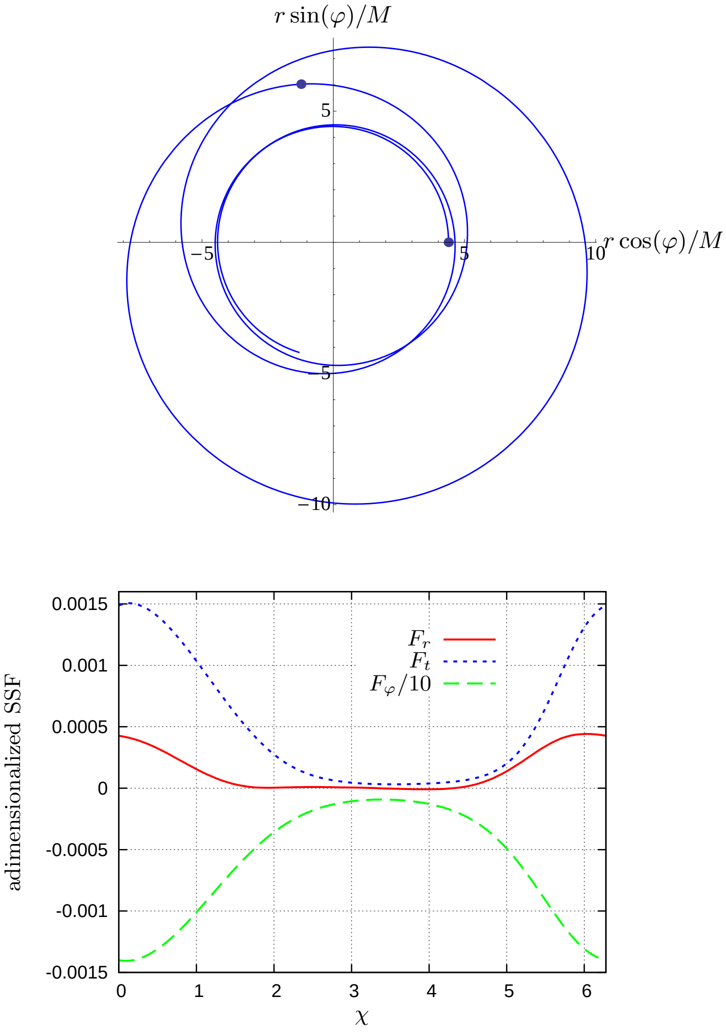

FIGURE 7.5: Shown in the upper panel is a 'zoom-whirl'-type orbit with parameters $(a, p, e) = (0.2M, 6.15, 0.4)$. The bottom panel shows the corresponding components of the SSF along the orbit. Periastron passage occurs at $\chi = 0$. Markers indicate the location of the data points shown in Tables 7.2 and 7.3.

Nonetheless, the required computation time for $e = 0.7$ is still only around 12 hours. For comparison, an equivalent time-domain computation [173] (on a similar machine and with similar accuracy standards) takes several days. At lower eccentricities, our gain in speed/accuracy is very substantial. Our results for $a = 0$ highlight the effiency of the EHS method.

At this point we remark that the computation time for TD SF calculations is only weakly dependent on the orbital eccentricity whereas, as discussed above, the run time of FD computations grows rapidly with increasing eccentricity. Consequently for moderate to high eccentricity orbits (i.e., orbits with $e \gtrsim 0.7$) TD computations will become more efficient than the FD approach. Similar conclusions and a discussion of how TD and FD methods can be used together to get the best from both approaches is given by Barton *et al.* [174].

In the Kerr case mode coupling adds to the computational burden. As an example, for $a = 0.9$ with $e = 0.2$, we find that the spheroidal-harmonic $l = 15$ mode has significant contributions from all tensor-harmonic modes $8 \leq \hat{l} \leq 22$. This results in a more rapid growth in CPU time as a function of e, compared to the Schwarzschild case. For spins as high as $|a| = 0.9$, eccentricities greater than ~ 0.5 are practically beyond reach for our current code. However, for

a/M	p	e	χ	$(M^2/q^2)F_t^{\rm cons}$	$(M/q^2)F_\varphi^{\rm cons}$	$(M^2/q^2)F_r^{\rm cons}$
0.9	10	0.2	0	0	0	$-4.176(4)\times10^{-5}$
0.9	10	0.2	$\pi/2$	$1.5694(3)\times10^{-5}$	$-2.3979(7)\times10^{-4}$	$-1.9233(9)\times10^{-5}$
0.9	10	0.5	0	0	0	$1.120(7)\times10^{-4}$
0.9	10	0.5	$\pi/2$	$4.461(2)\times10^{-5}$	$-6.072(3)\times10^{-4}$	$-2.746(4)\times10^{-5}$
0	10	0.2	0	0	0	$4.051(2)\times10^{-5}$
0	10	0.2	$\pi/2$	$2.0871(1)\times10^{-5}$	$-2.5827(3)\times10^{-4}$	$1.1272(3)\times10^{-5}$
0	10	0.5	0	0	0	$1.446(2)\times10^{-4}$
0	10	0.5	$\pi/2$	$5.6825(3)\times10^{-5}$	$-6.6652(8)\times10^{-4}$	$-3.06717(7)\times10^{-6}$
-0.5	10	0.2	0	0	0	$8.548(2)\times10^{-5}$
-0.5	10	0.2	$\pi/2$	$2.0868(1)\times10^{-5}$	$-2.4458(3)\times10^{-4}$	$3.09962(3)\times10^{-5}$
-0.5	10	0.5	0	0	0	$2.695(1)\times10^{-4}$
-0.5	10	0.5	$\pi/2$	$5.4479(5)\times10^{-5}$	$-6.421(1)\times10^{-4}$	$2.0327(7)\times10^{-5}$
0.2	6.15	0.4	0	0	0	$4.33(5)\times10^{-4}$
0.2	6.15	0.4	$\pi/2$	$2.2520(6)\times10^{-4}$	$-1.4005(8)\times10^{-3}$	$3.712(9)\times10^{-5}$

Table 7.3: Numerical results for the conservative piece of the SSF for a sample of orbits. The full SSF is obtained by adding the data in this table to that in Table 7.2. The SSF is sampled at χ values corresponding to the points marked along the orbits in Figs. 7.4 and 7.5. The shown results include an estimate of the uncertainty from the large-l extrapolation, which dominates the overall numerical error in these components; this is indicated by figures in brackets, showing the uncertainty in the last quoted decimal. We used the method described in Sec. 6.1.4 to estimate this error. The SSF data for this table was obtained with typical values of $l_{\rm max}$ between 15 and 20.

p	e	SSF component	This work	Cañizares *et al.*	Relative diff.
6.3	0.1	F_t	4.517994×10^{-4}	4.5171×10^{-4}	0.01%
		F_r	2.1257×10^{-4}	2.1250×10^{-4}	0.03%
		F_φ	-6.020401×10^{-3}	-6.02040×10^{-3}	0.0003%
6.7	0.3	F_t	7.71773×10^{-4}	7.6980×10^{-4}	0.25%
		F_r	3.6322×10^{-4}	3.6339×10^{-4}	0.04%
		F_φ	-9.04021×10^{-3}	-9.0402×10^{-3}	0.00015%
7.1	0.5	F_t	1.22331×10^{-3}	1.2330×10^{-3}	0.015%
		F_r	5.6179×10^{-4}	5.6122×10^{-4}	0.1%
		F_φ	-1.26857×10^{-2}	-1.2685×10^{-2}	0.0061%

Table 7.4: Comparison of the SSF for eccentric orbits with Cañizares *et al.* [93] in the *Schwarzschild* case ($a = 0$). The SSF values are extracted at certain near-periastron points as specified in Table I of [93]. Cañizares *et al.* do not indicate error bars on their results; for our data all figures are significant.

small eccentricities our algorithm is extremely efficient, even at high spin.

7.3 ISCEO shift

The innermost stable circular equatorial orbit (ISCEO) shift due to the conservative piece of the SSF for a particle in orbit about a Schwarzschild black hole, was first calculated by Diaz-Rivera *et al.* [87]. More recently, the ISCEO shift due to the conservative piece of the GSF for a similar orbital setup has also been calculated [67, 175]. Here, for the first time, we calculate the conservative SSF correction to the ISCEO for a particle in orbit about a Kerr black hole. The following derivation follows closely that of Ref. [67], but we adapt it here to Kerr spacetime.

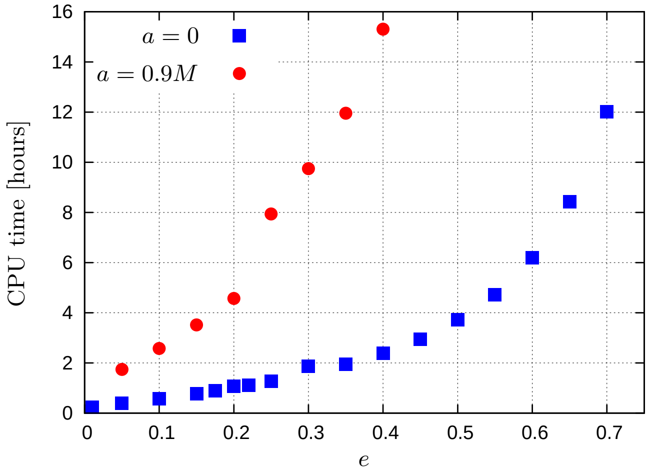

FIGURE 7.6: Computational cost. We show the total time required to calculate orbits with $p = 10$ for a variety of orbital eccentricities. In our calculations we take $l_{\rm max} = 15$, leading to fractional accuracies of order $\sim 10^{-4}$ in the SSF. In the Schwarzschild case ($a = 0$) we can compute the SSF for eccentricities up to $e = 0.7$ in around 12 hours. For $a = 0.9M$ the calculation requires more time, primarily because the coupling between the spheroidal and spherical harmonic modes necessitates calculation of higher spheroidal harmonic modes, which is computationally expensive. At low eccentricities, our frequency-domain algorithm is vastly faster than any existing time-domain method.

7.3.1 SSF correction to the ISCEO

We have reviewed the notion of the ISCO for a test particle in an equatorial orbit about a Kerr black hole in Sec. 2.2.4.1 and we will derive the conservative SSF correction to the ISCEO location along similar lines. With $\mathcal{F}_{\rm eff}$ as defined in Eq. (2.71) the perturbed equations of motion including conservative-only SSF effects are given by

$$\frac{d\bar{\mathcal{E}}}{d\bar{\tau}} = -\mu^{-1}F_t^{\perp({\rm cons})}, \qquad \frac{d\bar{\mathcal{L}}}{d\bar{\tau}} = \mu^{-1}F_\varphi^{\perp({\rm cons})} , \tag{7.18}$$

$$\frac{d^2\bar{r}_p}{d\bar{\tau}^2} = \mathcal{F}_{\rm eff}(\bar{r}_p, \bar{\mathcal{E}}, \bar{\mathcal{L}}) + \mu^{-1}F^r_{\perp({\rm cons})} , \tag{7.19}$$

where hereafter we denote perturbed quantities by an overbar, and we define $\bar{\mathcal{E}} \equiv -\bar{u}_t$ and $\bar{\mathcal{L}} \equiv \bar{u}_\varphi$ (no longer necessarily conserved along the orbit). We use the sub/superscript $\perp$(cons) to denote the conservative piece of the SSF perpendicular to the particle's 4-velocity [see Eq. (5.34) and Sec. 5.6].

We assume that the radius $\bar{r}_p(\tau)$ of the SSF-perturbed slightly-eccentric orbit can again be formally expanded about a circular orbit of radius r_0,

$$\bar{r}_p(\tau) = r_0 + e\bar{r}_1(\tau) + O(e^2) , \tag{7.20}$$

where $\bar{r}_1$ depends of r_0 but not on e. We similarly expand

$$\bar{\mathcal{E}} = \bar{\mathcal{E}}_0 + e\bar{\mathcal{E}}_1(\tau) + O(e^2), \qquad \bar{\mathcal{L}} = \bar{\mathcal{L}}_0 + e\bar{\mathcal{L}}_1(\tau) + O(e^2), \tag{7.21}$$

where $\bar{\mathcal{E}}_0$ and $\bar{\mathcal{L}}_0$ are the SSF-perturbed values of $\mathcal{E}_0$ and $\mathcal{L}_0$ along the circular orbit of radius r_0. To find $\bar{\mathcal{L}}_0$ and $\bar{\mathcal{E}}_0$ we simultaneously solve $d\bar{r}/d\bar{\tau} = 0$ and $d^2\bar{r}/d\bar{\tau}^2 = 0$ [hence $\mathcal{R}(\bar{r}_p, \bar{\mathcal{E}}_0, \bar{\mathcal{L}}_0) = 0$

with $\partial\mathcal{R}/\partial\bar{r}_p(\bar{r}_p,\bar{\mathcal{E}}_0,\bar{\mathcal{L}}_0)=0$]. This gives

$$\begin{aligned}\bar{\mathcal{E}}_0 &= (1-3v^2+2\tilde{a}v^3)^{-1/2}\left[1-2v^2+\tilde{a}v^3-\frac{r_0}{2\mu}F^r_{\perp 0}\right] , &(7.22)\\ \bar{\mathcal{L}}_0 &= r_0(1-3v^2+2\tilde{a}v^3)^{-1/2}\left[v(1-2\tilde{a}v^3+\tilde{a}^2v^4)-\frac{r_0(1+\tilde{a}v^3)}{2v\mu}F^r_{\perp 0}\right] , &(7.23)\end{aligned}$$

where $F^r_{\perp 0}$ is the circular-orbit value of $F^r_{\perp(\mathrm{cons})}$ (note the r component of the SSF is purely conservative along a circular orbit, so we can drop the 'cons' label).

The $O(e)$ part of Eq. (7.19) now takes the form

$$\frac{d^2\bar{r}_1}{d\tau^2}=-\bar{\omega}_r^2\bar{r}_1 , \tag{7.24}$$

where

$$\bar{\omega}_r^2 = -\frac{d}{d\bar{r}_p}\left[\mathcal{F}_{\mathrm{eff}}(\bar{r}_p,\bar{\mathcal{E}},\bar{\mathcal{L}})+\mu^{-1}F^r_{\perp(\mathrm{cons})}\right]_{\bar{r}=r_0} . \tag{7.25}$$

Here $\bar{\mathcal{E}}$, $\bar{\mathcal{L}}$ and $F^r_{\perp(\mathrm{cons})}$ are to be thought of as functions of $\bar{r}_p$ along the orbit (for given r_0,e), and the $\bar{r}_p$ derivative is taken with fixed r_0,e. The form (7.25) assumes that $\bar{\mathcal{E}}$, $\bar{\mathcal{L}}$ and $F^r_{\perp(\mathrm{cons})}$ depend explicitly on e (when r_0 and $\bar{r}_p$ are held fixed) only through e^2. That this is true in the Schwarzschild case was shown in Ref. [175] based on a simple symmetry argument, and the same argument carries over to the Kerr case. The perturbed radius thus takes the form of a simple harmonic oscillator in τ with frequency $\bar{\omega}_r$ (for $\bar{\omega}_r^2>0$), and choosing $t=0$ at periastron passage we have

$$\bar{r}_p(t)=r_0(1-e\cos\bar{\omega}_r\bar{\tau}) . \tag{7.26}$$

Using $\bar{r}_1=-r_0\cos\bar{\omega}_r\bar{\tau}$ and recalling Eq. (7.18), we may now write

$$\begin{aligned}F^r_{\perp(\mathrm{cons})} &= F^r_{\perp 0}+eF^r_{\perp 1}\cos\bar{\omega}_r\bar{\tau}+O(e^2) , &(7.27)\\ F^{\perp(\mathrm{cons})}_{\varphi} &= e\bar{\omega}_rF^{\perp 1}_{\varphi}\sin\bar{\omega}_r\bar{\tau}+O(e^2) , &(7.28)\\ F^{\perp(\mathrm{cons})}_{t} &= e\bar{\omega}_rF^{\perp 1}_{t}\sin\bar{\omega}_r\bar{\tau}+O(e^2) , &(7.29)\end{aligned}$$

where we have defined

$$F^r_{\perp 1}\equiv -r_0\left.\frac{dF^r_{\perp(\mathrm{cons})}}{d\bar{r}_p}\right|_{\bar{r}_p=r_0} , \qquad F^{\perp 1}_{\varphi}\equiv \mu r_0\left.\frac{d\bar{\mathcal{L}}}{d\bar{r}_p}\right|_{\bar{r}_p=r_0} , \qquad F^{\perp 1}_{t}\equiv -\mu r_0\left.\frac{d\bar{\mathcal{E}}}{d\bar{r}_p}\right|_{\bar{r}_p=r_0} . \tag{7.30}$$

Then, using these definitions in Eq. (7.25) and substituting for $\bar{\mathcal{E}}_0$ and $\bar{\mathcal{L}}_0$ from Eqs. (7.22) and (7.23), we obtain

$$\begin{aligned}\bar{\omega}_r^2 &= \omega_r^2+\frac{F^r_{\perp 1}}{r_0\mu}-\frac{3-12v^2+9\tilde{a}v^3}{r_0(1-3v^2+2\tilde{a}v^3)}\frac{F^r_{\perp 0}}{\mu}-2\frac{aM+a^2v+r_0(r_0-3M)v}{r_0^{9/2}\sqrt{r_0-3M+2av}}\frac{F^{\perp 1}_{\varphi}}{\mu} \qquad (7.31)\\ &\quad -2a\frac{a(r_0+M)+a^2v-3Mr_0v}{r_0^{9/2}\sqrt{r_0-3M+2av}}\frac{F^{\perp 1}_{t}}{\mu} ,\\ &\equiv \omega_r^2+\Delta\omega_r^2(r_0,a) ,\end{aligned}$$

where $\Delta\omega_r^2(r_0,a)$ denotes the terms proportional to the SSF and we have neglected terms quadratic in the SSF.

Near the ISCEO, the unperturbed frequency (squared) may be expanded in the form

$$\omega_r^2(r_0, a) = A(a)(r_0 - r_{\rm is}) + O(r_0 - r_{\rm is})^2 \ , \tag{7.32}$$

where, recall, $r_{\rm is}$ denotes the location of the unperturbed ISCEO, given in Eq. (2.77), and

$$\begin{aligned} A(a) &= \left.\frac{\partial \omega_r^2}{\partial r_0}\right|_{r_0 = r_{\rm is}} \ , \\ &= -3M\frac{r_{\rm is}^3 + M^2 r_{\rm is}(18 - 5\tilde{a}^2 - 38\tilde{a}v_{\rm is}) - 7\tilde{a}^2M^3(\tilde{a}v_{\rm is} - 4) + M r_{\rm is}^2(13\tilde{a}v_{\rm is} - 10)}{r_{\rm is}^5\left[r_{\rm is} + M(2\tilde{a}v_{\rm is} - 3)\right]^2} \ , \end{aligned} \tag{7.33}$$

with $v_{\rm is} \equiv \sqrt{M/r_{\rm is}}$. By definition, $\bar{\omega}_r^2$ vanishes at the (shifted) location of the ISCEO: $\bar{\omega}^2(r_0 = \bar{r}_{\rm is}) = 0$. By substituting Eq. (7.32) into Eq. (7.31), setting $r_0 = \bar{r}_{\rm is}$ and $\bar{\omega}_r = 0$, and solving for $\bar{r}_{\rm is}$ at linear order in the SSF, we find the SSF-induced shift in ISCEO radius to be [up to $O(q^2)$]

$$\Delta r_{\rm is} \equiv \bar{r}_{\rm is} - r_{\rm is} = -\frac{\Delta\omega_r^2(r_{\rm is}, a)}{A(a)} \ . \tag{7.34}$$

Note on the right-hand side of Eq. (7.34) we have substituted $r_{\rm is}$ for $\bar{r}_{\rm is}$ as this term is already of $O(q^2)$. When $a = 0$, Eq. (7.34) reduces (upon replacing the SSF components with the GSF components) to the ISCEO shift formula found in Ref. [67], namely

$$\Delta r_{\rm is}(a = 0) = (M^2/\mu)\left(216F^r_{\perp 0{\rm is}} - 108F^r_{\perp 1{\rm is}} + \sqrt{3}M^{-2}F^{\perp 1}_{\varphi{\rm is}}\right) \ , \tag{7.35}$$

where the 'is' subscript denotes a quantity's value at the unperturbed ISCEO.

We next consider the conservative SSF shift in the azimuthal frequency. The frequency associated with the perturbed circular orbit of radius $\bar{r} = r_0$ is given by

$$\bar{\Omega}_\varphi = \frac{d\bar{\varphi}_p}{d\bar{t}} = \frac{d\bar{\varphi}_p/d\bar{\tau}}{d\bar{t}/d\bar{\tau}} = \frac{\mathring{g}_0^{\varphi\varphi}\bar{\mathcal{L}}_0 - \mathring{g}_0^{\varphi t}\bar{\mathcal{E}}_0}{\mathring{g}_0^{t\varphi}\bar{\mathcal{L}}_0 - \mathring{g}_0^{tt}\bar{\mathcal{E}}_0} \ , \tag{7.36}$$

where $\mathring{g}_0^{\alpha\beta}$ are the background metric functions evaluated on the perturbed circular orbit. Substituting for $\bar{\mathcal{E}}_0$ and $\bar{\mathcal{L}}_0$ from Eqs. (7.22) and (7.23), taking $r_0 = r_{\rm is} + \Delta r_{\rm is}$ and keeping only terms of $O(q^2)$ or less, we find the relative frequency shift at the ISCEO to be given by

$$\frac{\Delta\Omega_{\varphi{\rm is}}}{\Omega_{\varphi{\rm is}}} \equiv \frac{\bar{\Omega}_{\varphi{\rm is}} - \Omega_{\varphi{\rm is}}}{\Omega_{\varphi{\rm is}}} = -\frac{3\Delta r_{\rm is}}{2(r_{\rm is} + av_{\rm is})} - \frac{r_{\rm is}^4(r_{\rm is} - 3M + 2av_{\rm is})\mu^{-1}F^r_{\perp 0{\rm is}}}{2M(r_{\rm is} + av_{\rm is})(r_{\rm is}^2 - 2Mr_{\rm is} + a^2)} \ . \tag{7.37}$$

For $a = 0$ the above formula reduces (when the SSF components are replaced by the GSF components) to that found in Refs. [67, 87], namely

$$\frac{\Delta\Omega_{\varphi{\rm is}}}{\Omega_{\varphi{\rm is}}}(a = 0) = -\frac{\Delta r_{\rm is}}{4M} - \frac{27M}{2\mu}F^r_{\perp 0{\rm is}} \ . \tag{7.38}$$

The last task is to rewrite the above expressions for $\Delta r_{\rm is}$ and $\Delta\Omega_{\varphi{\rm is}}$ in terms of the full Boyer-Lindquist components of the SSF (rather than the normal components $F^\perp_\alpha$). Specifically, recalling Eqs. (7.31) and (7.37), we will need expressions for $F^r_{0\perp}$, $F^r_{\perp 1}$, $F^{\perp 1}_\varphi$ and $F^{\perp 1}_t$ in terms of the quantities F^0_r, F^1_r, F^1_φ and F^1_t arising, in analogy with Eqs. (7.27)-(7.29), from the formal

e-expansion of the full conservative SSF:

$$F_r^{\rm cons} = F_r^0 + eF_r^1 \cos\bar{\omega}_r\bar{\tau} + O(e^2) \,, \tag{7.39}$$

$$F_\varphi^{\rm cons} = e\bar{\omega}_r F_\varphi^1 \sin\bar{\omega}_r\bar{\tau} + O(e^2) \,, \tag{7.40}$$

$$F_t^{\rm cons} = e\bar{\omega}_r F_t^1 \sin\bar{\omega}_r\bar{\tau} + O(e^2) \,. \tag{7.41}$$

Starting with the radial component, we write

$$F^r_{\perp({\rm cons})} = (\mathring{g}^{r\beta} + u^r u^\beta) F_\beta^{\rm cons} \,, \tag{7.42}$$

and formally expand both sides of the equation in e using Eqs. (7.27) and (7.39)–(7.41), noticing $u^r u^\beta F_\beta^{\rm cons} = O(e^2)$. Comparing the $O(e^0)$ and $O(e^1)$ terms on either side then gives

$$F^r_{\perp 0} = \mathring{g}_0^{rr} F_r^0 \,, \tag{7.43}$$

$$F^r_{\perp 1} = \mathring{g}_0^{rr} F_r^1 - r_0 \left.\frac{d\mathring{g}^{rr}}{dr}\right|_{r=r_0} F_r^0 \,. \tag{7.44}$$

For the t and φ components we obtain

$$F_\varphi^{\perp 1} = (1 + \mathcal{L}_0^2 \mathring{g}_0^{\varphi\varphi} - \mathcal{E}_0\mathcal{L}_0 \mathring{g}_0^{t\varphi}) F_\varphi^1 + (\mathcal{L}_0^2 \mathring{g}_0^{t\varphi} - \mathcal{E}_0\mathcal{L}_0 \mathring{g}_0^{tt}) F_t^1 + \mathcal{L}_0 r_0 F_r^0 \,, \tag{7.45}$$

$$F_t^{\perp 1} = (1 + \mathcal{E}_0^2 \mathring{g}_0^{tt} - \mathcal{E}_0\mathcal{L}_0 \mathring{g}_0^{t\varphi}) F_t^1 + (\mathcal{E}_0^2 \mathring{g}_0^{t\varphi} - \mathcal{E}_0\mathcal{L}_0 \mathring{g}_0^{\varphi\varphi}) F_\varphi^1 - \mathcal{E}_0 r_0 F_r^0 \,, \tag{7.46}$$

where we have also used $u^r = er_0\bar{\omega}_r \sin\bar{\omega}_r\bar{\tau}$ [see Eq. (7.26)].

The shifts in the location and frequency of the ISCEO can now be constructed from the full SSF by substituting Eqs. (7.43)–(7.46) (evaluated at the ISCEO) into Eqs. (7.34) and (7.37). The resulting formulae are cumbersome so we leave them implicit. For $a = 0$ the formula for the radial ISCEO shift is found to reduce to

$$\Delta r_{\rm is}(a=0) = (M^2/\mu)\left(216F^0_{r{\rm is}} - 72F^1_{r{\rm is}} + 6\sqrt{2}F^1_{t{\rm is}} + \frac{4}{\sqrt{3}}F^1_{\varphi{\rm is}}\right) \,, \tag{7.47}$$

which is in agreement with Eqs. (51) of Diaz-Rivera *et al.* [87].

7.3.2 Numerical results

In order to implement Eqs. (7.34) and (7.37) we require the values of F_r^0, F_r^1, F_t^1 and F_φ^1, all evaluated at $r = r_{\rm is}$. The first piece of data, F_r^0, is simply the radial SSF component evaluated along a circular equatorial orbit of radius $r_0 = r_{\rm is}$, and we can compute is with great accuracy using the circular-orbit code presented in Sec. 6.2. The computation of the other quantities, which are associated with a slightly eccentric orbit, is more delicate. Recalling Eqs. (7.39)–(7.41) we see that they may be extracted using

$$F^1_{r{\rm is}} = \lim_{p\to r_{\rm is}} \lim_{e\to 0} \hat{F}^1_r(p,e) \,, \qquad \hat{F}^1_r(p,e) \equiv 2\omega_r (e\pi)^{-1} \int_0^{\pi/\omega_r} F_r^{\rm cons} \cos(\omega_r\tau) d\tau \,, \tag{7.48}$$

$$F^1_{\alpha{\rm is}} = \lim_{p\to r_{\rm is}} \lim_{e\to 0} \hat{F}^1_\varphi(p,e) \,, \qquad \hat{F}^1_\alpha(p,e) \equiv 2 (e\pi)^{-1} \int_0^{\pi/\omega_r} F_\alpha^{\rm cons} \sin(\omega_r\tau) d\tau \,, \tag{7.49}$$

where $\alpha \in \{t, \varphi\}$ [note that here we are allowed to remove the bars from $\bar{\omega}_r$ and $\bar{\tau}$ since the quantities $F_\alpha^{\rm cons}$ are already $O(q^2)$]. As noted in Ref. [67], both limits can be taken simultaneously by picking points along a suitable curve in the e–p plane. As also discussed in Ref. [67], for our $O(e)$-expansions to be valid we must have both $e \ll 1$ and $e \ll (p - r_{\rm is})/M$ along the curve (so that we keep sufficient distance from the separatrix as we approach the ISCEO). The final result should be independent of the particular path taken through the (p, e) plane and we use this fact as a validation test of our numerical scheme. In practice we calculate $\hat{F}^r_1$, $\hat{F}^1_t$ and $\hat{F}^1_\varphi$ at various points along three curves given by $p = r_{\rm is} + M\sqrt{e}$, $p = r_{\rm is} + \frac{3}{2}M\sqrt{e}$ and $p = r_{\rm is} + Me^{1/3}$, and then extrapolate each set of data to the ISCEO—see Figs. 7.7 and 7.9. We use the (small) difference in the extrapolated values from the three curves to place error estimates on the F_1's.

Once the F_1's are known, we use Eqs. (7.34) and (7.38) to compute $\Delta r_{\rm is}$ and $\Delta\Omega_{\varphi\rm is}$ for a variety of a values. The main source of error in our final results comes from the $e \to 0$ extrapolation involved in extracting the F_1 functions (the error in $F^r_{0\rm is}$ is relatively much smaller and can be neglected). In order to estimate the error in $\Delta r_{\rm is}$ and $\Delta\Omega_{\varphi\rm is}$ we use the variance in the values of these quantities when using the three different extrapolation curves mentioned above.

Our results are presented in Table 7.5 and Fig. 7.10. We observe that $\Delta r_{\rm is}$ increases monotonically as the black hole spin is varied from $a = -0.9M$ to $a = 0.9M$, and it changes sign from negative to positive around $a = 0.8M$. The relative shift in the azimuthal frequency at the ISCEO, $\Delta\Omega_{\varphi\rm is}/\Omega_{\varphi\rm is}$, is always positive between $a = -0.9M$ and $a = 0.9M$. For retrograde orbits the relative frequency shift remains similar to that found in the Schwarzschild case ($a = 0$), while for prograde orbits it decreases rapidly with increasing spin a. Our code is not sufficiently accurate to explore the near-extremal case, so the behavior of $\Delta\Omega_{\varphi\rm is}$ (and of $\Delta r_{\rm is}$) there remains unclear.

7.4 Variation of rest mass

As discussed in Sec. 5.2, the SSF has a component tangential to the particle's worldline, which leads to the particle having a dynamically varying rest mass [130]. We remind that this situation is special to our particular SSF theory (see Sec. 5.2) and in the equivalent electromagnetic and gravitational cases the rest mass is conserved. It is possible to construct a scalar field theory where the particle's rest mass is conserved but only at the cost of making the field equation non-linear [130]. Previous studies of this phenomenon in cosmological spacetimes [177, 178] have found a range of possibilities, including a periodic mass variation as well as cases where the mass dissipates entirely.

In our setup, where the motion is intrinsically periodic, the field returns to its original value after one orbital revolution and thus from Eq. (5.36) we see that the net change in the particle's rest mass will be zero. Furthermore, examining Eq. (5.35) and recalling the symmetry relations expressed in Eq. (5.86), we can see that $d\mu/d\tau$ is symmetric about the apastron and hence the rest-mass change from periastron to apastron (and visa versa) must also be zero. To within our numerical accuracy we observe this behavior in our data—see Fig. 7.11.

It is also interesting to examine how the rest mass varies along the orbit. The total rest mass change from periastron to a point with phase χ along the orbit is given by

$$\Delta\mu(\chi) = -\int_0^\chi F^{\rm diss}_\alpha(\chi) u^\alpha(\chi') \frac{dt}{d\chi'} d\chi' \,. \tag{7.50}$$

As illustrated in Fig. 7.11, the particle's rest mass initially increases (though in our example

a/M	$r_{\rm is}/M$	$M\Omega_{\varphi{\rm is}}$	$(M^2/q^2)F^0_{r{\rm is}}$	$(M^2/q^2)F^1_{r{\rm is}}$	$(M^2/q^2)F^1_{t{\rm is}}$	$(M/q^2)F^1_{\varphi{\rm is}}$	$\Delta r_{\rm is}\left(\frac{\mu}{q^2}\right)$	$\frac{\Delta\Omega_{\varphi{\rm is}}}{\Omega_{\varphi{\rm is}}}\left(\frac{\mu M}{q^2}\right)$
0.9	2.32088	0.225442	-1.13367×10^{-2}	$-0.0551(4)$	0.1194(7)	$-0.2814(2)$	0.0309(5)	-0.0107(3)
0.8	2.90664	0.173747	-3.09398×10^{-3}	$-0.0149(6)$	0.0822(1)	$-0.230(6)$	0.004(1)	0.0013(5)
0.7	3.39313	0.143879	-1.08845×10^{-3}	$-4.96(9) \times 10^{-3}$	0.06215(7)	$-0.1985(8)$	-0.0226(7)	0.0118(7)
0.6	3.82907	0.123568	-3.71617×10^{-4}	$-1.77(5) \times 10^{-3}$	0.0499(2)	$-0.1818(7)$	-0.0471(2)	0.01802(6)
0.5	4.23300	0.108588	-6.92214×10^{-5}	$-2.50(3) \times 10^{-4}$	0.04105(2)	$-0.16449(2)$	-0.0651(6)	0.02203(5)
0.4	4.61434	0.096973	6.83682×10^{-5}	$3.32(3) \times 10^{-4}$	0.03485(8)	$-0.15321(5)$	-0.0804(6)	0.0248(6)
0.25	5.15554	0.083639	1.31790×10^{-4}	$7.53(3) \times 10^{-4}$	0.02783(1)	$-0.13753(9)$	-0.10070(4)	0.02779(1)
0.1	5.66930	0.073536	1.68212×10^{-4}	$8.371(1) \times 10^{-4}$	0.02295(2)	$-0.12610(2)$	-0.1172(2)	0.02948(4)
0.0	6.00000	0.068041	1.67728×10^{-4}	$8.293(6) \times 10^{-4}$	0.02043(1)	$-0.11983(5)$	-0.1268(1)	0.03020(3)
-0.1	6.32289	0.063294	1.62329×10^{-4}	$7.98(2) \times 10^{-4}$	0.01833(2)	$-0.1141(2)$	-0.1350(3)	0.03056(6)
-0.3	6.94927	0.055496	1.31790×10^{-4}	$7.13(2) \times 10^{-4}$	0.01504(5)	$-0.1050(5)$	-0.1505(9)	0.0309(4)
-0.5	7.55458	0.049348	1.27517×10^{-4}	$6.23(2) \times 10^{-4}$	0.01257(2)	$-0.0970(2)$	-0.1620(4)	0.03090(8)
-0.7	8.14297	0.044372	1.10762×10^{-4}	$5.36(2) \times 10^{-4}$	0.01068(3)	$-0.0909(6)$	-0.1723(8)	0.0306(2)
-0.9	8.71735	0.040260	9.60700×10^{-5}	$4.68(2) \times 10^{-4}$	0.00919(2)	$-0.08492(7)$	-0.1802(4)	0.02992(7)

TABLE 7.5: The conservative SSF effect upon the ISCEO location and frequency. Each row of the table corresponds to a particular value of the Kerr spin parameter a: the second and third columns show the values of the unperturbed ISCO radius $r_{\rm is}$ and frequency $\Omega_{\varphi{\rm is}}$, and the fourth through seventh columns show the numerically-computed values of the SSF coefficients $F^0_{r{\rm is}}$, $F^1_{r{\rm is}}$, $F^1_{t{\rm is}}$ and $F^1_{\varphi{\rm is}}$ defined through the small-e expansion in Eqs. (7.39)–(7.41). The last two columns display the SSF-induced shift in the radius and frequency of the ISCEO, as computed using Eqs. (7.34) and (7.37). Figures in brackets are estimates of the numerical error in the last displayed decimals (in the data for $F^0_{r{\rm is}}$ all figures are significant). Note the fractional error in the $a = 0.8M$ results for $\Delta r_{\rm is}$ and $\Delta\Omega_{\varphi{\rm is}}$ is particularly large: this is a consequence of a delicate cancellation between the various terms in Eqs. (7.34) and (7.38), which also leads to the vanishing of $\Delta r_{\rm is}$ and $\Delta\Omega_{\varphi{\rm is}}$ at two (slightly different) spin values close to $a = 0.8$. For $a = 0$ Diaz-Rivera *et al.* [87] obtained $\Delta r_{\rm is} = -0.122701q^2/\mu$ and $\Delta\Omega_{\varphi{\rm is}}/\Omega_{\varphi{\rm is}} = 0.0291657q^2/(\mu M)$. The small discrepancy is discussed briefly in the caption of Fig. 7.7.

zoom-whirl orbit there is an initial slight decreases before the increase begins) but then decreases so that the particle regains its original mass by the time it reaches apastron. Once the particle passes the apastron the mass continues to decrease, before increasing back to the original value at periastron. We also observe that the change in mass along the orbit is only weakly dependent on the black hole spin, for fixed (p, e)—again see Fig. 7.11.

In our setup, the particle's rest mass is conserved over an orbital period T_r, but in a setup which allowed for the orbit to evolve through the action of the SSF, this would no longer be the case (the field would no longer return to its original value after one orbit). It would be an interesting project, which we do not pursue here, to consider the effect of the net mass loss on the inspiral dynamics of the scalar charge (this was very recently considered for the case of a scalar particle in orbit about a Schwarzschild black hole by Diener *et al.* [95]).

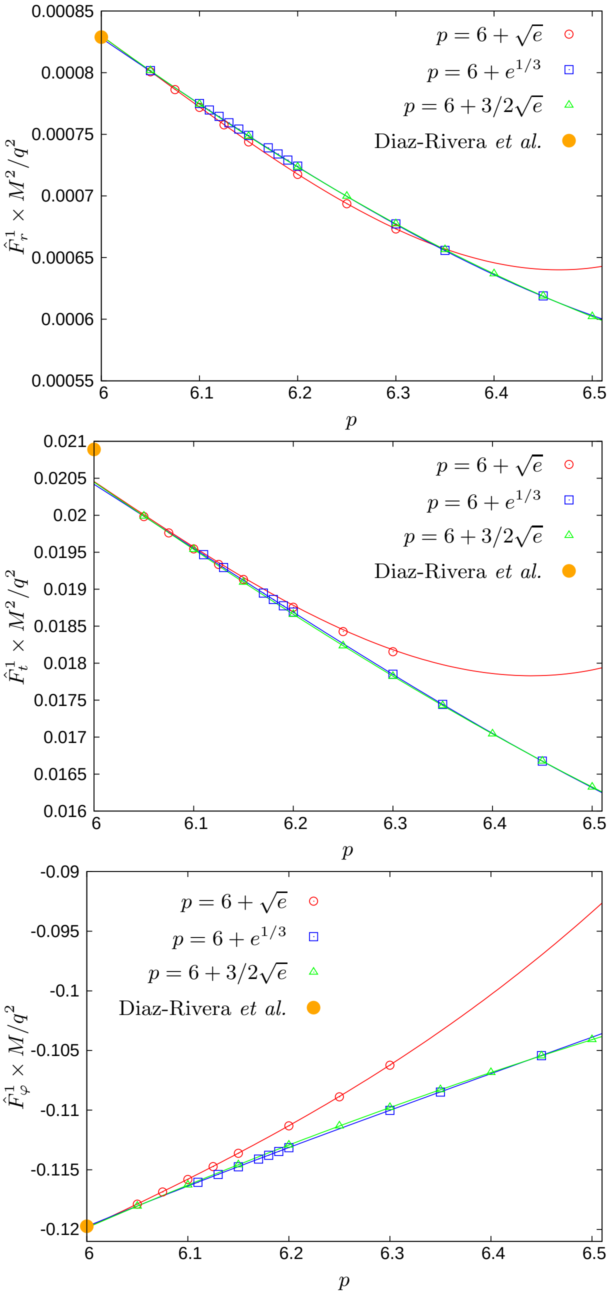

FIGURE 7.7: Calculation of $F^1_{r\text{is}}$, $F^1_{t\text{is}}$ and $F^1_{\varphi\text{is}}$ for the case of a Schwarzschild black hole ($a = 0$) by extrapolation along the three paths in the e–p plane show in figure 7.8 . The three panels, from top to bottom, show numerical data points for $\hat{F}^1_r$, $\hat{F}^1_\varphi$ and $\hat{F}^1_t$ respectively as extracted from the conservative piece of the SSF using Eqs. (7.48) and (7.49). Solid curves are cubic interpolations of the numerical data points, and the extrapolated values at $p = 6$ (which, in theory, should not depend on the choice of curve) represent our numerical predictions for $F^1_{r\text{is}}$, $F^1_{t\text{is}}$ and $F^1_{\varphi\text{is}}$. The small variance in these extrapolated values serves as a rough measure of error. The thick dot on the vertical axis marks the values found by Diaz-Rivera *et al.* [87]. For $F^1_{r\text{is}}$ and $F^{1\text{is}}_\varphi$ we find a close agreement with their results, but for $F^{1\text{is}}_t$ there is a discrepancy at a level ($\sim 2\%$) which we cannot explain. (The code used by Diaz-Rivera *et al.* cannot be retrieved to allow a careful examination of this discrepancy [176]; we are, however, quite confident in our results given the the good agreement between the values extrapolated from the different curves.)

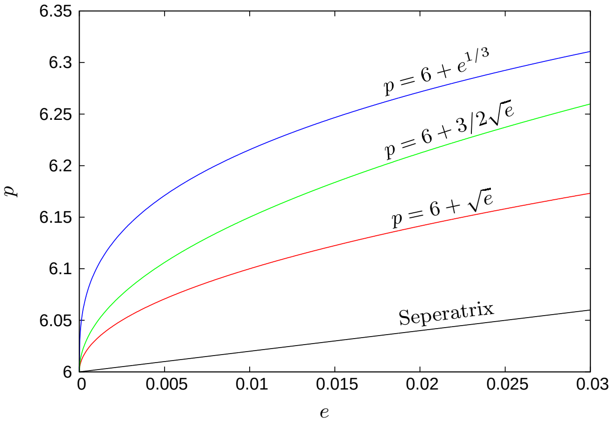

FIGURE 7.8: The sampling paths in the (p, e) plane used when computing $F^1_{r\mathrm{is}}$, $F^1_{t\mathrm{is}}$ and $F^1_{\varphi\mathrm{is}}$

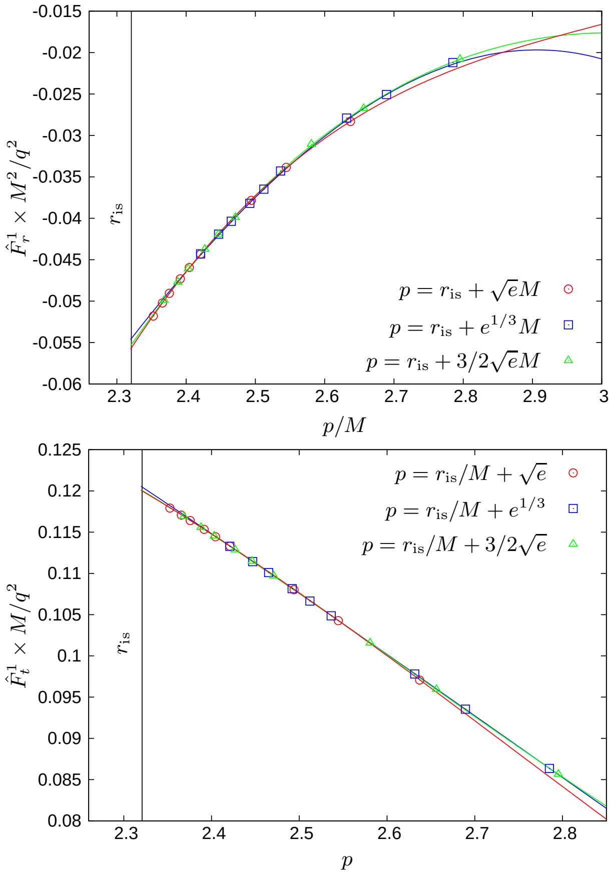

FIGURE 7.9: Same as in Fig. 7.7 but for $a = 0.9M$. We use the paths shown on the graphs to extract the values of $F^1_{r\mathrm{is}}$, $F^1_{t\mathrm{is}}$ and $F^1_{\varphi\mathrm{is}}$ via extrapolation to the ISCEO, whose location at $r_{\mathrm{is}} = 2.32088M$ is marked by the vertical line. (The results for $F^1_{\varphi\mathrm{is}}$, not shown here for brevity, are qualitatively similar to those of $F^1_{t\mathrm{is}}$.) Sample numerical values for $F^1_{r\mathrm{is}}$, $F^1_{t\mathrm{is}}$ and $F^1_{\varphi\mathrm{is}}$, and the resulting ISCEO shifts for different spins a, can be found in Table 7.5.

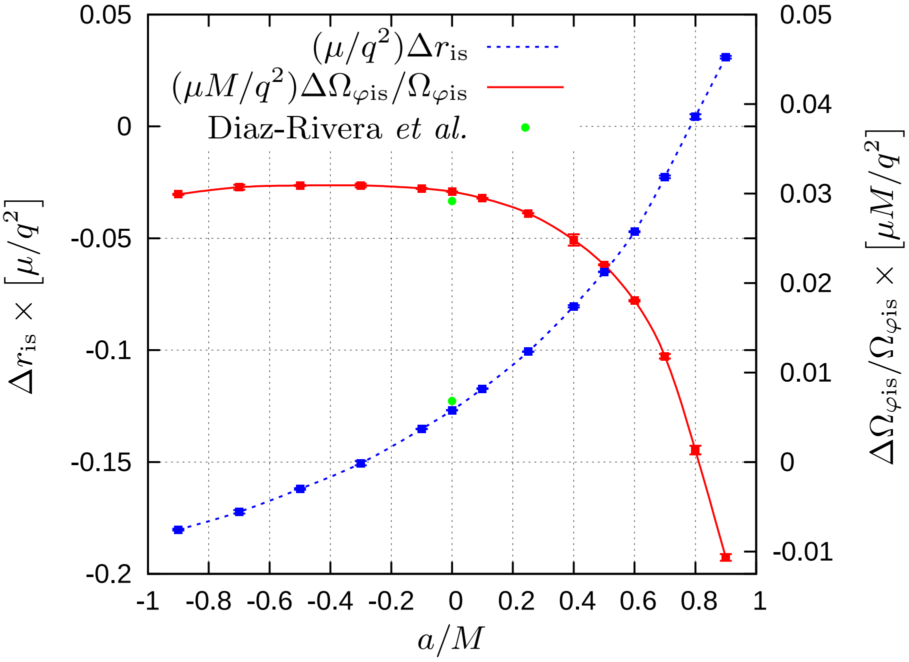

FIGURE 7.10: The conservative SSF effect upon the ISCEO location and frequency. We plot here the numerical results shown in Table 7.5 as a function of the Kerr spin parameter a (curves are cubic interpolations). Vertical error bars indicate the estimated numerical error. Notice in the graph that two separate scales are being used for $\Delta r_{\rm is}$ (left-hand scale) and $\Delta\Omega_{\varphi\rm is}/\Omega_{\varphi\rm is}$ (right-hand scale). The radial shift is monotonically increasing with a and changes sign around $a = 0.8M$. The frequency shift similarly changes its sign (and turns negative) at large spin values. Note that although the change of sign in the radial and frequency shifts occur near the same spin value ($a =\sim 0.8M$) the error bars on our results excludes the possiblity of the sign change occuring at the same spin value. The Schwarzschild ISCO shift results of Diaz-Rivera *et al.* [87] are marked (green, thick dots) for comparison. The small discrepancy is discussed briefly in the caption of Fig. 7.7.

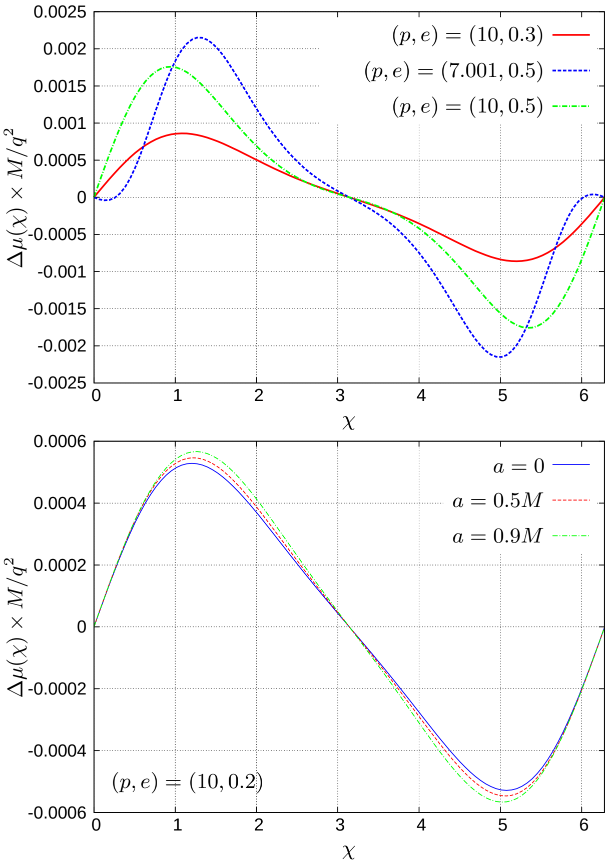

FIGURE 7.11: Rest-mass variation due to the SSF for a scalar charge in an eccentric equatorial orbit about a Kerr black hole. (Top panel) The change in the rest mass, for orbits about a Schwarzschild black hole, as a function of χ, is strongly dependent on the orbit's eccentricity. For e and p far away from the separatrix the mass initially increases and then returns to its original value at apastron before further decreasing and then once again returning to the original value at periastron. For a 'zoom-whirl'-type orbit the mass is observed to decrease slightly initially. (Bottom panel) Results for Kerr. The change in mass is weakly dependent on the black hole spin.

Chapter 8

Gravitational self-force in Schwarzschild spacetime: numerical implementation and results

In this chapter we detail the numerical computation of the GSF for a particle on a bound eccentric geodesic orbit in Schwarzschild spacetime. As usual we work in the frequency domain, with the required decomposition of the metric perturbation into tensor spherical harmonic and Fourier modes given in Chapter 4. As with our SSF eccentric orbit calculation presented in Chapter 7 we make use of the method of extended homogeneous solutions in our calculation. In order to do this we need to extend the original method first presented in Ref. [110] (and reviewed in Sec. 7.1.2) to cover the case of multiple coupled fields. We present this straightforward extension in Sec. 8.2 and then for clarity we present example cases of its use in Sec. 8.3.

In Secs. 8.5 and 8.6 we present sample results from our code for circular and eccentric orbits respectively. We find that in both cases our results compare well with those found in the literature [62, 63, 66, 67]. A key feature of our FD implementation is its efficiency when calculating the GSF along orbits with a low eccentricity and in Sec. 8.6.1 we discuss what qualifies as a low eccentricity orbit in this context. Lastly in Sec. 8.7 we highlight a numerical issue associated with nearly static modes that prevents our code from reaching greater eccentricity and that also places a limit on the orbit with the greatest p we can compute the GSF for. As part of this discussion we present a technique for mitigating some of the adverse effects of these modes and end with an outline of a potential solution that should allow the problem to be completely circumvented.

Before we consider any of the above we first consider the relevant numerical boundary conditions to use in our FD calculation.

8.1 Numerical boundary conditions

One of the main numerical tasks is to solve the radial equation (4.57) subject to the asymptotic boundary conditions presented in Sec. 4.6.3. Within our numerical implementation we cannot place our boundaries at spatial infinity and the event horizon. Instead we place boundary conditions at the edges of our numerical domain which runs from $r_*^{\rm in} \ll M$ to $r_*^{\rm out} \gg M$ (how we choose the boundary locations in practice will be discussed in the Algorithm section below).

As with the SSF numerical boundary conditions (Sec. 6.1.1), we assume that the radial fields admit an asymptotic expansion in $1/r$ at $r \to \infty$ and an asymptotic expansion in $r - 2M$ at $r \to 2M$. Combined with the leading order behaviour of the physical perturbation (Sec. 4.6.3), this leads us to take our ansätze for the numerical boundary conditions to be

$$R_-^{(i)} = e^{-i\omega r_*} \sum_{k=0}^{\infty} b_k^i (r_{\rm in} - 2M)^k \ , \tag{8.1}$$

$$R_+^{(i)} = e^{i\omega r_*} \sum_{k=0}^{\infty} \frac{a_k^i}{r_{\rm out}^k} \ , \tag{8.2}$$

for all modes (odd/even/static/radiating) with the exception of the outer field of the even static modes (the boundary conditions for which we will discuss shortly). By substituting the above ansätze into the field equations, we obtain recursion relations between the a_k^i's and (independently) the b_k^i. The resulting recursion relations are rather cumbersome so we do not give them here. Instead we refer to the work of Akcay [66] where they were first derived (as the BCs only depend upon the orbit through the mode frequency, Akcay's boundary conditions, derived as part of a work that developed a FD code to calculate the GSF for circular orbits in Schwarzschild spacetime, are applicable here).

For the radiating odd-partiy sector the first terms in the recursion relations for the a_k^i and b_k^i's are $a_{k=0}^{9,10}$ and $b_{k=0}^{9,10}$ respectively. We then construct a linearly independent basis of homogeneous solutions by setting $(a_0^9, a_0^{10}) = (1, 0)$ then $(a_0^9, a_0^{10}) = (0, 1)$ and likewise for (b_0^9, b_0^{10}). We shall label the resulting solutions to the field equation by $R_{\pm j}^{(i)}$ where i is the usual field index, j is the basis index and the $\pm$ distinguishes between the inner and outer solutions ('$-$' denotes an inner solution and '$+$' denotes an the outer solution). As an example, the '1' basis for the outer fields in the odd sector, $R_{+1}^{(9)}, R_{+1}^{(10)}$, are obtained by setting $(a_0^9, a_0^{10}) = (1, 0)$ when constructing the boundary conditions and then solving the odd sector field equations (4.62) and (4.63).

Construction of the basis of homogeneous solutions in the radiating even sector proceeds in much the same way. The first terms in the recursion relation are $(a_0^1, a_0^3, a_0^5, a_0^6, a_0^7)$ and $(b_0^1, b_0^3, b_0^5, b_0^6, b_0^7)$ and the basis solutions are constructed by setting $(a_0^1, a_0^3, a_0^5, a_0^6, a_0^7) = (1, 0, 0, 0, 0)$, $(0, 1, 0, 0, 0), \ldots$ and similarly for the b_0^i's.

If the ansatz in Eq. (8.2) is used to construct the outer field even-parity static mode boundary condition, one finds that the resulting recursion relation for the coefficients a_i^k does not have enough free parameters to represent a basis of three linearly independent solutions [66] (recall that for the even static modes we solve for 3 of the radial fields and construct the other two non-zero fields using the gauge equations — see Sec. 4.6.2). Instead for these modes we follow Akcay and take the ansatz

$$R_+^{(i)} = \sum_{k=k_{\rm start}}^{\infty} \frac{a_k^i + \bar{a}_k^i \log r_{\rm out}}{r_{\rm out}^k} \ , \tag{8.3}$$

which, when substituted into the homogeneous field equations (4.75)-(4.77), gives rise to a (coupled) recursion relation between the a_k^i's and $\bar{a}_k^i$'s which has the correct number of free parameters. The initial terms in the recursion relations for the even static modes are $\{a_l^3, a_l^5, a_{l+2}^5\}$ and $\{b_0^3, b_1^3, b_1^5\}$. The basis of homogeneous solutions are then constructed as before. Further details can be found in Ref. [66].

8.2 Construction of the inhomogeneous fields: method of extended homogeneous solutions for coupled fields

The goal of this section is to extend the method of EHS presented for a single scalar field in Ref. [110] (and overviewed in Sec. 7.1.2), to accommodate the multiple coupled fields we encounter when working on the Lorenz gauge GSF problem. This extension has already been carried out for the monopole ($l = 0$) and dipole ($l = 1$) modes by Golbourn [140] and implemented for those mode by Barack and Sago [67]. Here we present it for a generic lmn-mode.

For a given lmn mode our field equations take the form of a set of k coupled homogeneous ODEs. The linearly independent (by construction) homogeneous solutions – which, recall, we denote by $R^{(i)}_{\pm j}$, where j is the basis index ranging from 1 to k – form a k dimensional basis for the space of inhomogeous solutions. The correct EHS radial fields are then given by a weighted sum of the homogeneous solutions:

$$\tilde{R}^{(i)}_{\pm}(r) = \sum_{j=1}^{k} C^{\pm}_{j} R^{(i)}_{\pm j}(r) \ , \tag{8.4}$$

where hereafter an overtilde denotes an EHS version of a given quantity. The weighting coefficients, $C^{\pm}_j$, are computed via the matrix equation

$$\begin{pmatrix} C^-_j \\ C^+_j \end{pmatrix} = \int_{r_{\min}}^{r_{\max}} \Phi^{-1}(r) \begin{pmatrix} 0 \\ J^{(j)}(r) \end{pmatrix} dr \ , \tag{8.5}$$

where the $2k \times 2k$ matrix, Φ, of homogeneous solutions is given by

$$\Phi(r) = \left(\begin{array}{c|c} -R^{(i)}_{-j} & R^{(i)}_{+j} \\ \hline -\partial_r R^{(i)}_{-j} & \partial_r R^{(i)}_{+j} \end{array} \right) \ . \tag{8.6}$$

The source vector of length $2k$ in Eq. (8.5) is formed of k zeroes followed by the k FD sources $J^{(j)}(r)$ given in Appendix E. As with the scalar case these sources are singular at the orbital turning points ($J^{(j)} \propto 1/u^r$). Changing integration variable from r to t overcomes this difficulty and, as we use the χ orbital parametrization, it makes sense to further convert the integral from one over t to one over χ. Recalling that $dr/dt = u^r/u^t$ our practical formula for computing the weighting coefficients is given by

$$\begin{pmatrix} C^-_j \\ C^+_j \end{pmatrix} = \int_{0}^{\pi} \Phi^{-1}(\chi) \begin{pmatrix} 0 \\ J^{(j)}(\chi) \end{pmatrix} \frac{u^r}{u^t} \frac{dt}{d\chi} d\chi \ , \tag{8.7}$$

where the u^r in the integrand cancels the $1/u^r$ terms that appear in the FD sources.

Once the radial EHS fields have been obtained using Eqs. (8.4) and (8.7) the TD EHS fields $\tilde{h}^{(i)lm}(t, r)$ are then constructed via

$$\tilde{h}^{(i)lm}_{\pm}(t, r) = \sum_{n} \tilde{R}^{(i)lmn}_{\pm}(r) e^{-i\omega_{mn}t} \ . \tag{8.8}$$

The true TD solution is then given by

$$h^{(i)lm}(t, r) = \begin{cases} \tilde{h}^{(i)lm}_{+}(t, r), & r > r_p(t), \\ \tilde{h}^{(i)lm}_{-}(t, r), & r < r_p(t). \end{cases} \tag{8.9}$$

8.3 Construction of the inhomogeneous fields: examples

For clarity we now consider the practical use of Eq. (8.8) above when applied to the cases of odd and even sector fields.

8.3.1 Odd-parity sector

As discussed in Sec. 4.6.1 the non-zero fields in the non-static odd sector are $R^{(8)}$, $R^{(9)}$ and $R^{(10)}$. In practice we choose to solve for the $R^{(9)}$ and $R^{(10)}$ and construct the $R^{(8)}$ field using the gauge equation (4.61). The extended homogeneous radial fields are then given by

$$\tilde{R}_{\pm}^{(9)lmn}(r) = C_1^{\pm} R_{\pm 1}^{(9)lmn}(r) + C_2^{\pm} R_{\pm 2}^{(9)lmn}(r) \,, \tag{8.10}$$

$$\tilde{R}_{\pm}^{(10)lmn}(r) = C_1^{\pm} R_{\pm 1}^{(10)lmn}(r) + C_2 \pm R_{\pm 2}^{(10)lmn}(r) \,, \tag{8.11}$$

and the weighting coefficients are computed via

$$(C_1^- \; C_2^- \; C_1^+ \; C_2^+)^T = \int_{r_{\min}}^{r_{\max}} \Phi^{-1} (0 \; 0 \; J^{(9)} \; J^{(10)})^T \, dr \,, \tag{8.12}$$

where the 'T' superscript denotes transposition and the Φ matrix is given by

$$\Phi = \begin{pmatrix} -R_{1-}^{(9)} & -R_{2-}^{(9)} & R_{1+}^{(9)} & R_{2+}^{(9)} \\ -R_{1-}^{(10)} & -R_{2-}^{(10)} & R_{1+}^{(10)} & R_{2+}^{(10)} \\ -\partial_r R_{1-}^{(9)} & -\partial_r R_{2-}^{(9)} & \partial_r R_{1+}^{(9)} & \partial_r R_{2+}^{(9)} \\ -\partial_r R_{1-}^{(10)} & -\partial_r R_{2-}^{(10)} & \partial_r R_{1+}^{(10)} & \partial_r R_{2+}^{(10)} \end{pmatrix} . \tag{8.13}$$

Here, as we will often do, we have dropped the lmn indices for brevity where there is no ambiguity.

Information about the static odd modes is contained in a single field, $R^{(8)}$. In this case the extended homogeneous solution is constructed via

$$\tilde{R}_{\pm}^{(8)lmn} = C_{\pm}^{lmn} R_{\pm}^{(8)lmn} \,, \tag{8.14}$$

where the weighting coefficients are given by

$$\begin{aligned} \begin{pmatrix} C_- \\ C_+ \end{pmatrix} &= \int_{r_{\min}}^{r_{\max}} \begin{pmatrix} -R_-^{(8)} & R_+^{(8)} \\ -\partial_r R_-^{(8)} & \partial_r R_+^{(8)} \end{pmatrix}^{-1} \begin{pmatrix} 0 \\ J^{(8)} \end{pmatrix} dr \,, \\ &= \frac{1}{W} \int_{r_{\min}}^{r_{\max}} \begin{pmatrix} R_+^{(8)} \\ R_-^{(8)} \end{pmatrix} J^{(8)} \, dr \,, \end{aligned} \tag{8.15}$$

where we have defined W as the determinant of the matrix in Eq. (8.15). This turns out to be the (constant) Wronskian formed of the (linearly independent) inner and outer $R^{(8)}$ fields. The last line of Eq. (8.15) can be compared with the scalar field Eq. (7.4) and is seen to be of the same form, as would be expected.

8.3.2 Even-parity sector

The construction of the even sector inhomogeneous solutions is performed as above for the odd sector but now for the ($l \geq 2$) radiative modes the Φ matrix becomes 10×10 dimensional. The even dipole ($l = m = 1$) has one less field to solve for ($R^{(7)} = 0$) and thus the Φ matrix becomes

8×8 dimensional. For the static even modes the Φ matrix is 6×6 dimensional. For the static piece of the monopole ($l = 0$) there exist analytic solutions to the homogeneous field equations (see Sec. 4.6.4) and we construct the inhomogeneous modes numerically via the method of EHS with a 4×4 Φ matrix.

8.4 Algorithm and implementation

We now outline the required steps in computing the Lorenz gauge GSF for a particle on an eccentric orbit via the FD. The calculation algorithm is similar to the that of scalar particle in an eccentric orbit (Sec. 7.1.3).

- *Orbital parameters.* For a given orbital eccentricity, e, and semi-latus rectum, p, calculate the various properties of the orbit ($\mathcal{E}, \mathcal{L}, \Omega_r, \Omega_\varphi, T_r$, etc) using the formulae given in Chapter 4.

- *Compute the homogeneous fields.* For a given lmn mode the correct set of field equations and boundary conditions are selected (odd/even sector, static/non-static). If the homogeneous fields near the particle need to be computed numerically, as is the case for most modes, then we note that computing the boundary conditions is substantially computationally cheaper than integrating the field equations so it is advantageous to place the boundaries as close to the particle as possible. For the outer boundary series to converge we require that $\omega r_{\text{out}} \gg 1$. Through experimentation we find that setting $r_*^{\text{out}} = 10/\omega$ ensures rapid convergence of the series to our pre-specified relative accuracy of 10^{-14}. We then integrate the coupled field equations from the boundary to r_*^{min}, storing the values of the fields and their r_* derivatives at 5000 equally spaced in r_* radii between r_*^{min} and r_*^{max}. For a coupled set of k ODEs this process is repeated k times, each time with a different initial basis for the boundary conditions. A similar procedure is performed for the inner fields where we find it is always sufficient to place the boundary at $r_*^{\text{in}} = -50M$.

- *Construct the inhomogeneous fields.* Using Eqs. (8.4) and (8.5) the inhomogeneous radial fields are constructed. This is performed numerically for all lmn modes, even those for which we have analytic solutions for the homogeneous solutions. We find that is important that the integral in Eq. (8.5) is performed to a high accuracy, a task that is made more challenging by the oscillatory nature of the sources that appear in the integrand (see Appendix E). We achieve this high accuracy by coupling a standard adaptive integrator routine from the GSL [166] to the ODE solver. When the (adaptive) integrator requests the value of the integrand at a particular value of r_*, the ODE solver is loaded with information from the nearest of the 5000 points stored in the previous step, and integrates the homogeneous fields up to the requested r_* value in order to form the Φ matrix in Eq. (8.5) at the requested r_* value. We make use of this integration routine because we find that interpolating the data stored in the previous step does not produce sufficiently accurate results. For certain 'nearly static modes' we find that the Φ matrix is numerically difficult to invert — see discussion in Sec. 8.7.

- *Construct the gauge and EHS TD fields.* Following the hierarchical structure of the field equations described in Table 4.1 we use the gauge equations (4.58) to (4.61) to construct the remaining radial fields. The EHS TD fields are then constructed via Eq. (8.8).

- *Determine n_{max}.* Formally one needs to sum over all n in Eq. (8.8) but fortunately we are guaranteed that for large n, Eq. (8.8) converges exponentially so it is sufficient to truncate the sum at some $n_{\rm max}$, the precise value of which strongly depends on e but also (more weakly) on p, l and m. As each n-mode is added we evaluate how close the sum (8.8) is to the correct answer by calculating the jump in the r derivative of the fields at the particle and comparing it with the expected magnitude of the discontinuity (the 'jump') from the TD sources presented in Appendix E. Once the maximum relative difference between the numerically calculated jump and the expected jump drops below a certain threshold (which we take to be 10^{-8}) we consider the lm mode to have converged and select a new lm mode to compute. Note that there is no need to compute the lm modes in any particular order — see below Sec. 8.4.1.

- *Compute the GSF.* Using Eq. (5.58) compute $F_\alpha^{l({\rm full})}$, the l mode contribution to the full force. Recall that, owing to the coupling between scalar and tensor modes, if we wish to calculate a given $l_{\rm max}$ number of scalar l-modes we must calculate $l_{\rm max}+3$ tensor modes [see Eq. (5.58)]. As with the SSF we find it beneficial to split the GSF into dissipative and conservative pieces using Eq. (5.86) before regularizing (see Sec. 7.1.3 for a justification). It is then sufficient to simply sum the $F^{l\alpha}_{\rm diss}$ modes in order to compute the dissipative GSF as these modes converge exponentially. We find that an $l_{\rm max}$ of 15 modes typically suffices to capture the complete dissipative GSF to within our target relative accuracy of 10^{-6}. The conservative GSF requires regularizing using Eq. (5.42) with the regularization parameters from Eqs. (5.54)-(5.56). The resulting regularized contribution to the conservative component of the GSF exhibits power law behavior which necessitates estimating the contribution from the uncomputed high l modes. Our method for calculating the contribution from the uncalculated modes is the same as for the SSF detailed in Sec. 6.1.4.

8.4.1 Code structure and parallelization

The majority of our code is agnostic with regard to whether it is solving an odd/even or static/radiative mode. Instead it takes as input a structure that we call a 'coupled set'. This coupled set structure contains information about the ODE's to be solved, their boundary conditions and the relevant gauge equations. When the code is requested to solve a given lm mode it first determines which class the mode belongs to (odd/even etc.) and loads the correct coupled set. This provides a clear distinction in the code between the mode to be solved and the method of solution. We believe designing our code in this fashion aided rapid code development and testing and we also find that it provides for a high level of extensibility.

We also note that, owing to the tensor spherical harmonic mode decomposition, our problem naturally parallelizes as each lm mode of the metric perturbation can be calculated independently from the others. Our code is written to run on multiple CPU's, either within a single machine or on a cluster, using the Message Passing Interface (MPI). We also make use of dynamic load balancing whereby the root processor forks a thread which keeps track of which lm modes have already been computed. Once a processor has been assigned an lm mode it begins computing the n modes in the order $n = 0, -1, 1, -2, \dots$ and continues until a convergence criteria is met as discussed above. After a given processor completes an lm mode computation it contacts the thread on the root processor to request a new mode to work on. Each processor records its calculated contribution to the total GSF and once all the lm modes are computed upto $l = l_{\rm max}$ the results are combined.

8.5 Results: circular orbits

With the orbital eccentricity set to zero our code is able to compute the circular orbit GSF at a radius $r_0 = pM$ for $r_0 > 6M$ [this limitation exists as our (p, e) orbital parametrization is not valid below the separatrix]. Our code works in the circular orbit limit with no modification and as such the results provide a test of many of the routines in our code. In Table 8.1 we present a sample of our results for circular orbits along side results from other researchers. We find good agreement with previous published results as far out as $r_0 = 10000M$.

r_0/M	$(M/\mu)^2 F^r_{\text{(this thesis)}}$	$(M/\mu)^2 F^r_{\text{BS}}$	$(M/\mu)^2 F^r_{\text{A}}$	$(M/\mu)^2 F^r_{\text{B}}$
7	$2.149909(3) \times 10^{-2}$	2.14989×10^{-2}	$2.149907776(8) \times 10^{-2}$	2.1499068×10^{-2}
10	$1.33894710(9) \times 10^{-2}$	1.33895×10^{-2}	$1.3389470(2) \times 10^{-2}$	1.3389470×10^{-2}
20	$4.15705501(5) \times 10^{-2}$	4.15706×10^{-2}	$4.1570550(2) \times 10^{-2}$	4.1570550×10^{-2}
50	$7.44948606(1) \times 10^{-4}$	7.44949×10^{-4}	$7.44980(1) \times 10^{-4}$	7.4494860×10^{-4}
150	$8.6827445(5) \times 10^{-5}$	8.68274×10^{-5}	$8.673(1) \times 10^{-5}$	8.6827447×10^{-5}
500	$7.944104(2) \times 10^{-6}$	-	-	7.9441058×10^{-6}
800	$3.111342(3) \times 10^{-6}$	-	-	3.1113443×10^{-6}
10000	$1.998(2) \times 10^{-8}$	-	-	1.9993000×10^{-8}

TABLE 8.1: Comparison of circular orbit results for the (contravariant) radial component of the GSF. The first column shows the orbital radius and the second column shows the results from our code. The third through fifth columns show results from other researchers with F^r_{BS} = Barack and Sago [62], F^r_{A} = Akcay [66] and F^r_{B} = Berndtson [64]. A '–' is used when there is no published data available at the corresponding radius. Berndtson and Barack and Sago claim their results are accurate to all significant figures presented. The errors we quote on our results come our estimate of the error in the tail fit. Each data point in column 2 took less than a minute to compute on a single core of a standard 3GHz desktop machine.

8.6 Results: eccentric orbits

Using our code we can compute the GSF along a variety of bound eccentric geodesic orbits. In general we find that our code is efficient for orbits with $0 \leq e \lesssim 0.2$. For $e \neq 0$ we find that our code performs well for orbits with $6 + 2e < p \lesssim 50$ (recall that our orbital parametrization does not allow us to consider orbits with $p < 6 + 2e$). We present some discussion of the efficiency of our code in Sec. 8.6.1 and in Sec. 8.7 consider a major factor that hampers our ability to go to higher eccentricities/larger semi-latus rectum (as well as considering possible solutions).

In Tables 8.2 and 8.3 we present some sample GSF data for two orbits with $(p, e) = (7, 0.2)$ and $(p, e) = (10, 0.3)$. Data for these orbits is also presented by Barack and Sago [67] and we find our numerical results compare well with theirs. In Fig. 8.1 we plot the variation of the F^r and F^t components of the GSF over one orbital period for these two orbits.

8.6.1 Computational performance

As with the eccentric orbit SSF calculation we find that the computation burden of our GSF calculation increases rapidly with e (cf. Sec. 7.2.3). Nonetheless for orbits with $e \leq 0.2$ our code is capable of computing the GSF along the orbit in under 2 hours on a standard (3GHz, dual core) desktop machine (with an accuracy in the resulting GSF for approximately 6 significant figures). This is an order of magnitude faster than comparable time domain codes [67]. As discussed in Sec. 8.4.1 our code is written to run on a computer cluster where, as an example,

χ	$(M/\mu)^2 F^t_{\rm cons}$	$(M/\mu)^2 F^t_{\rm diss}$	$(M/\mu)^2 F^r_{\rm cons}$	$(M/\mu)^2 F^r_{\rm diss}$
0	0	-4.063301×10^{-3}	$3.35761(3) \times 10^{-2}$	0
$\pi/4$	$8.6476(2) \times 10^{-4}$	-2.156922×10^{-3}	$2.90989(2) \times 10^{-2}$	4.734955×10^{-3}
$\pi/2$	$8.2863(2) \times 10^{-4}$	-2.516802×10^{-4}	$2.1250350(9) \times 10^{-2}$	3.204190×10^{-3}
$3\pi/4$	$4.60755(7) \times 10^{-4}$	-1.124091×10^{-5}	$1.5901488(1) \times 10^{-2}$	9.633733×10^{-4}
π	0	-3.461415×10^{-5}	$1.40887697(9) \times 10^{-2}$	0

TABLE 8.2: Sample GSF data for an orbit with parameters $(p, e) = (7, 0.2)$. We present the dissipative and conservative components separately and remind that the total GSF is the sum of the two (see Fig. 8.1). We also only present results up to $\chi = \pi$ as the symmetries of the conservative and dissipative GSF components can be used to construct the results from $\chi = \pi$ to $\chi = 2\pi$ [see Eq. (5.86)]. The error bars given on the conservative components come from our estimate of the error in the tail fit. We believe all the digits presented for the dissipative components are accurate. We remind that the F^φ component can be constructed using the relation $u_\alpha F^\alpha = 0$ and that (by symmetry) $F^\theta = 0$.

χ	$(M/\mu)^2 F^t_{\rm cons}$	$(M/\mu)^2 F^t_{\rm diss}$	$(M/\mu)^2 F^r_{\rm cons}$	$(M/\mu)^2 F^r_{\rm diss}$
0	0	-1.024136×10^{-3}	$2.303161(3) \times 10^{-2}$	0
$\pi/4$	$1.1616640(9) \times 10^{-3}$	-3.678557×10^{-4}	$1.985394(2) \times 10^{-2}$	1.177843×10^{-3}
$\pi/2$	$1.087282(4) \times 10^{-3}$	3.343391×10^{-5}	$1.3621999(2) \times 10^{-2}$	5.654574×10^{-4}
$3\pi/4$	$5.122834(3) \times 10^{-4}$	1.104178×10^{-5}	$8.8100672(4) \times 10^{-2}$	1.063752×10^{-4}
π	0	2.836163×10^{-7}	$7.1108985(3) \times 10^{-2}$	0

TABLE 8.3: Same as for Table 8.2 but with sample GSF data for an orbit with parameters $(p, e) = (10, 0.3)$. See Fig. 8.1 for a plot of the total (dissipative plus conservative) GSF for this orbit.

by utilising 64 processors it is possible to compute the GSF for orbits with $e \leq 0.2$ in a matter of minutes — See Fig. 8.2. This ability of our code to produce large quantities of data for low eccentricity orbits is crucial to the work we present in Chapter 9. We have not explored the efficiency of our code for orbits with $e > 0.2$ as for these orbits the results of our code are less accurate. We outline one potential source of this loss of accuracy in the next section.

8.7 Nearly static modes

We now discuss a numerical issue that limits the regions of the (p, e) parameter space we can explore with our current code. The 'bad' regions, where our code struggles, correspond to regions of the parameter space where our code encounters lmn modes with a small mode frequency – see Fig. 8.3. The problem manifests itself in two ways. In Sec. 8.7.1 we outline the first problem and present a method for easing the difficulties associated with it. In Sec. 8.7.2 we discuss the more challenging second problem and present a potential solution in Sec. 8.7.3. It is important to note that the difficulties we encounter when attempting to compute nearly static modes are purely a numerical issue – there is nothing fundamentally wrong with our FD setup.

The root of both problems lies in the numerical task of accurately inverting the matrix Φ that appears in Eq. (8.5). The *condition number* is generally used to describe how difficult this task is. For a matrix A the condition number is defined to be

$$\kappa(A) = ||A|| \cdot ||A^{-1}|| \tag{8.16}$$

where $||\cdot||$ is a suitable matrix norm which gives $\kappa(A) \geq 1$ (the precise norm used is not relevant

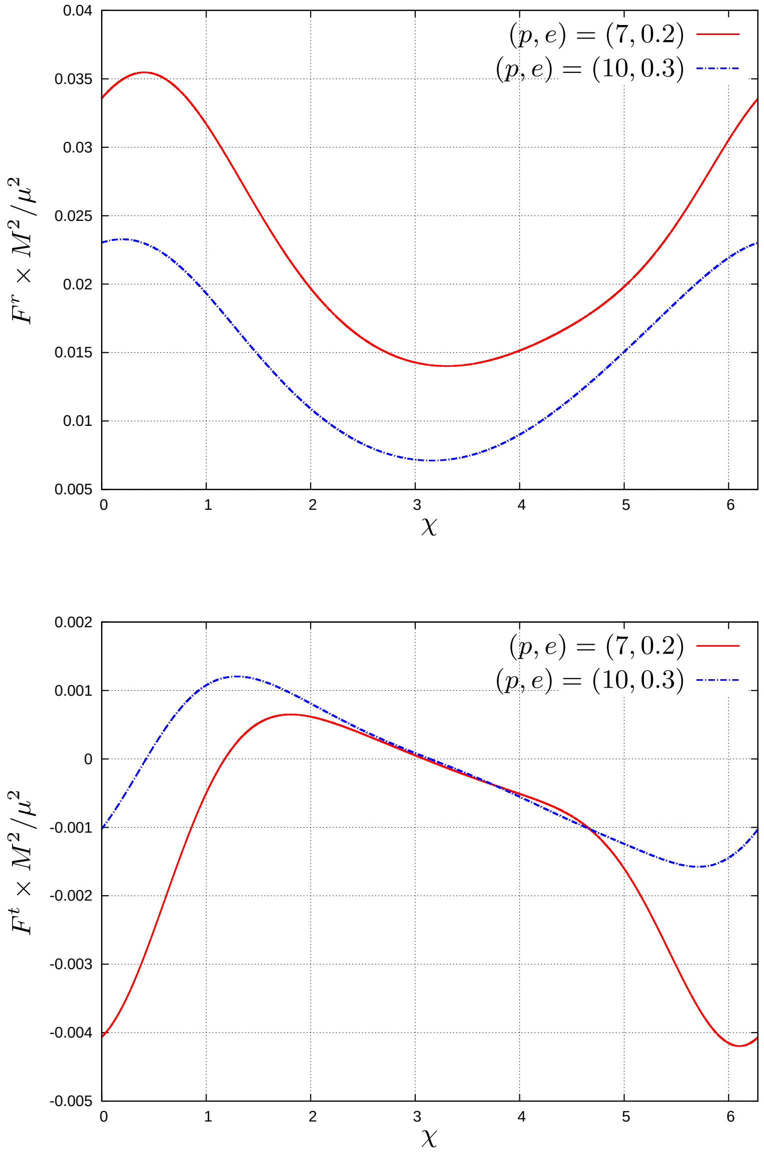

FIGURE 8.1: Variation of the total (dissipative plus conservative) GSF for orbits with parameters $(p, e) = (7, 0.2)$ and $(p, e) = (10, 0.3)$. The upper panel shows the variation of the radial component along the orbit and the lower panel shows variation of the temporal component. We remind that within our orbital parametrization periastron occurs at $\chi = 0$ and $\chi = 2\pi$ and that apastron is reached at $\chi = \pi$.

to our discussion). If κ is close to 1 then the matrix is said to be *well conditioned* and A^{-1} can be computed with good accuracy. On the other hand if κ is large the matrix is said to be *ill conditioned*. In practice this means that a loss of precision is associated with the computation of A^{-1}. Roughly speaking if $\kappa(A) = 10^k$ inverting A will lose k digits of accuracy over the normal numerical precision of the arithmetic operations (so if we have a matrix formed of double precision numbers the inverted matrix will be roughly accurate to $16 - k$ digits of precision). With this concept of a condition number in mind we now examine the two problems associated with nearly static modes.

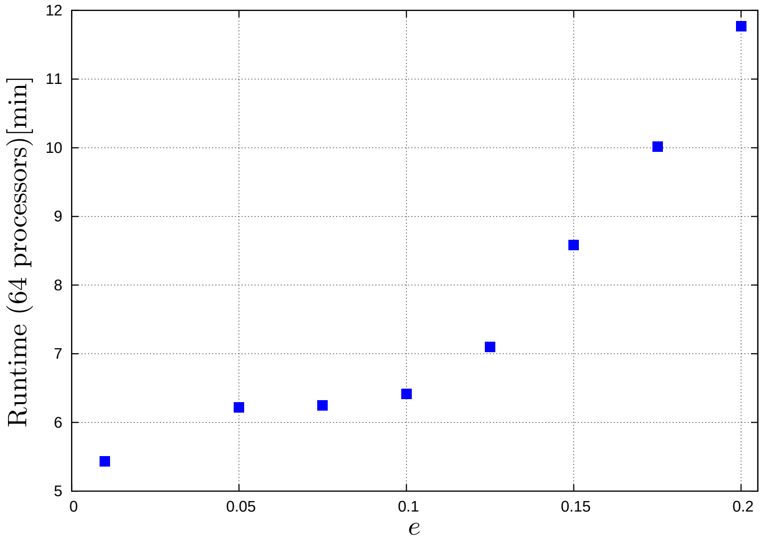

FIGURE 8.2: Computation time of our FD GSF code on a cluster of 64 processors to a relative accuracy of 10^{-6}. For orbits with $e < 0.1$ the run time is roughly constant at around 6 minutes. Between $e = 0.1$ and $e = 0.2$ we observe a fast increase in the runtime. Similar results are observed in the scalar case (see Fig 7.6). Orbits with $e > 0.2$ are not considered here as we find our code is less accurate for these orbits.

8.7.1 Power-law growth

The first numerical issue we face for nearly static modes is highlighted by considering the large r behavior of the field Eq. (4.57). We shall initially consider the case of the even dipole ($l = 1, m = 1$) mode and will generalize the results to the other modes at the end of the section. We shall first outline the issue and then present a technique that reduces its adverse effects. Defining $\vec{R} \equiv (R^{(1)}\ R^{(3)}\ R^{(5)}\ R^{(6)})^T$ we can express the large r behavior of the even dipole field equations in the form

$$\vec{R}''(r) + [Ar^{-2} - \omega^2]\vec{R}(r) = 0\ , \tag{8.17}$$

where we have ignored terms of $\mathcal{O}(M/r^{-3})$ and

$$A = \begin{pmatrix} -4 & 2 & 2 & 2 \\ 2 & -4 & -2 & -2 \\ 4 & -4 & -6 & -4 \\ 2 & -2 & -2 & -4 \end{pmatrix} . \tag{8.18}$$

We now seek to rotate the basis of homogeneous solutions in such a way as to separate the field equations. This is done by diagonalizing A which is possible if there exists a matrix Q, and a diagonal matrix L, such that $QA = LQ$. These two matrices do indeed exist and are given by $L = \mathrm{diag}(-2, -2, -2, -12)$ and

$$Q = \begin{pmatrix} 1 & 1 & 0 & 0 \\ 0 & 1 & 0 & -1 \\ 1 & -1 & 1 & 0 \\ 1 & -1 & -1 & -1 \end{pmatrix} . \tag{8.19}$$

We can therefore define the new variable

$$\vec{F} = Q\vec{R}\,, \tag{8.20}$$

in which the field equations separate and take the form

$$\vec{F}''(r) + \left[\tilde{V}_\ell(r) - \omega^2\right]\vec{F}(r) = 0\,, \qquad \text{with} \quad \tilde{V}_l(r) = \frac{\ell(\ell+1)}{r^2} + \mathcal{O}\left(\frac{M}{r^3}\right)\,, \tag{8.21}$$

where $\ell = 1$ or $\ell = 3$. With respect to the new variable $\vec{F}$ the coupling between the fields only enters at $\mathcal{O}(M/r^3)$. The regular solutions to Eq. (8.21) are $1/r$ and $1/r^3$ corresponding to $\ell = 1$ and $\ell = 3$ respectively. As $r \to \infty$ the potential, $\tilde{V}_\ell(r)$ becomes subdominant to the ω^2 term and $\vec{R}$ exhibits oscillatory behavior. This region is often referred to as the wavezone. On the other hand when $r^2 < [\ell(\ell+1)]/\omega^2$ the fields exhibit power law behavior. The transition between these two regimes takes place at $r_{\rm trans} \sim [\ell(\ell+1)]^{1/2}/\omega$.

We now observe that when ω is small (and/or ℓ large) the transition to the wavezone moves out to very large radius. In this case there is a long period of power law growth between our numerical boundary in the wavezone and the particle's location. This in itself is not a problem but as noted above the $\vec{F}$ fields (and therefore certain linear combinations of the $\vec{R}$ fields) exhibit power-law growth at different rates. The upshot of this is that the amplitude of the four fields will be widely separated at the particle, in turn endows the Φ matrix with a high condition number, making constructing Φ^{-1} accurately numerically difficult.

Our technique for mitigating this issue is to rescale one of the bases at the boundary in such a way that once the fields are integrated to the particle's location they all are of the same order of magnitude. In terms of the $\vec{F}$ variables, if we choose our initial boundary terms to be $\{a^1_0, a^3_0, a^5_0, a^6_0\}$ to be $\{1,0,0,0\}, \{0,1,0,0\}, \{0,0,1,0\}$ and $(\omega p)^2\{0,0,0,1\}$ we find that all the fields in the Φ matrix will have approximately the same amplitude around $r = p$ (we have inserted the ω to balance the dimensions of p). Of course rewriting our field equations in terms of $\vec{F}$ would require a lot of work. Fortunately we there is no need to do this if we work with our usual $\vec{R}$ variables and instead take the initial terms in the boundary conditions to be $(Q^{-1})_{i1}$, $(Q^{-1})_{i2}$, $(Q^{-1})_{i3}$ and $(\omega p)^2(Q^{-1})_{i4}$. Modulo a global factor of $1/5$ which we may omit, these initial boundary terms are given explicitly by $\{3,2,-1,2\}, \{-1,1,2,-4\}, \{1,-1,3,-1\}, (\omega p)^2\{1,-1,-2,-1\}$. With this choice of bases the $\vec{F}(= Q\vec{R})$ fields are scaled correctly.

The above analysis can be carried out for other modes. For generic even modes ($l \geq 2$) where we have $\vec{R} \equiv (R^{(1)}\ R^{(3)}\ R^{(5)}\ R^{(6)}\ R^{(7)})$ the A matrix in Eq. (8.17) reads

$$A = \begin{pmatrix} -(2-\mathfrak{L}) & 2 & 2 & 2 & 0 \\ 2 & -(2+\mathfrak{L}) & -2 & -2 & 0 \\ 2L & -2L & (-4+\mathfrak{L}) & -2L & 2 \\ 2 & -2 & -2 & (-2+\mathfrak{L}) & 0 \\ 0 & 0 & 2\lambda & 0 & 2-\mathfrak{L} \end{pmatrix}\,, \tag{8.22}$$

where, recall, $\mathfrak{L} = l(l+1)$ and $\lambda = (l+2)(l-1)$. For the generic odd modes ($l > 1$), where $\vec{R} \equiv (R^{(9)}\ R^{(10)})T$, the A matrix is given by

$$A = \begin{pmatrix} -(\mathfrak{L}+4) & 2 \\ 2\lambda & -(\mathfrak{L}-2) \end{pmatrix}\,. \tag{8.23}$$

In each case the various fields are found to exhibit power-law behavior with different rates of growth. Using the above technique the fields can be rescaled at the boundary so that at the particle all the fields are of the same order of magnitude. We find that without this technique we are generally restricted to areas of the parameter space where $|\omega M| > 10^{-4}$ but that when the rescaling is implemented we can explore all regions with $|\omega M| > 10^{-5}$. The difference between the area covered by these two regions is substantial. Further reduction of the area of the parameter space we are unable to explore with our code requires a solution to the matrix degeneracy problem that we outline now.

8.7.2 Matrix degeneracy problem

The source of the second, more challenging, problem encountered in the computation of nearly static modes lies in the different behaviors of the radiating and static modes that we recap now. For concreteness we discuss the problem with respect to the even ($l+m =$ even) modes, though the same difficulties present themselves for the odd sector modes. As discussed in Sec. 4.6.2 solving for the homogeneous radiating ($\omega \neq 0$) even sector field equations requires solving for seven $i = 1, 2, .., 7$ non-zero fields (the odd sector fields $i = 8, 9, 10$ are zero for the even sector). In practice we only need to solve for five fields as we can construct the remaining two fields from the gauge equations (4.58), (4.59) and (4.60).

By contrast for static ($\omega = 0$) even modes (see Sec. 4.6.2) we have only to solve for five fields as we have $R^{(2)} = R^{(4)} = 0$. Again in practice we solve for a reduced set, which we choose to be the $i = 1, 3, 5$ fields, and construct the remaining two fields from the gauge equations. It is important to note that it is not possible to solve for all five fields simultaneously. For the case of static modes the gauge equations imply that linear relations exist between the five fields and consequently the inhomogeneous solutions cannot be constructed via Eq. (8.8) with a 10×10 dimensional Φ matrix of the homogeneous solutions and their derivatives, as this matrix will be singular.

The difficulty with near static modes is now apparent: for radiating static modes we must use a 10×10 matrix in order to find the inhomogeneous fields, but as $\omega \to 0$ this matrix becomes ever more singular as the fields become closer to being linearly dependent (through the gauge conditions). This closeness to linear dependence manifests itself as a high condition number of the matrix Φ and, as discussed above, this implies a loss of numerical accuracy when computing these modes. This problem is challenging to overcome but in Sec. 8.7.3 (below) we present a method that we believe can mitigate the low accuracy issues resulting from the degeneracy problem for nearly static modes.

8.7.3 Degeneracy problem: potential solution via perturbations about a singular matrix

In this section we present a method that we believe will allow us to overcome the near static mode problem outlined above. Our goal will be to accurately evaluate the $\Phi^{-1}(r)J(r)$ term that appears in Eq. (8.8), where we have defined $J(r) \equiv (0 \; J^i_j(r))^T$. The proposed technique is to write the matrix of homogeneous solution, Φ, and the sources, $J^{(i)}$, in the expanded form

$$\Phi = \Phi_0 + \epsilon\Phi_1 + \epsilon^2\Phi_2 + \dots\ , \tag{8.24}$$

$$J = J_0 + \epsilon J_1 + \epsilon^2 J_2 + \dots\ , \tag{8.25}$$

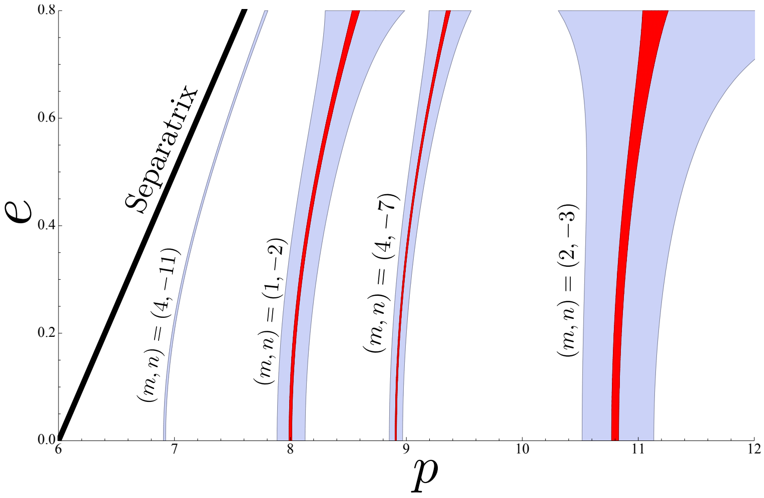

FIGURE 8.3: Regions of the (p,e) parameter space where $M|\omega| = M|m\Omega_\varphi + n\Omega_r|$ is small. The lighter (violet) shaded areas mark regions where $M|\omega| < 10^{-3}$. The darker (red) shared areas mark regions where $m|\omega| < 10^{-4}$. The particular (m,n) values for each region are shown to their left. As discussed in the main text lmn modes within these low ω regions can be numerically challenging for our code to evaluate accurately. Note that for any values of Ω_r and Ω_φ it will be possible to find m and n values that make $M|\omega|$ small. Consequently the entire parameter space is covered by low $M|\omega|$ regions, but often this is not an issue as the values of m and n for many of these regions are high and the corresponding mode does not need to be computed in order to calculate the GSF to the accuracy we seek. This is especially true for orbits with low eccentricity (where $n_{\max}$ is typically lower than for higher eccentricity orbits). Lastly we remind that as $p \to \infty$ the two orbital frequencies become degenerate (reducing to the usual Keplarian orbital frequency). This implies that for orbits with large p modes with $(m,n) = (1,-1)$ will have a small value of $M|\omega|$. This places a limit on the largest $(e \neq 0)$ orbit we can compute with our current code.

where ϵ is some small parameter with the properties that $\epsilon \to 0$ as $\omega \to 0$. The Φ_k are matrices with Φ_0 a singular matrix (whose elements we shall see are composed of the $i = 1,3,5,6,7$ static fields). Once Φ and the $J^{(i)}$'s are written in this form we can use the method outlined in Appendix I to accurately evaluate $\Phi^{-1}(r)J(r)$ order-by-order.

We first present the expansion of the sources. From Appendix E it can be seen that the ω dependence of the FD sources is entirely from terms of the form

$$\tilde{J}^{(i)} \sin(\omega t_p - m\varphi_p) \qquad \text{or} \qquad \tilde{J}^{(i)} \cos(\omega t_p - m\varphi_p)\ , \tag{8.26}$$

where the $\tilde{J}^{(i)}$'s are the coefficients of the oscillatory term in the FD sources. When expanding the sources it is important that we choose a good expansion parameter which we now define to be $\epsilon = \omega T_r$ where T_r is the radial orbital period. In particular this implies that over one orbit, starting with $t = 0$ at periastron, $t_p/T_r \leq 1$ and therefore $\omega t_p = \epsilon/T_r t_p \ll 1$ for $\epsilon \ll 1$. It is now straightforward to expand the source terms. For instance the expansion of the sin term reads

$$\begin{aligned} J^{(i)} \sin(\omega t_p - m\varphi_p) \approx & J^{(i)} \left[\frac{\epsilon}{T_r} t_p + \frac{1}{3!} \left(\frac{\epsilon}{T_r} t_p \right)^3 + \dots \right] \cos(m\varphi_p) \\ & - J^{(i)} \left[1 - \frac{1}{2} \left(\frac{\epsilon}{T_r} t_p \right)^2 + \dots \right] \sin(m_p)\ . \end{aligned} \tag{8.27}$$

The cos expansion is similarly computed. With both expansions in hand it is then straightforward to read off the value of the J_k source vectors from the coefficients of ϵ^k.

In order to construct the Φ_k's we need to expand the homogeneous field equations in powers of ϵ. From Sec. 4.6 we have that the radial field equations take the form

$$\partial^2_{r^*} R^{(i)} = \left[V_l(r) - \left(\frac{\epsilon}{T_r} \right)^2 \right] R^{(i)} + 4\tilde{\mathcal{M}}^{(i)}_{(j)} R^{(j)} = 0 \,, \tag{8.28}$$

where we have used $\omega = \epsilon/T_r$ and recall that $\tilde{\mathcal{M}}^{(i)}_{(j)}$ contains all the coupling between the fields and the potential is given by

$$V_l(r) = \frac{2Mf}{r^3} + \frac{l(l+1)f}{r^2} \,, \tag{8.29}$$

with $f = 1 - 2M/r$. Expanding the fields in the form

$$R^{(i)} = R^{(i)}_0 + \epsilon R^{(i)}_1 + \epsilon^2 R^{(i)}_2 + \dots \,, \tag{8.30}$$

and substituting this expansion into the field equation (8.28) gives us an iterative equation for the $R^{(i)}_k$:

$$\partial^2_{r^*} R^{(i)}_k = V_l(r) R^{(i)}_k - T_r^{-2} R^{(i)}_{k-2} + 4\tilde{\mathcal{M}}^{(i)}_{(j)} R^{(j)}_k = 0 \,, \tag{8.31}$$

where we take $R^{(i)}_{k<0} = 0$. The $R^{(i)}_0$ are the usual static modes, which we know how to solve for already (see Sec. 4.6.2). These fields are used to form the singular A matrix in Eq. (I.2). The $R^{(i)}_k$ fields are proportional to ϵ^k and hence these are used to form the B_k matrices in Eq. (I.2).

This technique remains to be implemented. Initial tests indicate that we can solve Eq. (8.31) as a single coupled set of ODEs even for very large k once suitable boundary conditions are applied. If the technique can be successfully applied to our current code it should allow for computation of the GSF for the points of the parameter space that have modes with low ωM values. This should include orbits with large p, which are currently excluded from the region of the parameter space our code can access [recall that as $p \to \infty$ the two orbital frequencies become degenerate and thus modes with $(m, n) = (1, -1)$ will be nearly static (as for these modes $\omega = \Omega_\varphi - \Omega_r \ll M^{-1}$)].

8.8 ISCO shift due to conservative GSF

One application of our eccentric orbit code is to compute the shift to the ISCO location due to the conservative GSF. We consider only the shift due to the conservative GSF as it was shown by Ori and Thorne [179] that when dissipative effects are included the location of the ISCO is not well defined (instead an inspiraling particle passes through a transition regime between the inspiral and the plunge). Though the shift due to the conservative GSF turns out to be too small to be observable, it is nonetheless useful as the frequency of a particle at the shifted ISCO is a gauge invariant quantity that can be used as a point of comparison with other approaches to the general relativistic two body problem [108, 71].

The calculation of the conservative GSF effect on the ISCO location was first carried out by Barack and Sago [67, 175] We nonetheless present the results of our own calculation in order to demonstrate the high accuracy of our FD code. In Ref. [67] Barack and Sago make two calculations of the ISCO shift. Their 'method I' is to use the results of their eccentric orbit TD code to compute two coefficients in the $\mathcal{O}(e)$ description of the orbital motion for orbits with $p = 6 + \sqrt{e}$ with small e. They then extrapolate to the $e \to 0$ limit to calculate the ISCO shift. This is the method we shall take here (this method closely follows that which we presented for the SSF in Sec. 7.3, or more precisely the method we presented there closely models that of Ref. [67]). Barack and Sago's 'method II' involves expanding the field equations and sources to $\mathcal{O}(e)$ and we will present a similar calculation using our FD code in an forthcoming paper [104].

Once the conservative piece of the GSF is computable making use of method I is straight forward. The correction to the radial location and the azimuthal frequency of the ISCO due to the conservative GSF is computed via Eqs. (7.35) and (7.38), first derived in Ref. [67]. For easy reference we repeat the formula here:

$$\Delta r_{\text{is}} = (M^2/\mu)\left(216F^r_{0\text{is}} - 108F^r_{1\text{is}} + \sqrt{3}M^{-2}F^1_{\varphi\text{is}}\right) , \tag{8.32}$$

$$\frac{\Delta\Omega_{\varphi\text{is}}}{\Omega_{\varphi\text{is}}} = -\frac{\Delta r_{\text{is}}}{4M} - \frac{27M}{2\mu}F^r_{0\text{is}} . \tag{8.33}$$

We cannot use our eccentric orbit code to calculate the circular orbit value $F^r_{0\text{is}}$ [as our (p,e) parametrization is not valid at the ISCO]. Instead we take the highly accurate result obtained using Akcay's circular orbit FD code [66]

$$F^r_{0\text{is}} = 2.4466495(4)\times 10^{-2} . \tag{8.34}$$

The $\mathcal{O}(e)$ coefficients $F^r_{1\text{is}}$ and $F^1_{\varphi\text{is}}$ in Eq. (8.32) are obtained numerically via Eqs. (7.48) and (7.49). In using these equations we compute the $\hat{F}^r_1$ and $\hat{F}^1_\varphi$ coefficients that appear in Eqs. (7.48) and (7.49) for a variety of orbits with $p = 6+\sqrt{e}$. We then produce a fit to our numerical data and extrapolate to the ISCO in order to extract the values of $F^r_{1\text{is}}$ and $F^1_{\varphi\text{is}}$ (see Fig. 8.4). Using our code we find

$$F^r_{1\text{is}} = 0.062094\mu/M^2 , \tag{8.35}$$

$$F^{1\text{is}}_\varphi = -1.06623\mu . \tag{8.36}$$

Equations (8.32) and (8.33) can then be used to calculate the conservative GSF effect on the radial location of the ISCO and the relative frequency shift of an orbit at the perturbed ISCO with respect to the unperturbed ISCO. With $F^r_{1\text{is}}$ and $F^{1\text{is}}_\varphi$ as given above we find

$$\Delta r_{\text{is}} = -3.2681\mu , \tag{8.37}$$

$$\frac{\Delta\Omega_{\varphi\text{is}}}{\Omega_{\varphi\text{is}}} = 0.4867\mu/M . \tag{8.38}$$

We present no error bars on the results in this section as, at the time of writing, we have yet to compute them. Nonetheless these results from our code are comfortably within the error bars of the highly accurate results obtained by Barack and Sago using their 'method II' technique. The increased accuracy of our method I results over those in Ref. [67] follows primarily from our code's ability to produce accurate results for $\hat{F}^r_1$ and $\hat{F}^1_\varphi$ closer to the ISCO.

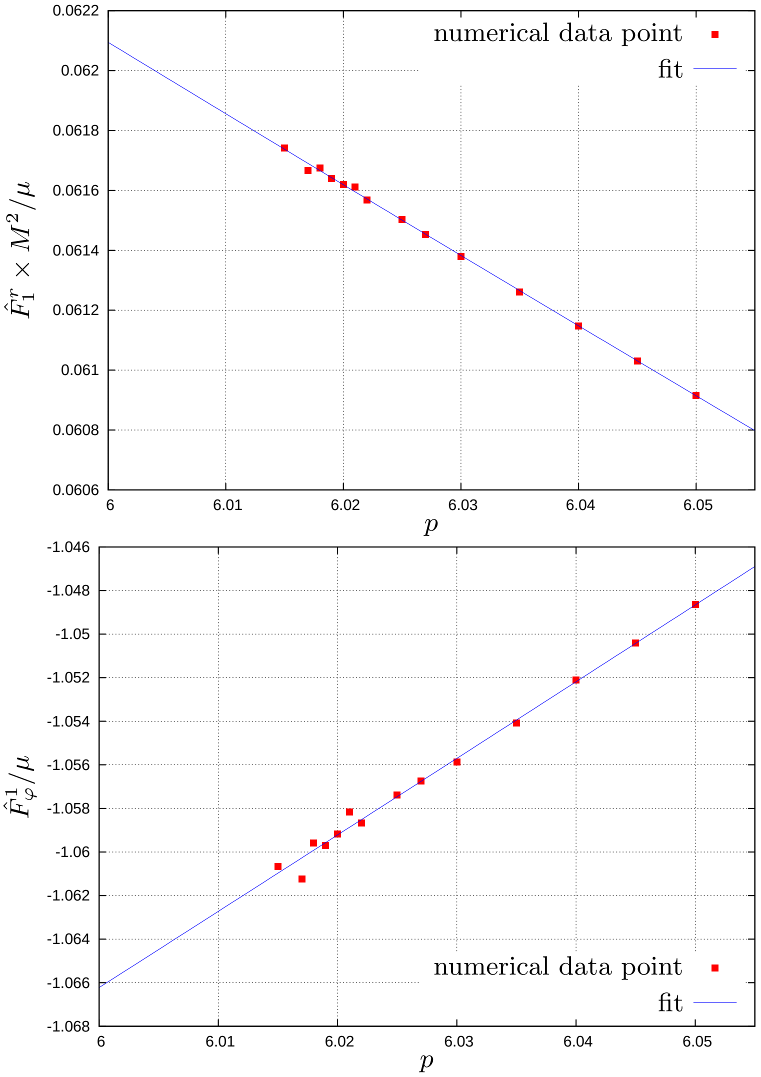

FIGURE 8.4: Calculation of F_1^r and F_φ^1 by extrapolation along the curve $p = 6+\sqrt{e}$. The same extrapolation method was described and performed as 'Method I' in Ref. [67] where they used a TD code to compute the GSF. Our FD domain code is capable of producing results close to the separatrix than their TD code, giving improved results using the same technique calculate the ISCO shift. We calculate the shift in the radial location and frequency of the ISCO due to the conservative GSF from our extrapolated F_1^r and F_φ^1 and find our result is within the error bars presented by the highly accurate 'Method II' technique presented in Ref. [67] (the next step in the calculation is to add error estimates to our results).

Chapter 9

Orbital evolution using osculating geodesics

In Chapter 8, we provided details of a FD code to compute the GSF for a particle on an eccentric geodesic orbit about a Schwarzschild black hole. As discussed in Chapter 1, our motivation for studying the self-force problem stems from a desire to model EMRI binary systems. In this chapter, we detail the implementation of a scheme to use our geodesic GSF data to evolve the inspiral over many thousands of orbits. This is the first orbital evolution to include all first-order-in-the-mass-ratio corrections to the particle's motion though, as we shall see, there is an important caveat to this statement.

In order to place the discussion of this caveat in context we will now very briefly review the results of a two timescale analysis EMRI systems carried out by Hinderer and Flanagan [164]. In their work they showed that the dominant contribution to the phase evolution during an inspiral comes from the orbit-averaged dissipative piece of the SF. In Schwarzschild spacetime this piece can be calculated directly from the asymptotic fluxes of energy and angular momentum passing out to spatial infinity and down through the event horizon, side stepping any need for a local computation of the SF. The sub-leading order contributions come from the oscillatory piece of the dissipative SF, the conservative piece of the SF and the second-order-in-the-mass-ratio orbit-averaged dissipative SF. Explicitly the scaling of the relative contributions from the SF to the phase evolution go as

$$\begin{aligned}\mathcal{O}(M/\mu):&\quad \text{Orbit averaged dissipative piece of the SF}\\ \mathcal{O}(1):&\begin{cases}\text{Oscillatory component of the dissipative SF}\\ \text{Conservative component of the SF}\\ \text{Orbit averaged dissipative piece of the second-order SF}\end{cases}\end{aligned}$$

In this chapter we shall calculate, for the first time, the magnitude of the first two order unity contributions (as listed above) to the phase evolution of an inspiralling CO into a massive black hole. To evolve the orbit we shall use the osculating orbit description of the inspiral (see Fig. 9.1). Whilst for a generic trajectory the osculating orbit description is exact, when computing an inspiral due to the SF the resulting inspiral is an approximation to the correct motion, as we now discuss.

The key assumption we shall make when using the osculating geodesic description of the motion is that the GSF felt but the particle at a given instance of time is the GSF felt by a particle that has spent its entire past history travelling along the osculating geodesic. We are forced to make this 'osculating assumption' because our GSF FD code detailed in Chapter 8 gives the GSF as a function along geodesics. Formally, the true contribution to the GSF at a given time is obtained by integrating over the entire past history of the inspiralling particle [see Eq. (5.37)]. In practice though there is an expectation that the contributions from the distant past will have a negligible effect on the present motion and in fact only the recent history of the particle contributes significantly to the current GSF felt by the particle. The idea then is that, for a 'slowly evolving' inspiral, the recent past of the particle can be closely approximated by the osculating geodesic. It then follows that the true GSF will be closely approximated by the GSF felt by a particle that spent all it past on the osculating geodesic.

We have been a little vague in the preceding paragraph about the errors made by using this approximation because, at the time of writing, they are unclear. Clearly as the mass ratio tends to zero the osculating orbit GSF and the true GSF converge (in the zero mass ratio limit the particle moves along a geodesic). On the other hand as the mass ratio shrinks the number of orbits in the inspiral increases and so, although the error from the osculating assumption decreases, it has longer to accumulated over the inspiral. It is currently unclear how these two competing effects will balance out and thus where the error from making the osculating assumption fits into Hinderer and Flanagan's analysis outlined above. In may in fact turn out that that the error in the phase evolution from making the osculating assumption is of order unity and thus competes with, for instance, the conservative GSF contribution to the phase evolution. If this turns out to be the case it will be the coefficients of each order-unity contribution that will determine if the osculating assumption can be used to accurately track the phase evolution of the inspiral.

Throughout the rest of this chapter we shall assume that the error in the phase evolution from making the osculating assumption can be neglected though we emphasise that this is a large assumption. In the concluding chapter of this work we will discuss how this error can and should be quantified with a future research program.

The key advance that allows us to make use of the osculating orbit description of motion to evolve the inspiral is the high efficiency of our FD GSF code. For low eccentricity orbits our FD code is orders of magnitude faster than the currently available TD implementations [67]. This allows us to rapidly fill a large portion of the (p, e) parameter space with GSF data. Our technique then is to fit the available data using a interpolation model. The resulting model allows us to calculate a good approximation to the GSF, for given orbital parameters, in a fraction of a second. With the interpolation model in hand, we evolve the orbital inspiral within the relativistic osculating orbit description of Pound and Poisson [180].

One of the key aims of calculating an actual orbital inspiral is to quantify the conservative GSF's effect on the orbital dynamics. It was recently shown by Barack and Sago [157] that the conservative GSF acts to decrease the rate of relativistic precession and one of the goals of the work presented in this chapter is to quantify for the first time how large this effect is for a physical inspiral.

9.1 Osculating orbit description of motion

The geodesic motion of a test body can be uniquely specified at any time by the three components of the test body's position vector, $\mathbf{r}$, and the three components of its velocity, $\dot{\mathbf{r}}$. Equivalently,

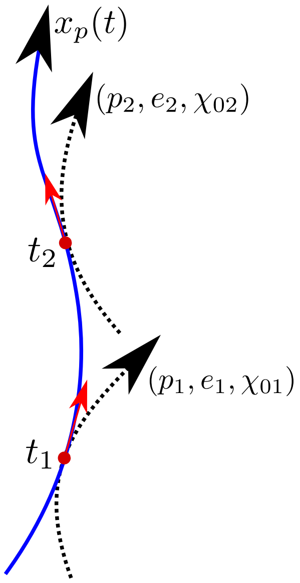

FIGURE 9.1: Osculating orbit description of motion. At a given time, t_1, along the particle's (non-geodesic) worldline, $x_p(t)$, the position and velocity of the particle can be matched to an osculating ('kissing') geodesic with parameters (p_1, e_1, χ_{01}). In general, at a subsequent times the true worldline and the osculating geodesic defined at $t = t_1$ will have diverged. At some later time t_2 the particle's position and velocity can be matched to another osculating geodesic with parameters $(p_2, e_2 \chi_{02})$. Knowledge of the osculating geodesic to the worldline at each instance of time provides an complete description of the particle's trajectory. This description is valid for any trajectory and does not require that the force moving the particle away from geodesic motion be small.

it can be specified by six orbital constants: three orbital constants of the motion [i.e. $(\mathcal{E}, \mathcal{L}, \mathcal{Q})$] and three initial phases [i.e., $(\varphi_0, \theta_0, \chi_0)$, the initial azimuthal, zenithal and radial phases] and there exists a one-to-one correspondence between these two parametrizations [181]. Therefore, *any* non-geodesic trajectory in the spacetime can, at an instant $t = t_0$, be identified with an osculating ('kissing') geodesic that has the same values of $\mathbf{r}$ and $\dot{\mathbf{r}}$. In general at any different instances of time, the trajectory and the osculating geodesic defined at $t = t_0$ will have diverged, but one can smoothly vary the osculating geodesic parameters in such a way that throughout the motion $\mathbf{r}$ and $\dot{\mathbf{r}}$ of the geodesic coincide with those of the non-geodesic trajectory.

For the case of an inspiral about a Schwarzschild black hole, we only need to evolve four orbital constants. We take them to be the semi-latus rectum, p, orbital eccentricity, e, the periastron phase, χ_0 [see Eq. (2.10)], and initial azimuthal phase, φ_0. Recall from Chapter 4 that the first two orbital elements are principal orbital parameters describing the 'shape' of the orbit and the latter two are positional elements describing the orientation of the major axis. It turns out to be more convenient not to evolve φ_0 and instead we directly solve for $\varphi_p(t)$ via Eq. (9.11) below (see Ref. [180] for details). Assuming that the inspiral trajectory is given by the equation $a^\alpha = \tilde{F}^\alpha$, where $\tilde{F}^\alpha = \mu^{-1} F^\alpha$, the remaining three osculating elements evolve according to [180]:

$$\frac{dp}{dt} = 2pf_0f_1\left[p^{1/2}f_1f_2(p-3-e^2\cos^2 v)M\tilde{F}^{\varphi} - e\sin v\tilde{F}^r\right] , \tag{9.1}$$
$$\frac{de}{dt} = p^{1/2}f_0f_2\left[\beta f_3\cos v + e(p^2-10p+12+4e^2)\right]M\tilde{F}^{\varphi} + \beta f_0f_1\sin v\tilde{F}^r , \tag{9.2}$$
$$\frac{d\chi_0}{dt} = p^{1/2}e^{-1}f_0f_2\sin v\left[(p-6)f_3 - 4e^3\cos v\right]M\tilde{F}^{\varphi} - e^{-1}f_0f_1\left[(p-6)\cos v + 2e\right]\tilde{F}^r , \tag{9.3}$$

where the GSF contributions $\tilde{F}^{\alpha} = \tilde{F}^{\alpha}(p,e,\chi_0,t)$ and we have defined

$$f_0 \equiv (p-2-2e\cos v)(p-3-e^2)[(p-2)^2-4e^2]^{-1/2}[(p-6)^2-4e^2]^{-1} , \tag{9.4}$$
$$f_1 \equiv (p-6-2e\cos v)^{1/2} , \tag{9.5}$$
$$f_2 \equiv (1+e\cos v)^{-2} , \tag{9.6}$$
$$f_3 \equiv f_1^2 e\cos v + 2(p-3) , \tag{9.7}$$
$$\beta \equiv p-6-2e^2 , \tag{9.8}$$
$$v \equiv \chi - \chi_0 . \tag{9.9}$$

Equations (9.1)-(9.3) and (2.11) (with the replacement $\chi \to v$) form a closed set of ODEs. We will solve this set with the initial conditions $\{p(0), e(0), \chi_0(0)\} = \{p_0, e_0, 0\}$ for some p_0, e_0. The inspiral trajectory will then be described by

$$r_p(t) = \frac{p(t)}{1+e(t)\cos[\chi(t)-\chi_0(t)]} , \tag{9.10}$$
$$\varphi_p(t) = \int_{\chi(0)}^{\chi(t)} \sqrt{\frac{p(t)}{p(t)-6-2e(t)\cos[\chi'-\chi_0(t)]}}\, d\chi' , \tag{9.11}$$

where $\chi(t)$ is obtained by inverting $t(\chi)$. We remark that in the osculating orbit setup above there is no requirement that the forcing terms in Eqs. (9.1)-(9.3) be small [180]. Instead we make that requirement in this work in order that the GSF on the true trajectory inspiralling trajectory is closely approximated by the GSF along the osculating geodesic (as discussed in the introduction to this chapter).

9.2 GSF interpolation model

Despite the high efficiency of our FD code, it is still not sufficiently fast to compute the GSF for each osculating (p,e) value encountered during an inspiral. To overcome this we construct an interpolation formula for our numerical data. Our choice of model is motivated by the observation that the GSF is a periodic function of $v = \chi - \chi_0$ along a geodesic, with $F^{\varphi}_{\rm diss}, F^r_{\rm cons}$ even in v, and $F^r_{\rm diss}, F^\varphi_{\rm cons}$ odd in v (see Sec. 5.6). This suggests the Fourier-like representation

$$F^r_{\rm cons} = (\mu/M)^2 \sum_{n=0}^{\bar{n}_a} A_n(p,e)\cos(nv) \ , \tag{9.12}$$

$$F^r_{\rm diss} = (\mu/M)^2 \sum_{n=0}^{\bar{n}_b} B_n(p,e)\sin(nv) \ , \tag{9.13}$$

$$F^\varphi_{\rm cons} = \mu^2/M^3 \sum_{n=0}^{\bar{n}_c} C_n(p,e)\sin(nv) \ , \tag{9.14}$$

$$F^\varphi_{\rm diss} = \mu^2/M^3 \sum_{n=0}^{\bar{n}_d} D_n(p,e)\cos(nv) \ , \tag{9.15}$$

where we have

$$A_n(p,e) = p^{-2} \sum_{j=n}^{\bar{j}_a} \sum_{k=0}^{\bar{k}_a} a^n_{jk} e^j p^{-k} \ , \tag{9.16}$$

$$B_n(p,e) = p^{-9/2} \sum_{j=n}^{\bar{j}_b} \sum_{k=0}^{\bar{k}_b} b^n_{jk} e^j p^{-k} \ , \tag{9.17}$$

$$C_n(p,e) = p^{-4} \sum_{j=n}^{\bar{j}_c} \sum_{k=0}^{\bar{k}_c} c^n_{jk} e^j p^{-k} \ , \tag{9.18}$$

$$D_n(p,e) = p^{-11/2} \sum_{j=n}^{\bar{j}_d} \sum_{k=0}^{\bar{k}_d} d^n_{jk} e^j p^{-k} \ . \tag{9.19}$$

The leading order powers in the $1/p$ expansions in Eqs. (9.16)-(9.19) are chosen so as to match the known large p behaviour of the various components. The dimensionless coefficients $a^n_{jk}, b^n_{jk}, c^n_{jk}$ and d^n_{jk} are to be determined by fitting to our numerical GSF data, with the summation cut-offs to $\bar{n}_i, \bar{j}_i, \bar{k}_i, (i = \{a,b,c,d\})$ to be chosen by experimentation.

We use a standard least-squares algorithm to fit the interpolation formula to our numerical data. Initially, due to the constraints from our FD GSF code, we choose to fit using data over the range $6+2e < p/M < 12+2e$ with $0 \le e \le 0.2$. In practice we use 1100 data point spread across this region (see Fig. 9.2). In fitting the interpolation model, we sought a fractional accuracy of 10^{-3} between the interpolation model and the numerical GSF data. More explicitly, defining $F_{\rm model}$ as the GSF value from the interpolation model and $F_{\rm GSF}$ as the numerical value from our code, we sought the condition

$$\max_\chi \left| \frac{F_{\rm model}(\chi) - F_{\rm GSF}(\chi)}{F_{\rm GSF}(\chi)} \right| < 10^{-3} \ , \tag{9.20}$$

for all four components $F = \{F^r_{\rm cons}, F^r_{\rm diss}, F^\varphi_{\rm cons}, F^\varphi_{\rm diss}\}$ of the interpolation model at all 1100 numerically calculated data points. We further ensured the accuracy of our results by comparing the output of our interpolation model to a sample of results from Barack and Sago's TD code [67]. After some experimentation we found that our desired accuracy can be achieved within a model with parameters $\bar{n}_i = 6, \bar{j}_i = 2$ and $\bar{k}_i = 9$ for $i = \{a,b,c,d\}$. Thus we end up fitting to $7 \times 3 \times 10 = 210$ parameters. Due to the large number of fitting parameters we do not give them explicitly in this thesis, instead we have made them available online as a "fast GSF calculator" [182]. The package contains an open-source (GPL licensed) C code for computing

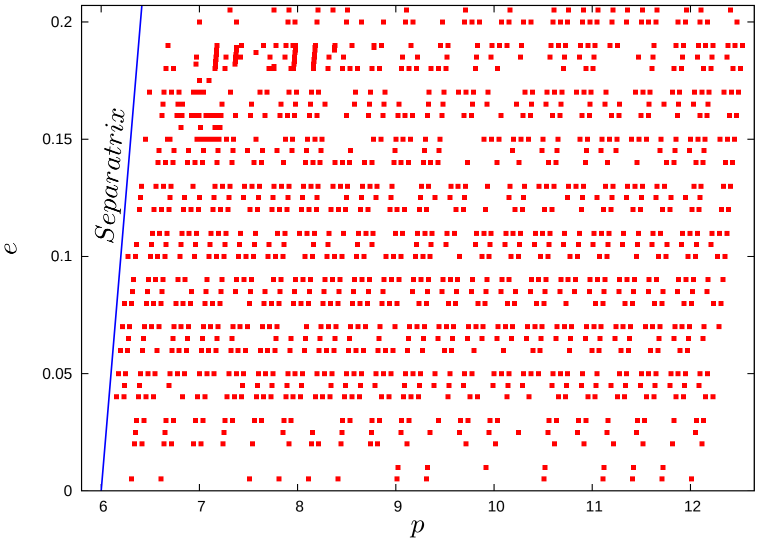

FIGURE 9.2: GSF sample points used to fit our analytic model. Each red mark shows a point in the (p, e) parameter space for which we successfully computed the GSF to our required accuracy threshold of 10^{-4}. The data is roughly sampled in a grid with $0 \leq e \leq 0.2$ and $6 + 2e < p < 12 + 2e$. Where points are missing from the grid, we believe this is because a nearly static mode (see Sec. 8.7) was encountered during the computation of the GSF for that orbit (and thus the code returned a result that did not meet our accuracy standard).

the GSF quickly based upon our interpolation model. We intend to update the database of fit parameters regularly as more GSF data [of improved accuracy and greater extent in the (p, e) space] becomes available.

9.3 Results: a sample inspiral

In this section, we present results for a sample inspiral computed using the osculating orbit technique coupled with our interpolation model. In this example we take $\mu = 10M_\odot$ and $M = 10^6 M_\odot$ (so the mass ratio is 10^{-5}) and initial orbital parameters $(p_0, e_0) = (12M, 0.2)$ with $\chi_0 = 0$. Figure 9.3 shows 1 hour snap shots of the inspiral at various stages and Fig. 9.4 shows the evolution of e and χ_0 as a function of p. The orbital eccentricity is observed to decrease over most of the inspiral but increases shortly before the onset of plunge, a phenomenon first described by Apostolatos *et al.* [183]. The complete inspiral lasts ~ 1443 days, during which time the orbit completes 75,550 periastron passages. Over the entire inspiral the periastron phase χ_0 is observed to shift secularly by 9 radians over the entire inspiral (in a retrograde sense as already observed by Barack and Sago [157]).

In order to explore the long-term effect of the GSF's conservative piece, let us construct a radiative approximation (RA) model by setting $F^\alpha_{\rm cons} = 0$ in the evolution equations (9.1)-(9.3), and additionally replacing the expressions on the right-hand side with their corresponding t-averages over an entire radial period of the instantaneous osculating geodesic. We now seek to compare the results of this RA model with the full GSF model described above.

As a point of comparison between the two models, we shall examine the total accumulated azimuthal phase $\varphi(t)$, denoting the values corresponding to the two models by $\varphi_{\rm RA/full}$. We shall then examine how the phase difference $\Delta\varphi_{\rm RA} \equiv \varphi_{\rm RA} - \varphi_{\rm full}$ builds up over time. In order to make a meaningful comparison between $\varphi_{\rm RA}$ and $\varphi_{\rm full}$ it is important to match the initial conditions of the inspirals correctly. This entails matching not just the initial phase but also

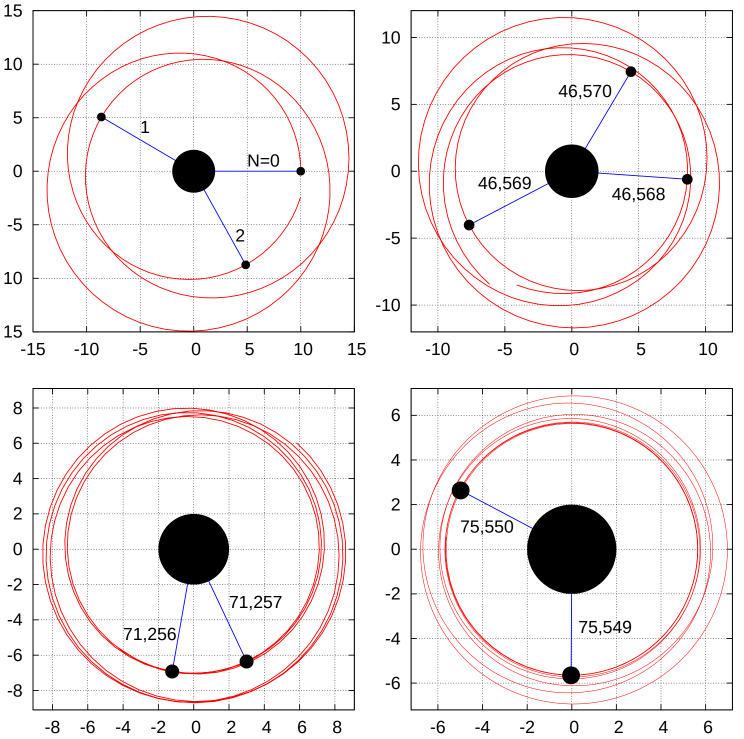

FIGURE 9.3: Snapshots of an orbital inspiral with $\mu = 10M_\odot$ and $M = 10^6 M_\odot$, starting at $(p_0, e_0) = (12, 0.2)$. We plot the orbit in the plane of $x = (r/M)\cos\varphi$ and $y = (r/M)\sin\varphi$. The four orbital episodes shown begin at 1443 days (top left), 500 days (top right), 75 days (bottom left) and 1 hour before plunge (bottom right). The red curve shows the trace of the previous 1 hour of orbital motion. The large black dot in the center of each panel shows the central Schwarzschild black hole (to scale). The location of the CO at periastron passage is marked by the small black dots (not to scale) connected to the central black hole with blue radial lines. The number of the periastron passage is shown next to the radial lines.

the first derivative of the phase with respect to time. This in turn implies matching the initial orbital frequencies as we now explain.

The azimuthal phase accumulation can be Taylor expanded about an initial time $t = 0$ as

$$\varphi(t) = \varphi_0 + \dot{\varphi}_0 t + \mathcal{O}(t^2) \,, \tag{9.21}$$

where hereafter a sub/superscript '0' denotes a quantity's value at $t = 0$ and an over dot denotes differentiation with respect to t. The phase difference can thus be expanded as

$$\Delta\varphi_{\mathrm{RA}} = (\varphi_0^{\mathrm{RA}} - \varphi_0^{\mathrm{full}}) + (\dot{\varphi}_0^{\mathrm{RA}} - \dot{\varphi}_0^{\mathrm{full}})t + \mathcal{O}(t^2) \,. \tag{9.22}$$

Setting the constant term to zero is straightforward and in this work we take $\varphi_0^{\mathrm{RA}} = \varphi_0^{\mathrm{full}} = 0$. We also wish to match the initial rate of aziumthal phase accumulation (i.e. set the coefficient of the term linear in t to zero). In order to see how we choose the initial orbital parameters to achieve this, we recall from Eq. (2.16) that the azimuthal phase for a geodesic orbit can be written in the form

$$\varphi(t) = \Omega_\varphi t + \tilde{\varphi}(t) \,, \tag{9.23}$$

where Ω_φ is the azimuthal frequency and $\tilde{\varphi}$ is an (odd) periodic function with period T_r which,

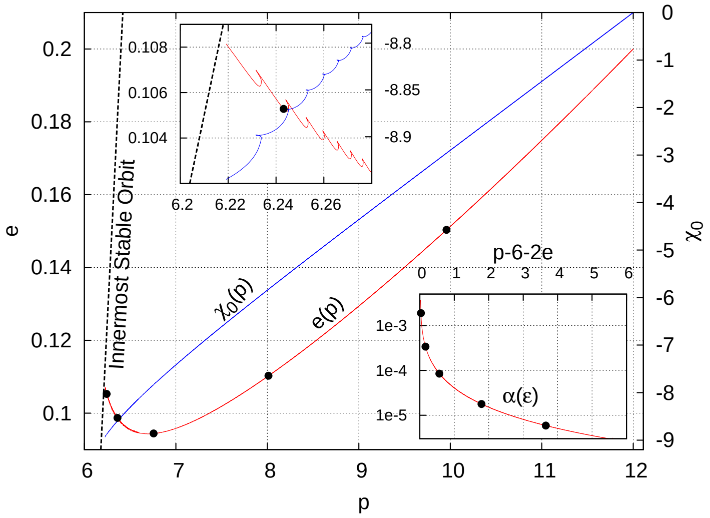

FIGURE 9.4: Evolution of the osculating elements in the sample case of Fig. 9.3. We plot the orbital eccentricity e [lighter (red), left axis] and periastron phase χ_0 [darker (blue) line, right axis] as a function of semi-latus rectum p, as the binary inspirals from $p_0 = 12M$ down to the last stable orbit (straight dashed line). The markers placed on the curves denote (from right to left) 500 days, 100 days, 10 days, 1 day and 1 hour to the onset of plunge. Note that the orbit initially circularizes, but that as the last stable orbit is approached the eccentricity begins to increase. Note also that the periastron phase χ_0 decreases monotonically, implying that the conservative GSF acts to reduce the rate of periastron advance. The upper inset shows an enlargement of the near plunge region. The lower inset shows the magnitude of the adiabaticity parameter $\alpha = \langle \dot{p}/p \rangle T_r$ against the distance to the last stable orbit $\epsilon = p - 6 - 2e$ and confirms that the evolution is strongly adiabatic until very near the the onset of the plunge.

using $T_r = 2\pi/\Omega_r$, we can Fourier expand as

$$\tilde{\varphi}(t) = \sum_{n=0}^{\infty} A_n \sin\left(\frac{n\Omega_r}{2\pi} t\right) , \tag{9.24}$$

$$= \sum_{n=0}^{\infty} A_n \left(\frac{n\Omega_r}{2\pi} t + \mathcal{O}(t^3)\right) , \tag{9.25}$$

$$\tag{9.26}$$

where the A_n series coefficients depend upon Ω_r and Ω_φ. For an inspiraling orbit the frequencies Ω_r and Ω_φ, as well as the A_n coefficients become time dependent. The linear coefficient of t in Eq. (9.22) can thus be written as

$$\dot{\varphi}_0^{\rm RA} - \dot{\varphi}_0^{\rm full} = (\Omega_{\varphi 0}^{\rm RA} - \Omega_{\varphi 0}^{\rm full}) + \sum_{n=0}^{\infty} \left[A_n(\Omega_{\varphi 0}^{\rm RA}, \Omega_{r0}^{\rm RA}) \left(\frac{n\Omega_{r0}^{\rm RA}}{2\pi}\right) - A_n(\Omega_{\varphi 0}^{\rm full}, \Omega_{r0}^{\rm full}) \left(\frac{n\Omega_{r0}^{\rm full}}{2\pi}\right) \right] , \tag{9.27}$$

where the subscript '0' on the orbital frequencies is used to denote the orbital frequency of the osculating orbit at $t = 0$. It is thus clear that by choosing $\Omega_{\varphi 0}^{\rm RA} = \Omega_{\varphi 0}^{\rm full}$ and $\Omega_{r0}^{\rm RA} = \Omega_{r0}^{\rm full}$ the linear coefficient in Eq. (9.22) can be made to vanish. Our orbit evolution scheme is cast in terms of (p, e) and so in practice we achieve this matching of frequencies by the following procedure. (1) Choose (p_0, e_0) values for the inspiral using the full (conservative and dissipative) GSF. (2) Compute the azimuthal and radial frequencies of the orbit at $t = 0$ including corrections coming from the inclusion of the conservative GSF. (3) Find the (p, e) values of a geodesic whose frequencies are those found in step 2. (4) Use these (p, e) values for the RA evolution. This choice

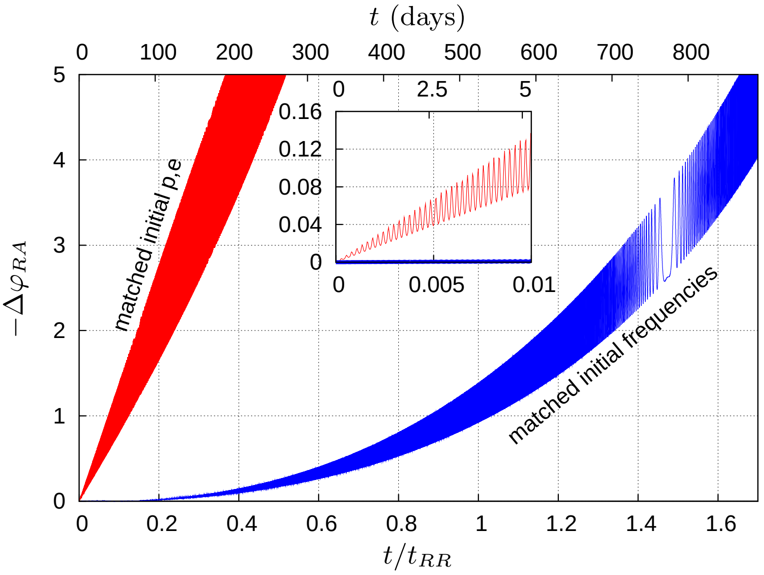

FIGURE 9.5: Effect of conservative GSF corrections on the long-term phase evolution. We show the accumulated azimuthal phase difference $\Delta\varphi_{\mathrm{RA}} = \varphi_{\mathrm{RA}} - \varphi_{\mathrm{full}}$ for the sample orbit shown in Fig. 9.3. The lower (blue) curve is obtained by matching the initial frequencies of the RA and the full evolutions [so both orbits start with slightly different principle elements (p, e)]. The upper (red) curve shows the phase difference between the two evolutions when both orbits are initiated at $(p, e) = (12, 0.2)$.

of initial conditions for the comparisons is physically motivated because the orbital frequencies (unlike p and e) are invariant characteristics of the orbit.

In Fig. 9.5 we show $\Delta\varphi_{\mathrm{RA}}(t)$ for the sample orbit discussed in this section. On the lower horizontal axis we express t in units of the radiation-reaction timescale $t_{RR} \equiv (M/\mu)T_c$, where as a characteristic orbital period we take the φ-period of the ISCO so that $T_c = 2\pi 6^{3/2} M$. As expected $\Delta\varphi_{\mathrm{RA}}$ grows on average quadratically in time with this growth attributed to the effects of the conservative GSF (the observed oscillations are due to the mismatch in radial phase between the two models). The phase difference between the two models remains small for quite some time, only reaching one radian difference on a timecsale $t \sim t_{RR}$. For reference, we also show in Fig. 9.5 the phase difference between the two models if, instead of matching the initial orbital frequencies, the initial (p, e) are matched. As is expected a rapid, linear growth in t of $\Delta\varphi_{\mathrm{RA}}$ is observed.

These preliminary results from our model suggest that the RA captures the full-GSF phase evolution rather well over long periods of time when the initial frequencies are correctly matched. This backs up the expectation that RA-based waveform templates could be usefully implemented in matched filtering searches for gravitational waves from I/EMRIs. We have also demonstrated that in order to obtain a fully phase-coherent model of the evolution beyond the radiation-reaction timescale the conservative GSF corrections must be included. Unfortunately, with the results of this work we are not yet placed to produce the necessary templates, as a consistent model also requires the (as yet unknown) second-order piece of the dissipative GSF (the magnitude of the effects of which are expected to compete with the first order conservative GSF [164]).

Chapter 10

Concluding remarks

In this thesis, as well as having studied isofrequency orbits, we have presented two new calculations of the SF. In both SF calculations, our approach has been to work in the frequency domain when solving the field equations of the perturbing field. The frequency domain approach has the key advantage of only requiring one to work with ordinary differential equations rather than the more numerically challenging partial differential equations encountered when working in the time domain. Until rather recently, when modelling non-circular orbits, the frequency-domain approach was hampered by the Gibbs phenomenon that arises from attempting to construct the discontinuous field derivatives as a sum of smooth functions. Fortunately this drawback was removed by the introduction by Barack, Ori and Sago of the method of extended homogeneous solutions [110], and we have been able to demonstrate in this work that their technique can be used to make frequency-domain self-force calculations highly competitive with similar time-domain computations when the orbital eccentricity under consideration is not too large.

Our work with scalar fields in Kerr spacetime represents the first self-force calculation for a realistic orbit about a rotating black hole. Our approach to this problem was to decompose the scalar field into spheroidal harmonic and frequency modes. It is worth noting that an angular decomposition (in particular decoupling of the θ component) necessitates a frequency-domain computation when working with scalar fields in Kerr spacetime. Key to the success of the numerical treatment is the fact that, for each mode of the decomposition, the scalar field is finite at the particle's location. Our technique then is to apply suitable boundary conditions and solve for the full retarded scalar field mode-by-mode. We then regularize the resulting modes using the standard method of mode-sum regularization [8]. In the mode-sum regularization scheme, the correct singular component of the field, as identified by Quinn [130], is subtracted from the full retarded field at the level of the individual spherical harmonic l-modes, and thus, before we can employ the scheme, we must first decompose our numerically computed spheroidal harmonic modes of the scalar field onto a basis of spherical harmonic modes. Fortunately the standard method for computing spheroidal harmonics (see Appendix B) is to construct them as series of spherical harmonics. This well known construction is then useful to us in two ways. Firstly, it allows for efficient computation of the spheroidal harmonics, and secondly, the series coefficients that appear during the construction are precisely the coefficients required to decompose the spheroidal harmonic modes of the scalar field into spherical harmonics. Another key feature to the success of our approach is, for a given spheroidal harmonic, the rapid (exponential) convergence of its spherical harmonic expansion. This has the practical upshot that, within a reasonable numerical tolerance, a given spherical harmonic l-mode couples only to a few spheroidal harmonic

$\hat{l}$-modes. As an example, we found that, for circular equatorial orbits in Kerr spacetime, the strongest coupling we encountered for any orbit we considered in this work implied that the contribution to a given spherical harmonic l-mode from the spheroidal harmonic modes with $|l - \hat{l}| > 6$ could be ignored within our numerical tolerances. This meant that, in the worst case scenario for circular, equatorial orbits, should we wish to calculate, say, 50 spherical harmonic l-modes, we needed to compute at most 56 spheroidal harmonic $\hat{l}$ modes (in order to achieve this).

Our results for circular, equatorial orbits showed that the central black hole's spin can have a pronounced effect upon the conservative SSF, which, in this case, coincides entirely with the radial component of the SSF. This effect of the spin can be so great that, though the radial component of the SSF is always positive (repulsive) in Schwarzschild spacetime, it can, for certain regions of the orbital radius-spin parameter space, change sign, becoming negative (attractive)—see Fig. 6.6. We also used our numerical results to inform a post-Newtonian-like fit based upon an extended version of the formula derived by Hikida *et al.* [165] for the SSF in Schwarzschild spacetime. We found that, with the addition of a single spin-orbit coupling term, we were able to accurately capture the behaviour of the SSF in Kerr spacetime for large orbital radii (see Fig. 6.8)

Our confidence in our circular orbit SSF results is based upon two important validation tests. The first follows from the mode-sum regularization procedure's sensitivity to errors in the high l-modes of our computation. This sensitivity follows from the cancellation of as many as three leading order terms in the spherical harmonic expansion of the retarded field. With the Barack and Ori regularization parameters subtracted from the full retarded field, theory tells us that the resulting regularized modes should converge like $1/l^2$, and we see precisely this behaviour in our numerical results (see Figs. 6.2, 6.9, 7.1 and 7.2). With the addition of extra regularization parameters, as recently derived by Heffernan *et al.* [159], the regularized l-modes are expected to converge faster by a further factor of $1/l^2$ for each extra regularization parameter employed. Again we observe this behaviour in our numerical data (see Fig. 6.3). The second validation test is more quantitative and involves checking that the energy and angular momentum radiated by the particle is balanced by the fluxes of energy and angular momentum passing to spatial infinity and down through the central black hole's event horizon. As the contribution to the radiated energy and angular momentum per l-mode drops off exponentially, this test probes primarily the low l-modes of our calculation. In that sense it is complimentary to the first validation test. We were able to show an excellent match between the radiated energy and angular momentum and the associated fluxes passing through the spacetime boundaries in our numerical data. We also observed certain modes of the scalar field to be superradiant, as theory predicts, and showed that, for tightly bound orbits around rapidly rotating black holes, this amplification of the scalar field can be quite large ($\sim 25\%$)—see Fig. 6.4. Recently our circular, equatorial results have been by verified Dolan, Wardell and Barack [98] and also by Thornburg [107], both working in the TD and making use of the m-mode scheme [81, 91] (see also the brief discussion in Sec. 5.5).

As was mentioned at the start of this chapter, our approach to the frequency domain calculation of SSF along eccentric equatorial orbits was to use the recently introduced method of extended homogeneous solution [110]. We found that this technique allowed for the computation of the SSF for orbits with eccentricities up to $e \sim 0.7$ for non-rotating black holes (see Fig. 7.6). As with circular equatorial orbits, when the central black hole is rotating the spheroidal-to-spherical harmonic decomposition adds an extra layer of computational burden, and in the case of eccentric equatorial orbits this burden is greater. This follows as the spheroidicity $\sigma^2 = -a^2\omega^2$. Eccentric equatorial orbits have a bi-period spectrum and thus the mode frequency can be substantially greater than for circular equatorial orbits. Correspondingly, the coupling between the spheroidal harmonic and spherical harmonic modes of different l is stronger. Despite this, we nonetheless find that, for the most challenging orbit we calculate in this work, the coupling requires us to compute up to at most $\hat{l} = l_{\max} + 10$ spheroidal harmonic modes in order to recover $l_{\max}$ spherical harmonic modes. We thus find it practical to compute the SSF for orbits with eccentricities up to $e \sim 0.5$ when the black hole is rapidly rotating (again see Fig. 7.6). We employ the same two validation tests for eccentric equatorial orbits as we did for circular equatorial orbits, and in both cases find our results pass both checks to a good degree of accuracy. Very recently our SSF eccentric orbit results have been verified by Thornburg [94].

The computation of the SSF along eccentric orbits enables access to more ‘physical’ consequences of the SSF than the circular orbit SSF alone can provide[1]. In particular, we calculated how the conservative component of the SSF affects the location and (relatedly) the orbital frequency of a particle at the innermost stable circular orbit (ISCO). For the SSF in Schwarzschild spacetime, this calculation was first performed by Diaz-Rivera *et al.* [87]. In this thesis we extend their work and derive the required formulae to compute the shift in the ISCO parameters in Kerr spacetime for equatorial orbits. We then make use of our code to compute various quantities that appear in the formulae. For prograde orbits, the effect of the black hole spin on the ISCO location and frequency is quite pronounced, causing both quantities to change sign when the central black hole has a spin of $a \sim 0.8M$ (see Fig. 7.10). Using our SSF eccentric equatorial results, we also examined the rest mass variation phenomenon noted by Quinn [130]. A particle endowed with a scalar charge is able to radiate monopole waves, and so its rest mass is not a constant along the orbit [75]. For our bound geodesic setup, it transpires that the mass returns to the same value at each periastron passage, but for the first time we compute the rest mass variation along the orbit—see Fig. 7.11 (the rest mass variation has also been recently computed by Diener *et al.* [95] as part of the first self-consistent evolution for a scalar particle in Schwarzschild spacetime).

In this thesis we also tackled the computation of the gravitational self-force in the frequency domain. Our previous work on the toy-model SSF became well justified at this point, as the numerical techniques developed there carried straight over to the gravitational calculation and aided the speedy development of the code. The calculation itself is much like the scalar calculation, but with the added challenge of solving for multiple coupled fields. This task was greatly simplified by the previous work of others in decomposing the Lorenz gauge metric perturbation into tensor spherical harmonics [61], computing the tensor-harmonic to scalar-harmonic coupling formula for the metric perturbation [67] and decomposing the Lorenz gauge metric perturbation into the frequency domain [66]. In particular, we were greatly assisted in our work by the work of Barack and Sago [67] (whose results we could compare against during development of our code) and by the calculation of the FD boundary conditions by Akcay [66]. We will not detail the many other smaller challenges that led to the completion of that work as they are presented elsewhere in this thesis (see Chapter 8).

Our resulting code to compute the gravitational self-force along bound geodesic orbits was, as hoped, extremely efficient for low eccentricity ($e \lesssim 0.2$) orbits and, there is further hope that, once some of the remaining numerical difficulties associated with the computation of nearly static

---

[1] Though see the recent work by Le Tiec *et al.* [73] where they show that the shift in the ISCO location due to the conservative GSF can be extracted from circular orbit data alone.

modes are overcome (see Sec. 8.7), we should be able to efficiently compute the GSF for higher eccentricity orbits. The practical upshot of our code's speed is that it has allowed us to compute the gravitational self-force for a great many (1100+) bound geodesic orbits—see Fig. 9.2. With this wealth of data, we fitted an analytical model, which allows us to rapidly evaluate a good approximation to the GSF within a portion of the parameter space (i.e., for low eccentricity orbits).

With our fitted analytical model of the GSF, we were able, for the first time, to compute the inspiral of a compact body into a non-rotating massive black hole, including all first-order-in-the-mass-ratio effects. Our technique to do this was to employ the relativistic osculating orbit method developed by Pound and Poisson [180]. The key assumption we make is that if the orbital evolution is sufficiently slow the GSF felt by the compact object will be closely approximated by the GSF felt by a particle that has spent its entire past history on an osculating ('kissing') geodesic orbit. That said, as we discussed in Chapter 9, the precise scaling with the mass ratio of the error made by using the osculating orbit method is currently unclear. A future program of research is required to understand these errors and thus the domain of validity (in terms of the mass ratio) of the method of osculating orbits.

The main result of our work on orbital evolution was the quantification of the effect of the conservative self-force upon a realistic orbital inspiral. As was found by Barack and Sago, the conservative self-force leads to a decrease in the rate of relativistic precession [157]. Across the sample orbit we considered [with initial orbital parameters $(p,e) = (12M, 0.2)$ and $\mu = 10M_\odot, M = 10^6 M_\odot$] the inclusion of the conservative self-force during the orbital inspiral, in addition to the radiative self-force, induced a nine radian discrepancy in the orbital phase by the onset of the plunge (with respect to an inspiral driven only by the radiative GSF). Though nine radians is small compared with the total phase accumulation during the inspiral ($\sim 7.72 \times 10^5$ radians), it will be significant when attempting to extract accurate orbital parameters from a gravitational wave signal. The small contribution from the conservative self-force also indicates that current radiative-only models will likely be sufficient for detection, but we stress that accurate parameter estimation must include the conservative effects.

Lastly, we mention the phenomenon of isofrequency orbits, which we also investigate in this thesis. Isofrequency orbits are pairs of physically distinct geodesic orbits that share the same orbital frequencies. Unlike the orbital energy and angular momentum (and Carter constant in Kerr spacetime), it turns out that specification of the orbital frequencies does not uniquely specify the orbit 'shape'. This property of the orbital frequencies was first noticed by Barack and Sago [157] for orbits about a Schwarzschild black hole, and in this thesis we examine if their results extend to the include generic, bound geodesic orbits about Kerr black holes. Despite the addition of a third orbital frequency (associated with the zenithal motion), we find that the phenomenon does indeed extend to generic orbits about Kerr black holes, and thus we conclude that, just as in Schwarzschild spacetime, generic bound geodesic orbits in Kerr spacetime are not uniquely identifiable by their orbital frequencies.

10.1 Future work

We now briefly consider the numerous possible extensions to the work presented in this thesis.

10.1.1 Isofrequency orbits

Now that it is known that isofrequency orbits exist about astrophysical (Kerr type) black holes, it remains to be seen if their existence will have any physically observable effects. For instance, the frequencies of an inspiraling orbit are imprinted in the gravitational waveform, and so it may be asked how, if at all, this orbital duality might affect the data analysis task. Another possibility is the existence of orbital resonances, say, between clumps of matter in accretion disks.

10.1.2 Scalar-field self-force

The obvious extension to the work on the SSF in Kerr spacetime presented in this thesis is to tackle the computation of the SSF for generic (eccentric and inclined) orbits. Some care would be required, though, as the structure of generic geodesic orbits is more complicated than for any of the orbits we consider in this thesis. In particular, generic orbits are bi-periodic which makes decomposition of the point-like source into spheroidal and Fourier modes more complicated [for instance, one can no longer integrate over a single orbital period as in Eq. (4.8)]. That said, techniques for working with generic orbits in the frequency domain are known [184] and should be applicable to this problem. An SSF calculation for generic orbits is further made challenging by the nature of the the mode frequency for these orbits:

$$\omega = m\Omega_\varphi + n\Omega_r + k\Omega_\theta \;, \qquad \text{generic orbits} \;, \tag{10.1}$$

where m, n and k are integers. This has two important implications. Firstly, during a FD calculation modes with large spheroidicity ($= -a^2\omega^2$) will likely be encountered, and thus some spheroidal modes will couple (within a specified accuracy) to many spherical harmonic modes, necessitating the computation of a large number of spheroidal modes in order to recover comparatively few spherical harmonic modes. Secondly, there will simply be many more modes to compute to construct each l-mode. Both of these considerations will greatly increase the computational burden and will likely severely reduce the portion of the $(a, p, e, \theta_{\rm min})$ parameter space that can be explored by excluding orbits about a rapidly rotating black hole with moderate eccentricity and/or a large inclination angle.

With the SSF for generic orbits computed, there are two interesting phenomenon that could be investigated. Firstly, one could consider orbital evolution. Despite this not being a physically motivated problem, it would nonetheless be interesting to pursue, as it would allow for the exploration of the orbital resonance effect discovered by Hinderer and Flanagan [185]. This phenomenon takes place when the osculating orbit to the inspiral goes through a low ratio resonance between the radial and zenithal frequencies. When this happens the orbital evolution will (briefly) cease to be adiabatic. This in turn will produce a large change in the principal orbital parameters during this period. If the SSF for generic orbits was computed via FD techniques then, in order to explore orbital evolution, a suitable analytical model fitted by numerical data would have to be produced in a similar fashion to our work on GSF driven inspirals in Schwarzschild spacetime (Chapter 9). With a suitable model for the SSF, the osculating orbit technique (which has been extended to cover orbits in Kerr spacetime by Gair *et al.* [181]) could be employed. Within this approach, care must be taken to track the adiabaticity of the orbit near the resonance, as, if adiabaticity grows too large, the SSF during the inspiral might not be well approximated by the associated osculating geodesic, potentially invalidating the use of the osculating geodesic approach to model the inspiral.

The second potentially interesting phenomenon to investigate with regard to the SSF would be to consider the rest mass variation associated with the orbital inspiral of a scalar charge into a black hole (this has very recently been considered in the case of an inspiral into a Schwarzschild black hole by Diener *et al.* [95]).

10.1.3 Gravitational self-force

The most immediate extension to the FD GSF work outlined in this thesis is to implement the proposed solution to the numerical difficulties associated with nearly static modes via solving the problem perturbatively as outlined in Sec. 8.7. The main task remaining before our proposed technique can be implemented in the code is to derive the correct boundary conditions. Once the difficulties associated with nearly static modes have been cured, our code should be able to explore much more of the parameter space with high accuracy. This would have two effects. Firstly, it should improve the accuracy of the data we use to fit the analytical model we employ to rapidly compute the GSF for use with the osculating orbit scheme. Secondly, as our code is accurate to large radii for circular orbit GSF calculations, solving the nearly static mode problem should allow our code to accurately compute the GSF for eccentric orbits with large semi-latus rectums. This in turn would allow a comparison of gauge invariant quantities with results from post-Newtonian theory, similar to what has been achieved for circular orbits [70].

The extension of our FD work to orbits about Kerr black holes is much less straightforward. At the time of writing, to the best of our knowledge, no one has written down the required tensor basis to separate the field equations in the Lorenz gauge. Without this, the only way to proceed with a FD calculation in the Lorenz gauge seems to be to decompose the field into tensor spherical harmonics and correctly account for the coupling between the spherical harmonic modes. Fortunately, as our SSF work shows, the bandwidth of this coupling is likely to not be too large but, nonetheless, this approach to the problem would be very technically challenging. Perhaps a more promising approach is to work in a hybrid gauge, which, far from the particle, has the algebraic simplicity of, say, the radiation gauge, but is locally the Lorenz gauge so that the mode-sum regularization procedure can be applied. Such techniques are being actively pursued [186]. Puncture/effective source time-domain techniques in $(2+1)$ and $(3+1)$ dimensions are also promising routes towards calculating the GSF for orbits in Kerr spacetime [142, 90].

Very recently, work by Pound [187] (see also Gralla [188] and Detweiler [189]) has shown how to go about computing the second-order-in-the-mass-ratio contribution to the GSF. The output of a successful numerical implementation of Pound's results would be very interesting indeed. For one, as we discuss below, these results are necessary to compute meaningful self-force waveforms for matched filtering with detector data. Secondly, it was recently shown that GSF results seem to apply to a much wider range of mass ratios than previously thought [72, 73]. Consequently, computation of the second order effects might allow GSF results to accurately model not just EMRIs, but also IMRIs, and maybe even have something meaningful to say about comparable mass systems. There is a strong physical motivation to make this calculation: IMRIs are considered a possible source for the advanced LIGO detector due to come online in the next few years (and certainly a long time before eLISA is expected to be launched and provide access to gravitational wave data from EMRI systems). Calculation of the second order GSF requires accurate knowledge of the first-order-in-the-mass-ratio metric perturbation and to date this is most accurately known via FD techniques. The calculation is unlikely to be straightforward, though, as within a spherical harmonic decomposition, whilst at the particle the first-order-in-the-mass-ratio-metric perturbation is finite, the second order metric perturbation is divergent [187], necessitating the development of a suitable puncture technique in the frequency domain. Once this is done, though, a code to compute the GSF in Schwarzschild spacetime through to second order in the mass ratio could feasibly be developed quite rapidly, building upon the techniques presented in this thesis.

10.1.4 Orbital evolution

Aside from improvements to the analytic fit model of the GSF (mostly to be obtained via higher accuracy GSF data), the orbital evolution scheme we present in this thesis can be extended in various ways. Firstly, it would be desirable to have the analytical model cover more of the parameter space of geodesics. To get the best coverage would require improvements in our FD code but also working with the results from TD codes which are able to both access higher eccentricity regions of the orbital parameter space as well as producing data for zoom-whirl orbits near the separatrix, where, owing to the requirement to sum over many Fourier modes, our FD code struggles.

Beyond these straightforward extensions, we believe the next steps in the orbit evolution program are as follows. Firstly, once a fully TD code becomes available to compute the GSF[2], a self-consistent evolution needs to be performed. The results of this will be an important check of the key assumption made when using the osculating orbit method: that the instantaneous self-force felt by the particle is well approximated by the self-force felt by a particle on the osculating geodesic.

It may be possible to get a handle on the errors made using the osculating orbit method by considering the scalar field case. There are already a number of codes that can compute the scalar self-force along an eccentric orbit in Schwarzschild spacetime [92, 93, 99]. The data from these codes could be incorporated into an interpolation model similar to the one presented in Sec. 9.2. The osculating orbit method could then be used to evolve the orbit of a scalar particle and the outcome compared with the recent results of Diener *et al.*'s code for computing self consistent orbits of scalar particles [95]. For this comparison it would not be necessary to evolve thousands of orbits as we did in Chapter 9 which is fortunate as this would be an extremely challenging task for any time domain code. Instead the goal of the comparison would be to ascertain how the error made by using the osculating orbit method scales with the mass ratio. Most likely this would require a few hundred orbits at most.

Finally, it will be important to include second-order-in-the-mass-ratio effects. Though in this thesis we have made a first assessment of the conservative effects upon an orbital inspiral through to the linear order in the mass ratio, we cannot construct a meaningful gravitational waveform from these results, as the orbit averaged second-order-in-the-mass-ratio dissipative effects compete in magnitude with the first order conservative effects [164]. For this reason it will be important to compute the second order gravitational self-force.

---

[2] Barack and Sago's code is not entirely TD. They find the monopole and dipole modes do not evolve in a stable manner and thus resort to FD methods for these modes. Recent work by Dolan and Barack [142] might allow for the stable evolution of these two modes in the TD.

Appendix A

Calculation of $\mathcal{E}, \mathcal{L}, \mathcal{Q}$ for generic bound orbits about a Kerr black hole

The formulae presented in Sec. 2.2.5 to calculate the orbital frequencies for a generic bound geodesic orbit about a Kerr black hole require the orbital energy, $\mathcal{E}$, angular momentum $\mathcal{L}$ and Carter constant, $\mathcal{Q}$, as functions of $(p, e, \theta_{\rm min})$. We given now the relationship between these two sets of principal orbital parameters, as given by Schmidt [125].

Throughout this Appendix we shall use an overtilde to denote the dimensionless version of a given quantity. The square of the dimensionless energy, $\tilde{\mathcal{E}}$, can be calculated via

$$\tilde{\mathcal{E}}^2 = \frac{\kappa\rho + 2\epsilon\sigma \pm 2\sqrt{\sigma(\sigma\epsilon^2 + \rho\epsilon\kappa - \eta\kappa^2)}}{\rho^2 + 4\eta\sigma}\ , \tag{A.1}$$

where we have defined

$$\kappa = \begin{vmatrix} d_1 & h_1 \\ d_2 & h_2 \end{vmatrix}, \qquad \epsilon = \begin{vmatrix} d_1 & g_1 \\ d_2 & g_2 \end{vmatrix}, \tag{A.2}$$

$$\rho = \begin{vmatrix} f_1 & h_1 \\ f_2 & h_2 \end{vmatrix}, \qquad \eta = \begin{vmatrix} f_1 & g_1 \\ f_2 & g_2 \end{vmatrix}, \tag{A.3}$$

$$\sigma = \begin{vmatrix} g_1 & h_1 \\ g_2 & h_2 \end{vmatrix}, \tag{A.4}$$

with

$$(f_1, g_1, h_1, d_1) = \begin{cases} (f(\tilde{r}_p), g(\tilde{r}_p), h(\tilde{r}_p), d(\tilde{r}_p)) & \text{if } e > 0\ , \\ (f(\tilde{r}_0), g(\tilde{r}_0), h(\tilde{r}_0), d(\tilde{r}_0)), & \text{if } e = 0, \end{cases} \tag{A.5}$$

$$(f_2, g_2, h_2, d_2) = \begin{cases} (f(\tilde{r}_a), g(\tilde{r}_a), h(\tilde{r}_a), d(\tilde{r}_a)) & \text{if } e > 0\ , \\ (f'(\tilde{r}_0), g'(\tilde{r}_0), h'(\tilde{r}_0), d'(\tilde{r}_0)), & \text{if } e = 0, \end{cases} \tag{A.6}$$

The functions $f, g, h, d, f', g', h', d'$ are given by

$$\begin{aligned}
f(r) &= \tilde{r}^4 + \tilde{a}^2 \left[\tilde{r}(\tilde{r}+2) + z_-^2 \tilde{\Delta}\right], && \text{(A.7)}\\
g(r) &= 2\tilde{a}\tilde{r}, && \text{(A.8)}\\
h(r) &= \tilde{r}(\tilde{r}-2) + \frac{z_-}{1-z_-^2}\tilde{\Delta}, && \text{(A.9)}\\
d(r) &= (\tilde{r}^2 + \tilde{a}^2 z_-^2)\tilde{\Delta}, && \text{(A.10)}\\
f'(r) &= 4\tilde{r}^3 + 2\tilde{a}^2\left[(1+z_-^2)\tilde{r} + (1-z_-^2)\right], && \text{(A.11)}\\
g'(r) &= 2\tilde{a}, && \text{(A.12)}\\
h'(r) &= \frac{2(\tilde{r}-1)}{1-z_-^2}, && \text{(A.13)}\\
d'(r) &= 2(2\tilde{r}-3)\tilde{r}^2 + 2\tilde{a}^2\left[(1+z_-^2)\tilde{r} - z_-^2\right]. && \text{(A.14)}
\end{aligned}$$

where $z_- = \cos\theta_{\min}$. The dimensionless angular-momentum, $\tilde{\mathcal{L}}$, can be obtained by solving either of the following two quadratics

$$\begin{aligned}
f_1\tilde{\mathcal{E}}^2 - 2g_1\tilde{\mathcal{E}}\tilde{\mathcal{L}} - h_1\tilde{\mathcal{L}} - d_1 &= 0, && \text{(A.15)}\\
f_2\tilde{\mathcal{E}}^2 - 2g_2\tilde{\mathcal{E}}\tilde{\mathcal{L}} - h_2\tilde{\mathcal{L}} - d_2 &= 0. && \text{(A.16)}
\end{aligned}$$

Lastly the dimensionless Carter constant, $\tilde{Q}$, can be expressed in terms of $\theta_{\min}, \tilde{\mathcal{E}}$ and $\tilde{\mathcal{L}}$ in the following manner

$$\tilde{Q} = z_-^2\left[\tilde{a}^2(1-\tilde{\mathcal{E}}^2) + \frac{\tilde{\mathcal{L}}^2}{1-z_-^2}\right]. \tag{A.17}$$

Appendix B

Spherical and Spheroidal harmonics

B.1 Spherical Harmonics

The spherical harmonics, Y_{lm} are eigenfunctions of Laplace's equation, $\nabla^2 f = 0$, on a spherically symmetric background. Their eigenvalues are given by

$$\nabla^2 Y_{lm} = -l(l+1)Y_{lm} \ , \tag{B.1}$$

$$\partial_\varphi^2 Y_{lm} = -m^2 Y_{lm} \ , \tag{B.2}$$

Explicitly the spherical harmonics take the form

$$Y_{lm}(\theta,\varphi) = c_{lm} P_{lm}(\cos\theta) e^{im\varphi} \ , \tag{B.3}$$

where the P_{lm} are the usual associated Legendre polynomials and the normalization coefficient, c_{lm} is chosen in such a way that the orthogonality relation between the spherical harmonics takes the form

$$\oint Y_{lm}(\theta,\varphi) Y^*_{l'm'}(\theta,\varphi) d\Omega = \delta_{ll'}\delta_{mm'} \ , \tag{B.4}$$

where a '$*$' denotes complex conjugation. Explicitly c_{lm} is given by

$$c_{lm} = \sqrt{\frac{(2l+1)}{4\pi}\frac{(l-m)!}{(l+m)!}} \ . \tag{B.5}$$

We also note the useful property

$$Y_{l(-m)} = (-1)^m Y^*_{lm} \ . \tag{B.6}$$

B.1.1 Identities

At various points during this thesis we find the following identities useful [67]

$$
\begin{aligned}
\sin^2\theta Y^{lm} &= \alpha^{lm}_{(+2)}Y^{l+2,m} + \alpha^{lm}_{(0)}Y^{lm} + \alpha^{lm}_{(-2)}Y^{l-2,m} \ , && \text{(B.7)}\\
\cos\theta\sin\theta Y^{lm}_{,\theta} &= \beta^{lm}_{(+2)}Y^{l-2,m} + \beta_{(0)}Y^{lm} + \beta^{lm}_{(-2)}Y^{l-2,m} \ , && \text{(B.8)}\\
\sin\theta Y^{lm}_{,\theta} &= \delta^{lm}_{(+1)}Y^{l+1,m} + \delta^{lm}_{(-1)}Y^{l-1,m} \ , && \text{(B.9)}\\
\sin^2\theta Y^{lm}_{,\theta\theta} &= \gamma_{(+2)}Y^{l+2,m} + \gamma_{(0)}Y^{lm} + \gamma^{lm}_{(-2)}Y^{l-2,m} \ , && \text{(B.10)}\\
\cos\theta Y^{lm} - \sin\theta Y^{lm}_{,\theta} &= \epsilon^{lm}_{(+1)}Y^{l+1,m} + \epsilon^{lm}_{(-1)}Y^{l-1,m} \ , && \text{(B.11)}\\
\sin^3\theta Y^{lm}_{,\theta} &= \zeta^{lm}_{(+3)}Y^{l+3,m} + \zeta^{lm}_{(+1)}Y^{l+1,m} + \zeta^{lm}_{(-1)}Y^{l-1,m} + \zeta^{lm}_{-3}Y^{l-3,m} \ , && \text{(B.12)}
\end{aligned}
$$

Defining

$$C_{lm} = \left[\frac{l^2-m^2}{(2l+1)(2l-1)}\right]^{1/2} \ , \qquad \text{(B.13)}$$

the explicit form of the lm-dependent coefficients (α, β, etc) in Eqs. (B.7)-(B.12) are then given by

$$\alpha^{lm}_{(+2)} = -C_{l+1,m}C_{l+2,m} \ , \qquad a^{lm}_{(0)} = 1 - C^2_{lm} - C^2_{l+1,m} \ , \qquad a^{lm}_{(-2)} = -C_{lm}C_{l-1,m} \ , \qquad \text{(B.14)}$$

$$
\begin{aligned}
\beta^{lm}_{(+2)} &= lC_{l+1,m}C_{l+2,m} \ , && \text{(B.15)}\\
\beta^{lm}_{(0)} &= lC^2_{l+1,m} - (l+1)C^2_{lm} \ , && \text{(B.16)}\\
\beta^{lm}_{(-2)} &= -(l+1)C_{lm}C_{l-1,m} \ , && \text{(B.17)}\\
\gamma^{lm}_{(+2)} &= l^2C_{l+1,m}C_{l+2,m} \ , && \text{(B.18)}\\
\gamma^{lm}_{(0)} &= m^2 - l(l+1) + l^2C^2_{l+1,m} + (l+1)^2C^2_{lm} \ , && \text{(B.19)}\\
\gamma^{lm}_{(+2)} &= (l+1)^2C_{lm}C_{l-1,m} \ , && \text{(B.20)}
\end{aligned}
$$

$$
\begin{aligned}
\delta^{lm}_{(+1)} &= lC_{l+1,m} \ , \qquad & \delta^{lm}_{(-1)} &= -(l+1)C_{lm} \ , && \text{(B.21)}\\
\epsilon^{lm}_{(+1)} &= (1-l)C_{l+1,m} \ , \qquad & \epsilon^{lm}_{(-1)} &= (l+2)C_{lm} \ , && \text{(B.22)}
\end{aligned}
$$

$$
\begin{aligned}
\zeta^{lm}_{(+3)} &= -lC_{l+1,m}C_{l+2,m}C_{l+3,m} \ , && \text{(B.23)}\\
\zeta^{lm}_{(+1)} &= C_{l+1,m}[l(l - C^2_{l+1,m} - C^2_{l+2,m}) + (l+1)C^2_{lm}] \ , && \text{(B.24)}\\
\zeta^{lm}_{(-1)} &= -C_{lm}[m^2 - l(l+1) + l^2C^2_{l+1,m} + (l-1)^2C^2_{lm} + (l+1)^2C^2_{l-1,m}] \ , && \text{(B.25)}\\
\zeta^{lm}_{(-3)} &= (l+1)^2C_{lm}C_{l-1,m}C_{l-2,m} \ . && \text{(B.26)}
\end{aligned}
$$

B.2 Spheroidal Harmonics

The spheroidal harmonics $S_{\hat{l}m}(\theta;\sigma^2)e^{im\varphi}$ satisfy the differential equation

$$\left[\frac{1}{\sin\theta}\frac{\partial}{\partial\theta}\left(\sin\theta\frac{\partial}{\partial\theta}\right) + \left(\lambda_{\hat{l}m} - \sigma^2\cos^2\theta - \frac{1}{\sin^2\theta}\frac{\partial^2}{\partial\varphi^2}\right)\right] S_{\hat{l}m}(\theta;\sigma^2)e^{im\varphi} \quad = \quad 0 \ , \qquad \text{(B.27)}$$

where the constant parameter σ^2 is the spheroidicity. The spheroidal harmonic differential equation (B.27) takes the form of a Sturm-Lioville equation and as such its eigenfunctions, the spheroidal harmonics $S_{\hat{l}m}(\theta;\sigma^2)e^{im\varphi}$, are orthonormal with normalization given by

$$\oint S_{\hat{l}m}(\theta;\sigma^2)e^{im\varphi}S_{\hat{l}'m'}(\theta;\sigma^2)e^{-im'\varphi}d\Omega = \delta_{\hat{l}\hat{l}'}\delta_{mm'} \ , \tag{B.28}$$

where the integration is over a 2-sphere with area element $d\Omega = \sin\theta d\theta d\varphi$, and $\delta_{n_1 n_2}$ is the standard Kronecker delta. The un-normalized versions of the spheroidal Legendre functions $S_{\hat{l}m}(\theta;\sigma^2)$ (which coincide with the associated Legendre polynomials when $\sigma = 0$) are related to their normalized counter-parts by the factor

$$c_{\hat{l}m} = \left(\frac{2\hat{l}+1}{4\pi}\frac{(\hat{l}-m)!}{(\hat{l}+m)!}\right)^{1/2} \tag{B.29}$$

The functions $S_{\hat{l}m}(\theta;\sigma^2)e^{im\varphi}$ are called *oblate* or *prolate* spheroidal harmonics, depending on whether σ^2 is negative or positive, respectively. A useful and efficient method for calculating the spheroidal harmonics is via decomposition in spherical harmonics. This method is doubly useful in our case as it produces as a by-product the coupling coefficients required to make use of the mode-sum scheme in Kerr spacetime (see Sec. 5.4).

The expansion of a given spheroidal harmonic as a series of spherical harmonics, for given m, takes the form

$$S_{\hat{l}m}(\theta;\sigma^2)e^{im\varphi} = \sum_{l=l_{\min}}^{\infty} b^{l}_{\hat{l}m}(\sigma^2)Y_{lm}(\theta,\varphi) \ , \tag{B.30}$$

where $l_{\min} = |m|$. In order to calculate the coefficients $b^{l}_{\hat{l}m}$ we substitute this expansion into Eq. (B.27). Noting that the Y_{lm} satisfy (B.27) when $\sigma = 0$ with $\lambda_{lm} = l(l+1)$, we get

$$\sum_{l=l_{\min}}^{\infty} b^{l}_{\hat{l}m}[\sigma^2\cos^2\theta + l(l+l)]Y_{lm} = \lambda_{\hat{l}m}\sum_{l=l_{\min}}^{\infty} b^{l}_{\hat{l}m}Y_{lm} \ . \tag{B.31}$$

Next we multiply the above expression by $Y^{*}_{\hat{l}m}$ and integrate over the sphere. The resulting inner products are given by

$$\oint Y^{*}_{\hat{l}m}Y_{lm}\,d\Omega \quad = \quad \delta_{\hat{l}l} \ , \tag{B.32}$$

$$\oint Y^{*}_{\hat{l}m}\cos^2\theta\, Y_{lm}d\Omega \quad = \quad \frac{1}{3}\delta_{\hat{l}l} + \frac{2}{3}\sqrt{\frac{2l+1}{2\hat{l}+1}}\langle l,2,m,0|\hat{l},m\rangle\langle l,2,0,0|\hat{l},0\rangle \equiv k^{l}_{\hat{l}m} \ . \tag{B.33}$$

Here the numbers $\langle j_1,j_2,m_1,m_2|j,m\rangle$ are standard Clebsch-Gordan coefficients, the form of which implies that $k^{l}_{\hat{l}m} \neq 0$ only for $l \in \{\hat{l}-2,\hat{l}-1,\hat{l},\hat{l}+1,\hat{l}+2\}$. Consequently, Eq. (B.31) reduces to the recursion relation

$$\sigma^2 k^{\hat{l}-2}_{\hat{l}m}b^{\hat{l}-2}_{\hat{l}m} + \sigma^2 k^{\hat{l}-1}_{\hat{l}m}b^{\hat{l}-1}_{\hat{l}m} + [\sigma^2 k^{\hat{l}}_{\hat{l}m} + l(l+1)]b^{\hat{l}}_{\hat{l}m} + \sigma^2 k^{\hat{l}+1}_{\hat{l}m}b^{\hat{l}+1}_{\hat{l}m} + \sigma^2 k^{\hat{l}+2}_{\hat{l}m}b^{\hat{l}+2}_{\hat{l}m} = \lambda_{\hat{l}m}b^{\hat{l}}_{\hat{l}m} \ , \tag{B.34}$$

for the expansion coefficients $b^{l}_{\hat{l}m}$ (with given $\hat{l},m$). This can be put in a matrix form, $K\mathbf{b} = \lambda\mathbf{b}$ (keeping the indices $\hat{l},m$ implicit), where K is a known band-diagonal matrix (made up of the known σ^2 and $k^{l}_{\hat{l}m}$) and $\mathbf{b} = (b^{\hat{l}=1}_{\hat{l}m}, b^{\hat{l}=2}_{\hat{l}m}, \ldots)$. This is a standard eigenvalue problem for the eigenvectors $\mathbf{b}$ and eigenvalues λ (for each $\hat{l}, m$), and the band-diagonality of K simplies the numerical treatment. This method we have presented for obtaining the expansion coefficients $b^{\hat{l}}_{\hat{l}m}$ and spheroidal-harmonic eigenvalues $\lambda_{\hat{l}m}$ follows closely that of Hughes [117].

Appendix C

The discrete spectrum of the FD sources

In general the (t, r) component of the source can be Fourier decomposed as

$$T_{lm}(t,r) = \int \tilde{T}_{lm}(r) e^{-i\omega t}\, d\omega \;, \tag{C.1}$$

In this appendix we demonstrate that, due to the periodic nature of bound geodesic orbits, we can replace the integral in the above equation with a sum so that (in general)

$$T_{lm}(t,r) = \sum_{n,k} \tilde{T}_{lmnk}(r) e^{-i\omega_{mnk} t} \;. \tag{C.2}$$

where the sum is over some suitable harmonics n, k (which depend on the particular orbit being considered).

C.1 The eccentric equatorial source and its spectrum

The azimuthal frequency Ω_φ represents the t-average rate of increase of φ_p over one radial period [see Eq. (2.69)] so that we have

$$\Omega_\varphi = \frac{1}{T_r} \int_0^{T_r} \frac{d\varphi_p}{dt} dt \;. \tag{C.3}$$

We now recall Eq. (2.16) (and the proceeding discussion) which tells we can express the azimuthal motion in the form

$$\varphi_p(t) = \Omega_\varphi t + \tilde{\varphi}(t) \;, \tag{C.4}$$

where $\tilde{\varphi}$ is periodic in t with period T_r [that the azimuthal motion can be written in this form is readily seen by substituting Eq. (C.4) into Eq. (C.3)]. Substituting φ_p from Eq. (C.4) into the SSF source term we get:

$$\begin{aligned} T_{\hat{l}m}(t,r) &= q \left[(r^2 u^t)^{-1} S_{\hat{l}m}(\pi/2; -a^2\omega^2) \delta[r - r_p(t)] e^{-im\tilde{\varphi}(t)} \right] e^{-im\Omega_\varphi t} \;, && \text{(C.5)} \\ &= q \beta_{\hat{l}m}(t,r) e^{-im\Omega_\varphi t} \;, && \text{(C.6)} \end{aligned}$$

where the function $\beta_{\hat{l}m}(t,r)$ is periodic in t with periodicity T_r. Thus we can Fourier decompose $\beta(t,r)$

$$\beta_{\hat{l}m}(t,r) = \sum_n \tilde{\beta}_{\hat{l}mn}(r) e^{-in\Omega_r t} \ , \tag{C.7}$$

and hence we see that $\rho_{\hat{l}m}$ is given by

$$T_{\hat{l}m}(t,r) = q \sum_n \beta_{\hat{l}mn}(r) e^{-i(n\Omega_r + m\Omega_\varphi)t} \ , \tag{C.8}$$

and thus the spectrum of the source is given by

$$\omega = n\Omega_r + m\Omega_\varphi \ , \tag{C.9}$$

where n and m are integers and Ω_φ and Ω_r are defined in Eq. (2.69).

C.2 Spectrum for circular orbits

The periodicity of circular equatorial orbits implies that the spectrum of the Fourier transform in Eqs. (4.4) and (4.7) is given, in our case, by $\omega = n\Omega_\varphi \equiv \omega_n$ for integer n. Hence for circular equatorial orbits ($r_p = r_0$, $\theta_p = \pi/2$, $\varphi_p = \Omega_\varphi t$) $\tilde{T}_{\hat{l}m\omega}$ is given explicitly by

$$\begin{aligned} \tilde{T}_{\hat{l}m\omega_n}(r) &= \frac{\Omega_\varphi}{2\pi} \int_0^{2\pi/\Omega_\varphi} S_{\hat{l}m}(\theta;\sigma^2)\, \rho^2 T \, e^{i(n-m)\Omega_\varphi t} \, dt \ , \\ &= \frac{q}{u^t} S_{\hat{l}m}(\pi/2;\sigma^2) \delta(r - r_0) \delta^n_m \ , \end{aligned} \tag{C.10}$$

where in the second line we have substituted for T from Eq. (4.3). Thus, each m mode contains a single n-harmonic, and the spectrum is given by $\omega_n = \omega_m$ with

$$\omega_m \equiv m\Omega_\varphi \ , \tag{C.11}$$

where m is an integer and Ω_φ is given by (2.44).

Arguing along similar lines as for eccentric equatorial orbits it can be shown that the spectrum for circular inclined orbits is also discrete and given by

$$\omega = \omega_{mk} = m\Omega_\varphi + k\Omega_\theta \ , \tag{C.12}$$

where m and k are integers and Ω_φ and Ω_θ are defined in Eq. (2.56).

Appendix D

Frequency domain field equations

In this appendix we give the explicit form of the coupling terms that appear in (4.57) for ($i = 1, ..., 10$). For brevity we drop the lmn indices and define $f' = 2M/r^2$. The coupling terms are then given by

$$4\tilde{\mathcal{M}}^{(1)}_{(j)}R^{(j)} = \frac{4M}{r^2}f\partial_{r_*}R^{(3)} + \frac{2f}{r^2}\left(1-\frac{4M}{r}\right)\left(R^{(1)}-R^{(5)}-fR^{(3)}\right) - \frac{2f^2}{r^2}\left(1-\frac{6M}{r}\right)R^{(6)} \,, \tag{D.1}$$

$$\begin{aligned}4\tilde{\mathcal{M}}^{(2)}_{(j)}R^{(j)} &= \partial_{r_*}\left(2ff'R^{(3)}\right) + 2(i\omega+\partial_{r_*})\left[f'(R^{(2)}-R^{(1)})\right] - \frac{12Mf}{r^3}R^{(1)} + \frac{2(r+2M)f}{r^3}R^{(2)} \\ &+ \frac{4(3r-8M)Mf}{r^4}R^{(3)} - \frac{2f^2}{r^2}R^{(4)} + \frac{2ff'}{r}R^{(5)} + \frac{4f^2f'}{r}R^{(6)}\end{aligned} \tag{D.2}$$

$$4\tilde{\mathcal{M}}^{(3)}_{(j)}R^{(j)} = -\frac{2f}{r^2}\left[R^{(1)}-R^{(5)}-\left(1-\frac{4M}{r}\right)\left(R^{(3)}+R^{(6)}\right)\right] \,, \tag{D.3}$$

$$\begin{aligned}4\tilde{\mathcal{M}}^{(4)}_{(j)}R^{(j)} &= 2\left(i\omega+\partial_{r_*}\right)\left[\frac{f'}{2}(R^{(4)}-R^{(5)})\right] - \frac{2\mathfrak{L}f}{r^2}R^{(2)} - \frac{2Mf}{r^3}\left(R^{(4)}+4R^{(5)}\right) \\ &+ \frac{ff'}{r}\left(R^{(7)}-\mathfrak{L}R^{(6)}\right) \,,\end{aligned} \tag{D.4}$$

$$4\tilde{\mathcal{M}}^{(5)}_{(j)}R^{(j)} = \frac{4f}{r^2}\left[\left(1-\frac{9M}{2r}\right)R^{(5)} - \frac{\mathfrak{L}}{2}\left(R^{(1)}-fR^{(3)}\right) + \frac{1}{2}\left(1-\frac{3M}{r}\right)\left(\mathfrak{L}R^{(6)}-R^{(7)}\right)\right] \,, \tag{D.5}$$

$$4\tilde{\mathcal{M}}^{(6)}_{(j)}R^{(j)} = -\frac{2f}{r^2}\left[R^{(1)}-R^{(5)}-\left(1-\frac{4M}{r}\right)\left(R^{(3)}+R^{(6)}\right)\right] \,, \tag{D.6}$$

$$4\tilde{\mathcal{M}}^{(7)}_{(j)}R^{(j)} = -\frac{2f}{r^2}\left(R^{(7)}-\lambda R^{(5)}\right) \,, \tag{D.7}$$

$$4\tilde{\mathcal{M}}^{(8)}_{(j)}R^{(j)} = 2\left(i\omega+\partial_{r_*}\right)\left[\frac{f'}{2}(R^{(8)}-R^{(9)})\right] - \frac{2Mf}{r^3}\left(R^{(8)}-2R^{(9)}+R^{(10)}\right) \,, \tag{D.8}$$

$$4\tilde{\mathcal{M}}^{(9)}_{(j)}R^{(j)} = \frac{f}{r^2}\left(1-\frac{9M}{2r}\right)R^{(9)} - \frac{2f}{r^2}\left(1-\frac{3M}{r}\right)R^{(10)} \,, \tag{D.9}$$

$$4\tilde{\mathcal{M}}^{(10)}_{(j)}R^{(j)} = \frac{f}{2r^2}R^{(10)} - \frac{2f\lambda}{r^2}R^{(9)} \,, \tag{D.10}$$

where recall, $\mathfrak{L} = l(l+1)$ and $\lambda = (l+2)(l-1)$.

Appendix E

Time and frequency domain sources

The delta function coefficients, $\mathcal{S}^{(i)}_{lm} \equiv \mathcal{S}^{(i)}_{lm}(t,r)$, in the time domain source terms that appear in Eq. (4.50) are given by [67]

$$\mathcal{S}^{(1)}_{lm} = \frac{4\pi f_p^2}{\mathcal{E} r_p^3}(2\mathcal{E}^2 r_p^2 - f_p r_p^2 - \mathcal{L}^2 f_p) Y^*_{lm}(\pi/2, \varphi_p) \tag{E.1}$$

$$\mathcal{S}^{(2)}_{lm} = -\frac{8\pi f_p^2}{r_p} u^r Y^*_{lm}(\pi/2, \varphi_p) \tag{E.2}$$

$$\mathcal{S}^{(3)}_{lm} = \frac{4\pi}{\mathcal{E} r_p^3} f_p^2 (r_p^2 + \mathcal{L}^2) Y^*_{lm}(\pi/2, \varphi_p) \tag{E.3}$$

$$\mathcal{S}^{(4)}_{lm} = \frac{8\pi i m f_p^2 \mathcal{L}}{r_p^2} Y^*_{lm}(\pi/2, \varphi_p) \tag{E.4}$$

$$\mathcal{S}^{(5)}_{lm} = -\frac{8\pi i m f_p^2 u^r \mathcal{L}}{r_p^2 \mathcal{E}} Y^*_{lm}(\pi/2, \varphi_p) \tag{E.5}$$

$$\mathcal{S}^{(6)}_{lm} = \frac{4\pi f_p^2 \mathcal{L}^2}{r_p^3 \mathcal{E}} Y^*_{lm}(\pi/2, \varphi_p) \tag{E.6}$$

$$\mathcal{S}^{(7)}_{lm} = \left[l(l+1) - 2m^2\right] \mathcal{S}^{(6)}_{lm} \tag{E.7}$$

$$\mathcal{S}^{(8)}_{lm} = \frac{8\pi f_p^2 \mathcal{L}}{r_p^2} Y^*_{lm,\theta}(\pi/2, \varphi_p) \tag{E.8}$$

$$\mathcal{S}^{(9)}_{lm} = -\frac{8\pi f_p^2 u^r \mathcal{L}}{r_p^2 \mathcal{E}} Y^*_{lm,\theta}(\pi/2, \varphi_p) \tag{E.9}$$

$$\mathcal{S}^{(10)}_{lm} = \frac{8\pi i m f_p^2 \mathcal{L}^2}{r_p^3 \mathcal{E}} Y^*_{lm,\theta}(\pi/2, \varphi_p) \tag{E.10}$$

where, recall, a subscript ‘p’ denotes the value of that quantity at the particle.

The equivalent FD source functions $J^{(i)}_{lmn} \equiv J^{(i)}_{lmn}(r)$ that appear in Eq. (8.7) are derived from the TD sources above in the following manner where as an example we shall take the $i = 5$ TD source and decompose it into the FD. The first step is to write

$$\mathcal{S}^{(5)}_{lm}(t,r)\delta(r - r_p) = \sum_{n=0}^{\infty} J^{(5)}_{lmn}(r) e^{-i\omega t} \tag{E.11}$$

The FD source, $J^{(5)}_{lmn}$ is then computed via

$$J^{(5)}_{lmn} = \frac{1}{T_r}\int_0^{T_r} \mathcal{S}^{(5)}_{lm}\delta(r-r_p)e^{i\omega t}\,dt \tag{E.12}$$

Explicitly we have

$$J^{(5)}_{lmn} = \frac{8\pi i m P_{lm}(\pi/2)}{T_r\mathcal{E}}\int_0^{T_r}\frac{f_p^2 u^r}{r_p^2}e^{i(\omega t - m\varphi)}\delta(r-r_p)\,dt \tag{E.13}$$

$$J^{(5)}_{lmn} = -\frac{16\pi m P_{lm}(\pi/2)}{T_r\mathcal{E}}\int_0^{T_r/2}\frac{f_p^2 u^r}{r_p^2}\sin(\omega t - m\varphi)\delta(r-r_p)\,dt \tag{E.14}$$

where in moving from the first to the second line we have made use of the fact that as $t \to -t$, $u^r \to -u^r$ and $\varphi \to -\varphi$ (as well as the even and odd properties of the cos and sin functions respectively). Finally changing integration variable from t to r, and noting that $dt/dr = u^t/u^r$, we arrive at

$$J^{(5)}_{lmn} = -\frac{16\pi f_p^2 m u^t \mathcal{L}}{T_r\mathcal{E}r_p^2}\hat{P}_{lm}(\pi/2)\sin(\omega_{mn}t_p - m\varphi_p) \tag{E.15}$$

The other FD domain source functions are derived in a similar fashion with the results giving

$$J^{(1)}_{lmn} = -\frac{8\pi u^t f_p^2}{T_r\mathcal{E}r_p^3 u^r}(2\mathcal{E}^2 r_p^2 - f r_p^2 - \mathcal{L}^2 f_p)\hat{P}_{lm}(\pi/2)\cos(\omega_{mn}t_p - m\varphi_p) \tag{E.16}$$

$$J^{(3)}_{lmn} = -\frac{8\pi u^t f_p^2}{T_r\mathcal{E}r_p^3 u^r}(r_p^2 + \mathcal{L}^2)\hat{P}_{lm}(\pi/2)\cos(\omega_{mn}t_p - m\varphi_p) \tag{E.17}$$

$$J^{(6)}_{lmn} = -\frac{8\pi u^t f_p^2\mathcal{L}^2}{T_r\mathcal{E}r_p^3 u^r}\hat{P}_{lm}(\pi/2)\cos(\omega_{mn}t_p - m\varphi_p) \tag{E.18}$$

$$J^{(7)}_{lmn} = \left[l(l+1) - 2m^2\right]J^{(6)_{lmn}} \tag{E.19}$$

$$J^{(9)}_{lmn} = -\frac{16 i\pi f_p^2 u^t\mathcal{L}}{T_r\mathcal{E}r_p^2}\hat{P}_{lm,\theta}(\pi/2)\sin(\omega_{mn}t_p - m\varphi_p) \tag{E.20}$$

$$J^{(10)}_{lmn} = -\frac{16 i\pi m u^t\mathcal{L}^2 f_p^2}{T_r\mathcal{E}r_p^3 u^r}\hat{P}_{lm,\theta}(\pi/2)\cos(\omega_{mn}t_p - m\varphi_p) \tag{E.21}$$

where the $\hat{P}_{lm}$ are normalized associated Legendre polynomials i.e. $\hat{P}_{lm} = c_{lm}P_{lm}$ with c_{lm} as defined in Eq. (B.5) and P_{lm} being the standard associated Legendre polynomials. In the above equations we have not provided frequency domain sources for fields $(i) = 2, 4, 8$ as these fields can be constructed from the other fields using the gauge equations (4.58)-(4.61) (and thus the FD sources are not required).

Appendix F

Coupling formula for $h_{\alpha\beta}u^{\alpha}u^{\beta}$

In this appendix we derived the necessary formula to construct the scalar spherical harmonic contribution to the quantity $h_{\alpha\beta}u^{\alpha}u^{\beta}$ from the $\bar{h}^{(i)}$ fields associated with the tensor spherical harmonic decomposition of the trace reversed metric perturbation. Recall that this projection from tensor spherical harmonics to scalar spherical harmonics must be performed before regularization can performed via Eq. (5.47).

For an eccentric orbit in the equatorial plane of a Schwarzschild black hole we have

$$h_{\alpha\beta}u^{\alpha}u^{\beta} = h_{tt}(u^{t})^{2} + h_{rr}(u^{r})^{2} + h_{\varphi\varphi}(u^{\varphi})^{2} + 2h_{tr}u^{r}u^{t} + 2h_{t\varphi}u^{t}u^{\varphi} + 2h_{r\varphi}u^{r}u^{\varphi} \ . \tag{F.1}$$

The components of the metric perturbation are constructed from the $\bar{h}^{(i)}$ fields via [67]

$$h_{\alpha\beta} = \frac{\mu}{2r}\sum_{l=0}^{\infty}\sum_{m=-l}^{l} h^{lm}_{\alpha\beta} \ , \tag{F.2}$$

with

$$h^{lm}_{tt} = \left(\bar{h}^{(1)} + f\bar{h}^{(6)}\right)Y^{lm} \ , \tag{F.3}$$

$$h^{lm}_{tr} = f^{-1}\bar{h}^{(2)}Y^{lm} \ , \tag{F.4}$$

$$h^{lm}_{rr} = f^{-2}\left(\bar{h}^{(1)} - f\bar{h}^{(6)}\right)Y^{lm} \ , \tag{F.5}$$

$$h^{lm}_{t\theta} = r\left(\bar{h}^{(4)}Y^{lm}_{V1} + \bar{h}^{(8)}Y^{lm}_{V2}\right) \ , \tag{F.6}$$

$$h^{lm}_{t\varphi} = r\sin\theta\left(\bar{h}^{(4)}Y^{lm}_{V2} - \bar{h}^{(8)}Y^{lm}_{V1}\right) \ , \tag{F.7}$$

$$h^{lm}_{r\theta} = rf^{-1}\left(\bar{h}^{(5)}Y^{lm}_{V1} + \bar{h}^{(9)}Y^{lm}_{V2}\right) \ , \tag{F.8}$$

$$h^{lm}_{r\varphi} = rf^{-1}\sin\theta\left(\bar{h}^{(5)}Y^{lm}_{V2} - h^{(9)}Y^{lm}_{V1}\right) \ , \tag{F.9}$$

$$h^{lm}_{\theta\theta} = r^{2}\left(\bar{h}^{(3)}Y^{lm} + \bar{h}^{(7)}Y^{lm}_{T1} + \bar{h}^{(9)}Y^{lm}_{V1}\right) \ , \tag{F.10}$$

$$h^{lm}_{\theta\varphi} = r^{2}\sin\theta\left(\bar{h}^{(7)}Y^{lm}_{T2} - \bar{h}^{(10)}Y^{lm}_{T1}\right) \ , \tag{F.11}$$

$$h^{lm}_{\varphi\varphi} = r^{2}\sin^{2}\theta\left(\bar{h}^{(3)}Y^{lm} - \bar{h}^{(7)}Y^{lm}_{T1} - \bar{h}^{(10)}Y^{lm}_{T2}\right) \ . \tag{F.12}$$

The metric components involving θ are not required in this appendix [they multiply factors of $u^{\theta}(=0)$ in Eq. (F.1)] but we give them here for completeness. The angular functions appearing in the above relations are defined as

$$Y^{lm}_{V1} \equiv \frac{1}{l(l+1)} Y^{lm}_{,\theta} \qquad (\text{for } l > 0)\ , \tag{F.13}$$

$$Y^{lm}_{V2} \equiv \frac{1}{l(l+1)} \frac{Y^{lm}_{,\varphi}}{\sin\theta} \qquad (\text{for } l > 0)\ , \tag{F.14}$$

$$Y^{lm}_{T1} \equiv \frac{(l-2)!}{(l+2)!} \left[\sin\theta \left(\frac{Y^{lm}_{,\theta}}{\sin\theta} \right)_{,\theta} - \frac{Y^{lm}_{\varphi\varphi}}{\sin^2\theta} \right] , \qquad (\text{for } l > 1)\ , \tag{F.15}$$

$$Y^{lm}_{T2} \equiv \frac{2(l-2)!}{(l+2)!} \left(\frac{Y^{lm}_{,\varphi}}{\sin\theta} \right)_{,\theta} , \qquad (\text{for } l > 1)\ . \tag{F.16}$$

Each of these needs to be expanded in terms of scalar spherical harmonics which we perform using the identities given in Appendix Sec. B.1.1 the result of which gives

$$\sin\theta Y^{lm}_{V1} = \frac{1}{l(l+1)} \left[\delta^{lm}_{(+1)} Y^{l+1,m} + \delta^{lm}_{(-1)} Y^{l-1,m} \right] , \tag{F.17}$$

$$\sin\theta Y^{lm}_{V2} = \frac{im}{l(l+1)} Y^{lm} , \tag{F.18}$$

$$\sin^2\theta Y^{lm} = \alpha^{lm}_{(+2)} Y^{l+2,m} + \alpha^{lm}_{(0)} Y^{lm} + \alpha^{lm}_{(-2)} Y^{l-2,m} , \tag{F.19}$$

$$\begin{aligned} \sin^2\theta Y^{lm}_{T1} =& \frac{(l-2)!}{(l+2)!} \Big[(\gamma^{lm}_{(+2)} - \beta^{lm}_{(+2)}) Y^{l+2,m} + (\gamma^{lm}_{(0)} - \beta^{lm}_{(0)} + m^2) Y^{lm} \\ & + (\gamma^{lm}_{(-2)} - \beta^{lm}_{(-2)}) Y^{l-2,m} \Big] , \end{aligned} \tag{F.20}$$

$$\sin^2\theta Y^{lm}_{T2} = -\, 2im \frac{(l-2)!}{(l+2)!} \left[\epsilon^{lm}_{(+1)} Y^{l+1,m} + \epsilon^{lm}_{(-1)} Y^{l-1,m} \right] . \tag{F.21}$$

Combining all of the above equations we can write

$$h^{lm}_{\alpha\beta} u^\alpha u^\beta = \left\{ \mathcal{G}^{l+2,m}_{(+2)} + \mathcal{G}^{l+1,m}_{(+1)} + \mathcal{G}^{lm}_{(0)} + \mathcal{G}^{l-1,m}_{(-1)} + \mathcal{G}^{l-2,m}_{(-2)} \right\} Y^{lm} , \tag{F.22}$$

where

$$\mathcal{G}^{lm}_{(+2)} = r^2 (u^\varphi)^2 \left[\alpha^{lm}_{(-2)} \bar{h}^{(3)} - \frac{(l-2)!}{(l+2)!} \left(\gamma^{lm}_{(-2)} - \beta^{lm}_{(-2)} \right) \bar{h}^{(7)} \right] , \tag{F.23}$$

$$\mathcal{G}^{lm}_{(+1)} = 2imr^2 (u^\varphi)^2 \frac{(l-2)!}{(l+2)!} \epsilon^{lm}_{(-1)} \bar{h}^{(10)} - \frac{2ru^t u^\varphi}{l(l+1)} \delta^{lm}_{(-1)} \bar{h}^{(8)} - \frac{2ru^r u^\varphi}{fl(l+1)} \delta^{lm}_{(-1)} \bar{h}^{(9)} , \tag{F.24}$$

$$\begin{aligned} \mathcal{G}^{lm}_{(0)} =& \left(\bar{h}^{(1)} + f\bar{h}^{(6)} \right) (u^t)^2 + 2f^{-1} \bar{h}^{(2)} u^t u^r + f^{-2} \left(\bar{h}^{(1)} - f\bar{h}^{(6)} \right) (u^r)^2 \\ & + \frac{2imr\bar{h}^{(4)}}{l(l+1)} u^t u^\varphi + \frac{2imr\bar{h}^{(5)}}{fl(l+1)} u^r u^\varphi \\ & + r^2 (u^\varphi)^2 \left[\alpha^{lm}_{(0)} \bar{h}^{(3)} - \frac{(l-2)!}{(l+2)!} \left(\gamma^{lm}_{(0)} - \beta^{lm}_{(0)} + m^2 \right) \bar{h}^{(7)} \right] , \end{aligned} \tag{F.25}$$

$$\mathcal{G}^{lm}_{(-1)} = 2imr^2 \frac{(l-2)!}{(l+2)!} \epsilon^{lm}_{(+1)} \bar{h}^{(10)} (u^\varphi)^2 - \frac{2r\bar{h}^{(8)}}{l(l+1)} \delta^{lm}_{(+1)} u^t u^\varphi - \frac{2r\bar{h}^{(9)}}{fl(l+1)} \delta^{lm}_{(+1)} u^r u^\varphi , \tag{F.26}$$

$$\mathcal{G}^{lm}_{(-2)} = r^2 (u^\varphi)^2 \left[\alpha^{lm}_{(+2)} \bar{h}^{(3)} - \frac{(l-2)!}{(l+2)!} \left(\gamma^{lm}_{(+2)} - \beta^{lm}_{(+2)} \right) \bar{h}^{(7)} \right] . \tag{F.27}$$

Appendix G

Regularization parameters in Kerr geometry

The regularization parameters for the SSF in a generic orbit about a Kerr black hole were calculated by Barack and Ori and given in their Ref. [154] (see [76] for a detailed derivation). Their form for generic orbits is rather unweildy but for circular, equatorial orbits they reduce to

$$C_\mu = D_\mu = 0 \, , \tag{G.1}$$

and (in Boyer-Lindquist coordinates)

$$\begin{aligned} A_r^\pm &= \mp q^2 \Delta^{-1/2} \left(g_{\varphi\varphi} + \mathcal{L}^2 \right)^{-1/2} \, , & \text{(G.2)} \\ A_t^\pm &= A_\theta^\pm = A_\varphi^\pm = 0 \, , & \text{(G.3)} \end{aligned}$$

where the metric function $g_{\varphi\varphi}$ is evaluated on the equatorial orbit. The expression for B_μ is more complicated. It can be written in the form

$$B_\mu = q^2 P_{\mu abcd} I^{abcd} \, , \tag{G.4}$$

where hereafter Roman indices run over the two Boyer-Lindquist angular coordinates θ, φ only. The coefficients $P_{\mu abcd}$ are given by

$$P_{\mu abcd} = (4\pi)^{-1} [3 P_{\mu d} P_{abc} - (2 P_{\mu ab} + P_{ab\mu}) P_{cd}] \, , \tag{G.5}$$

where

$$\begin{aligned} P_{\alpha\beta} &\equiv g_{\alpha\beta} + u_\alpha u_\beta \, , & \text{(G.6)} \\ P_{\alpha\beta\gamma} &\equiv (u_\lambda u_\gamma \Gamma^\lambda_{\alpha\beta} + g_{\alpha\beta,\gamma}/2) \, , & \text{(G.7)} \end{aligned}$$

with the Kerr connections $\Gamma^\lambda_{\alpha\beta}$ and metric functions $g_{\alpha\beta}$ all evaluated on the equatorial orbit. The quantities I^{abcd} are

$$I^{abcd} = \int_0^{2\pi} G(\gamma)^{-5/2} (\sin\gamma)^N (\cos\gamma)^{4-N} \, d\gamma \, , \tag{G.8}$$

where

$$G(\gamma) \equiv P_{\varphi\varphi} \sin^2 \gamma + 2P_{\theta\varphi} \sin\gamma \cos\gamma + P_{\theta\theta} \cos^2 \gamma \ , \tag{G.9}$$

and $N \equiv N(abcd)$ is the number of times the index φ occurs in the combination (a, b, c, d), namely

$$N = \delta^a_\varphi + \delta^b_\varphi + \delta^c_\varphi + \delta^d_\varphi \ . \tag{G.10}$$

The quantities I^{abcd} can be written explicitly in terms of complete elliptic integrals [154, 76]. In the case of a circular, equatorial orbit these expressions become

$$I^{abcd} = \frac{2(1-w)I_K^{(N)}\hat{K}(w) + I_E^{(N)}\hat{E}(w)}{24P_{\varphi\varphi}^{5/2}w^4(1-w)^2} \ , \tag{G.11}$$

where $\hat{K}(w) \equiv \int_0^{\pi/2}(1 - w\sin^2 x)^{-1/2}\, dx$ and $\hat{E}(w) \equiv \int_0^{\pi/2}(1 - w\sin^2 x)^{1/2}\, dx$ are complete elliptic integrals of the first and second kind respectively, and

$$w \equiv 1 - \frac{P_{\theta\theta}}{P_{\varphi\varphi}} \ . \tag{G.12}$$

The coefficients $I_K^{(N)}$ and $I_E^{(N)}$ are given by

$$\begin{aligned} I_K^{(0)} &= 16w^2(2-3w) \ , & I_E^{(0)} &= 64w^2(2w-1) \ , \\ I_K^{(1)} &= I_E^{(1)} = 0 \ , & I_K^{(2)} &= 32w^2(w-1) \ , \\ I_E^{(2)} &= 32w^2(w^2-3w+2) \ , & I_K^{(3)} &= I_E^{(3)} = 0 \ , \\ I_K^{(4)} &= -16w^2(w^2+w-2) \ , & I_E^{(4)} &= -64w^2(w^3-w^2-w+1) \ . \end{aligned} \tag{G.13}$$

Recently Heffernan *et al.* [161, 159] provided a substantially simpler formula for this regularization parameter as well as deriving the next order regularization parameter (D_2 in the notation of Sec. 5.4).

Appendix H

Boundary conditions for the radial scalar-field equation

In order to derive recurrence relations for the asymptotic expansion coefficients c_l^{∞} and c_k^{eh} in Eqs. (6.1) and (6.2), we substitute these equations into the homogeneous part of the radial equation (4.16). By comparing the coefficients of r^{-k} (at infinity) or $(r-r_+)^k$ (at the event horizon) we obtain 5-term recurrence relations for each of $c_{k>0}^{\infty}$ and $c_{k>0}^{eh}$. Setting $c_{k<0}^{\infty,eh}=0$ and $c_{k=0}^{\infty,eh}=1$ determines all coefficients $c_{k>0}^{\infty,eh}$ in a recursive fashion.

Explicitly, the above recurrence relations are given by

$$\sum_{i=0}^{5} f_i^{\infty} c_{k-i}^{\infty} = 0, \qquad \sum_{i=0}^{5} f_i^{eh} c_{k-i}^{eh} = 0\,, \tag{H.1}$$

where the various coefficients f_i^{∞} and f_i^{eh} read

$$\begin{aligned}
f_0^{\infty} &= -2k\omega_m i\,,\\
f_1^{\infty} &= k^2-\lambda_{\hat{l}m}+\omega_m(a^2\omega_m-4iM)+k(4iM\omega_m-1)\,,\\
f_2^{\infty} &= 2[ia^2(2-k)\omega_m+M(a^2\omega_m^2-2am\omega_m-2k^2+5k-3+\lambda_{\hat{l}m})]\,,\\
f_3^{\infty} &= 4(k-2)^2M^2-a^2(\lambda_{\hat{l}m}-2k^2+8k-8-m^2)\,,\\
f_4^{\infty} &= -2a^2M(2k^2-11k+15)\,,\\
f_5^{\infty} &= a^4\left(k^2-7k+12\right)\,,
\end{aligned} \tag{H.2}$$

$$\begin{aligned}
f_0^{eh} &= -a^4\left[k^2+k(-3-4ir_+\omega_m)-r_+^2\omega_m^2+2\right]+2a^3mr_+(r_+\omega_m+2ik)\\
&\quad -a^2r_+\left[2M\left(6k^2+k(-12-6ir_+\omega_m)-r_+^2\omega_m^2+3\right)+r_+\left(-12k^2+2k(9+8ir_+\omega_m)+r_+^2\omega_m^2+\lambda_{\hat{l}m}-2\right)\right]\\
&\quad +2amr_+^2\left[r_+\omega_m(r_+-2M)-2ik(3M-2r_+)\right]\\
&\quad +r_+^2\left[4\left(6k^2-9k+1\right)M^2+2Mr_+\left(-20k^2+10ikr_+\omega_m+24k+\lambda_{\hat{l}m}-1\right)\right.\\
&\quad \left.+r_+^2\left(15k^2-12ikr_+\omega_m-15k-\lambda_{\hat{l}m}\right)\right]\ ,\\
f_1^{eh} &= 2\left\{a^4\omega_m(ik+r_+\omega_m-i)-ia^3m(k-2ir_+\omega_m-1)+a^2M\left[2k^2-k(9+6ir_+\omega_m)-3r_+^2\omega_m^2+6ir_+\omega_m+10\right]\right.\\
&\quad +a^2r_+\left[-4k^2+3k(5+4ir_+\omega_m)+2r_+^2\omega_m^2-12ir_+\omega_m+\lambda_{\hat{l}m}-13\right]\\
&\quad +2amr_+[3M(ik+r_+\omega_m-i)+r_+(-3ik-2r_+\omega_m+3i)]\\
&\quad +r_+\left(-8k^2+30k-26\right)M^2+Mr_+^2\left(20k^2-20ikr_+\omega_m-66k+20ir_+\omega_m-3\lambda_{\hat{l}m}+49\right)\\
&\quad \left.+r_+^3\left(-10k^2+15ikr_+\omega_m+30k-15ir_+\omega_m+2\lambda_{\hat{l}m}-20\right)\right\}\ ,\\
f_2^{eh} &= a^4\omega_m^2-2a^3m\omega_m\\
&\quad +a^2\left[-2k^2+4k(-iM\omega_m+4ir_+\omega_m+3)-6Mr_+\omega_m^2+8iM\omega_m+6r_+^2\omega_m^2-32ir_+\omega_m+\lambda_{\hat{l}m}-18\right]\\
&\quad +4iam[M(k-3ir_+\omega_m-2)+r_+(-2k+3ir_+\omega_m+4)]\\
&\quad +2Mr_+\left(10k^2-20ikr_+\omega_m-54k+40ir_+\omega_m-3\lambda_{\hat{l}m}+71\right)\\
&\quad +r_+^2\left(-15k^2+40ikr_+\omega_m+75k-80ir_+\omega_m+6\lambda_{\hat{l}m}-90\right)-4(k-3)^2M^2\ ,\\
f_3^{eh} &= -2a^2\omega_m(-2ik+M\omega_m-2r_+\omega_m+6i)+2am(-ik+2M\omega_m-4r_+\omega_m+3i)\\
&\quad +M\left[4k^2-k(30+20ir_+\omega_m)+60ir_+\omega_m-2\lambda_{\hat{l}m}+56\right]\\
&\quad +2r_+\left[-3k^2+3k(7+5ir_+\omega_m)-45ir_+\omega_m+2\lambda_{\hat{l}m}-36\right]\ ,\\
f_4^{eh} &= a^2\omega_m^2-2am\omega_m-k^2+k(-4iM\omega_m+12ir_+\omega_m+9)+16iM\omega_m-48ir_+\omega_m+\lambda_{\hat{l}m}-20\ ,\\
f_5^{eh} &= 2i(k-5)\omega_m\ . \qquad \text{(H.3)}
\end{aligned}$$

Appendix I

Perturbations of singular matrices

In the following sections we shall denote matrices with capital letters, vectors with bold-type and scalars with lower case regular-type. A vector $\mathbf{a}$ shall be considered a column vector and its transpose, denoted $\mathbf{a^T}$ a row vector. The product $\mathbf{a^T}.\mathbf{b}$ denotes the inner product of vectors $\mathbf{a}$ and $\mathbf{b}$ whereas the product $\mathbf{b}.\mathbf{a^T}$ denotes the outer product of the two vectors.

The goal in this appendix is to provide a method to accurately solve a linear system of the form

$$M\mathbf{x} = \mathbf{b} \ , \tag{I.1}$$

where M is a nearly singular matrix. Such a matrix has a high condition number which indicates that numerically inverting M and solving the system via $\mathbf{x} = M^{-1}\mathbf{b}$ will produce inaccurate results when using double precision arithmetic.

Instead we propose a solution if M and $\mathbf{b}$ can be expanded in the following manner

$$M = A + \epsilon B_1 + \epsilon^2 B_2 + \dots \ , \tag{I.2}$$

$$\mathbf{b} = \mathbf{b_0} + \epsilon\mathbf{b_1} + \epsilon^2\mathbf{b_2} + \dots \ , \tag{I.3}$$

where A is a singular matrix, B_n are matrices which can be either regular or singular, the $\mathbf{b_n}$ are vectors and ϵ is small parameter.

I.1 Perturbation of a singular linear system with null space of dimension one

In this section we will, for simplicity, assume that null space of A has dimension one such that null$(A) = \{\mathbf{u_0}\}$, where $\mathbf{u_0}$ is the eigenvector associated with the zero eigenvalue $\lambda_0 = 0$. The problem we face is of the form

$$(A + \epsilon B_1 + \epsilon^2 B_2 + \dots)\mathbf{y} = \epsilon(\mathbf{b_0} + \epsilon\mathbf{b_1} + \epsilon^2\mathbf{b_2} + \dots) \ , \tag{I.4}$$

where we have defined $\mathbf{y} = \epsilon\mathbf{x}$. The first step is to expand $\mathbf{y}$ in the form

$$\mathbf{y} = \mathbf{y_0} + \epsilon\mathbf{y_1} + \epsilon^2\mathbf{y_2} + \dots \ , \tag{I.5}$$

and substitute it into Eq. (I.4). Our goal is now to solve for $\mathbf{y}$ (and hence $\mathbf{x}$) order by order. Collecting $\mathcal{O}(\epsilon^0)$ terms we see

$$A\mathbf{y_0} = 0\ , \tag{I.6}$$

implying that $\mathbf{y_0}$ is a multiple of the null eigenvector of A and so can be written as $\mathbf{y_0} = c_0\mathbf{u_0}$ where c_0 is a constant. We determine c_0 by examining the $\mathcal{O}(\epsilon^1)$ piece of Eq. (I.4) which gives

$$A\mathbf{y_1} = \mathbf{b_0} - c_0 B_1 \mathbf{u_0}\ . \tag{I.7}$$

where we have substituted for $\mathbf{y_0}$. We now introduce the left null eigenvector $\mathbf{v_0^T}$ associated with λ_0 defined through $\mathbf{v_0^T}A = A^T\mathbf{v_0} = 0$. Multiplying Eq. (I.7) through by $\mathbf{v_0^T}$ and rearranging we get

$$c_0 = \frac{\mathbf{v_0^T}.\mathbf{b_0}}{\mathbf{v_0^T}B_1\mathbf{u_0}}\ . \tag{I.8}$$

We now turn our attention to constructing the $\mathbf{y_1}$ vector. Equation (I.7) is under-determined and so we look for another condition on $\mathbf{y_1}$. The $\mathcal{O}(\epsilon^2)$ piece of Eq. (I.4) gives us the relation

$$A\mathbf{y_2} = \mathbf{b_1} - B_1\mathbf{y_1} - B_2\mathbf{y_0}\ . \tag{I.9}$$

As before we multiply through by $\mathbf{v_0^T}$ and, upon rearranging, we find

$$\mathbf{v_0^T}.B_1\mathbf{y_1} = \mathbf{v_0^T}.\mathbf{b_1} - \mathbf{v_0^T}.B_2\mathbf{y_0}\ . \tag{I.10}$$

This gives us a condition on $\mathbf{y_1}$ which when combined with Eq. (I.7) allows for a unique solution for $\mathbf{y_1}$. It is straightforward now to carry this to any order with the iterative equations given by

$$A\mathbf{y_n} = \mathbf{b_{n-1}} - \sum_{i=1}^{n} B_i\mathbf{y_{n-i}}\ , \tag{I.11}$$

$$\mathbf{v_0^T}.B_1\mathbf{y_n} = \mathbf{v_0^T}.\mathbf{b_n} - \mathbf{v_0^T}.\sum_{i=2}^{n} B_i\mathbf{y_{n-i-1}}\ , \tag{I.12}$$

where we take $\mathbf{b_{n<0}} = \mathbf{y_{n<0}} = 0$. When M and $\mathbf{b}$ have the form of Eqs. (I.2) and (I.3), Eqs. (I.7)-(I.12) allow for the solution to Eq. (I.1) to be constructed without having to invert any near singular matrices.

I.2 Extension to a system with null space of dimension two

If our singular matrix A has a null space of dimension two such that null$(A) = \{\mathbf{u_0}, \mathbf{u_1}\}$ then Eq. (I.6) implies

$$\mathbf{y}_0 = c_0\mathbf{u_0} + c_1\mathbf{u_1}\ . \tag{I.13}$$

To find c_0 and c_1 we, as before, introduce the left eigenvectors of A which we denote by $\mathbf{v_0^T}$ and $\mathbf{v_1^T}$. Left multiplying Eq. (I.7) by both of these vectors gives two relations that when solved simultaneously gives

$$c_0 = \frac{\mathbf{v_0^T}.\mathbf{b_0}(\mathbf{v_1^T}.B_1\mathbf{u_1}) - \mathbf{v_0^T}B_1\mathbf{u_1}(\mathbf{v_1^T}\mathbf{b_0})}{\mathbf{v_0^T}.B_1\mathbf{u_1}(\mathbf{v_1^T}.B_1\mathbf{u_0}) - \mathbf{v_0^T}.B_1\mathbf{u_0}(\mathbf{v_1^T}.B_1\mathbf{u_1})} \;, \tag{I.14}$$

$$c_1 = \frac{\mathbf{v_0^T}.\mathbf{b_0}(\mathbf{v_1^T}.B_1\mathbf{u_0}) - \mathbf{v_0^T}B_1\mathbf{u_0}(\mathbf{v_1^T}\mathbf{b_0})}{\mathbf{v_0^T}.B_1\mathbf{u_1}(\mathbf{v_1^T}.B_1\mathbf{u_0}) - \mathbf{v_0^T}.B_1\mathbf{u_0}(\mathbf{v_1^T}.B_1\mathbf{u_1})} \;. \tag{I.15}$$

The $\mathbf{y_{n>0}}$'s are found much as before except instead of getting one constraint from the $\mathcal{O}(\epsilon^{n+1})$ equation we get two. The system of equations (I.11) and (I.12) are thus extended with the addition of one extra constraint equation:

$$\mathbf{v_1^T}.B_1\mathbf{y_n} = \mathbf{v_1^T}.\mathbf{b_n} - \mathbf{v_1^T}.\sum_{i=2}^{n} B_i\mathbf{y_{n-i-1}} \;. \tag{I.16}$$

I.3 Practical implementation

Equations (I.11), (I.12) and (I.16) form a closed system of linear equations. In order to solve the system numerically it is convenient to express the system as a single matrix equation. One technique to achieve this is to diagonalize the matrix A and use this information to extract the 'bad row(s)' of the matrix equation and replace them with the constraints. We present an alternative technique that we believe is simpler to implement in code. We present the technique for a general system of equations that take the form

$$A\mathbf{y} = \mathbf{b} \;, \tag{I.17}$$

$$\mathbf{c^T}.\mathbf{y} = s \;, \tag{I.18}$$

where Eq. (I.17) is an under-determined system of linear equations with the matrix A having a null space of dimension one and Eq. (I.18) is a constraint that closes the system of equations. With $\mathbf{v_0^T}$ as the left null eigenvector of A we propose that the unique solution to the above system of equations coincides with the solution of the equation

$$(A + \mathbf{v_0}.\mathbf{c^T})\mathbf{y} = b + \mathbf{v_0}s \;. \tag{I.19}$$

To show that this does indeed give the same solution as the original set of equations we suppose that A can be diagonalized such that $PA = DP$ where P is a matrix of eigenvectors of A and D is the diagonal matrix of eigenvalues of A. Multiplying Eq. (I.19) on the left by P we get

$$(DP + P\mathbf{v_0}.\mathbf{c^T})\mathbf{y} = P(\mathbf{b} + \mathbf{v_0}s) \;. \tag{I.20}$$

We now suppose, without loss of generality, that the null eigenvector is in the j'th row of P which we will denote by $[P]_j = \mathbf{v_0^T}$. Correspondingly the 0 eigenvalue is in the j'th row of D. Furthermore we must have $[P\mathbf{b}]_j = 0$ in order for our original system of equations to have a solution. Examining the j'th row of Eq. (I.20) we therefore find a scalar equation that reads

$$[P\mathbf{v_0}.\mathbf{c^T}.\mathbf{y}]_j = [P\mathbf{v_0}s]_j \;, \tag{I.21}$$

which implies the constraint Eq. (I.18) so long as $[P]_j v_0 \neq 0$ which turns out to always hold: recall that the j'th row of P is the null eigenvector, namely $\mathbf{v_0^T}$, and therefore $[P]_j\mathbf{v_0} = |\mathbf{v_0}|^2 \neq 0$.

Bibliography

[1] LIGO website, `http://www.ligo.caltech.edu/`

[2] VIRGO website, `http://www.ego-gw.it/`

[3] GEO 600 webite, `http://www.geo600.org/`

[4] N. J. Cornish, ArXiv e-prints(Apr. 2012), arXiv:1204.2000

[5] LISA website, `http://lisa.nasa.gov/`

[6] Y. Mino, M. Sasaki, and T. Tanaka, Phys. Rev. D **55**, 3457 (1997), arXiv:gr-qc/9606018

[7] T. C. Quinn and R. M. Wald, Phys. Rev. D **56**, 3381 (1997), arXiv:gr-qc/9610053

[8] L. Barack and A. Ori, Phys. Rev. D **61**, 061502 (2000), arXiv:gr-qc/9912010

[9] P. Amaro-Seoane, S. Aoudia, S. Babak, P. Binétruy, E. Berti, A. Bohé, C. Caprini, M. Colpi, N. J. Cornish, K. Danzmann, J.-F. Dufaux, J. Gair, O. Jennrich, P. Jetzer, A. Klein, R. N. Lang, A. Lobo, T. Littenberg, S. T. McWilliams, G. Nelemans, A. Petiteau, E. K. Porter, B. F. Schutz, A. Sesana, R. Stebbins, T. Sumner, M. Vallisneri, S. Vitale, M. Volonteri, and H. Ward, ArXiv e-prints(Jan. 2012), arXiv:1201.3621

[10] M. Camenzind, *Compact Objects in Astrophysics: White Dwarfs, Neutron Stars, and Black Holes*, Astronomy and Astrophysics Library (Springer, 2007) ISBN 9783540257707

[11] S. S. Doeleman, J. Weintroub, A. E. E. Rogers, R. Plambeck, R. Freund, R. P. J. Tilanus, P. Friberg, L. M. Ziurys, J. M. Moran, B. Corey, K. H. Young, D. L. Smythe, M. Titus, D. P. Marrone, R. J. Cappallo, D. C.-J. Bock, G. C. Bower, R. Chamberlin, G. R. Davis, T. P. Krichbaum, J. Lamb, H. Maness, A. E. Niell, A. Roy, P. Strittmatter, D. Werthimer, A. R. Whitney, and D. Woody, Nature **455**, 78 (Sep. 2008), arXiv:0809.2442

[12] A. M. Ghez, S. Salim, S. D. Hornstein, A. Tanner, J. R. Lu, M. Morris, E. E. Becklin, and G. Duchêne, Ap. J. **620**, 744 (Feb. 2005), arXiv:astro-ph/0306130

[13] A. M. Ghez, S. Salim, N. N. Weinberg, J. R. Lu, T. Do, J. K. Dunn, K. Matthews, M. R. Morris, S. Yelda, E. E. Becklin, T. Kremenek, M. Milosavljevic, and J. Naiman, Ap. J. **689**, 1044 (Dec. 2008), arXiv:0808.2870

[14] C. Hopman and T. Alexander, Ap. J **645**, L133 (Jul. 2006), arXiv:astro-ph/0603324

[15] M. A. Gürkan and C. Hopman, MNRAS. **379**, 1083 (Aug. 2007), arXiv:0704.2709

[16] M. C. Miller, M. Freitag, D. P. Hamilton, and V. M. Lauburg, Ap. J **631**, L117 (Oct. 2005), arXiv:astro-ph/0507133

[17] Y. Levin, MNRAS. **374**, 515 (Jan. 2007), arXiv:astro-ph/0603583

[18] M. Freitag, Classical and Quantum Gravity **18**, 4033 (2001)

[19] L. Ferrarese and D. Merritt, Ap. J **539**, L9 (Aug. 2000), arXiv:astro-ph/0006053

[20] L. Barack and C. Cutler, Phys. Rev. D **70**, 122002 (Dec. 2004), arXiv:gr-qc/0409010

[21] L. Barack and C. Cutler, Phys. Rev. D **69**, 082005 (Apr. 2004), arXiv:gr-qc/0310125

[22] J. R. Gair, L. Barack, T. Creighton, C. Cutler, S. L. Larson, E. S. Phinney, and M. Vallisneri, Classical and Quantum Gravity **21**, 1595 (Oct. 2004), arXiv:gr-qc/0405137

[23] K. Glampedakis, Classical and Quantum Gravity **22**, 605 (Aug. 2005), arXiv:gr-qc/0509024

[24] N. Yunes, P. Pani, and V. Cardoso, ArXiv e-prints(Dec. 2011), arXiv:1112.3351

[25] K. Glampedakis and S. Babak, Classical and Quantum Gravity **23**, 4167 (Jun. 2006), arXiv:gr-qc/0510057

[26] J. R. Gair, C. Tang, and M. Volonteri, Phys. Rev. D **81**, 104014 (May 2010), arXiv:1004.1921

[27] A. Einstein, Annalen der Physik **354**, 769 (1916), ISSN 1521-3889

[28] L. Blanchet, ArXiv e-prints(Jul. 2009), arXiv:0907.3596

[29] A. Einstein, L. Infeld, and B. Hoffmann, The Annals of Mathematics, Second Series **39**, pp. 65 (1938), ISSN 0003486X

[30] J. H. Taylor, L. A. Fowler, and P. M. McCulloch, Nature **277**, 437 (1979)

[31] J. H. Taylor and J. M. Weisberg, Ap. J. **253**, 908 (1982)

[32] J. M. Weisberg and J. H. Taylor, in *Binary Radio Pulsars*, Astronomical Society of the Pacific Conference Series, Vol. 328, edited by F. A. Rasio & I. H. Stairs (2005) p. 25, arXiv:astro-ph/0407149

[33] M. Kramer, I. H. Stairs, R. N. Manchester, M. A. McLaughlin, A. G. Lyne, R. D. Ferdman, M. Burgay, D. R. Lorimer, A. Possenti, N. D'Amico, J. M. Sarkissian, G. B. Hobbs, J. E. Reynolds, P. C. C. Freire, and F. Camilo, Science **314**, 97 (Oct. 2006), arXiv:astro-ph/0609417

[34] L. Blanchet, G. Faye, B. R. Iyer, and S. Sinha, Classical and Quantum Gravity **25**, 165003 (Aug. 2008), arXiv:0802.1249

[35] A. Buonanno, B. R. Iyer, E. Ochsner, Y. Pan, and B. S. Sathyaprakash, Phys. Rev. D **80**, 084043 (Oct. 2009), arXiv:0907.0700

[36] L. Smarr, A. Čadež, B. DeWitt, and K. Eppley, Phys. Rev. D **14**, 2443 (Nov 1976)

[37] F. Pretorius, APS Meeting Abstracts, 13006(2004)

[38] F. Pretorius, Phys. Rev. Lett. **95**, 121101 (2005)

[39] M. Campanelli, C. O. Lousto, P. Marronetti, and Y. Zlochower, Phys. Rev. Lett. **96**, 111101 (2006)

[40] J. G. Baker, J. Centrella, D. Choi, M. Koppitz, and J. van Meter, Phys. Rev. D **73**, 104002 (May 2006), arXiv:gr-qc/0602026

[41] S. A. Hughes, M. Favata, and D. E. Holz, in *Growing Black Holes: Accretion in a Cosmological Context*, edited by A. Merloni, S. Nayakshin, & R. A. Sunyaev (2005) pp. 333–339, arXiv:astro-ph/0408492

[42] P. A. Sundararajan, G. Khanna, and S. A. Hughes, Phys. Rev. D **81**, 104009 (May 2010), arXiv:1003.0485

[43] L. Rezzolla, R. P. Macedo, and J. L. Jaramillo, Physical Review Letters **104**, 221101 (Jun. 2010), arXiv:1003.0873

[44] S. E. Gralla, A. I. Harte, and R. M. Wald, Phys. Rev. D **80**, 024031 (2009), arXiv:0905.2391

[45] H. P. Pfeiffer, ArXiv e-prints(Mar. 2012), arXiv:1203.5166

[46] C. O. Lousto and Y. Zlochower, Physical Review Letters **106**, 041101 (Jan. 2011), arXiv:1009.0292

[47] A. Buonanno and T. Damour, Phys. Rev. D **59**, 084006 (1999)

[48] A. Buonanno, G. B. Cook, and F. Pretorius, Phys. Rev. D **75**, 124018 (Jun. 2007), arXiv:gr-qc/0610122

[49] T. Damour and A. Nagar arXiv:0906.1769v1

[50] T. Regge and J. A. Wheeler, Physical Review **108**, 1063 (Nov. 1957)

[51] F. J. Zerilli, Phys. Rev. D **9**, 860 (Feb. 1974)

[52] V. Moncrief, Phys. Rev. D **9**, 2707 (May 1974)

[53] V. Moncrief, Phys. Rev. D **10**, 1057 (Aug. 1974)

[54] S. A. Teukolsky, Phy. Rev. Lett. **29**, 1114 (1972)

[55] S. A. Teukolsky, Ap. J. **185**, 635 (Oct. 1973)

[56] L. Barack and A. Ori, Phys. Rev. D **64**, 124003 (Dec. 2001), arXiv:gr-qc/0107056

[57] Y. Mino, Phys. Rev. D **67**, 084027 (2003), arXiv:gr-qc/0302075

[58] N. Sago, T. Tanaka, W. Hikida, and H. Nakano, Progress of Theoretical Physics **114**, 509 (2005), arXiv:gr-qc/0506092

[59] S. Drasco and S. A. Hughes, Phys. Rev. D **73**, 024027 (2006), arXiv:gr-qc/0509101

[60] R. Fujita, W. Hikida, and H. Tagoshi, Progress of Theoretical Physics **121**, 843 (Apr. 2009), arXiv:0904.3810

[61] L. Barack and C. O. Lousto, Phys. Rev. D **72**, 104026 (2005), arXiv:gr-qc/0510019

[62] L. Barack and N. Sago, Phys. Rev. D **75**, 064021 (2007), arXiv:gr-qc/0701069

[63] S. Detweiler, Phys. Rev. D **77**, 124026 (2008), arXiv:0804.3529

[64] M. V. Berndtson, ArXiv e-prints(2009), arXiv:0904.0033

[65] A. G. Shah, T. S. Keidl, J. L. Friedman, D.-H. Kim, and L. R. Price, Phys. Rev. D **83**, 064018 (Mar. 2011), arXiv:1009.4876

[66] S. Akcay, Phys. Rev. D **83**, 124026 (2011), arXiv:1012.5860

[67] L. Barack and N. Sago, Phys. Rev. D **81**, 084021 (2010), arXiv:1002.2386

[68] M. Boyle, D. A. Brown, L. E. Kidder, A. H. Mroué, H. P. Pfeiffer, M. A. Scheel, G. B. Cook, and S. A. Teukolsky, Phys. Rev. D **76**, 124038 (Dec. 2007), arXiv:0710.0158

[69] L. Blanchet, S. Detweiler, A. Le Tiec, and B. F. Whiting, Phys. Rev. D **81**, 064004 (Mar. 2010), arXiv:0910.0207

[70] L. Blanchet, S. Detweiler, A. Le Tiec, and B. F. Whiting, Phys. Rev. D **81**, 084033 (2010), arXiv:1002.0726

[71] M. Favata, Phys. Rev. D **83**, 024027 (Jan. 2011), arXiv:1008.4622

[72] A. Le Tiec, A. H. Mroué, L. Barack, A. Buonanno, H. P. Pfeiffer, N. Sago, and A. Taracchini, Physical Review Letters **107**, 141101 (Sep. 2011), arXiv:1106.3278

[73] A. Le Tiec, E. Barausse, and A. Buonanno, Physical Review Letters **108**, 131103 (Mar. 2012), arXiv:1111.5609

[74] S. E. Gralla and R. M. Wald, Class. Quantum. Grav. **25**, 205009 (2008), arXiv:0806.3293

[75] E. Poisson, Living Reviews in Relativity **7**, 6 (2004), arXiv:gr-qc/0306052

[76] L. Barack, Class. and Quantum. Grav. **26**, 213001 (2009), arXiv:0908.1664

[77] W. G. Anderson and A. G. Wiseman, Classical and Quantum Gravity **22**, 783 (Aug. 2005), arXiv:gr-qc/0506136

[78] M. Casals, S. Dolan, A. C. Ottewill, and B. Wardell, Phys. Rev. D **79**, 124043 (2009), arXiv:0903.0395

[79] B. F. Whiting and L. R. Price, Classical and Quantum Gravity **22**, 589 (Aug. 2005)

[80] T. S. Keidl, A. G. Shah, J. L. Friedman, D. Kim, and L. R. Price, Phys. Rev. D **82**, 124012 (2010), arXiv:1004.2276

[81] L. Barack and D. A. Golbourn, Phys. Rev. D **76**, 044020 (2007), arXiv:0705.3620

[82] I. Vega and S. Detweiler, Phys. Rev. D **77**, 084008 (Apr. 2008), arXiv:0712.4405

[83] I. Vega, B. Wardell, and P. Diener, Classical and Quantum Gravity **28**, 134010 (Jul. 2011), arXiv:1101.2925

[84] L. M. Burko, Class. Quant. Grav. **17**, 227 (2000), arXiv:gr-qc/9911042

[85] A. G. Wiseman, Phys. Rev. D **61**, 084014 (Apr. 2000), arXiv:gr-qc/0001025

[86] L. Barack and L. M. Burko, Phys. Rev. D **62**, 084040 (2000), arXiv:gr-qc/0007033

[87] L. M. Diaz-Rivera, E. Messaritaki, B. F. Whiting, and S. Detweiler, Phys. Rev. D **70**, 124018 (2004), arXiv:gr-qc/0410011

[88] P. Cañizares and C. F. Sopuerta, Phys. Rev. D **79**, 084020 (2009), arXiv:0903.0505

[89] J. Thornburg, ArXiv e-prints(Jun. 2010), arXiv:1006.3788

[90] I. Vega, P. Diener, W. Tichy, and S. Detweiler, Phys. Rev. D **80**, 084021 (Oct. 2009), arXiv:0908.2138

[91] S. R. Dolan and L. Barack, Phys. Rev. D **83**, 024019 (Jan. 2011), arXiv:1010.5255

[92] R. Haas, Phys. Rev. D **75**, 124011 (2007), arXiv:0704.0797

[93] P. Canizares, C. F. Sopuerta, and J. L. Jaramillo, Phys. Rev. D **82**, 044023 (2010), arXiv:1006.3201

[94] J. Thornburg, private communication

[95] P. Diener, I. Vega, B. Wardell, and S. Detweiler, ArXiv e-prints(Dec. 2011), arXiv:1112.4821

[96] L. M. Burko and Y. T. Liu, Phys. Rev. D **64**, 024006 (2001)

[97] N. Warburton and L. Barack, Phys. Rev. D **81**, 084039 (2010), arXiv:1003.1860

[98] S. R. Dolan, L. Barack, and B. Wardell, Phys. Rev. D **84**, 084001 (Oct. 2011), arXiv:1107.0012

[99] N. Warburton and L. Barack, Phys. Rev. D **83**, 124038 (Jun. 2011), arXiv:1103.0287

[100] A. G. Smith and C. M. Will, Phys. Rev. D **22**, 1276 (1980)

[101] T. S. Keidl, J. L. Friedman, and A. G. Wiseman, Phys. Rev. D **75**, 124009 (Jun. 2007), arXiv:gr-qc/0611072

[102] R. Haas, ArXiv e-prints(Dec. 2011), arXiv:1112.3707

[103] L. Barack and C. O. Lousto, Phys. Rev. D **66**, 061502 (2002), arXiv:gr-qc/0205043

[104] S. Akcay, "A Fast Frequency-Domain Algorithm for Gravitational Self-Force: II, Eccentric Orbitsin Schwarzschild Spacetime," In preparation

[105] J. E. McClintock, R. Narayan, S. W. Davis, L. Gou, A. Kulkarni, J. A. Orosz, R. F. Penna, R. A. Remillard, and J. F. Steiner, Classical and Quantum Gravity **28**, 114009 (Jun. 2011), arXiv:1101.0811

[106] M. J. Valtonen, S. Mikkola, D. Merritt, A. Gopakumar, H. J. Lehto, T. Hyvönen, H. Rampadarath, R. Saunders, M. Basta, and R. Hudec, Ap. J. **709**, 725 (Feb. 2010), arXiv:0912.1209

[107] See J. Thornburg's talk at Capra2011 Southampton

[108] T. Damour, Phys. Rev. D **81**, 024017 (2010), arXiv:0910.5533

[109] N. Warburton, S. Akcay, L. Barack, J. R. Gair, and N. Sago, Phys. Rev. D **85**, 061501 (Mar. 2012), arXiv:1111.6908

[110] L. Barack, A. Ori, and N. Sago, Phys. Rev. D **78**, 084021 (2008), arXiv:0808.2315

[111] C. Darwin, Royal Society of London Proceedings Series A **263**, 39 (Aug. 1961)

[112] C. Cutler, D. Kennefick, and E. Poisson, Phys. Rev. D **50**, 3816 (Sep. 1994)

[113] H. Goldstein, C. Poole, and J. Safko, *Classical mechanics* (Addison Wesley, 2002) ISBN 9780201657029

[114] R. P. Kerr, Phys. Rev. Lett. **11**, 237 (1963)

[115] E. Poisson, *A Relativist's Toolkit : The Mathematics of Black-Hole Mechanics* (Cambridge University Press, 2004) pp. 10–60

[116] C. Misner, K. Thorne, and J. Wheeler, *Gravitation* (W.H.Freeman, 1973)

[117] S. A. Hughes, Phys. Rev. D **61**, 084004 (2000)

[118] K. Glampedakis and D. Kennefick, Phys. Rev. D **66**, 044002 (2002), arXiv:gr-qc/0203086

[119] J. M. Bardeen, W. H. Press, and S. A. Teukolsky, Ap. J. **178**, 347 (1972)

[120] J. Levin and G. Perez-Giz, Phys. Rev. D **79**, 124013 (Jun. 2009), arXiv:0811.3814

[121] S. Babak, H. Fang, J. R. Gair, K. Glampedakis, and S. A. Hughes, Phys. Rev. D **75**, 024005 (Jan 2007)

[122] S. Babak, H. Fang, J. R. Gair, K. Glampedakis, and S. A. Hughes, Phys. Rev. D **77**, 049902 (Feb 2008)

[123] R. Grossman, J. Levin, and G. Perez-Giz, Phys. Rev. D **85**, 023012 (Jan. 2012), arXiv:1105.5811

[124] R. Grossman, J. Levin, and G. Perez-Giz, ArXiv e-prints(Aug. 2011), arXiv:1108.1819

[125] W. Schmidt, Classical and Quantum Gravity **19**, 2743 (May 2002), arXiv:gr-qc/0202090

[126] R. Fujita and W. Hikida, Classical and Quantum Gravity **26**, 135002 (Jul. 2009), arXiv:0906.1420

[127] R. Fujita, private communication

[128] P. A. Sundararajan, Phys. Rev. D **77**, 124050 (Jun. 2008), arXiv:0803.4482

[129] L. Barack and N. Sago, Phys. Rev. D **83**, 084023 (Apr. 2011), arXiv:1101.3331

[130] T. C. Quinn, Phys. Rev. D **62**, 064029 (2000), arXiv:gr-qc/0005030

[131] B. Carter, Physical Review **174**, 1559 (1968)

[132] D. R. Brill, P. L. Chrzanowski, C. M. Pereira, E. D. Fackerell, and J. R. Ipser, Phys. Rev. D **5**, 1913 (1972)

[133] S. Chandrasekhar, "The mathematical theory of black holes," (Oxford University Press, 1992) Chap. 58

[134] C. W. Misner, Phys. Rev. Lett. **28**, 994 (1972)

[135] W. H. Press and S. A. Teukolsky, Nature **238**, 211 (Jul. 1972)

[136] S. E. Gralla, Phys. Rev. D **84**, 084050 (Oct. 2011), arXiv:1104.5635 [gr-qc]

[137] C. O. Lousto and B. F. Whiting, Phys. Rev. D **66**, 024026 (Jul. 2002), arXiv:gr-qc/0203061

[138] A. Ori, Phys. Rev. D **67**, 124010 (Jun. 2003), arXiv:gr-qc/0207045

[139] S. Detweiler and E. Poisson, Phys. Rev. D **69**, 084019 (Apr 2004)

[140] S. R. Golbourn, *Perturbations from a Particle Orbiting a Black Hole with an Application to Self Force Calculations*, Ph.D. thesis, University of Southampton (2009)

[141] L. Barack, unpublished notes

[142] D. Dolan and L. Barack, in preparation

[143] P. A. M. Dirac, Royal Society of London Proceedings Series A **167**, 148 (1938)

[144] B. S. Dewitt and R. W. Brehme, Annals of Physics **9**, 220 (1960)

[145] J. M. Hobbs, Annals of Physics **47**, 141 (1968)

[146] R. Geroch and J. Traschen, Phys. Rev. D **36**, 1017 (Aug 1987)

[147] A. Pound, Phys. Rev. D **81**, 024023 (2010), arXiv:0907.5197

[148] E. Poisson, ArXiv General Relativity and Quantum Cosmology e-prints(Dec. 1999), arXiv:gr-qc/9912045

[149] J. Jackson, *Classical electrodynamics* (Wiley, 1999) ISBN 9780471309321

[150] J. D. Jackson, American Journal of Physics **75**, 844 (2007)

[151] R. Penrose, *The Road to Reality: A Complete Guide to the Laws of the Universe*, Vintage Series (Vintage Books, 2007) ISBN 9780679776314

[152] S. Detweiler and B. F. Whiting, Phys. Rev. D **67**, 024025 (2003), arXiv:gr-qc/0202086

[153] B. S. DeWitt and C. M. DeWitt, Physics. N.Y. **1**, 3 (1964)

[154] L. Barack and A. Ori, Phys. Rev. Lett. **90**, 111101 (2003), see [76] for the explicit expressions of the regularization parameters in terms of elliptic integrals.

[155] S. Detweiler, E. Messaritaki, and B. F. Whiting, Phys. Rev. D **67**, 104016 (2003), arXiv:gr-qc/0205079

[156] N. Sago, L. Barack, and S. Detweiler, Phys. Rev. D **78**, 124024 (Dec. 2008), arXiv:0810.2530

[157] L. Barack and N. Sago, Phys. Rev. D **83**, 084023 (Apr. 2011), arXiv:1101.3331

[158] L. Barack and A. Ori, Phys. Rev. D **67**, 024029 (Jan. 2003), arXiv:gr-qc/0209072

[159] A. Heffernan, A. Ottewill, and B. Wardell(Apr. 2012), arXiv:1204.0794

[160] L. Barack, Y. Mino, H. Nakano, A. Ori, and M. Sasaki, Phys. Rev. Lett. **88**, 091101 (2002), arXiv:gr-qc/0111001

[161] See A. Heffernan's talk at Capra2011 Southampton

[162] L. Barack, D. A. Golbourn, and N. Sago, Phys. Rev. D **76**, 124036 (2007), arXiv:0709.4588

[163] B. Wardell, I. Vega, J. Thornburg, and P. Diener, ArXiv e-prints(Dec. 2011), arXiv:1112.6355

[164] T. Hinderer and É. É. Flanagan, Phys. Rev. D **78**, 064028 (2008), arXiv:0805.3337

[165] W. Hikida, H. Nakano, and M. Sasaki, Class. Quantum. Grav. **22**, 753 (2005), arXiv:gr-qc/0411150

[166] GNU Scientific Library, `http://www.gnu.org/software/gsl/`

[167] S. E. Gralla, J. L. Friedman, and A. G. Wiseman(2005), arXiv:gr-qc/0502123

[168] D. V. Gal'tsov, Journal of Physics A Mathematical General **15**, 3737 (1982)

[169] R. Haas and E. Poisson, Phys. Rev. D **74**, 044009 (2006), arXiv:gr-qc/0605077

[170] L. M. Burko, Phys. Rev. Lett. **84**, 4529 (2000), arXiv:gr-qc/0003074

[171] T. Damour and G. Esposito-Farèse, Phys. Rev. D **53**, 5541 (1996), arXiv:gr-qc/9506063

[172] S. Hopper and C. R. Evans, Phys. Rev. D **82**, 084010 (2010), arXiv:1006.4907

[173] R. Haas, private communication

[174] J. L. Barton, D. J. Lazar, D. J. Kennefick, G. Khanna, and L. M. Burko, Phys. Rev. D **78**, 064042 (2008), arXiv:0804.1075

[175] L. Barack and N. Sago, Phys. Rev. Lett. **102**, 191101 (2009), arXiv:0902.0573

[176] S. Detweiler, private communication

[177] R. Haas and E. Poisson, Class. Quantum. Grav. **22**, 739 (2005), arXiv:gr-qc/0411108

[178] L. M. Burko, A. I. Harte, and E. Poisson, Phys. Rev. D **65**, 124006 (2002), arXiv:gr-qc/0201020

[179] A. Ori and K. S. Thorne, Phys. Rev. D **62**, 124022 (2000), arXiv:gr-qc/0003032

[180] A. Pound and E. Poisson, Phys. Rev. D **77**, 044013 (2008), arXiv:0708.3033

[181] J. R. Gair, E. E. Flanagan, S. Drasco, T. Hinderer, and S. Babak, Phys. Rev. D **83**, 044037 (2011)

[182] Gravitational self force calculator webpage: `http://www.personal.soton.ac.uk/njw1g08/GSF/`

[183] T. Apostolatos, D. Kennefick, A. Ori, and E. Poisson, Phys. Rev. D **47**, 5376 (Jun 1993)

[184] S. Drasco and S. A. Hughes, Phys. Rev. D **69**, 044015 (Feb. 2004), arXiv:astro-ph/0308479

[185] E. E. Flanagan and T. Hinderer, ArXiv e-prints(Sep. 2010), arXiv:1009.4923

[186] C. Merlín González and L. Barack, private communication

[187] A. Pound, ArXiv e-prints(Jan. 2012), arXiv:1201.5089

[188] S. E. Gralla, ArXiv e-prints(Mar. 2012), arXiv:1203.3189

[189] S. Detweiler, Phys. Rev. D **85**, 044048 (Feb. 2012), arXiv:1107.2098

[190] K. S. Thorne, Rev. Mod. Phys. **52**, 299 (Apr 1980)